UNIVERSITY OF EASTERN PIEDMONT "AMEDEO AVOGADRO"

DEPARTMENT OF SCIENCES AND TECHNOLOGICAL INNOVATION

Non-destructive X-ray based characterization of materials assisted by multivariate methods of data analysis: from theory to application

Mattia Lopresti

Thesis for the degree of

Doctor of Philosophy in
Chemistry & Biology, XXXIV cycle

Supervisor: Prof. Marco Milanesio
Co-supervisor: Dott. Luca Palin
Coordinator: Prof. Gian Cesare Tron

SSD: CHIM/02

Non-destructive X-ray based characterization of materials assisted by multivariate methods of data analysis: from theory to application

DECLARATION AND AUTHORISATION TO ANTIPLAGIARISM DETECTION

The undersigned ...... Mattia Lopresti ......student of the Chemistry & Biology

Ph.D course (.34.th Cycle)

declares:

- to be aware that the University has adopted a web-based service to detect plagiarism through
  a software system called "Turnit.in",

- his/her Ph.D. thesis was submitted to Turnit.in scan and reasonably it resulted an original
  document, which correctly cites the literature;

acknowledges:

- his/her Ph.D. thesis can be verified by his/her Ph.D. tutor and/or Ph.D Coordinator in order
  to confirm its originality.

Date: 15/11/2021 ...... Signature: ......

XY/tcs
Percorso del file

Ai miei genitori

Acknowledgements

«Nove gloriosi anni dopo io completa mia tesi di dottorato.
Duecentomila schede perforate in preciso preciso ordine che
compone primissimo programma di mondo di gioco di tris.
Ordine preciso preciso rende lui imbattibile.»
(Nahasapeemapetilon, A., Ph.D.)

Abstract

Non-destructive techniques based on X-rays are an increasingly important tool in many sectors, ranging from industry to fine arts, from medicine to basic research. Over the last century, the study of the physical phenomena underlying the interaction between X-rays and matter has led to the development of many different techniques suitable for morphological, textural, elementary and compositional analysis. Furthermore, with the development of the hardware technology and its automation thanks to IT advancements, enormous progress has been made also from the point of view of data collection and nowadays it is possible to carry out measurement campaigns by collecting many GigaBytes of data in a few hours. Already huge data sets are further enlarged when samples are analyzed with a multitechnique approach and/or at *in situ* conditions with time becoming an additional variable. This Ph.D. project was born by a collaboration between UniUPO and Bytest, a company specialized in non-destructive analysis for quality control and certification. During the project period, innovative materials related to Bytest's skills and needs were developed, in particular regarding innovative radiodense materials for the replacement of lead and steel in X-ray shielding and protective coatings for ultralight magnesium alloys. In this context, it was therefore necessary to develop both materials and methods for their characterization. The new approaches have been grown up

from an instrumental viewpoint and with regard to the analysis of the data obtained, for which the use and development of multivariate methods was central. In this context, extensive use has been made of principal component analysis and experimental design methods. One prominent topic of the study involved the development of in situ analysis methods of evolving samples as a response to different types of gradients (time, space, chemical, concentration and temperature). In fact, while in large structures such as synchrotrons carrying out analyzes under variable conditions is now consolidated practice, on a laboratory scale this type of experiments is still relatively young and the methods of data analysis of data sets evolving over time still have large perspectives for development especially, if integrated by multivariate methods. The purpose of this thesis, in addition to present the materials developed during the three-year Ph.D. course, is to propose new methods of data analysis and innovative instrumental setups for conducting non-destructive experiments. The materials developed during the three-year doctorate were exploited as test cases for the developed methods of data analysis and innovative instrumental setups will be proposed to conduct experiments in a sample-conservative way.

Keywords: NDT, materials composite, Magnesium alloys, X-ray radiography, X-Ray diffraction, X-ray tomography, X-ray Fluorescence, epoxy resins, HVOF, nanomaterials, Multivariate analysis, PCA, nonlinear regression methods, Qualitative analysis, Quantitative analysis, Gradients, temporal series, spatial gradients, temperature gradients, microdiffraction, temperature gradients, eutectics, method development, LCA, IET, Geant4, X-ray simulation method, X-ray Shielding

Sommario

Le tecniche non distruttive basate sui raggi X sono uno strumento sempre più importante in molti settori, che spaziano dall'industria alle belle arti, dalla medicina alla ricerca di base. Nel corso dell'ultimo secolo, lo studio dei fenomeni fisici alla base dell'interazione tra i raggi X e la materia ha portato allo sviluppo di molte tecniche differenti adatte all'analisi morfologica, tessiturale, elementare e composizionale. Inoltre, con lo sviluppo del settore informatico sono stati fatti enormi passi in avanti anche dal punto di vista della raccolta dati ed oggigiorno è possibile fare campagne di misura raccogliendo molti GigaBytes di dati in poche ore. Data set già enormi vengono ulteriormente ingranditi quando campioni vengono analizzati con approccio multitecnica: essenziale per avere una panoramica completa su di un campione in analisi. Questo progetto di dottorato nasce dalla collaborazione tra UniUPO e Bytest, azienda specializzata nelle analisi non distruttive per controllo qualità e certificazione. Durante il periodo del progetto sono stati sviluppati materiali innovativi legati alle competenze e necessità di Bytest, in particolare riguardanti materiali radiodensi innovativi per la sostituzione del piombo e dell'acciaio e di rivestimenti per leghe di magnesio. In questo contesto, si è quindi reso necessario lo sviluppo sia di materiali che di metodi di analisi, sia dal punto di vista strumentale, sia riguardo l'analisi dei dati ottenuti, per cui l'integrazione di metodi multivariati è stata centrale. Un

altro importante oggetto di studio ha riguardato lo sviluppo di metodi di analisi in situ di campioni sottoposti a diversi tipi di gradienti (di tempo, spaziali, e di temperatura). Infatti, mentre nelle grandi strutture come i sincrotroni effettuare analisi in condizioni variabili è ormai pratica consolidata, su scala di laboratorio questo tipo di esperimenti sono ancora relativamente giovani, con appena un paio di decenni di vita, ed i metodi di analisi dati di dataset che evolvono nel tempo hanno ancora ampio margine di sviluppo specialmente se integrati con i metodi multivariata. Di seguito in questa tesi saranno presentati i materiali sviluppati nel corso del triennio di dottorato e saranno proposti nuovi metodi di analisi dati e setup strumentali innovativi per condurre esperimenti in maniera conservativa.

Parole Chiave: NDT, materials composite, Magnesium alloys, X-ray radiography, X-Ray diffraction, X-ray tomography, X-ray Fluorescence, epoxy resins, HVOF, nanomaterials, Multivariate analysis, PCA, non-linear regression methods, Qualitative analysis, Quantitative analysis, Gradients, temporal series, spatial gradients, temperature gradients, microdiffraction, temperature gradients, eutectics, method development, LCA, IET, Geant4, X-ray simulation method, X-ray Shielding

LIST OF PUBLICATIONS

[1] Lopresti M, Alberto G, Cantamessa S, Cantino G, Conterosito E, Palin L, Milanesio M. Light Weight, Easy Formable and Non-Toxic Polymer-Based Composites for Hard X-ray Shielding: A Theoretical and Experimental Study. International Journal of Molecular Sciences. 2020; 21(3):833.
https://doi.org/10.3390/ijms21030833

[2] Conterosito E, Lopresti M, Palin L. In Situ X-ray Diffraction Study of Xe and CO2 Adsorption in Y Zeolite: Comparison between Rietveld and PCA-Based Analysis. Crystals. 2020; 10(6):483.
https://doi.org/10.3390/cryst10060483

[3] Lopresti, M., Palin, L., Alberto, G., Cantamessa, S., Milanesio, M. (2021). Epoxy resins composites for X-ray shielding materials additivated by coated barium sulfate with improved dispersibility. In Materials Today Communications (Vol. 26, p. 101888). Elsevier BV.
https://doi.org/10.1016/j.mtcomm.2020.101888

[4] Guccione P, Lopresti M, Milanesio M, Caliandro R. Multivariate Analysis Applications in X-ray Diffraction. Crystals. 2021; 11(1):12.
https://doi.org/10.3390/cryst11010012

[5] Mangolini, B., Palin, L., Milanesio, M., Lopresti, M. (2021). XRF

and XRPD data sets in ternary mixtures with high level micro-absorption and/or preferred orientations problems for phase quantification analysis. In Data in Brief (Vol. 36, p. 107043). Elsevier BV.
https://doi.org/10.1016/j.dib.2021.107043

[6] Mangolini B, Lopresti M, Conterosito E, Rombolà G, Palin L, Gianotti V, Milanesio M. Low-Cost Biobased Coatings for AM60 Magnesium Alloys for Food Contact and Harsh Environment Applications. International Journal of Molecular Sciences. 2021; 22(9):4915.
https://doi.org/10.3390/ijms22094915

[7] Massara, N., Boccaleri, E., Milanesio, M., Lopresti, M. (2021). IETeasy: An open source and low-cost instrument for impulse excitation technique, applied to materials classification by acoustical and mechanical properties assessment. In HardwareX (Vol. 10, p. e00231). Elsevier BV.
https://doi.org/10.1016/j.ohx.2021.e00231

[8] Massara, N., Boccaleri, E., Milanesio, M., Lopresti, M. (2021). Impulse excitation technique data set collected on different materials for data analysis methods and quality control procedures development. In Data in Brief (Vol. 36, p. 107503). Elsevier BV.
https://doi.org/10.1016/j.dib.2021.107503

List of published Data Sets

[1] Mangolini, B., Palin, L., Milanesio, M., Lopresti, M. (2021). Dataset for "XRF and XRPD data sets in ternary mixtures with high level micro-absorption and/or preferred orientations problems for phase quantification analysis" [Data set]. Mendeley. https://doi.org/10.17632/JS2NZWF5MD.5

[2] Massara, N., Boccaleri, E., Milanesio, M., Lopresti, M. (2021). Dataset for "Impulse excitation technique data set collected on different materials for data analysis methods and quality control procedures development" [Data set]. Mendeley. https://doi.org/10.17632/SRFP7X6WXM.1

Contents

List of Figures

LIST OF TABLES

LISTINGS

Glossary

Eutectic   A mixture of substances whose melting point is lower than that of its constituent substances taken individually.

Geant4   Geant4 (for GEometry ANd Tracking) is a platform for "the simulation of the passage of particles through matter" using Monte Carlo methods. The platform was developed at the European Center for Nuclear Research (CERN). In the present work, it was mainly used to simulate the behavior of photons produced by X-ray based instruments.

LAG   A mechanochemical techniques in which a small amount of liquid (usually few drops) is used to enhance or control a solid state reaction driven by the mechanical action of grinding.

Radiodensity   The property of a particular material not to be crossed by the portion of the electromagnetic spectrum referred to as "ionizing radiation", which includes X-rays and gamma rays. Also defined radiopacity.

Radiopacity   See radiodensity.

ROOT   ROOT is a powerful framework for data analysis developed at the European Center for Nuclear Research (CERN). Among its notable features are some of the most efficient minimization algorithms (Minuit, Migrad), a system of data management and compression and an the Cling interpreter for C++ macros.

RootProf   RootProf is a software for multivariate analysis of profiles obtained by diffraction of spectroscopic measurements. The software is based on the ROOT framework for data analysis developed at the European Center for Nuclear Research (CERN). RootProf can carry various analyses, such as: qualitative, quantitative, morphological, crystallinity, covariance analysis.

Acronyms

ATR-IR   Attenuated total reflectance infra-red

DES   Deep eutectic solvents
DoE   Design of experiments

EDS   Energy-dispersive X-ray spectroscopy

FP   Fundamental parameters

HVOF   High velocity oxygen fuel

IET   Impulse excitation technique
IL   Ionic liquids

LAG   Liquid assisted grinding
LCA   Life cycle assessment
LDH   Layered double hydroxides

MA   Micro absorption
MSA   Multivariate statistical analysis

NDT   Non Destructive Technique, or Non Destructive Test

PA11   Polyamide 11

PC   Principal component
PCA   Principal components analysis
PO   Preferred orientation
PONKCS   Partial or no known crystal structure
POSS   Polyhedral olygomeric silsesquioxanes

QPA   Quantitative phase analysis

RIR   Relative intensity ratio
RR   Rietveld refinement

SC-XRD   Single crystal X-ray diffraction
SGF   Savitzky-Golay filtering
SSR   Squared sum of residuals
SVD   Singular value decomposition

TGA   Thermogravimetric analysis

XRCT   X-ray computed tomography
XRD   X-ray diffraction
XRDR   X-ray digital radiography
XRF   X-ray fluorescence
XRPD   X-ray powder diffraction

Symbols

A Area of a surface.

E Elastic modulus of a material.

ϕ Average diameter of a particle

I Inertia moment.

$\mathbf{F}_{(n,n)}$ Forcefield matrix

$\mathbf{L}_{(m,p)}$ Matrix of the loadings for m principal components and p variables.

$\mathbf{T}_{(n,m)}$ Matrix of the scores for n cases and m principal components.

$\mathbf{X}_{(n,p)}$ Experimental matrix of n cases and p variables.

$\mathbf{M}$ Matrix of the model

n General number of cases, samples or rows in matrix notation.

$\overline{y}$ Mean of a group of samples

p General number of variables, samples or rows in matrix notation.

q	Number of components of a mixture
ρ	Density of a material.
σ	Standard deviation of a group of samples
σ^2	Variance of a group of samples
$\%CV$	Variance of a group of samples
Z	Atomic number.

Part I

Introduction

State of the art in Bytest/UniUPO

In America, first you get the sugar, then you get the power, then you get the women.

Simpson, H.J.

Non-destructive testing (NDT) is a group of techniques of major importance in many fields of materials science[1–3], natural science[4], medicine[5] and fine arts[6]. The main advantage of NDT is that it is not invasive and does not require the removal of parts of the analysed samples[7, 8]. The techniques based on X-rays are some among the most important as they allow to conduct qualitative analyses, both at the elementary level (Energy-dispersive X-ray spectroscopy - EDS, X-ray fluorescence - XRF), and as regards the crystalline habit (X-ray powder diffraction - XRPD, Single crystal X-ray diffraction - SC-XRD) of a given substance, or the presence of voids, defects or density gradients in massive samples (X-ray digital radiography - XRDR, X-ray computed tomography - XRCT). Some

of this techniques can be found in the gemmological[9, 10] and petrographic fields[11], where the identification of the crystalline structure and the cell parameters of a given mineral under analysis are essential information for conducting surveys, for identifying a gem or to determine the features and stresses to which a mineral has been subjected[12]. In the mineralogical field, XRPD and SC-XRD are two essential techniques for the aforementioned reasons and are often accompanied by elementary analysis techniques to dispel any doubts regarding the atomic composition and the presence of inclusions or impurities. In the medical field, NDTs are preferred over interventions such as biopsies. XRDR is a technique that every hospital and dental office is equipped with and is essential for making diagnoses without having to first intervene surgically[13]. In the dental field, radiography is used on very small areas to analyse whether a tooth or groups of a few teeth at a time have a homogeneous density, if there are defects or microfractures or if a filling is firmly fixed on the tooth or not. Both computed tomography and radiography, in addition to monitoring bone and chest-related problems[14], can be used to identify effusions or the state of internal organs that would otherwise be difficult to observe[15]. In pneumonia-related emergencies, radiography and tomography are widely used to monitor the state of the lungs of patients in hospital and intervene in case of severe complications[16]. Regarding materials science, NDTs are commonly used as characterization methods in synthesis laboratories to verify reaction products. X-ray diffraction-based tools can be used to investigate transformations that develop under different environmental conditions[17], then run high or low temperature experiments and in combination with other techniques, in particular XRF[18–21], but also infrared or Raman spectroscopies[22, 23]. With the arrival on the market of detectors with rapid signal processing it was also possible to start performing experiments in situ[17, 22], in the presence of time, temperature, spatial or chemical gradients, allowing experiments that in the last decades would have been possible mainly in

large scale facilities, such as synchrotrons. Within the cultural heritage field, X-ray-based techniques are used to analyse the materials of various artifacts and findings. The fluorescence of X-rays in particular can be used for the elementary analysis of pigments[24], in order to be able to intervene in restorations with materials similar to those present on a work of art. They can also help to understand how certain pigments or materials used by ancient populations may have been produced[25]. Finally, XRF and EDS can also be used for provenance analyses, which can help reconstruct ancient trade routes or raw material extraction sites[26, 27]. However, probably the largest area of use of NDTs lies in the industrial field, in particular the part dedicated to quality control and certification. Many companies are equipped with one or more techniques for the non-destructive analysis of their products, for example cement factories, metallurgical and pharmaceutical industries. Other companies, such as Bytest s.r.l., are born to perform quality analysis and product certification, in support of large companies, such as those that are part of the world of rail, road or aerospace transports. In this scenario, the development of new analysis methods and new data analysis techniques, i.e. the topics of the present thesis, are an important goal for a more complete and deep understanding of future materials and their characterization. In the following sections, the state of the art of materials preparation and characterization within Bytest and UniUPO will be presented, both at industrial level and in university research laboratories. Moreover, the state of the art of the methods of analysis of innovative and traditional materials will be described, with a particular note dedicated to the interpretation of the collected data. Modern methods of data analysis will be described with a focus on multivariate analysis, still scarcely used in many of the previously mentioned fields. Finally, process optimization techniques will be illustrated that can accompany and optimize both the development of innovative materials and the quality control procedures.

1.1 Non-destructive techniques

Bytest is a company owned by TUV that is placed in the field of certifications and quality control for third-party companies, in particular those related to the world of transport and energy production. The company is expert in several characterization methods, which include: destructive, nondestructive, chemical and metallographic tests. The samples in analysis are from different materials classes, the most common being metal alloys and composite materials. Bytest's experience in NDT includes the most spread techniques in the sector, such as: radiography (both digital and analogical), computed tomography, ultrasound analysis, magnetic particles, penetrating liquids, visual examination, induced currents, leak detection and Nital Etch. The first two techniques in the list are both based on X-rays and are becoming more and more widespread and popular in the industrial field for the analysis of finished pieces. However, the most widespread form of radiography is still the analogical one, based on the development of radiographic plates, which has various environmental and logistical implications:

- development solvents are often toxic and not environmentally sustainable;

- the slabs can be damaged over time if not stored properly and in an air-conditioned environment;

- certification companies must keep the analyses for tens of years (for aircraft, the plates must be kept for the entire life of the aircraft), with consequent problems of space and storage.

The instrumental upgrade that took place within the project that financed this Ph.D., has allowed the introduction of booths for digital radiography, which, however, do not have standardized and tested methodologies for automatic data analysis and recognition. Detection of defects in the samples still needs, at the state of the art, a

human intermediary.

Computed tomography, on the other hand, does not present environmental problems, as the data collection is completely digital. However, special computers with a very large RAM memory are required to be able to view the collected files and Petabytes of space for their storage, since in the new instruments, the collected files can weigh up to hundreds of Gigabytes. Most modern softwares are also capable of automatically identifying defects and voids within samples, making tomography one of the most promising techniques for morphological characterization of samples. The University of Eastern Piedmont (UPO) has, in the various locations of the multicampus, state of the art equipment to meet all the needs of research in the various fields of science and medicine. In the centers of Alessandria and Vercelli various instruments dedicated to the science of materials and chemistry are present. A large part of the department equipment is composed by non-destructive techniques. The techniques based on X-rays available are X-ray diffraction and X-ray fluorescence. Diffraction is mainly carried out with an instrument for powder diffraction, which is equipped with different stages that allow various types of measurements, both in standard conditions and at variable temperatures and atmospheres. The X-ray fluorescence instrument by Nova Res S.r.l., on the other hand, is a small benchtop instrument with a low power (4 W) X-ray tube, capable of supporting the results obtained by other techniques with a compositional analysis. Due to the type of instrument and physical limitations it is not able to identify atoms lighter than sodium and attempts to compensate for this criticality are presented in Part II.

1.2   State of the art on materials

In the following sections the state of the art and the most common applications of the studied materials are presented. During the doctoral period, research work was carried out on many types of materials, almost always analysed with at least one NDT technique. Those listed below are those on which an in-depth study was conducted, characterized by the presence of innovative methods of analysis or extensive use of NDTs. In Section 1.2.1, an overview of radiodense materials, their main applications and the most common additives for X-ray shielding in scientific literature are presented. In Section 1.2.2 the problems of light weight magnesium alloys will be presented, in particular corrosion. The most common methods of protection and preservation of alloys, through the use of innovative coatings will be presented in detail. Finally, in Section 1.2.3, eutectic materials and their uses in the refrigeration industry are presented.

1.2.1   Radiodense materials for X-Ray shielding

The use of X-ray sources also implies the use of adequate protections[28]. For XRPD and XRF instruments such as those described in the previous section, lead and barium based glass and the steel parts of the booths are usually sufficient to stop the X-rays, as the energies involved and the penetrating power are not high. A similar situation can be found in medical and dentistry fields, where the energies of the X-rays are even lower[29]. As for radiographic booths such as those present in Bytest, reinforced concrete bunkers or booths with lead walls several centimeters thick are often required in order to ensure adequate protection. Industrial radiography, in order to carry out analyses on materials with a high atomic number and high density, requires much higher photon energies to increase penetration. A common radiographic booth emits photons in a range between 20 keV to 300 keV, while in more modern booths the energies also

rise to 500 keV to 600 keV[30]. X-ray shielding materials tradition-ally consist of thick concrete walls for bunkers and steel or lead plates for compact cabins. However, these metals present various problems related to excessive weight, difficult workability as regards steel and very poor mechanical properties as regards lead[31]. Issues like the described ones prevent a cabin to be transported entirely to the place of installation, forcing it to be disassembled and carried by means of winches to be assembled once the location has been found. A further disadvantage is also given by the environmental implications of the use of these traditional materials, as extraction processes, pollution caused by processing and long-term toxicity (of the product or its pro-duction processes) are scarcely sustainable and dangerous for both the environment than for man[31]. In the last thirty years, more atten-tion has been paid to the environmental issue to which human health is in any case connected as a consequence. In the same period of time, the scientific literature has been filled with articles proposing alter-native solutions to materials that traditionally involve environmental problems. The same was also done for the radiological field, where alternatives to traditional lead and steel screens were proposed and other types of materials, such as composites and nanoparticles based, began to be considered. The most common solutions take into con-sideration polymeric matrices which are given radiodense properties, which they normally would not have. To do this, the most considered ways are two:

- synthesize a new polymer with high atomic number elements, so that it inherently has radiopacity properties[32–34];

- add an existing polymer with highly shielding additives, dis-persing it during the polymerization phase[31, 35, 36].

The second type of solution certainly has disadvantages compared to the first, such as the potential problems of adhesion to the polymer-additive interface, which inevitably affect the degree of dispersion

of the additives, the mechanical properties of the resulting piece and the releases of the additives. On the other hand, finding a solution to the interface problems is a more environmentally friendly solution than synthesizing polymers with high Z elements (typically iodine[32, 34]) which generally require polluting solvents. The additives most widespread to increase the radiodensity of polymers are also in this case divided into two categories:

- heavy metal particles[37], such as lead, tungsten, gadolinium and bismuth;

- powders of inert compounds with high density and/or with at least one high Z atom: barium sulphate[31, 35, 38, 39], bismuth oxide, tin oxide and calcium carbonate.

Due to the low interfacial interaction between metals and polymers, the first solution is not a valid alternative to traditional screens, as over time the toxic additives would be released from the matrix, also by virtue of the radiative degradation of the piece. Inert and non-toxic minerals such as barium sulphate and bismuth oxide instead constitute a good alternative to traditional screens, as even in the event of releases they would not have adverse effects on human health and toward the environment.

In the context of the Ph.D. period, a new line of research was created on innovative and eco-friendly radiopaque composite materials (Chapter 7). Particular attention was paid to the study of the interface between polymers and additives and to the sedimentation process that occurs during the polymerization phase (Chapter 8).

1.2.2 Coatings for light-weight magnesium alloys

Light weight magnesium-based alloys are characterized by a low density and a high strength-to-weight ratio. The density of magnesium in fact is only $1.74 \, \mathrm{g \, cm^{-3}}$ (aluminum is $2.70 \, \mathrm{g \, cm^{-3}}$), a value very close to those belonging to polymers. Due to these characteristics,

magnesium-based alloys are used in the automotive and aerospace fields, where the lightness of the pieces, necessary for a reduction in fuel consumption, combined with a high resistance, necessary for structural applications, make them ideal materials. Another advantage of magnesium is the relatively low melting point of its alloys (around 650 °C), which also makes them suitable for casting.

The major disadvantage of magnesium, however, consists in its low reduction potential (from −2.36 V to −2.69 V depending on the reaction involved), which causes the it to be easily oxidized. Corrosion induced by magnesium oxidation occurs when in contact with water and acids and can be described with the following general reaction:

$$Mg + 2\,H_3O^+ \longrightarrow Mg(OH)_2\downarrow + 2\,H_2\uparrow \qquad (1.1)$$
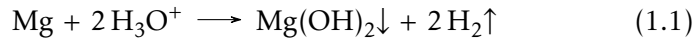
Factors that increases the tendency of magnesium to oxidize are the presence of surface defects, particular shapes that exposes edges and a high surface/volume ratio: this condition occurs when it is reduced to powder or fine chips[40]. For this reason, the mechanical processing of magnesium and its alloys requires caution. While the machining problems have been partially solved by using with consolidated procedures and adding ligands in the alloy that dampen the tendency of magnesium (i.e. calcium) to ignite, the problems related to galvanic corrosion are still a significant obstacle. Surface defects can be corrosion initiators, since, unlike aluminum, the oxide given by the passivation film of magnesium is not resistant to abrasion and is not stable.

Ligands play a key role in defining the stability of magnesium alloys. Copper, iron and nickel are elements that, due to higher reduction potentials, tend to induce galvanic corrosion[41]. On the contrary, aluminum, zinc and manganese help protect the alloy by forming more stable and dense surface phases, which reduce water, acids and oxygen permeation[41]. For the said motives, the most widespread magnesium alloys both in the industrial world and in that of academic research are those with aluminum and manganese as solute

(type AM) and with aluminum, zinc and manganese (type AZ)[41]. Although the ligands are able to mitigate the tendency to corrode, magnesium alloys are not immune to the effects of aggressive conditions, such as the presence of acids or bases (even diluted), humid and saline atmospheres and abrasions that cross the passivation layer[42]. Despite advances in corrosion prevention, magnesium alloys still require protective coatings in the most common applications to protect them from the external environment[43]. The technologies and materials for the coating of metal alloys are many and well known in scientific literature, but the technology of magnesium is relatively young and the compatibility of these methods in many cases has yet to be verified. The choice of the most appropriate coating depends mainly on the intended use and, consequently, various parameters are evaluated, first of all costs, the environmental impact, the ease of use (not only at the laboratory scale, but also consequently to an industrial scale up) and the performance of the resulting material. Among the best known and most popular methods are laser surface melting[44], which however is a process that requires long processing times and a lot of energy for machinery and electrophoretic deposition of graphene[45]. In the scientific literature one solution consists in the use of powder bio-based coatings[46], mainly Polyamide 11 (PA11)[47, 48], which are sprayed on the product. An alternative deposition method consists in heating the sample and dipping it in the powder, making it melt on contact and forming a compact layer of material. Alternatives include liquid paints and a dip coating of other bio-based materials, such as silicon based varnishes. A second promising technology consists in depositing coating materials (other alloys or compound with high hardness, such as carbides) through High Speed Oxygen Fuel technology (HVOF)[49, 50], which is a powder spraying technique that is carried out at a high temperature. Particles, heated by the flame of a torch, are sprayed onto the sample and directly sintered on its surface, forming a dense coating with exceptional surface adhesion strength. In chapter 9 the work carried

out on coatings for magnesium alloys is presented in two separate strands: the first as a continuation of the work in ref.[42], in which the PA11 coatings have been additivated with different nanomaterials (Graphite, layered double hydroxides and POSS) to improve the mechanical, functional and surface properties. The second line, on the other hand, is carried out in collaboration with the University of Modena and is based on the coating using the HVOF technique on a AZ31 magnesium alloy with an aluminum bronze (Cu-9Al-1Fe) and with tungsten carbide (WC-10Co4Cr). As many tests and materials characterizations are ongoing, the chapter is accompanied by a section in which are displayed expected results and future perspectives on this work.

1.2.3   Eutectic materials

An eutectic mixture, or eutectic, is defined as "*a mixture of substances whose melting point is lower than that of its constituent substances taken individually*"[51]. Figure 1.1 shows an example of a phase diagram in which the eutectic point is highlighted by a black arrow. The eutectic point is a system invariant[53] and is identified by a precise composition and at a precise temperature. At the eutectic composition, the eutectic reaction occurs by varying temperature as described in the following reaction[53]:

$$L_e \xrightleftharpoons[\text{heating}]{\text{cooling}} \alpha_e + \beta_E \qquad (1.2)$$
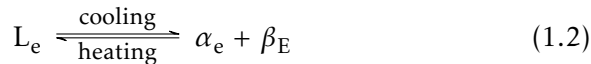
Where L_e is the liquid phase at the eutectic composition and $\alpha_e + \beta_e$ are the two components of the mixture. Eutectic mixtures have some important properties that make them used in various industrial fields. One of these, which is the one that characterized the study presented in Chapter 11, is that the solidification in the eutectic reaction occurs isothermally up to complete solidification. Furthermore, the phase transformation always occurs without a phase separation[54], which happens instead intersecting the liquidus curves in the phase
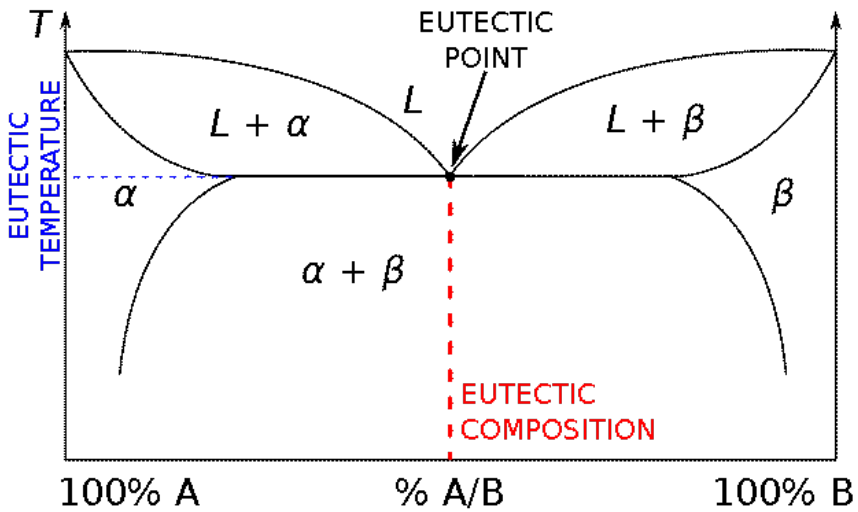
Figure 1.1: Example of a phase diagram with the coordinates of the eutectic point evidenced and projected on the temperature and composition axes. Figure from ref.[52]

diagram, that is any composition except the eutectic one.

The applications of eutectic mixtures are many and widespread in different aspects of daily life. In the field of metallurgy, the austenite-cementite eutectic mixture is a composition that is typically used for welding steels. Other metal alloys, such as that of tin and lead, respectively with composition $0.63w/w$ - $0.37w/w$, are used for soldering. Specifically, the latter is used for soldering in the field of electronics and for the repair of low voltage and low amperage electrical circuits. Another eutectic mixture that is used in everyday life is galinstan, an alloy composed of gallium, indium and tin that has replaced mercury in thermometers due to the toxicity problems associated with it. Remaining in home use, homes and offices can often be found inkjet printers, whose cartridges contain eutectic mixtures, so that the ink can be used at a relatively low temperature. Among the most famous eutectic mixtures is the one between sodium chloride and water, with composition $0.233w/w$ - $0.767w/w$ respectively, which has a eutectic

point a equal to −21.2 °C. This mixture is used for melting ice and snow for safety reasons, for the ice cream industry and for refrigeration. In collaboration with a company that deals with refrigeration, a study reported in Chapter 11 was conducted on eutectic mixtures through in situ X-ray diffraction experiments.

Bibliography

[1] I. Amenabar, F. Lopez, and A. Mendikute. «In Introductory Review to THz Non-Destructive Testing of Composite Mater.» In: *Journal of Infrared, Millimeter, and Terahertz Waves* 34.2 (Nov. 2012), pp. 152–169. DOI: 10.1007/s10762-012-9949-z. URL: https://doi.org/10.1007/s10762-012-9949-z.

[2] M. Bhat. «Non-destructive evaluation of defects and damage in composite materials and structures.» In: *Journal of the Indian Institute of Science* 93.4 (2013). cited By 0, pp. 751–766.

[3] B. Wang et al. «Non-destructive testing and evaluation of composite materials/structures: A state-of-the-art review.» In: *Advances in Mechanical Engineering* 12.4 (Apr. 2020), p. 168781402091376. DOI: 10.1177/1687814020913761. URL: https://doi.org/10.1177/1687814020913761.

[4] V. Cnudde and M. Boone. «High-resolution X-ray computed tomography in geosciences: A review of the current technology and applications.» In: *Earth-Science Reviews* 123 (Aug. 2013), pp. 1–17. DOI: 10.1016/j.earscirev.2013.04.003. URL: https://doi.org/10.1016/j.earscirev.2013.04.003.

[5] K. Kim and W. R. Wagner. «Non-invasive and Non-destructive Characterization of Tissue Engineered Constructs Using Ultrasound Imaging Technologies: A Review.» In: *Annals of Biomedical Engineering* 44.3 (Oct. 2015), pp. 621–635. DOI:

10.1007/s10439-015-1495-0. URL: https://doi.org/10.1007/s10439-015-1495-0.

[6]   D. Thickett et al. «Using non-invasive non-destructive techniques to monitor cultural heritage objects.» In: *Insight - Non-Destructive Testing and Condition Monitoring* 59.5 (May 2017), pp. 230–234. DOI: 10.1784/insi.2017.59.5.230. URL: https://doi.org/10.1784/insi.2017.59.5.230.

[7]   L. Cartz. *Nondestructive Testing: Radiography, Ultrasonics, Liquid Penetrant, Magnetic Particle, Eddy Current.* ASM International, 1995. ISBN: 9780871705174.

[8]   C. Hellier. *Handbook of Nondestructive Evaluation, 3E.* McGraw-Hill Education, 2020. ISBN: 9781260441444.

[9]   F. A. Herzog. «The Potential of a Portable EDXRF Spectrometer for Gemmology.» In: *The Journal of Gemmology* 34.5 (2015), pp. 404–418. DOI: 10.15506/jog.2015.34.5.404. URL: https://doi.org/10.15506/jog.2015.34.5.404.

[10] D. Mannes et al. «Gemmological Investigations on Pearls and Emeralds using Neutron Imaging.» In: *Physics Procedia* 88 (2017), pp. 134–139. DOI: 10.1016/j.phpro.2017.06.018. URL: https://doi.org/10.1016/j.phpro.2017.06.018.

[11] A. Ahmad and K. Al-Bashaireh. «Provenance Determination and Condition Assessment of Archaeological Marble Statues from Gerasa Using Non-Destructive Ultrasonic Technique.» In: *Studies in Conservation* 66.7 (Dec. 2020), pp. 397–412. DOI: 10.1080/00393630.2020.1848268. URL: https://doi.org/10.1080/00393630.2020.1848268.

[12] C. Giacovazzo et al. *Fundamentals of Crystallography.* IUCr texts on crystallography. Oxford University Press, 2002. ISBN: 9780198509585.

[13] P. van der Stelt. «Improved diagnosis with digital radiography.» In: *Current opinion in dentistry* 2 (1992). cited By 10, pp. 1–6.

[14] K. Eguchi, T. Yamada, and M. Kaneko. «Coronet status of digital radiography in chest medicine.» In: *Nihon Kyōbu Shikkan Gakkai zasshi* 30 Suppl (1992). cited By 0, pp. 233–239.

[15] E. Confino. «The use of radiography in reproductive medicine.» In: *Infertility and Reproductive Medicine Clinics of North America* 14.2 (2003). cited By 0, pp. 227–240.

[16] R. S. Al-Umairi et al. «COVID-19 Associated Pneumonia.» In: *Sultan Qaboos University Medical Journal [SQUMJ]* 21.1 (Mar. 2021), e4–11. DOI: 10.18295/squmj.2021.21.01.002. URL: https://doi.org/10.18295/squmj.2021.21.01.002.

[17] E. Conterosito et al. «Facile preparation methods of hydrotalcite layered materials and their structural characterization by combined techniques.» In: *Inorganica Chimica Acta* 470 (Jan. 2018), pp. 36–50. DOI: 10.1016/j.ica.2017.08.007. URL: https://doi.org/10.1016/j.ica.2017.08.007.

[18] M. Bortolotti, L. Lutterotti, and G. Pepponi. «Combining XRD and XRF analysis in one Rietveld-like fitting.» In: *Powder Diffraction* 32 (2017), pp. 225–230. DOI: 10.1017/S0885715617000276.

[19] L. V. Prandel et al. «Mineralogical analysis of clays in hard-setting soil horizons , by X-ray fluorescence and X-ray diffraction using Rietveld method.» In: *Radiation Physics and Chemistry* 95 (2014), pp. 65–68. ISSN: 0969-806X. DOI: 10.1016/j.radphyschem.2012.12.017.

[20] L. Lutterotti et al. «Combined X-Ray diffraction and fluorescence analysis in the cultural heritage field.» In: *Microchemical Journal* 126 (Dec. 2015). DOI: 10.1016/j.microc.2015.12.031.

[21] L. Beck et al. «First use of portable system coupling X-ray diffraction and X-ray fluorescence for in-situ analysis of pre-historic rock art.» In: *Talanta* 129 (2014), pp. 459–464. ISSN: 0039-9140. DOI: https://doi.org/10.1016/j.talanta.2014.04.043.

[22] E. Boccaleri et al. «In situsimultaneous Raman/high-resolution X-ray powder diffraction study of transformations occurring in materials at non-ambient conditions.» In: 40.4 (July 2007), pp. 684–693. DOI: 10.1107/s0021889807025113. URL: https://doi.org/10.1107/s0021889807025113.

[23] M. L. Thomas, I. S. Butler, and J. A. Kozinski. «In situ synchrotron-based X-ray powder diffraction and micro-Raman study of biomass and residue model compounds at hydrothermal conditions.» In: *Energy Science & Engineering* 3.3 (Mar. 2015), pp. 189–195. DOI: 10.1002/ese3.68. URL: https://doi.org/10.1002/ese3.68.

[24] M. Aceto and E. Calà. «Analytical evidences of the use of iron-gall ink as a pigment on miniature paintings.» In: *Spectrochimica Acta Part A: Molecular and Biomolecular Spectroscopy* 187 (Dec. 2017), pp. 1–8. DOI: 10.1016/j.saa.2017.06.017. URL: https://doi.org/10.1016/j.saa.2017.06.017.

[25] M. Aceto et al. «New evidence of non-traditional Egyptian blue manufacture in the 6th century Ashburnham Pentateuch.» In: *Journal of Archaeological Science: Reports* 33 (Oct. 2020), p. 102487. DOI: 10.1016/j.jasrep.2020.102487. URL: https://doi.org/10.1016/j.jasrep.2020.102487.

[26] V. Renda et al. «A multivariate statistical approach of X-ray fluorescence characterization of a large collection of reverse glass paintings.» In: *Spectrochimica Acta Part B: Atomic Spectroscopy* 159 (Sept. 2019), p. 105655. DOI: 10.1016/j.sab.2

019.105655. URL: https://doi.org/10.1016/j.sab.2019
.105655.

[27]   M. Vadrucci et al. «Analysis of Roman Imperial coins by
        combined PIXE, HE-PIXE and μ-XRF.» In: *Applied Radia-
        tion and Isotopes* 143 (Jan. 2019), pp. 35–40. DOI: 10.1016
        /j.apradiso.2018.10.016. URL: https://doi.org/10.101
        6/j.apradiso.2018.10.016.

[28]   R. Mirji and B. Lobo. «24. Radiation shielding materials: A
        brief review on methods, scope and significance.» In: *National
        Conference on 'Advances in VLSI and Microelectronics.'In PC
        Jabin Science College, Huballi, India.* 2017, pp. 96–100.

[29]   M. Petrantonaki et al. «Calculating shielding requirements
        in diagnostic X-ray departments.» In: *The British journal of
        radiology* 72.854 (1999), pp. 179–185.

[30]   R. Behling. *Modern diagnostic x-ray sources: technology, manu-
        facturing, reliability.* CRC Press, 2021.

[31]   M. Lopresti et al. «Light Weight, Easy Formable and Non-
        Toxic Polymer-Based Composites for Hard X-ray Shielding: A
        Theoretical and Experimental Study.» In: *International Journal
        of Molecular Sciences* 21.3 (Jan. 2020), p. 833. DOI: 10.3390
        /ijms21030833. URL: https://doi.org/10.3390/ijms2103
        0833.

[32]   V. S. Nisha and R. Joseph. «Preparation and properties of
        iodine-doped radiopaque natural rubber.» In: *Journal of Ap-
        plied Polymer Science* 105.2 (2007), pp. 429–434. DOI: 10.100
        2/app.26040. URL: https://doi.org/10.1002/app.26040.

[33]   K. R. Houston et al. «Iodinated polyesters as a versatile plat-
        form for radiopaque biomaterials.» In: *Journal of Polymer Sci-
        ence Part A: Polymer Chemistry* 55.13 (May 2017), pp. 2171–
        2177. DOI: 10.1002/pola.28596. URL: https://doi.org/1
        0.1002/pola.28596.

[34]   W. Wang et al. «Development of X-ray opaque poly(lactic acid) end-capped by triiodobenzoic acid towards non-invasive micro-CT imaging biodegradable embolic microspheres.» In: *European Polymer Journal* 108 (Nov. 2018), pp. 337–347. DOI: 10.1016/j.eurpolymj.2018.09.018. URL: https://doi.org/10.1016/j.eurpolymj.2018.09.018.

[35]   M. R. Ambika, N. Nagaiah, and S. K. Suman. «Role of bismuth oxide as a reinforcer on gamma shielding ability of unsaturated polyester based polymer composites.» In: *Journal of Applied Polymer Science* 134.13 (Nov. 2016). DOI: 10.1002/app.44657. URL: https://doi.org/10.1002/app.44657.

[36]   L. Yu et al. «Lightweight Bismuth Titanate (Bi4Ti3O12) Nanoparticle-Epoxy Composite for Advanced Lead-Free X-ray Radiation Shielding.» In: *ACS Applied Nano Materials* 4.7 (2021), pp. 7471–7478.

[37]   M. Kazempour et al. «Assessment of the radiation attenuation properties of several lead free composites by Monte Carlo simulation.» In: *Journal of biomedical physics & engineering* 5.2 (2015), p. 67.

[38]   S. Suman et al. «Development of highly radiopaque flexible polymer composites for X-ray imaging applications and copolymer architecture-morphology-property correlations.» In: *European Polymer Journal* 95 (Oct. 2017), pp. 41–55. DOI: 10.1016/j.eurpolymj.2017.07.021. URL: https://doi.org/10.1016/j.eurpolymj.2017.07.021.

[39]   S. Nambiar, E. K. Osei, and J. T. W. Yeow. «Polymer nanocomposite-based shielding against diagnostic X-rays.» In: *Journal of Applied Polymer Science* 127.6 (June 2012), pp. 4939–4946. DOI: 10.1002/app.37980. URL: https://doi.org/10.1002/app.37980.

[40] M. Esmaily et al. «Fundamentals and advances in magnesium alloy corrosion.» In: *Progress in Materials Science* 89 (Aug. 2017), pp. 92–193. DOI: 10.1016/j.pmatsci.2017.04.011. URL: https://doi.org/10.1016/j.pmatsci.2017.04.011.

[41] G. L. Song and A. Atrens. «Corrosion Mechanisms of Magnesium Alloys.» In: *Advanced Engineering Materials* 1.1 (Sept. 1999), pp. 11–33. DOI: 10.1002/(sici)1527-2648(199909)1:1<11::aid-adem11>3.0.co;2-n. URL: https://doi.org/10.1002/(sici)1527-2648(199909)1:1%3C11::aid-adem11%3E3.0.co;2-n.

[42] B. Mangolini et al. «Low-Cost Biobased Coatings for AM60 Magnesium Alloys for Food Contact and Harsh Environment Applications.» In: *International Journal of Molecular Sciences* 22.9 (May 2021), p. 4915. DOI: 10.3390/ijms22094915. URL: https://doi.org/10.3390/ijms22094915.

[43] G. Song. «Recent Progress in Corrosion and Protection of Magnesium Alloys.» In: *Advanced Engineering Materials* 7.7 (July 2005), pp. 563–586. DOI: 10.1002/adem.200500013. URL: https://doi.org/10.1002/adem.200500013.

[44] J. D. Majumdar et al. «Effect of laser surface melting on corrosion and wear resistance of a commercial magnesium alloy.» In: *Materials Science and Engineering: A* 361.1-2 (Nov. 2003), pp. 119–129. DOI: 10.1016/s0921-5093(03)00519-7. URL: https://doi.org/10.1016/s0921-5093(03)00519-7.

[45] K. Zhang et al. «Electrophoretic deposition of graphene oxide on NiTi alloy for corrosion prevention.» In: *Vacuum* 161 (Mar. 2019), pp. 276–282. DOI: 10.1016/j.vacuum.2018.12.032. URL: https://doi.org/10.1016/j.vacuum.2018.12.032.

[46] P. Borg et al. «Example of industrial valorisation of derivative products of Castor oil.» In: *Oléagineux, Corps gras, Lipides*

16.4-5-6 (July 2009), pp. 211–214. DOI: 10.1051/ocl.2009
.0276. URL: https://doi.org/10.1051/ocl.2009.0276.

[47] M. L. D. Lorenzo, A. Longo, and R. Androsch. «Polyamide
11/Poly(butylene succinate) Bio-Based Polymer Blends.» In:
Materials 12.17 (Sept. 2019), p. 2833. DOI: 10.3390/ma12172
833. URL: https://doi.org/10.3390/ma12172833.

[48] O. Moshynets et al. «Antibiofilm Activity of Polyamide 11
Modified with Thermally Stable Polymeric Biocide Polyhex-
amethylene Guanidine 2-Naphtalenesulfonate.» In: *Interna-
tional Journal of Molecular Sciences* 20.2 (Jan. 2019), p. 348.
DOI: 10.3390/ijms20020348. URL: https://doi.org/10.3
390/ijms20020348.

[49] M. Parco et al. «Investigation of HVOF spraying on magne-
sium alloys.» In: *Surface and Coatings Technology* 201.6 (Dec.
2006), pp. 3269–3274. DOI: 10.1016/j.surfcoat.2006.06
.047. URL: https://doi.org/10.1016/j.surfcoat.2006.0
6.047.

[50] R. V. Raj, R. S. Unnithan, and G. R. Krishnan. «The charac-
teristics study of HVOF coated AZ91D magnesium alloy with
silicon carbide and stainless steel.» In: *AIP Conference Pro-
ceedings*. Vol. 2105. 1. AIP Publishing LLC. 2019, p. 020024.

[51] F. Guthrie. «On Eutexia.» In: *Proceedings of the Physical Society
of London* 6.1 (Apr. 1884), pp. 124–146. DOI: 10.1088/1478-
7814/6/1/312. URL: https://doi.org/10.1088/1478-7814
/6/1/312.

[52] *Eutectic system*. 2021. URL: https://en.wikipedia.org/
wiki/Eutectic_system.

[53] W. Callister and D. Rethwisch. *Materials Science and Engi-
neering*. Wiley, 2014. ISBN: 9781118507070. URL: https:
//books.google.it/books?id=8ixEDwAAQBAJ.

[54] L. Luo and N. L. Pierrès. «Innovative Systems for Storage of Thermal Solar Energy in Buildings.» In: *Solar Energy Storage*. Elsevier, 2015, pp. 27–62. DOI: 10.1016/b978-0-12-409540 -3.00003-7. URL: https://doi.org/10.1016/b978-0-12-4 09540-3.00003-7.

2

Methods

"Heat makes metal expand". Now who's talking mumbo-jumbo?

Simpson, B.J.

In Chapter 1, the state of the art of the materials on which the research carried out during the Ph.D. period was focused. Similarly, this chapter focuses on the state of the art of methods, both theoretical and instrumental, that are used in materials science. In the following sections, larger space is given to methods that are still scarcely used in the world of materials science, such as tools for the simulation of matter-particle interactions, experimental design techniques and multivariate analysis.

An overview of the use of non-destructive techniques (NDT) commonly applied in materials science is given in Section 2.1, taking for granted a basic knowledge for each of the presented techniques. Section 2.2 describes in depth the use of Geant4 and the key role it can play in the study of materials and their interaction with electromagnetic radiations. The section provides some code examples of the

structure of an application built with Geant4 libraries and on the results that can be achieved. In Section 2.3, the theory of experimental designs is described giving particular attention to two different types of continuous planning: Full Factor Design and Simplex design for mixtures. Finally, in Section 2.4, Multivariate techniques and their main uses in the field of X-ray diffraction are presented, completing the informations given in the sections with a review article published on Crystals (MDPI)[1].

2.1   Materials characterization by X-ray based techniques

X-ray based NDTs are often the beating heart of research centers on materials, archaeological findings, fine arts and other sectors where sample conservation is important, or even essential[2, 3]. The great versatility of X-rays is demonstrated by the wide spectrum of techniques based on them, which even belong to different classes of analysis: morphological (radiography, tomography), compositional and textural analysis (X-ray diffraction) or elementary (energy-dispersive X-ray Spectrometry and X-ray fluorescence). The instrumental equipment of Bytest and UniUPO has already been anticipated in Section 1.1, where the different types of analysis undertaken by the two facilities have been described. In scientific literature more applications for materials science of such techniques can be found.

X-ray diffraction (XRD) is a technique capable of providing information on crystalline structures under analysis by exploiting the coherent scattering of the incident radiation[4]. Each crystal structure, characterized by a unique of cell parameters, produces a characteristic diffraction pattern which can be used as a fingerprint for materials analysis[5]. In general, in this thesis speaking of diffraction, the technique of X-ray diffraction from powders (XRPD) is referred to, more suitable for the study of complex materials than the single crystal

technique (SC-XRD)[4, 5]. Given its elevate discriminating power
and sensibility, XRPD is mainly used for qualitative analysis, consist-
ing in phase recognition. This use is typical in companies where solid
mixtures are analysed for quality control purposes. Some notable
examples can be found in the pharmaceutical area[6], where the pu-
rity mixtures of active pharmaceutical ingredients must be evaluated
with highly sensible techniques[7]. The intensity of the peaks of the
XRPD patterns can be exploited for semi-quantitative analyses, while
the width and shape of the peaks can be used for the analysis of the
average size of the powders[5]. Defects and stresses in the materials
can also easily be recognized by using XRPD[5, 6]. In the last decades,
the analysis of the entire diffraction range (total scattering) has been
used to study long-range disordered structures and to comprehend
the local atomic structures, using both Bragg reflections and diffuse
scattering within the diffraction pattern[8, 9]. This particular appli-
cation is very successful in the study of nanomaterials and materials
related to energy production or storage, such as those for solid oxide
fuel cells, magnetic materials or metal-organic frameworks[8, 9].

X-ray fluorescence (XRF) is an elemental analysis technique that ex-
ploits the characteristic emission of X radiation by the atoms within a
sample[10, 11] after being irradiated by an X-ray source. The absorp-
tion of the X radiation excites one or more electrons belonging to the
inner sphere. At this point, the electrons on superior orbitals go to
occupy the underlying empty levels: the transitions bring more ener-
getic electrons to less energetic positions and the excess is disposed of
through an electromagnetic emission in the X-ray field[10, 11]. The
mechanism of this phenomenon suggests a important factor, namely
that the emissions do not depend on the way in which the atom in-
volved is bound, but only on its atomic number. It follows that the
re-emitted radiations are characteristic for each element[10, 11]. The
most common instruments for XRF,are unable to identify elements
smaller than sodium ($Z = 11$). Despite this, its use for qualitative
and quantitative analyses are widespread not only within materials

science, but also in analytical chemistry and in the cultural heritage sector. In some applications XRF has been used in combination with XRPD to exploit their complementarity for the qualitative and quantitative analysis of powder mixtures[12]. Sensibility of benchtop XRF instruments is usually not sufficient for trace element detection[13], but by combining it with other techniques it can be used even for provenance analysis, as done by Artioli et al. in the analysis of the ice man ax found in the South Tyrolean Alps[14].

Radiography and tomography are two techniques closely related to each other as they are both based on counting the amount of X radiation passing through a sample. Once the proper energy range has been selected, it is possible to see images in which variations in grayscale shades indicate variations in density, porosity or even different compositions within a sample[15]. In the industrial field, the main applications of radiographic techniques concern the automotive and aerospace fields for safety and quality control. Furthermore, digital radiography, compared to traditional analogue radiography, has some key advantages, which include a much higher image quality and result, which also increase the likelihood of identifying defects. Furthermore, the environmental impact due to the use of the analog technology is not negligible and the conversion to digital radiography could be a great step towards eco-compatibility.

Computed X-ray tomography (XRCT) is a scanning technique, developed from radiography, in which the sample in analysis rotates around one among the perpendicular axes to the detector and the x-ray source[1]. The rotation of the sample allows the collection of many images (radiographs) of different points of view of the specimen, which are then recombined by a computer, reconstructing the object in three dimensions[16]. XRCT is extremely efficient in identifying voids, defects and superficial or internal cracks in the samples

---

[1]In medical technology source and detector rotate instead of the patient.

in a totally conservative way[17, 18]. Moreover, the technique is suitable for the analysis of complex materials such as cements[19] and composite materials, as presented in a recent study of Bull et al.[18]. Through the use of special software, computed tomography allows the visual exploration of the internal parts of complex and large objects, such as engines. In addition, automated porosity and defect analyzes can be performed and statistical distributions for cavities and crack sizes can be created.

Each of the presented techniques was used in the works that follows in the subsequent parts of this thesis work. In particular, the most used and the object of developments of specific experimental methods and setups was the XRPD as the most rapid and versatile tool for material analysis.

2.2 Geant4 for the simulation of the interactions between matter and X-Rays

Geant4 [20–22] is the most updated version of a set of libraries for C++ developed at CERN and constitutes a powerful and versatile tool for the study of materials carried out through Monte Carlo simulations. Its power and precision have meant that, starting from the 90s, most of the instruments used at the Large Hadron Collider (LHC), but not only, have been first simulated with Geant4 [23] before being installed. The toolkit allows you to create applications in which "geometries"are defined to represent solids whose details can be specified: dimensions, shape, composition, charge, magnetic field, temperature, density, . . . These solids are subsequently irradiated with simulated particles customized in typology, energy, charge, spin, and so on. The result of the simulation has a content depending on the information saved, for example it is possible to make counts on the angles of reflection of the particles, on the energy deposited

in the geometry, how many and which types of particles were generated after the collision at which point of the solid. These are just some examples extracted from the enormous range of possibilities that constitutes Geant4 concerning the interaction between particles and matter. Within this project, the use of Geant4 has proved to be very useful for understanding the behavior of different materials when exposed to X-rays, in particular radiopacity. The high customizability of Geant4 has also made it possible to carry out simulations by exposing materials to monochromatic X-ray photons (as in the case of an instrument for optimal diffraction) or to directly simulate entire spectra, as done by Pandola et al. [24], in order to better approximate the radiographic and tomographic conditions. Here are some code examples extracted from the developed applications are described as example. The first in particular shows how a new material can be defined starting from its constituent elements.

```
1  //Define bismuth oxide
2  G4Material* Bi2O3 = new G4Material("Bi2O3", 8.93*g/cm3, ncomponents
       ↪ =2, kStateSolid, temperature = 293.15*kelvin, pressure = 1*
       ↪ atmosphere);
3  Bi2O3->AddElement(O, natoms=3);
4  Bi2O3->AddElement(Bi, natoms=2);
5
6  //Material of absorber
7  SetAbsorberMaterial("Bi2O3");
```

Listing 2.1: Materials definition in Geant4

It should be noted that no crystallographic information is specified in the definition of a material, which means that this instrument cannot be used, under these conditions, for simulation of diffraction experiments. However, libraries developed by Kittelmann et al. [25] and by Bagli et al. [26] can be implemented so that all the missing information about the crystalline structures (cell parameters, space group, average crystal size, . . .) can be given as useful data for the simulation. Once the desired geometries have been built and all the

events to be monitored by the application have been defined, the
executable can be used through an input file such as the one reported:

```
1   //Parameters of geometry elements
2
3   /testem/det/setTarThick 300 um
4   /testem/det/setAbsThick 1 cm
5   /testem/det/setAbsYZ     1 cm
6   /testem/det/setTarMat G4_W        //Tungsten target
7   /testem/det/setAbsMat MIXTURE     //Custom absorber material
8   //Parameters of the gun
9   /run/initialize
10  /testem/gun/setDefault
11  /gun/particle e-
12  /gun/energy 300 keV
```

Listing 2.2: Example of a Geant4 input file

By defining different materials, it is possible, as in this case, to change
them directly through the input file without having to recompile the
application. The same is true for any other variables, such as dimen-
sional ones. Finally, the parameters of the beam that will be gener-
ated by the simulation are defined. In the case shown, it is a beam of
electrons of energy equal to 300 keV which subsequently impact on a
tungsten target for the production of X-rays with a characteristic spec-
trum of this material (standard spectrum for X-ray tubes for radiog-
raphy and tomography). The results, for 10^3 incident electrons, can
be viewed and analysed through a graphic user interface, as shown
in Figure 2.1. In the image the Cartesian references and the solids
positioned in space can be seen. A 300 micron thick plate of tungsten,
acting like a target for the X-ray tube, is placed in front of and a 1
centimeter thick box which acts as a radiopaque material. Along the
red arrow, indicating the x-axis, a beam of electrons hits the target.
The electrons trajectories, evidenced by red lines, take on different
behaviors: some are reflected while others are absorbed. When ab-
sorbed, the consequent emission generate X-rays (green lines), which
in turn can pass through the absorbent material, be absorbed and
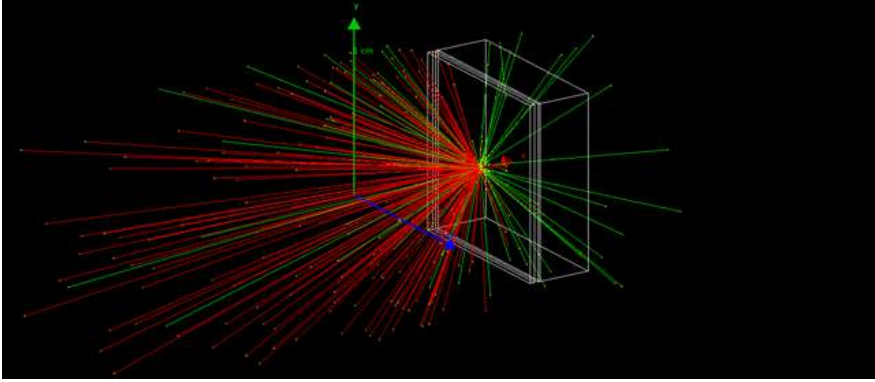
Figure 2.1: Example of a simulation result with Geant4.

dissipated in the form of thermal energy or reflected from the surface of the material. The number of incident particles can also be specified by the user, but for a good approximation the number of events should be greater than $10^5 - 10^6$. In Chapter 7, the use of Geant4 allowed first of all to carry out a screening of the materials present in the scientific literature and to evaluate how different mixtures of these could have behaved in the operational phase. Then, by combining the use of Geant4 with experimental planning theory, different solutions were simulated with mixtures of epoxy resin, barite and bismite. Only the samples with the most promising results in terms of radiopacity, cost and mechanical performance were then actually developed in the laboratory and characterized. The use of Geant4 was an essential part of a more environmentally friendly approach in the study of radiopaque materials, as the simulations highlight the characteristics of the materials even before their production in the laboratory. This allows a saving of materials in the initial phase of exploration of the experimental domain. Details regarding this process are described in Chapter 7 and in the article in Annex V. Geant4 was also used in the study of magnesium alloys treated with HVOF described in Chapter 10: in particular, the shielding power given by the thin layer of deposited materials was investigated.

2.3 Design of experiments for materials optimization and experimental domain exploration

The core of many works in the context of this thesis, such as those presented in Chapter 5 or the works reported in Part III, is represented by a meticulous planning of the experiments. According to the type of problem that one faces, it is essential to be in the best conditions to collect as much information as possible on a system under examination with the least number of experiments[27]. This concept, which is known in analytical chemistry as the "parsimony principle"[28], is what underlies the theory of the Design of Experiments (DoE). DoE, which is a well-established practice in analytical chemistry and industrial analytical chemistry experiments, is still not very widespread in the fields of Chemistry and Materials Science. However, using the theories for optimal experimentation is a great way to reduce the number of experiments to a minimum and consequently save energy, time, reagents and money. Nevertheless, minimizing experiments does not mean having to give up studying an experimental domain in depth, as there are several ways to obtain the maximum information that a system can provide[27, 29, 30]. Another problem that is implicitly solved with the use of DoE is that linked to the collinearity of the experiments[27].

The theory of the DoE gives the experimenter the best possible conditions to explore an unknown experimental domain [29]. Before starting an experiment campaign, having a clear objective associated to one or more response functions is always necessary. In physical chemistry samples are often analysed by a multi-technique approach in order to exploit system properties in a qualitative and not in a quantitative way. For this reason, often the lack of need for a regression model that numerically links the experimental factors with the response function is the cause of the absence of planning according

to DoE in experimental chemistry. On the contrary, the advantage of using different analysis techniques paired with the DoE theory combines the advantages of being able to observe an ordered and homogeneous distribution of experiments by different points of view, helping to correlate not only the factors, but also all the various response functions. In scientific literature there are many solutions, however for convenience experimental designs will be divided into two classes: continuous designs (which includes optimal, composite, box-Behnken plans, ...) and discontinuous designs (Evolutionary process, steepest ascent, metaheuristic algorithms, ...). Continuous designs are built by using the method of optimization of response curves[27]. All the experiments are planned and carried out, only at a later stage result obtained is analysed. In the case of discontinuous designs, on the other hand, through the use of different techniques, few experiments are performed at a time (often one at a time), the result is analysed and only after the analysis the next experiment is designed and executed.

2.3.1 Definitions and mathematical basis

Before proceeding with the experimental planning as described in the following two sections, it is necessary to verify that some conditions are met and that the aim of the experimentation is well defined to the experimenter. If not, it is necessary to focus on the desired result and on which factors (or independent variables) can be exploited during the research work. The first condition is to choose one or more dependent variables that can be measured as a response function. Experiments are often started, especially in the field of physical chemistry, without a parameter to evaluate the goodness of a result, taking into account that the material will be characterized at a later time. The considered variable (or variables) can be of different types: categorical, numeric, discontinuous or continuous (such as spectral

ones). The second condition is that the measurement of the response variable is repeatable, otherwise another function to monitor has to be chosen. The repeatability of an experiment within an experimental domain can be assessed by positioning in the center of the domain and making repeated experiments (at least three repetitions). By having repeated measurements, the mean of the response variable $\overline{y}$ can be evaluated as:

$$\overline{y} = \frac{\sum_{i=1}^{n} y_i}{n} \tag{2.1}$$

Where y_i are the individual results of the measurements of the n samples (or observations). Then, the variance σ^2 can be calculated as the squared sum of the deviations of the samples from the mean, divided by the number of observations minus one:

$$\sigma^2 = \frac{\sum_{i=1}^{n}(y_i - \overline{y})^2}{n - 1} \tag{2.2}$$

Standard deviation is then defined as the square root of σ^2 and can be used for a rapid evaluation of the repeatability of an experiment by the calculation of coefficient of variation:

$$\%CV = \frac{\sigma}{\overline{y}} \tag{2.3}$$

In the chemical field, an experiment with a good repeatability has a $\%CV$ not greater than 10%, preferably lower than 5%, but in biological field, depending on the situation, even values of 20% can be acceptable. If the value of $\%CV$ for a response variable surpasses the 10% it does not necessarily means that the experiment is not repeatable, but only that the selected response variable does not comply with the requirements, therefore it can be changed for another monitored parameter.

2.3.2 Full factor designs

Factor designs belong to the D-optimal class of experimental de-signs, which aim to minimize the determinant of the dispersion ma-trix[31]. Among the many types of optimal designs (A-optimal, E-optimal,...[29]), the D-optimal ones turn out to be the most widespread and popular. The advantage lies in the fact that these plans are able to minimize the uncertainty associated with the estimation of the pa-rameters of a regression model associated with the plan and to use few experiments to homogeneously explore the experimental domain. The most efficient method of using factorial plans is to use two levels for the factors, which means that two values are attributed to each factor in analysis that will be explored: one low and one high (often indicated in the experimental matrix as − and +). For example, if the factor to be varied is temperature and the allowed range for the variation is from 1 °C to 50 °C, the − value can be 5 °C and the + value can be 45 °C^2. The construction of a 2-levels factor design is dictated by a simple rule: the number of experiments n is equal to 2^p, where p is the number of factors to be considered in the experiment. For example, in the case of a three-dimensional experimental domain in which we want to vary the three independent factors A, B and C and monitor the effects of the variations on the response variable Y, we would have $n = 2^3 = 8$ experiments. The construction of the 2-level factor design at this point is done in a simple way through the permu-tation of the − and the + for the three factors A, B and C as in Table 2.1. Factors design with two levels allow the creation of regression models that take into account not only the influence of single factors, but also of two- and three-factor interactions. The effect can be vi-sualized by extending Table 2.1 by multiplying the signs according to the corresponding factors in the headers, as shown in Table 2.2: In addition to the interactions between the factors, a further column

---

^{2}At least in the initial stages of exploration, experiments at the extremes of the experimental domain are often avoided, to leave room for subsequent explorations.

Table 2.1: Table with the permutations of low and high levels for the three factors *A*, *B* and *C*

A	B	C
-	-	-
+	-	-
-	+	-
+	+	-
-	-	+
+	-	+
-	+	+
+	+	+

Table 2.2: Extension of Table 2.1 with all the factor interactions.

i	A	B	AB	C	AC	BC	ABC
+	-	-	+	-	+	+	-
+	+	-	-	-	-	+	+
+	-	+	-	-	+	-	+
+	+	+	+	-	-	-	-
+	-	-	+	+	-	-	+
+	+	-	-	+	+	-	-
+	-	+	-	+	-	+	-
+	+	+	+	+	+	+	+

i is inserted in Table 2.2, which corresponds to the intercept of the regression model that can be constructed from the experiments of the design. By re-coding the − as −1 and + as 1 and writing it as a matrix,

the model matrix of the experimental design is obtained:

$$\mathbf{M} = \begin{pmatrix} 1 & -1 & -1 & 1 & -1 & 1 & 1 & -1 \\ 1 & 1 & -1 & -1 & -1 & -1 & 1 & 1 \\ 1 & -1 & 1 & -1 & -1 & 1 & -1 & 1 \\ 1 & 1 & 1 & 1 & -1 & -1 & -1 & -1 \\ 1 & -1 & -1 & 1 & 1 & -1 & -1 & 1 \\ 1 & 1 & -1 & -1 & 1 & 1 & -1 & -1 \\ 1 & -1 & 1 & -1 & 1 & -1 & 1 & -1 \\ 1 & 1 & 1 & 1 & 1 & 1 & 1 & 1 \end{pmatrix} \qquad (2.4)$$

An important property of the model matrix, which is the core of the factor design theory, is that all the rows and columns of the matrix are linearly independent and orthogonal. Mathematically, therefore, each row and each column defines a direction in the 8-dimensional space of the matrix. The consequence is that each factor, even multi-factor interactions, can be estimated independently one from another[27, 29]. This property can be demonstrated easily by other two important matrices: the information matrix, and the dispersion matrix. The first one is calculated as ($\mathbf{M}^T\mathbf{M}$):

$$\mathbf{M}^T\mathbf{M} = \begin{pmatrix} 8 & 0 & 0 & 0 & 0 & 0 & 0 & 0 \\ 0 & 8 & 0 & 0 & 0 & 0 & 0 & 0 \\ 0 & 0 & 8 & 0 & 0 & 0 & 0 & 0 \\ 0 & 0 & 0 & 8 & 0 & 0 & 0 & 0 \\ 0 & 0 & 0 & 0 & 8 & 0 & 0 & 0 \\ 0 & 0 & 0 & 0 & 0 & 8 & 0 & 0 \\ 0 & 0 & 0 & 0 & 0 & 0 & 8 & 0 \\ 0 & 0 & 0 & 0 & 0 & 0 & 0 & 8 \end{pmatrix} \qquad (2.5)$$

and by calculating the inverse the information matrix, the dispersion matrix $(\mathbf{M}^T\mathbf{M})^{-1}$ is obtained:

$$(\mathbf{M}^T\mathbf{M})^{-1} = \begin{pmatrix} 1/8 & 0 & 0 & 0 & 0 & 0 & 0 & 0 \\ 0 & 1/8 & 0 & 0 & 0 & 0 & 0 & 0 \\ 0 & 0 & 1/8 & 0 & 0 & 0 & 0 & 0 \\ 0 & 0 & 0 & 1/8 & 0 & 0 & 0 & 0 \\ 0 & 0 & 0 & 0 & 1/8 & 0 & 0 & 0 \\ 0 & 0 & 0 & 0 & 0 & 1/8 & 0 & 0 \\ 0 & 0 & 0 & 0 & 0 & 0 & 1/8 & 0 \\ 0 & 0 & 0 & 0 & 0 & 0 & 0 & 1/8 \end{pmatrix} \tag{2.6}$$

As can be seen, all diagonal terms of the dispersion matrix are equal to $1/n$, where n corresponds to the number of performed experiments. The diagonal terms provide the estimation of the variance of the coefficients of the regression model that can be constructed from these experiments. The uncertainty on the estimation of the coefficients (multiplication between each diagonal term and the experimental error) is therefore the same for all factors and the lowest possible. The extra-diagonal elements, all equal to zero, represent the covariances between factors or combinations of factors, emphasizing again their orthogonality[27, 29]. Finally, the minimization of the determinant of the dispersion matrix can be calculated as the multiplication of the all the diagonal terms:

$$det|(\mathbf{M}^T\mathbf{M})^{-1}| = (1/8)^8 \tag{2.7}$$

Where the obtained value of $5.9*10^{-8}$ is the lowest possible for 8 experiments[29]. For all the aforementioned reasons, factor designs are widely used in the analytical field. In this work, a modified version of a factor design was used together with the a design for mixtures for the optimization of radiopaque materials (Chapter 8).

2.3.3 Simplex designs for mixtures

The designs for mixtures arise from the need to solve the demand for independence between the factors to be explored[30]. Factors A, B and C used for the example of factor designs in the previous section are all independent of each other and can be considered as physical variables to be monitored in a process, such as temperature, pressure or quantity of a substance. When it comes to analysing a mixture and the factors to be explored become the concentrations of the components of the mixture, the independence required to apply the theory of the factor design is lacking. Considering again the three factors A, B, and C, this time as quantities of some substance, it is easily demonstrable that the first experiment of the two-level factor design ($A = -1$, $B = -1$, $C = -1$) is equal to the last one ($A = +1$, $B = +1$, $C = +1$), as the relative ratios between A, B and C are the same, but only the total quantity of mixture is changed. This lack of independence between factors is caused by what is called the "closing rule"[30, 32]. A mixture of q components is the sum of the fractions x_i (weight, volume, molar, ...) of each component. The sum always closes to 1, which is the hundred percent of the composition.

$$\sum_{i=1}^{q} x_i = x_1 + x_2 + \cdots + x_q = 1 \tag{2.8}$$

This rule implies that none of the factors studied can vary independently, because each can be defined through a linear operation of the remaining factors. While there are ways to substitute compositional variables to use traditional experimental designs[30, 32], the most convenient thing to do is to use designs for mixtures, as Simplex lattices[33]. Mixture designs were used for planning experiments most of the works of the present thesis and in other unreported works that have been faced during the doctoral period. In the following subsections, the two most used designs are described: Simplex-lattice design and Simplex-centroid design.

Simplex-lattice design
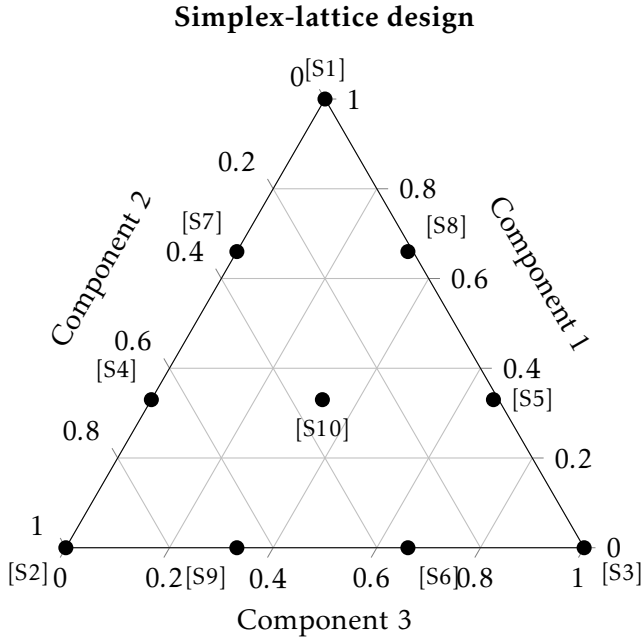
Figure 2.2: A $\{3,3\}$-Simplex-lattice experimental design.

2.3.3.1   Simplex-lattice design

Simplex-lattice design is a type of DoE conceptually similar to factor designs. Once the desired number of components for a mixture q and the desired number of levels l have been chosen, the experiments are defined through a few simple formulas and placed on a lattice within the experimental domain. The regression model that can be calculated starting from the programmed experiments directly depends on the level chosen for the design. Then for a Simplex-lattice design with 3 components and 3 levels, the maximum degree of the resulting polynomial will be 3. The number of experiments of Simplex-lattice can be defined as follows:

$$\binom{q+l-1}{l} = \frac{(q+l-1)!}{l!(q-1)!} \tag{2.9}$$

Therefore, for the 3,3 design of the example, the total number of experiments is ten. The compositions of these experiments are all possible permutations given by:

$$x_i = 0, \frac{1}{l}, \frac{2}{l}, \frac{3}{l}, \dots, 1 \tag{2.10}$$

In this case, the identity is reached after a few steps, and the values that the components can assume are only 0, 1/3, 2/3 and 1. The ten legitimate permutations of these numbers generate the mixtures shown in Figure 2.2.

2.3.3.2 Simplex-centroid design

The name of the Simplex-centroid design is due to the position of each experiment, which is in the centroid of each simplex of smaller dimensionality of the one that builds up the experimental domain. In other words, if the space of the mixture to be considered has $q = 4$ components, the resulting simplex will be a tetrahedron ed each experiment will be placed in the baricenter of each simplex of equal or lower dimensionality: center of the tetrahedron for a 4-dimensional simplex, the center of each face (3-dimensional simplexes), the center of each edge (2-dimensional simplexes), each vertex of the tetrahedron (1-dimensional simplexes). Levels has therefore not to be defined for the construction of the experimental design, because it depends exclusively on the number of components of the mixture[33]. The example presented can be described by the simple following equation:

$$n = 2^q - 1 \tag{2.11}$$

In which n is the number of experiments and for the described example of a 4-components mixture it gives 15 as a result (1 central point, 4 faces, 6 edges, 4 vertexes). The positions of each experiment can be
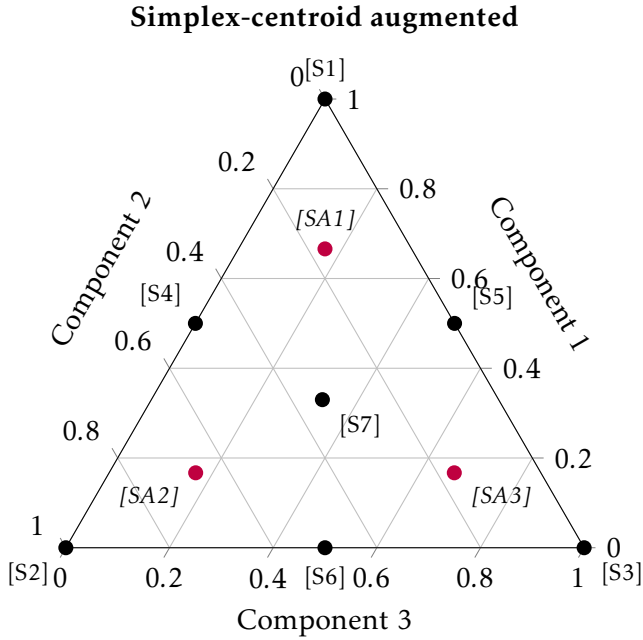
Figure 2.3: A Simplex-centroid experimental design for a three-components mixture. Points S1-S7 indicate the points designed by equation 2.11. Red points, labeled from SA1 to SA3, indicate the augmented experiments.

also defined by the following permutations:

$$q \quad \text{pure substances;}$$

$$\binom{q}{2} = \frac{q!}{2!\,(q-2)!} \quad \text{two-components mixtures;}$$

$$\binom{q}{3} = \frac{q!}{3!\,(q-3)!} \quad \text{three-components mixtures;}$$

$$\cdots$$

$$1 \quad \text{mixture with every component equal to } 1/q.$$

In Figure 2.3 a three-components Simplex-centroid design is reported. Black points in the graph represent the experiments planned with the design, while red point indicate some additional points that

can be calculated. The need of additional points comes from the limitation given by the structure of the design itself: being the number of experiments directly bound to the number of components of the mixture, the information that could be extracted from the design would always be less than the one that could be obtained by using a Simplex-lattice design. However, by performing additional experiments (augmented), a better coverage of the experimental domain can be attained if compared to the Simplex-lattice and, consequently, a better description of the response surface[30]. The red augmented experiments of Figure 2.3 can be calculated as mixtures in which one component is equal to $\frac{q+1}{2q}$ and the others are equal to $\frac{1}{2q}$[33].

2.4 Multivariate methods

Multivariate methods can be defined as a set of mathematical tools used to tackle problems involving more than one variable (generally tens to thousands) in large data sets. Typically, the use of these methods is intended for the comparison between variables, both coming from different analytical techniques, and coming from the same (i.e. spectroscopic variables), so as to be able to determine correlations between variables or, more generally, hidden relationships [1]. Multivariate statistical analysis (MSA) allows you to break down complex data matrices into components that are much easier to analyse, to exclude much of the noise and to build analytical models that take into account numerous variables. Multi-dimensional analysis of relationships and dependencies arose from Gauss's work on linear regressions, but the use of more than one independent variable was formalized and generalized at the turn of the twentieth century, with an early work by Yule [34], followed from a second work six years later, co-written with Pearson [35]. The need to simplify multivariate systems immediately caught the eye of Pearson who, with his work, laid the foundations of an algorithm for the decomposition of the experimental matrix based mainly on a rotation of the reference system

of data and variables. This algorithm, later taken up by Hotelling in 1933 [31], was formalized as Principal Component Analysis (PCA)[3]. Despite having understood the potential of PCA, first of all the ability to reduce the dimensionality of the problem under analysis, its use was limited until the 1980s, when computers, already sufficiently powerful, allowed matrix operations that, handmade, would have taken a disproportionate amount of time. Mathematically speaking, principal component analysis consists in the decomposition of an experimental matrix $\mathbf{X}_{(n,p)}$ of n rows (cases or samples) and p columns (variables) through an eigenvalue problem. From the eigenvalue problem we obtain eigenvalues and eigenvectors, which respectively represent the variance of the system explained by a particular principal component and its unit vector in the new space. Since the eigenvalue problem is hierarchical, the highest eigenvalues (and therefore the largest slices of information about a system) fall into the first principal components and gradually decrease in importance. From this, two matrices $\mathbf{T}_{(n,m)}$ and $\mathbf{L}_{(m,p)}$ are generated, respectively matrix of scores and matrix of loadings, which are linked to the experimental matrix through the relationship:

$$\mathbf{T}_{(n,m)} = \mathbf{X}_{(n,p)}\mathbf{L}_{(m,p)} \tag{2.12}$$

The value m, reported as a subscript in equation 2.12, corresponds to the number of principal components (PCs) and, by definition, as many as there are system variables are generated. If $m = p$, then the procedure consists of a simple rotation of the experimental matrix along a new coordinate system (defined by the eigenvectors), without any modification. By choosing instead the appropriate values of m, and therefore how many eigenvalues and eigenvectors to take in consideration, the amount of information contained in the starting matrix is selected, thus excluding a large part of the experimental noise, which, being defined by random fluctuations and not related

---

[3]For a more in-depth description of the history of PCA and origin of multivariate analysis, see the review published by Ian Jolliffe at ref. [36].
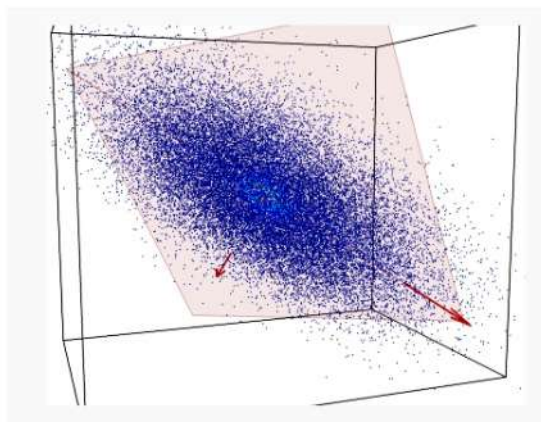
Figure 2.4: Representation of PCA: in the data cloud represented by the blue points, the algorithm identifies the directions of maximum variance (red arrows) and uses those as new coordinate system. Figure from ref. [1]

to variables, it falls into the last PCs. a typical representation of the functioning of the principal components analysis is shown in Figure 2.4, where it is possible to see the blue points, representing the samples being analysed being distributed in an elliptical cloud. The PCA algorithm hierarchically defines the directions of maximum variance, in this case simplified the two axes of the ellipse (red arrows). In this way, by projecting original samples and variables into this new coordinate system, it is possible to obtain a simplified view of the problem and to determine relationships between the variables in analysis and groupings of samples. Generally this practice is called "Pattern recognition"and has become fundamental in subjects such as chemometrics and psychometrics, but in general in all -omics sciences. Starting from PCA or parallel to it, other techniques have been developed mainly used for pattern recognition, such as factor analysis (FA), multivariate curve resolution (MCR), optimum constrained components rotation (OCCR). Other techniques, such as the

principal component regression (PCR), the multivariate curve resolution (MCR) and the partial least squares (PLS), were instead born by extending the multivariate approach to regression, therefore to the construction of models, always with the aim of reducing dimensionality and being able to describe with few coefficients a system under analysis. Extensive use of multivariate analysis will be made in the following chapters, especially of PCA. In Chapter 4 a novel approach for the quantification of mixtures will be presented. The method, totally blind and without *a priori* information about the system, is based on the PCA and does not use regression methods. A working version of the code that has to be associated with the PCA is then presented in Appendix A. In Chapter 5, the methods developed are applied to real cases of quantification of data from XRPD and XRF, with a comparison with the traditional techniques that represent the current state of the art. Preliminary data were presented by Dr. Rocco Caliandro at the 25th Congress of the International Union of Crystallography (IUCr)[4] and the abstract is reported on Acta Cryst. sect. A vol. 77. In Chapter 8, PCA is used to monitor the sedimentation process of radiodense additives to epoxy resins in the polymerization phase. In fact, the additives, added in low quantities (less than 60% by weight) to the monomer mixture, tend to migrate towards the lower part of the sample. Exploiting PCA, it was possible to quantify the migration process in the same way it could have been done with Rietveld refinement, but with much higher data analysis rates. Partial results were at first reported at the EXPO & more International Workshop[5] by Prof. Marco Milanesio and later published on Materials Communication Today (Annex V).

These results and an overview of the most used multivariate techniques in crystallography, with an in-depth mathematical description of the methods can be found in the review article [1] reported in full

---

[4]25th IUCr Congress: http://iucr25.org.

[5]EXPO & more International Workshop: http://www.ba.ic.cnr.it/expo-more-workshop2019.

in Annex I.

Bibliography

[1]   P. Guccione et al. «Multivariate Analysis Applications in X-ray Diffraction.» In: *Crystals* 11.1 (Dec. 2020), p. 12. DOI: 10.3390/cryst11010012. URL: https://doi.org/10.3390/cryst11010012.

[2]   L. Cartz. *Nondestructive Testing: Radiography, Ultrasonics, Liquid Penetrant, Magnetic Particle, Eddy Current*. ASM International, 1995. ISBN: 9780871705174.

[3]   C. Hellier. *Handbook of Nondestructive Evaluation, 3E*. McGraw-Hill Education, 2020. ISBN: 9781260441444.

[4]   C. Giacovazzo et al. *Fundamentals of Crystallography*. IUCr texts on crystallography. Oxford University Press, 2002. ISBN: 9780198509585.

[5]   R. Dinnebier, S. Billinge, and R. S. of Chemistry (Great Britain). *Powder Diffraction: Theory and Practice*. Royal Society of Chemistry, 2008. ISBN: 9780854042319. URL: https://books.google.it/books?id=wmQ%5C_1FIMkFYC.

[6]   F. Karavassili et al. «In Quest for Improved Drugs against Diabetes: The Added Value of X-ray Powder Diffraction Methods.» In: 7.4 (Aug. 2017), p. 63. DOI: 10.3390/biom7030063. URL: https://doi.org/10.3390/biom7030063.

[7]   R. Pantola and R. Bahuguna. «Polymorphism: Quality rationalization, mitigation and authentication strategies with respect to regulatory compliances in pharmaceutical industry.»

In: *Research Journal of Pharmacy and Technology* 5.10 (2012), pp. 1264–1269.

[8] S. J. L. Billinge. «The rise of the X-ray atomic pair distribution function method: a series of fortunate events.» In: 377.2147 (Apr. 2019), p. 20180413. DOI: 10.1098/rsta.2018.0413. URL: https://doi.org/10.1098/rsta.2018.0413.

[9] D. A. Keen. «Total scattering and the pair distribution function in crystallography.» In: 26.3 (July 2020), pp. 143–201. DOI: 10.1080/0889311x.2020.1797708. URL: https://doi.org/10.1080/0889311x.2020.1797708.

[10] R. Van Grieken and A. Markowicz. *Handbook of X-ray Spectrometry*. CRC press, 2001.

[11] B. Beckhoff et al. *Handbook of practical X-ray fluorescence analysis*. Springer Science & Business Media, 2007.

[12] M. Bortolotti, L. Lutterotti, and G. Pepponi. «Combining XRD and XRF analysis in one Rietveld-like fitting.» In: *Powder Diffraction* 32 (2017), pp. 225–230. DOI: 10.1017/S0885715617000276.

[13] J. Q. McComb et al. «Rapid Screening of Heavy Metals and Trace Elements in Environmental Samples Using Portable X-Ray Fluorescence Spectrometer, A Comparative Study.» In: 225.12 (2014). DOI: 10.1007/s11270-014-2169-5. URL: https://doi.org/10.1007/s11270-014-2169-5.

[14] G. Artioli et al. «Correction: Long-distance connections in the Copper Age: New evidence from the Alpine Iceman's copper axe.» In: 12.12 (Dec. 2017), e0189561. DOI: 10.1371/journal.pone.0189561. URL: https://doi.org/10.1371/journal.pone.0189561.

[15] P. Russo. *Handbook of X-ray imaging: physics and technology*. CRC press, 2017.

[16] E. Seeram. *Computed Tomography-E-Book: Physical Principles, Clinical Applications, and Quality Control.* Elsevier Health Sciences, 2015.

[17] J. Lambert et al. «3D damage characterisation and the role of voids in the fatigue of wind turbine blade materials.» In: 72.2 (2012), pp. 337–343. DOI: 10.1016/j.compscitech.2011.11.023. URL: https://doi.org/10.1016/j.compscitech.2011.11.023.

[18] D. Bull et al. «A comparison of multi-scale 3D X-ray tomographic inspection techniques for assessing carbon fibre composite impact damage.» In: 75 (Feb. 2013), pp. 55–61. DOI: 10.1016/j.compscitech.2012.12.006. URL: https://doi.org/10.1016/j.compscitech.2012.12.006.

[19] D. Gastaldi et al. «In situ tomographic investigation on the early hydration behaviors of cementing systems.» In: 29 (Apr. 2012), pp. 284–290. DOI: 10.1016/j.conbuildmat.2011.10.016. URL: https://doi.org/10.1016/j.conbuildmat.2011.10.016.

[20] S. Agostinelli et al. «Geant4—a simulation toolkit.» In: *Nuclear Instruments and Methods in Physics Research Section A: Accelerators, Spectrometers, Detectors and Associated Equipment* 506.3 (July 2003), pp. 250–303. DOI: 10.1016/s0168-9002(03)01368-8. URL: https://doi.org/10.1016/s0168-9002(03)01368-8.

[21] J. Allison et al. «Geant4 developments and applications.» In: *IEEE Transactions on Nuclear Science* 53.1 (Feb. 2006), pp. 270–278. DOI: 10.1109/tns.2006.869826. URL: https://doi.org/10.1109/tns.2006.869826.

[22] J. Allison et al. «Recent developments in Geant4.» In: *Nuclear Instruments and Methods in Physics Research Section A: Accelerators, Spectrometers, Detectors and Associated Equipment* 835

(2016), pp. 186–225. DOI: 10.1016/j.nima.2016.06.125. URL: https://doi.org/10.1016/j.nima.2016.06.125.

[23]   A. Bagulya et al. «Recent progress of GEANT4 electromagnetic physics for LHC and other applications.» In: *Journal of Physics: Conference Series* 898 (2017), p. 042032. DOI: 10.1088/1742-6596/898/4/042032. URL: https://doi.org/10.1088/1742-6596/898/4/042032.

[24]   L. Pandola, C. Andenna, and B. Caccia. «Validation of the Geant4 simulation of bremsstrahlung from thick targets below 3 MeV.» In: *Nuclear Instruments and Methods in Physics Research Section B: Beam Interactions with Materials and Atoms* 350 (May 2015), pp. 41–48. DOI: 10.1016/j.nimb.2015.03.033. URL: https://doi.org/10.1016/j.nimb.2015.03.033.

[25]   T. Kittelmann and M. Boin. «Polycrystalline neutron scattering for Geant4: NXSG4.» In: *Computer Physics Communications* 189 (Apr. 2015), pp. 114–118. DOI: 10.1016/j.cpc.2014.11.009. URL: https://doi.org/10.1016/j.cpc.2014.11.009.

[26]   E. Bagli et al. «Allowing for crystalline structure effects in Geant4.» In: *Nuclear Instruments and Methods in Physics Research Section B: Beam Interactions with Materials and Atoms* 402 (July 2017), pp. 304–307. DOI: 10.1016/j.nimb.2017.03.092. URL: https://doi.org/10.1016/j.nimb.2017.03.092.

[27]   D. Cox and N. Reid. *The Theory of the Design of Experiments*. Chapman & Hall/CRC Monographs on Statistics & Applied Probability. CRC Press, 2000. ISBN: 9781420035834.

[28]   M. B. Seasholtz and B. Kowalski. «The parsimony principle applied to multivariate calibration.» In: *Analytica Chimica Acta* 277.2 (May 1993), pp. 165–177. DOI: 10.1016/0003-26

70(93)80430-s. URL: https://doi.org/10.1016/0003-26
70(93)80430-s.

[29] G. Box, J. Hunter, and W. Hunter. *Statistics for Experimenters: Design, Innovation, and Discovery*. Wiley Series in Probability and Statistics. Wiley, 2005. ISBN: 9780471718130.

[30] J. Cornell. *Experiments with Mixtures: Designs, Models, and the Analysis of Mixture Data*. Wiley Series in Probability and Statistics. Wiley, 2011. ISBN: 9781118150498.

[31] H. Hotelling. «Analysis of a complex of statistical variables into principal components.» In: *Journal of Educational Psychology* 24.6 (1933), pp. 417–441. DOI: 10.1037/h0071325. URL: https://doi.org/10.1037/h0071325.

[32] H. Scheffé. «Experiments with Mixtures.» In: *Journal of the Royal Statistical Society: Series B (Methodological)* 20.2 (July 1958), pp. 344–360. DOI: 10.1111/j.2517-6161.1958.tb00 299.x. URL: https://doi.org/10.1111/j.2517-6161.195 8.tb00299.x.

[33] H. Scheffé. «The Simplex-Centroid Design for Experiments with Mixtures.» In: *Journal of the Royal Statistical Society: Series B (Methodological)* 25.2 (July 1963), pp. 235–251. DOI: 10.1111/j.2517-6161.1963.tb00506.x. URL: https://doi.org/10.1111/j.2517-6161.1963.tb00506.x.

[34] G. U. Yule. «On the Theory of Correlation.» In: *Journal of the Royal Statistical Society* 60.4 (Dec. 1897), p. 812. DOI: 10.230 7/2979746. URL: https://doi.org/10.2307/2979746.

[35] K. Pearson. «The law of ancestral heredity.» In: *Biometrika* 2.2 (1903), pp. 211–228.

[36] I. Jolliffe. «Principal component analysis.» In: *Encyclopedia of statistics in behavioral science* (2005).

3

Outline of the thesis

The wax never lies.

Simpson, L.M.

In Part I, an introduction to the state of the art of both materials and methods are presented. The state of the art in Bytest and UniUPO (industrial partner and academic research centre) before the present thesis, with different aspects and applications of the most largely spread non destructive techniques (NDTs), is described in Chapter 1. Moreover, the state of the art of the materials studied in this thesis (radiodense materials, magnesium alloys and eutectic solutions) is also presented. In Chapter 2, X-ray based NDTs, such as X-ray powder diffraction (XRPD), X-ray fluorescence (XRF), X-ray direct radiography (XRDR) and X-ray computed tomography (XRCT), are presented in their fundamentals and applications, being the *trait d'union* of the work. These techniques have large popularity and spread among both academic laboratories, industries and large-scale facilities, for this reason their use is exploited in the following parts. Among the described techniques, XRPD is the less used in the industrial world and,

at the same time, the most suited to perform *in situ* measurements, studying materials transformations. Diffraction measurements were collected in all of the the faced case studies, not only for qualitative purposes, but also for quantitative phase analysis of polycrystalline mixtures and *in situ* experiments. Moreover, multivariate statistical analysis (MSA) is extensively described. In particular, principal components analysis (PCA) is one of the most diffuse algorithms in chemometrics and in analytical chemistry. The importance of this method can be ascribed to the idea of the experimental matrix decomposition, which is the cornerstone for other different methods for both pattern recognition (such as the orthogonal constrained component rotation) or regression methods (principal component regression, partial least squares). In the same chapter, Geant4, a collection of tools for the simulation of the interaction between particles and matter, is presented as an instrument for theoretical simulations to predict the behavior of materials.

In Part II the developed new methods and instruments are presented. In Chapter 4, the approaches for data analysis and the instrument developed during the Ph.D. are presented, with a particular focus on novel methods for quantitative phase analysis (QPA) on real-world-like data sets collected by XRPD and XRF and affected by serious issues of preferred orientations (PO) and micro absorption (MA). Moreover, the developments made to the software RootProf are described, such as the implementation of multithreading to exploit parallel computing and Savitzky-Golay filtering algorithm. In addition, a specific algorithm, named Forcefield, was developed for the analysis of samples subjected to gradients, linked to the context of the analysis of time series. In Chapter 5, the novel methods for quantitative phase analysis are compared to the traditional ones (Rietveld Refinement-RR and PONKCS for XRPD, fundamental parameters-FP for XRF). Then, a deep analysis of the commonly best-performing pre-processes for multivariate analysis for XRPD and XRF data is reported, alongside to some future implementations for RootProf.

In the the second quarter of 2020, the lockdown restrictions made impossible to access to the laboratories and equipments. Because of this, the focus had shifted to NDT techniques that could be used outside a research laboratory not requiring particular precautions. During that time, a self-built and low-cost version of an impulse excitation technique (IET) instrument for NDT analysis of materials, named IETeasy, has been developed and is presented in Chapter 6. The technique can provide in a few seconds the Young's modulus of a sample in a totally conservative way. In addition, data were analyzed by PCA to perform pattern recognition and cluster analysis.

In Part III, materials development is described, exploiting the approaches developed in Part II. In Chapter 7, the development of composite materials with controlled radiodensity is presented from the theoretical simulations made by Geant4 to a full characterization of the prototypes, in order to obtain composites with "tunable"properties, depending on the user's requirements of radiodensity, tensile strength, cost and environmental performances. A life cycle assessment (LCA) is also performend to compare the environmental impacts of traditional shielding materials to the innovative epoxy-based composites. In Chapter 8, the liquid assisted grinding (LAG) method is exploited for the first time in the polymer science to inhibit the sedimentation effects of the additives that occur in the monomer mixture during the polymerization. In Chapter 9 novel bio-based coatings for magnesium alloys are tested to resist corrosion due to different degrees of aggressiveness. Then, in Chapter 10, coatings performed by high velocity oxygen fuel (HVOF) and additivation of polyamide coatings with nanoparticles, are tested by the previously described methods to verify surface homogeneity, defects and other properties.

In Part IV, the application of multivariate techniques for the analysis of data by *in situ* experiments is presented, in order to complete the analysis of XRPD data in presence of gradients: temporal (as described in Chapter 7, where the sedimentation of additives in epoxy resin is studied), spatial (Chapter 10, where XRPD is used for

the identification of surface defects and corrosion) and temperature (Chapters 11), with eutectic solutions studied in variable temperature conditions.

Finally, in Part V, the main results achieved during the thesis period are summarized and discussed, focusing on the future perspectives of the works in progress.

Methods and instrument development

4

MULTIVARIATE METHODS FOR QUALITATIVE AND QUANTITATIVE ANALYSIS

Whenever the wind whistles through the leaves, I'll think, "Lowenstein, Lowenstein".

Simpson, M.J.

The amount of useful information that can be extracted from a system under analysis is the heart of multivariate analysis in general and of the use of principal component analysis (PCA) in the scientific field in particular. The possibility of reducing or even isolating experimental noise through the transformation of experimental data obtained is one of the most powerful means available to the researcher. In this chapter, some procedures for the pre-process, analysis or transformation of data, useful to improve their interpretation are described. In Section 4.1, Savitzky-Golay filtering[1], one of the most famous and widespread algorithms in data analysis, is described. For its importance, the article in which the algorithm is described has been

indicated among the ten most important publications for analytical
chemistry[2, 3]. In addition to a brief description of the algorithm,
the procedure for its implementation within RootProf[4], is described.
In the same section, the implementation of implicit multithreading
within the software and its importance for the analysis of big data
matrices will also be described.

In Section 4.2, the automated procedure for transforming points from
a Euclidean coordinate system to a barycentric system will be de-
scribed. The method, originally proposed by Cornell in the Appendix
IIIB of his book [5], is implemented exploiting R code and improved
with an automated procedure for the simplex centering and orienta-
tion. This procedure, combined to PCA, can provide new possibilities
for phase quantification of mixtures as reported in the preliminary
studies of ref. [6]. An example of use of this algorithm is given in
Chapter 5, where mixtures are quantified directly from the PCA score
plot without any prior knowledge on the system. The obtained results
have been reported in a dedicated article recently submitted to the
Journal of Applied Crystallography. In Section 4.3, an algorithm for
the transformation of data from evolutionary processes is proposed
as a method for the observation and analysis of gradients. Examples
of application of this algorithm on simulated data are reported in the
same section and the algorithm code is reported in Appendix B.

4.1 Savitzky-Golay filtering and parallel programming updates for RootProf

RootProf[4, 7] is a software for the analysis of one-dimensional pro-
files developed at the Institute of Crystallography in Bari by Dr. Rocco
Caliandro and widely used to handle multivariate problems related
to the world of crystallography, but not only. The software is written
in C/C++ language and based on the libraries of the ROOT frame-
work developed at CERN in Geneva[8, 9]. RootProf is particularly

Figure 4.1: Effect of Savitzky-Golay filtering on data affected by noise. The black dashed line in the graph represent the original function without the added noise. The red continuous line represent data after being treated with Savitzky-Golay filtering.

suitable for quantitative analysis of mixtures exploiting spectroscopic data thanks to the MultiFit algorithm[4]. This procedure uses whole one-dimensional profiles, such as powder diffraction patterns, to obtain regression models. The fitting of the profiles is done through the Minuit library[10]. Since 2016, the author of this thesis has collaborated, in the development and dissemination of RootProf in the scientific community, in particular in the crystallographic field. As part of this project, some improvements have been proposed and successfully included within the software, the most important of which are Savitzky-Golay filtering (SGF) as an option for data pre-treatment and parallel computing. SGF consists in a convolution operation in

65

which a subset of points w from the equally spaced raw data is fitted by a polynomial of degree m [1]. The central point of the subset, which must therefore be odd, is the one on which the new value of the ordinate y_i' is calculated. At the next iteration, the window moves to the next point and the operation is repeated. For continuous and equidistant data series on the ordinate axis, the polynomial fitting has well-defined coefficients[11] based on the size of the window of points and the degree of the polynomial used for the approximation. This convolution procedure is called moving average as the central point is estimated by weighting the surrounding points for the convolution coefficients. Consider a set of points $\{x_j, y_j\}$ with $j = 1, 2, 3, \ldots, n$, with equidistant x_j. By selecting a proper window of points w, the smoothed central point y_j' of the window can be treated with convolution coefficients C_i according to [1]:

$$y_j' = \sum_{i=\frac{1-w}{2}}^{\frac{w-1}{2}} C_i\, y_{j+i}, \qquad \frac{w+1}{2} \leq j \leq n - \frac{w-1}{2} \tag{4.1}$$

Where $\frac{w+1}{2}$ and $\frac{w-1}{2}$ are the lower and the upper limits of the window of points respectively. With $w = 5$ and $m = 2$, then the set of coefficients described by Equation 4.1 becomes:

$$y_j' = \frac{1}{35}(-3y_{j-2} + 12y_{j-1} + 17y_j + 12y_{j+1} - 3y_{j+2}) \tag{4.2}$$

The result of this operation can be observed in Figure 4.1, where a set of points was generated starting from the black dashed curve by adding random noise. The red curve is obtained using the Savitzky-Golay smoothing on the black points with the coefficients described in Equation 4.2. Using the lowest possible degree polynomial and a small window of points, the shape of the starting function is very well approximated. By increasing the degree of the polynomial and/or the window of points, the result can be further improved. An additional parameter p is usually included within the algorithm. This parameter

is used to establish the order of derivation of the polynomial fitting function. In this way, it is possible, while smoothing the data profile, to perform the numerical derivative of order p of the smoothed spectrum.

Including the Savitzky-Golay filtering in a program can be done in two ways: the first, almost always preferred, consists in creating tables with the convolution parameters for each combination of p, m and w. By using this strategy, the algorithm is faster and the program only has to use on each y_j of Equation 4.1. In the second method, the fitting polynomial is calculated on the points at each step of the iteration starting from zero. Ordinary least squares are defined, for a general model matrix $\mathbf{M}$ as:

$$a = \left(\mathbf{M}^T\mathbf{M}\right)^{-1}\mathbf{M}^T Y \tag{4.3}$$

where a is the vector with the coefficient for the regression model, $\mathbf{M}^T$ is the transposed of the model matrix and T is the vector with the results. For the calculation of ordinary least squares, it is necessary to go through a matrix inversion, which in computer science most often is a slow step. This is not true in the ROOT framework, as the fitting procedure performed by the Minuit minimizer, based on Cholesky decomposition, is very fast and efficient. A custom polynomial of the desired degree m is used as a starting point and Minuit refines its coefficient fitting the points of the window w without using the matrix notation of Equation 4.3. The polynomial is stored as a ROOT's proprietary TF1 function and its coefficient are available for further analysis, being for instance the derivation. The calculation is further speeded up by the implicit parallelization procedure, implemented by the author of the present work during the doctoral period, in the last version of RootProf.

Parallelization is a process that consists in dividing the operations of a software on multiple processor's cores (implicit parallelism or multithreading), or on multiple processor (explicit parallelism). In a recent work by Piparo[12] and colleagues, the distinction between

implicit parallelism and explicit parallelism is deepened, referring to
the specific case of ROOT and also underlining how the two systems
are complementary.

The purpose of splitting the calculations is to increase the perfor-
mance of the machine on which the calculation is performed and to
drastically reduce the execution times of an algorithm. The concept
can be visualized in a very intuitive way assuming that a number n
of tasks T_i has to be completed within a program. By executing all n
tasks on a single unit, the time t taken by the computer to complete
the operations will be:

$$t = \sum_{i=1}^{n} T_i \tag{4.4}$$

By dedicating a unit to each single task, assuming therefore to have
n units, the computer will be able to execute all the tasks simulta-
neously and the time required to execute the program will be the
time necessary to execute the slowest among n tasks, as described by
equation 4.5:

$$t \approx MAX\left(T_i\right) \tag{4.5}$$

The implementation made in RootProf by the author of this work is
the implicit parallelism, as RootProf still is not optimized to run on
computer clusters. The computation speed has been increased by a
order of magnitude, based on the architecture of the host computer.
The machine used for the tests has an AMD Ryzen 5 3600X processor
with 6 cores, each of which can handle 12 threads. On this machine,
the program had a performance boost by completing the tasks in a
time close to one tenth of the one previously required.

4.2 Automated transformation from Euclidean to barycentric coordinate system

In 1928, August Ferdinand Möbius introduced the barycentric coordinate system, which is a coordinate system defined within a simplex[13–15]. This type of space, as seen in Section 2.3.3, is particularly useful to describe mixtures. Each point inside the simplex is described by a set of q coordinates equal to the order of the simplex minus one and the sum of all coordinates of a point is equal to 1, as described by the closure rule (Equation 2.8).

The Euclidean coordinate system is closely linked to the barycentric system and transformations of points from one space into another are possible with relative simplicity. Cornell, in the book "Experiments with Mixtures"[5] describes a convenient method for projecting the points belonging to a q-dimensional Simplex-centroid design (Section 2.3.3.2) to a $q-1$ independent coordinate system. For this operation, a q-dimensional simplex (i.e. $q = 3$), defined as in Figure 2.3 is represented through its barycentric coordinates as in Table 4.1. The

A	B	C
1.000	0.000	0.000
0.000	1.000	0.000
0.000	0.000	1.000
0.500	0.500	0.000
0.500	0.000	0.500
0.000	0.500	0.500
0.333	0.333	0.333

Table 4.1: Compositions of a Simplex-centroid design.

system is then reduced to a $(q-1)$-components system by removing one column from the compositional table. The simplex can now be represented in the $(q-1)$-dimensional system of independent coordinates just by rotating the simplex and centering one vertex on $\{0, 0\}$.

In the proposed example, to the three-component simplex of Table
4.1, the C column is removed and then all the points are projected
in the two-dimensional Euclidean space, as represented as in Figure
4.2. This can be done by multiplying the $q - 1$ dimensional system for
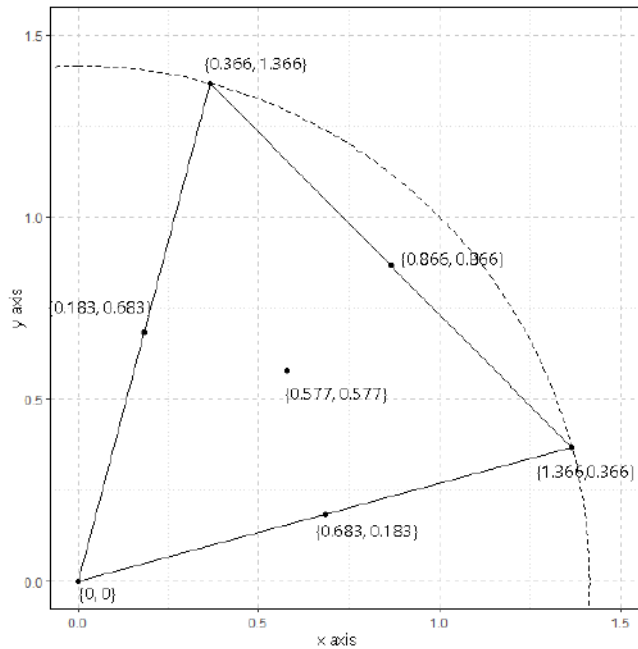
Figure 4.2: Simplex-centroid design as described in Table 4.1 pro-
jected in the x, y plane of independent coordinates.

the appropriate matrix $\mathbf{A}$ which has been generalized by Cornell as
follows[5]:

$$\mathbf{A} = a\mathbf{I} + b\mathbf{J} \qquad (4.6)$$

Where $\mathbf{I}$ is the identity matrix of order $q - 1$, $\mathbf{J}$ is a $(q - 1)$-dimensional
square matrix with all elements equal to 1 and a and b are respectively
the scalars:

$$a = 1; \qquad b = \frac{1}{1 + \sqrt{q}}; \qquad (4.7)$$

The inverse problem, passing from a set of points represented by Cartesian coordinates to the space of a simplex, is a relatively simple operation if the set is optimally arranged in space. If the group of points does not correspond to a simplex projected in Euclidean space, with the right orientation along the bisector of the axes, the problem can be more complex. When principal component analysis is performed on observations different one from another, samples are arranged in the score plot to be as far away from each other as possible[16–18]. The consequence of this behavior is that $q - 1$ significant principal components are generated to represent q objects. This phenomenon is intuitive when considering that a $(q - 1)$-dimensional space is the minimum required to represent a q-dimensional simplex (e.g. a triangle can be drawn on a 2D space and a tetrahedron on a 3D space).

PCA, as described in Chapter 2, is a technique mainly used for pattern recognition. For this use, in general, only the separation between samples is observed, often for classification purposes, although it is not optimized for this purpose[19]. However, in several occasions the relative distance between classes of samples was quantified to evaluate their separation[20, 21]. Moreover, the orthonormal basis of the PC space guarantees that the Euclidean metric can be used and then, it is possible to transform simplexes that may appear among the scores or between the loadings to a barycentric system for the estimation of the relative distances between a point and the other. A special algorithm was written for this purpose during the doctoral period. The R code for the case $q = 3$ is reported in Appendix A and has been successfully applied for the quantification of components in mixtures, the results of which are reported in Chapter 5. The algorithm uses the $q - 1$ generated scores as coordinates for the points, as in Figure 4.3(a). The scores are all range scaled in $[0, 1]$ and one vertex, the nearest one, is centered in $(0, 0)$. The q vertices of the simplex are identified and the $q - 1$ PC scores are range scaled for the interval $a + b$, with a and b as described in Equation 4.7 (Figure 4.3(b)). An
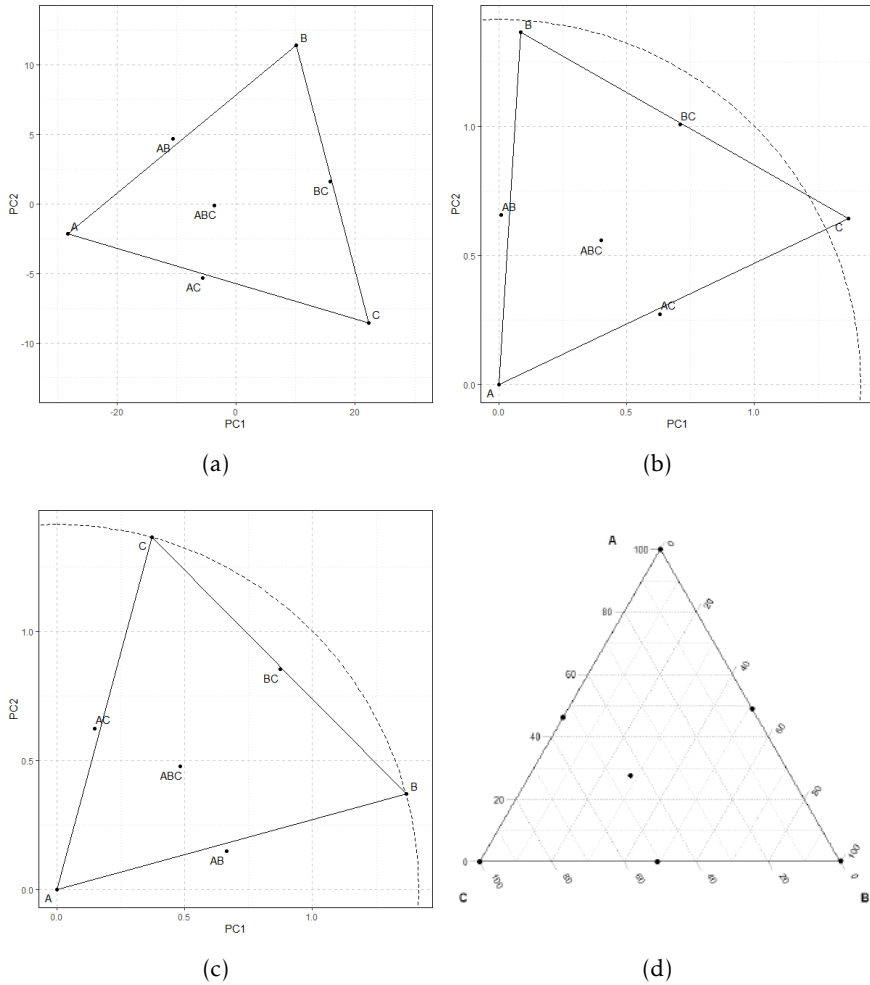
Figure 4.3: The four phases of Cornell rotation algorithm. 4.3(a): obtaining a simplex in a Euclidean space; 4.3(b): scaling and centering the simplex; 4.3(c): refine the simplex orientation until the stop condition is met; 4.3(d) transform independent coordinates into barycentric coordinates.

iterative loop then searches for the correct orientation of the simplex
in space by multiplying the $q-1$ scores matrix by a rotation matrix
defined as:

$$\begin{pmatrix} cos\theta & -sin\theta \\ sin\theta & cos\theta \end{pmatrix} \tag{4.8}$$

The loop refines the θ by dicotomic search until the difference be-
tween the coordinates of the vertices reach the stop condition, which
is met when the difference between the coordinates of the vertices is
lower than 10^{-10} (line 29 of listing 2 in Appendix A). The result of
this operation can be observed in Figure 4.3(c).

Finally, scores, in form of a matrix, are multiplied by the inverse of
the **A** matrix from Equation 4.6:

$$\begin{pmatrix} x_{1,1} & x_{1,2} & \dots & x_{1,q-1} \\ x_{2,1} & x_{2,2} & \dots & x_{2,q-1} \\ \vdots & \vdots & \ddots & \vdots \\ x_{n,1} & x_{n,2} & \dots & x_{n,q-1} \end{pmatrix} \cdot \mathbf{A}^{-1} \tag{4.9}$$

and the qth component is calculated by difference. The result, in
barycentric coordinates appears as in Figure 4.3(d). The last step of
the transformations gives as a result the weight of the three variables
which is, in the case of mixtures, the weight ratio of each component.
In Chapter 5, the algorithm is used in a practical case for the direct
quantification of mixtures starting from PCA score plots.

4.3 Forcefield: a novel algorithm for evolutionary process analysis

A second method for data transformation is proposed in this section
with the name of "Forcefield transformation". In physics, a field is
defined as a physical quantity which is expressed as a function of
the position in space and which therefore takes on a value for each
position of them[22, 23]. In the classical electromagnetic case, the

electric field is represented as the coulomb force divided by a point
reference charge q_0 as in equation 4.10:

$$E_{(x_0)} = \frac{F}{q_0} = \frac{1}{4\pi\epsilon_0} \frac{q_1}{(x_1 - x_0)^2} \vec{r}_{1,0} \tag{4.10}$$

Similarly, samples within a data set may not be independent from
each other, and this concept is the basic assumption of the trans-
formation. This particular condition is verified when the analyzed
samples are part of a changing set and, therefore, of a dataset col-
lected on an evolutionary process due to a gradient, which can be
time, temperature, concentration, spatial, and so on.

The Forcefield algorithm falls within the field of historical series[24]
and is closely linked to the study of recurrence plots[25, 26], in which
series of samples that present small differences each from the next,
are recoded and represented in graphical form for a better interpreta-
tion of their relations over time or for the identification of recurring
phenomena (eg meteorological data). In an experimental matrix $\mathbf{X}_{(n,p)}$
of n samples and p variables, sample x_1, according to the described
principles, could be defined by how it is related to the surrounding
samples, thus as a vector of "forces"F between it and all the other
samples in the dataset:

$$x_1 = \left(F_{(x_1, x_1)}, F_{(x_1, x_2)}, F_{(x_1, x_3)}, \dots, F_{(x_1, n)} \right) \tag{4.11}$$

The physical concept of force in the Forcefield transformation is de-
fined by the equation:

$$F_{(x_1, x_2)} = \frac{cor(x_1, x_2)}{d(x_1, x_2)^2} \tag{4.12}$$

Where the numerator is Pearson's correlation coefficient between the
two samples x_1 and x_2 and d_p is their Euclidean distance in the p-
dimensional space of matrix $\mathbf{X}_{(n,p)}$:

$$d(x_1, x_2) = \sqrt[p]{(x_{(2,1)} - x_{(1,1)})^2 + (x_{(2,2)} - x_{(1,2)})^2 + \cdots + (x_{(2,p)} - x_{(1,p)})^2} \tag{4.13}$$

Substituting equation 4.12 into 4.11, the transformation for of each sample of the matrix is obtained:

$$x_1 = \left(\frac{cor(x_1, x_1)}{d(x_1, x_1)^2}, \frac{cor(x_1, x_2)}{d(x_1, x_2)^2}, \frac{cor(x_1, x_3)}{d(x_1, x_3)^2}, \ldots, \frac{cor(x_1, x_n)}{d(x_1, x_n)^2} \right) \quad (4.14)$$

In the transformation, the terms related to autocorrelation and the distance of a point from itself are replaced by 1 to avoid errors. Repeating the process for all the n samples, the new matrix $F_{(n,n)}$ of the Forcefield-transformed data, is obtained. The first and most important observation on the $F_{(n,n)}$ matrix is that properties regarding the p variables of $X_{(n,p)}$ are lost: the only retained information is the correlation among samples. A second observation can be made: if the data matrix $X_{(n,p)}$ has a gradient along n, the produced $F_{(n,n)}$ matrix is a diagonal constant band matrix (Toeplitz-like matrix[27]) and behaves accordingly. In Figure 4.4, two data matrices (4.4(a) and 4.4(b)) are reported. Matrix 4.4(a) is obtained by generating 100 random samples described by 200 variables. The same is done for matrix 4.4(b), but with a gradient that progressively widens the range of variables values. The added gradient simulate an evolution of the pattern (for instance in the case of interest, a chemical reaction) along the 100 samples and affects all 200 variables coherently. By performing the Forcefield transformation on both matrices, the relative distances between samples are calculated according to Equation 4.14. The result for a matrix of unrelated samples is a map as in Figure 4.4(c), consisting of statistical fluctuations, apart from the autocorrelation diagonal. A matrix with data linked each other by a gradient appears instead as in Figure 4.4(d), i.e. as a Toeplitz matrix. Plotting the logarithm of the first row or column of the $F_{(n,n)}$ matrix against the index n indicating the sample number, different trends are observed in the data, typical for each dependence that binds one sample to the next on. Figure 4.5 shows some examples of dependencies between data: linear in 4.5(a), exponential in 4.5(b), reciprocal in 4.5(c) and null in 4.5(d). The trends are easily recognizable and it is easy to trace the type of
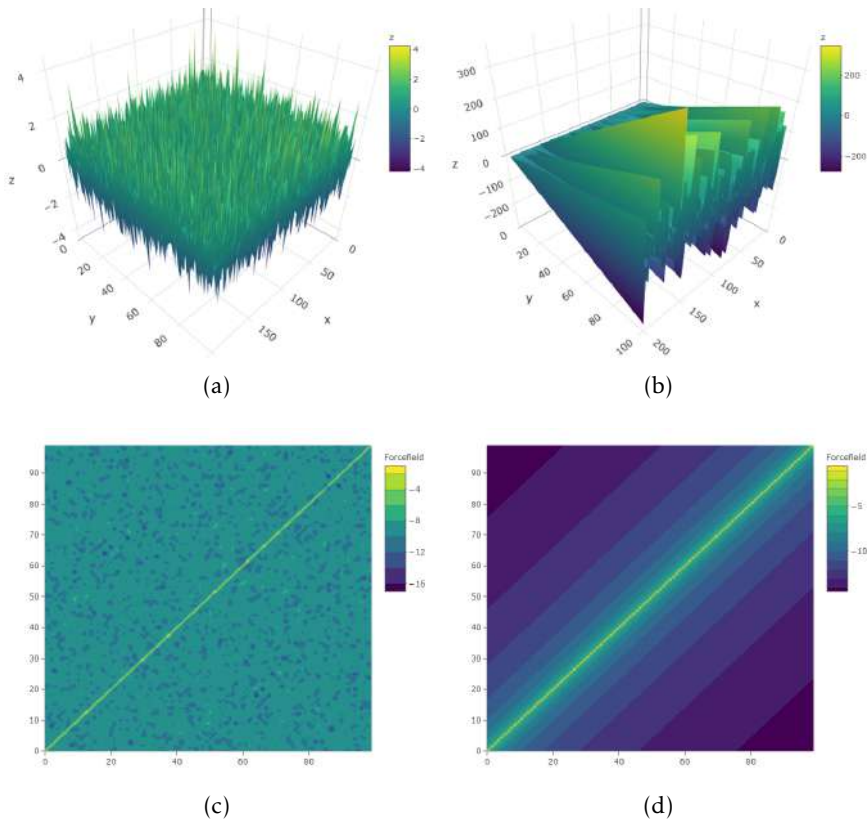
Figure 4.4: Uncorrelated and evolving data pre-and post-Forcefield.
4.4(a): random generated samples; 4.4(b): random generated samples with values progressively increasing along matrix rows; 4.4(c): Forcefield on 4.4(a); 4.4(d): Forcefield on 4.4(b).

phenomenon that is occurring in the samples. A noteworthy case consists in performing the spectral decomposition of a matrix $\mathbf{F}_{(n,n)}$: if data are connected to each other by a gradient, by performing the matrix decomposition of $\mathbf{F}_{(n,n)}$ (i.e. performing PCA) the projection of the samples of $\mathbf{F}_{(n,n)}$ in the new coordinates space will turn out to assume the typical horseshoe shape, known in literature as Horseshoe effect or Guttmann effect[28–30]. This phenomenon appears precisely when a gradient affects the data and is due to the projection
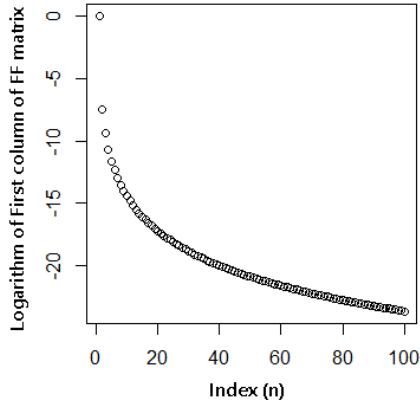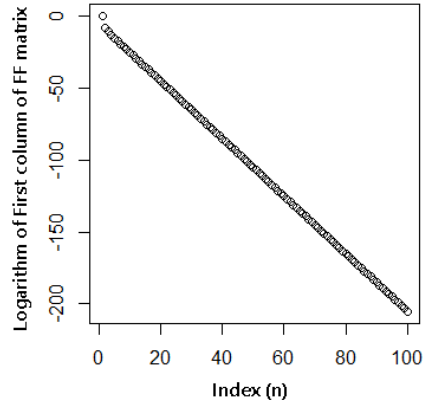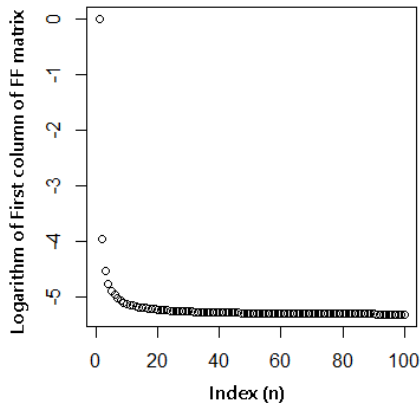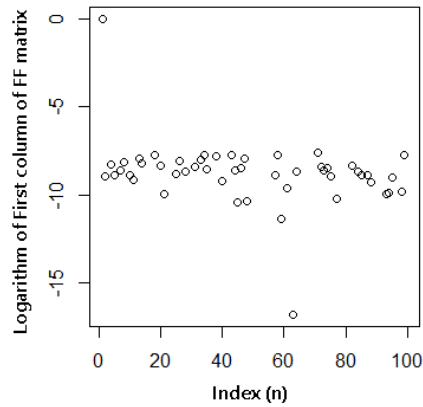
Figure 4.5: Graphs of the logarithm of the first columns of Forcefield matrix affected by different types of gradients. 4.5(a): linear gradient; 4.5(b): exponential gradient; 4.5(c): reciprocal gradient; 4.5(d): random data.

of equally distanced samples into the new coordinate system, as it was observed in a recent publication by some of us[31]. We can conclude that the Forcefield approch can extract from a data matrix the evolution underlying the data and it thus a promisining new tool for the analysis of *in situ* data. The algorithm, presented in Section 4.3, was completely designed, developed and tested by me. Few examples of this novel approach are reported in Appendix B.

Bibliography

[1] A. Savitzky and M. J. E. Golay. «Smoothing and Differentiation of Data by Simplified Least Squares Procedures.» In: 36.8 (July 1964), pp. 1627–1639. DOI: 10.1021/ac60214a047. URL: https://doi.org/10.1021/ac60214a047.

[2] C. K. Larive and J. V. Sweedler. «Celebrating the 75th Anniversary of the ACS Division of Analytical Chemistry: A Special Collection of the Most Highly Cited Analytical Chemistry Papers Published between 1938 and 2012.» In: 85.9 (May 2013), pp. 4201–4202. DOI: 10.1021/ac401048d. URL: https://doi.org/10.1021/ac401048d.

[3] J. Riordon, E. Zubritsky, and A. Newman. «Top 10 Articles.» In: 72.9 (May 2000), 324 A–329 A. DOI: 10.1021/ac002801q. URL: https://doi.org/10.1021/ac002801q.

[4] R. Caliandro and D. B. Belviso. «RootProf: software for multivariate analysis of unidimensional profiles.» In: *Journal of Applied Crystallography* 47.3 (2014), pp. 1087–1096.

[5] J. Cornell. *Experiments with Mixtures: Designs, Models, and the Analysis of Mixture Data.* Wiley Series in Probability and Statistics. Wiley, 2011. ISBN: 9781118150498.

[6] P. Guccione et al. «Multivariate Analysis Applications in X-ray Diffraction.» In: *Crystals* 11.1 (Dec. 2020), p. 12. DOI: 10.3390/cryst11010012. URL: https://doi.org/10.3390/cryst11010012.

[7]   R. Caliandro. *RootProf - An interactive, general purpose tool for processing unidimensional profiles with specific applications to diffraction and spectroscopic measurements*. 2020. URL: https://users.ba.cnr.it/ic/crisrc25/RootProf/RootProf%5C_help.html.

[8]   R. Brun and F. Rademakers. «ROOT — An object oriented data analysis framework.» In: 389.1-2 (Apr. 1997), pp. 81–86. DOI: 10.1016/s0168-9002(97)00048-x. URL: https://doi.org/10.1016/s0168-9002(97)00048-x.

[9]   R. Brun et al. *root-project/root: v6.18/02*. 2019. DOI: 10.5281/ZENODO.3895860. URL: https://zenodo.org/record/3895860.

[10]   F. James. «MINUIT Function Minimization and Error Analysis: Reference Manual Version 94.1.» In: (1994).

[11]   P. Guest and P. Guest. *Numerical Methods of Curve Fitting*. Cambridge University Press, 2012. ISBN: 9781107646957. URL: https://books.google.it/books?id=UjnBOFIWv%5C_AC.

[12]   D. Piparo et al. «Expressing Parallelism with ROOT.» In: 898 (Oct. 2017), p. 072022. DOI: 10.1088/1742-6596/898/7/072022. URL: https://doi.org/10.1088/1742-6596/898/7/072022.

[13]   A. F. Mobius. *Der barycentrische Calcul ein neues Hülfsmittel zur analytischen Behandlung der Geometrie dargestellt und insbesondere auf die Bildung neuer Classen von Aufgaben und die Entwickelung mehrerer Eigenschaften der Kegelschnitte angewendet von August Ferdinand Mobius Professor der Astronomie zu Leipzig*. Verlag von Johann Ambrosius Barth, 1827.

[14]   M. Koecher and A. Krieg. *Ebene Geometrie*. Springer-Verlag, 2007.

[15] E. Hille. *Analytic function theory, Volume I*. Vol. 269. American Mathematical Soc., 2012.

[16] H. Hotelling. «Analysis of a complex of statistical variables into principal components.» In: *Journal of Educational Psychology* 24.6 (1933), pp. 417–441. DOI: 10.1037/h0071325. URL: https://doi.org/10.1037/h0071325.

[17] K. Pearson. «The law of ancestral heredity.» In: *Biometrika* 2.2 (1903), pp. 211–228.

[18] I. Jolliffe. «Principal component analysis.» In: *Encyclopedia of statistics in behavioral science* (2005).

[19] K. Fukunaga. *Introduction to statistical pattern recognition*. Elsevier, 2013.

[20] E. Alizadeh et al. «Measuring systematic changes in invasive cancer cell shape using Zernike moments.» In: 8.11 (2016), pp. 1183–1193. DOI: 10.1039/c6ib00100a. URL: https://doi.org/10.1039/c6ib00100a.

[21] A. M. Goodpaster and M. A. Kennedy. «Quantification and statistical significance analysis of group separation in NMR-based metabonomics studies.» In: 109.2 (Dec. 2011), pp. 162–170. DOI: 10.1016/j.chemolab.2011.08.009. URL: https://doi.org/10.1016/j.chemolab.2011.08.009.

[22] R. Feynman. *The Feynman lectures on physics*. Redwood City, Calif: Addison-Wesley, 1989. ISBN: 978-0-201-02115-8.

[23] E. McMullin. In: 4.1 (Feb. 2002), pp. 13–39. DOI: 10.1007/s00016-002-8357-5. URL: https://doi.org/10.1007/s00016-002-8357-5.

[24] T. Scagliarini et al. *Quantifying high-order interdependencies on individual patterns via the local O-information: theory and applications to music analysis*. 2021. eprint: arXiv:2108.11625.

[25] T. March, S. Chapman, and R. Dendy. «Recurrence plot statistics and the effect of embedding.» In: 200.1-2 (Jan. 2005), pp. 171–184. DOI: 10.1016/j.physd.2004.11.002. URL: https://doi.org/10.1016/j.physd.2004.11.002.

[26] D. F. Silva, V. M. D. Souza, and G. E. Batista. «Time Series Classification Using Compression Distance of Recurrence Plots.» In: IEEE, Dec. 2013. DOI: 10.1109/icdm.2013.128. URL: https://doi.org/10.1109/icdm.2013.128.

[27] A. Bottcher. *Toeplitz matrices, asymptotic linear algebra, and functional analysis*. Basel, Switzerland Boston: Birkhauser, 2000. ISBN: 978-3-0348-8395-5.

[28] J. T. Morton et al. «Uncovering the Horseshoe Effect in Microbial Analyses.» In: *mSystems* 2.1 (2017). Ed. by J. K. Jansson. DOI: 10.1128/mSystems.00166-16. eprint: https://msystems.asm.org/content/2/1/e00166-16.full.pdf. URL: https://msystems.asm.org/content/2/1/e00166-16.

[29] B. Le Roux and F. Murtagh. «B. Le Roux and H. Rouanet, Geometric Data Analysis, From Correspondence Analysis to Structured Data Analysis, Dordrecht, Kluwer, 2004, pp. xi + 475.» In: *Journal of Classification* 25 (2008), pp. 137–141. DOI: 10.1007/s00357-008-9007-7.

[30] P. Diaconis, S. Goel, and S. Holmes. «Horseshoes in multidimensional scaling and local kernel methods.» In: *Ann. Appl. Stat.* 2.3 (2008), pp. 777–807. DOI: 10.1214/08-AOAS165. URL: https://doi.org/10.1214/08-AOAS165.

[31] E. Conterosito, M. Lopresti, and L. Palin. «In Situ X-ray Diffraction Study of Xe and CO2 Adsorption in Y Zeolite: Comparison between Rietveld and PCA-Based Analysis.» In: 10.6 (June 2020), p. 483. DOI: 10.3390/cryst10060483. URL: https://doi.org/10.3390/cryst10060483.

5

Quantitative phase analysis of mixtures from XRPD and XRF data set.

That's where I saw the Leprechaun. He tells me to burn things.

Wiggum, R.J.

A project dedicated to the development of new methods for quantitative analysis from polycrystalline mixtures (a typical concentration gradient) was carried out during the doctoral period, in the context of methods development. The aim of the project is to demonstrate how multivariate methods for quantitative analysis can become part of the toolkit available to the researcher, together with established methods such as Rietveld refinement (RR) and the partial or no known crystal structure (PONKCS) for X-ray powder diffraction (XRPD) and the fundamental parameters method (FP) for X-ray fluorescence (XRF) data. Results given by traditional methods were compared to the ones obtained by multivariate approach that were

presented in Chapter 2 and in the review article of ref. [1]. Analyses were performed on XRPD and XRF data from four different data sets consisting of 10 samples each, prepared according to the Simplex-centroid augmented experimental design presented in Section 2.3.3.2. The mixtures have been designed in order introduce issues for quantification in the samples, such as the microabsorption (MA), that was obtained by choosing samples with large differences in densities and in the atomic number Z. Phases were selected as representative of real world cases. For example, graphite is used as a lubricant, urea i.e. is used in the automotive field as an ADBlue additive, while the inorganic phases are used in a mixture with light phases as additives for polymers. Furthermore, the preparation is carried out in such a way as to simulate the industrial reality, in which "as received"samples are analysed without careful grinding and without trying to avoid preferred orientations (PO). A the main characteristics of each dataset is reported in Table 5.1 and in more detail in Appendix C. A dedicated article containing all details on sample preparation and data collection was published in Data in Brief (Elsevier BV)[2] and is reported in Annex IV.

5.1 Traditional approach

The traditional methods used for quantitative XRPD analysis, excluding single peak ones, such as the reference intensity ratio (RIR), are the whole profile fitting refinements, such as Rietveld method. Other approaches were developed starting from Rietveld refinement, trying to compensate limitations, such as PONKCS (partial or not known crystal structure) method.

The first method, introduced by H. M. Rietveld in the late 1960s, consists of a least squares whole pattern refinement approach. The refinement is obtained minimizing the differences between the experimental diffraction pattern and the reference one, calculated from a known crystal structure. The fit also takes into account all the

Dataset	Chemicals	Description
D1	$BaSO_4$, Bi_2O_3, sieved C	Graphite has a diameter ϕ<90 µm to introduce limited PO effects. Large differences in density of the three phases for MA effect. Absence of characteristic XRF signal for graphite.
D2	$BaSO_4$, Bi_2O_3, mixed C	Same of data set D1, but graphite has a 30% in weight content with diameter larger than 90 µm for moderate PO effects.
D3	$BaSO_4$, Bi_2O_3, $ZnC_4H_6O_4$	All phases have an XRF signal. Zinc acetate introduces moderate PO and has lower a density than graphite, enhancing MA effects. Zinc acetate has a larger unit cell, to increase peak superposition in XRPD.
D4	$BaSO_4$, Bi_2O_3, CH_4N_2O	Absence of XRF signal, slight PO effect. Urea presents larger average particle size and has a lower density than zinc acetate, with increased micro-absorption effects.

Table 5.1: Description of four different data sets analysed by XRPD and XRF.

morphological and textural contributions coming from the samples (crystal size, preferred orientations) and from the instrumental setup. The least squares approach then allows to obtain the scale factor of each phase present in the polycrystalline mixture, which is related to the mass fraction by the equation[3]:

$$W_i = \frac{S_i (ZMV)_i \mu_m^*}{K} \qquad (5.1)$$

where W_i is the mass fraction of the i-th component of the mixture, S_i is its scale factor, Z is the number of formula units per unit cell, M is the mass of the formula unit and V the volume of the unit cell, μ_m^* is the mass absorption coefficient of the mixture and K is the value of the instrumental constant, if a standard is used as reference for the instrumental profile. The mass absorption coefficient is unknown for each mixture, but assuming that all phases are crystalline, it can be eliminated from the equation, along with the instrumental constant[4]. However, the presence of PO can cause errors in the estimation of the scale factor, even using common corrections such as the

March Dollase or the spherical harmonics functions[5, 6]. Another
problem is caused by MA, which causes the light phases to be always
overestimated compared to the heavy components, as part of the inci-
dent or outgoing X-rays are absorbed by the last ones. Some solutions
such as the Brindley correction can reduce the effect of microabsorp-
tion, but it is necessary to assume that all particles are spherical and
of the same diameter, which is unrealistic[7], especially in real world
samples.

The PONKCS method[8], developed by Scarlett and Madsen, acts
as a hybrid between the Rietveld method and the pure multivariate
multiregression method. PONKCS is able to partially overcome the
problem related to the mandatory knowledge of the crystalline struc-
tures, estimating the quantities of the unsolved phases exploiting the
equation:

$$(ZMV)_i = \frac{W_i}{W_s} \cdot \frac{S_s}{S_i} \cdot (ZMV)_s \qquad (5.2)$$

Where i is the unknown phase and, consequently, the structural pa-
rameters $(ZMV)_i$ are not known. The quantification of what is not
refined against the experimental structure is made by difference us-
ing a standard sample of know composition from which s parameters
of Equation 5.2 are known. The advantage that PONKCS has over the
multivariate approach described in Chapter 4, is that known phases
and unknown phases can be refined starting from the same diffrac-
tion pattern, optimizing information management.

The FP method for XRF data allows to perform quantitative elemen-
tary analysis without the need for calibration conducted empirically,
such as through the use of standards or calibration lines[9]. The
method, introduced by Criss and Birks[10] at the end of the 1960s,
allows to carry out quantitative analysis starting from the equations
governing the interactions between X-rays and matter. The FP equa-
tions allow to model the background of the spectrum, to perform an
automatic deconvolution in case of overlapping of the peaks and to
quantify the area of the peaks associated with each transition. The

method is nowadays included in most instruments on the market and the calculation of the composition of each sample can be reduced to a simple equation, also reported by Rousseau[11–13]:

$$C_i = k_i \cdot I_i \cdot M_{is} \qquad (5.3)$$

where C_i is the concentration of the specie in analysis i, I_i are the intensities of the peaks, k_i is a calibration constant and M_{is} is the correction for the matrix effect of the i-th analyte in the sample s. The key step is the determination of the parameter M_{is}, as it changes according to the composition of the sample and is affected by MA, that change the relative intensities of the emissions. Furthermore, as reported in Chapter 4, benchtop instruments are not able to detect atoms lighter than sodium, therefore the quantification is even more complex when, as in the case of data sets D1, D2 and D4, one phase is completely invisible to the instrument, except for its Compton signal. The silver-based X-ray source produces a characteristic K_α, capable of passing through the light phases, producing nonelastic (Compton) scattering. This effect is greatly reduced in the presence of heavy phases, such as barite and bismite, which absorb Compton scattering. It follows that the signal linked to nonelastic scattering can be used to indirectly estimate the lighter phases.

The data obtained by XRF varies significantly according to the measurement conditions. When dealing with mixtures containing heavy elements, it would be optimal to measure at the highest voltage of the X-ray tube, typically 50 kV. However, the silver tube used can produce a high Compton effect due to the presence of the light phases in the sample. However, the Compton effect produced at 50 kV is almost completely reabsorbed by the barite and bismite, which would not allow any method to be used to estimate phase 3 of the mixture. Analyzing at 20 kV, on the other hand, there are no large variations in the relative intensities of the bismuth and barium peaks, but a band is produced, attributable to the Compton effect, which is not absorbed by the two heavier elements, useful for the estimation of
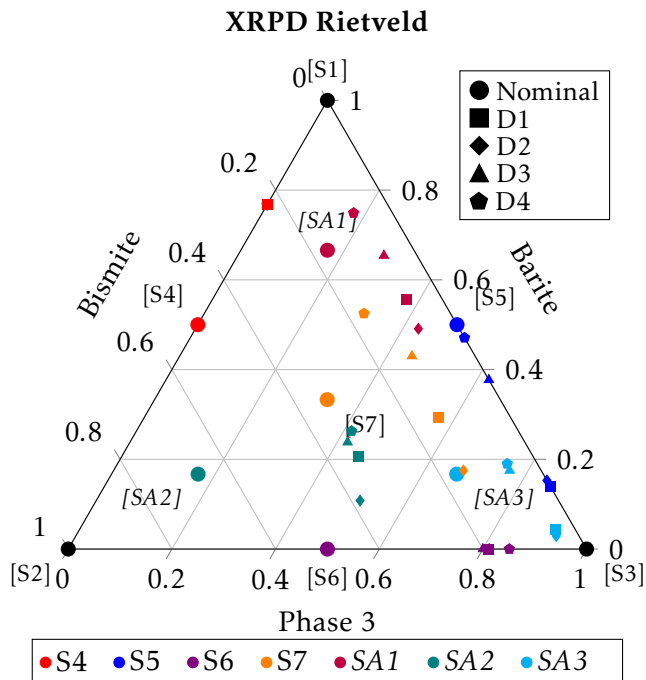
Figure 5.1: Results of the Rietveld analysis reported on the ternary graph representing the mixtures experimental domain; S1-S7 are the single, binary and ternary samples of the simplex design, while SA1-3 are the augmented simplex samples; Phase 3 is graphite, oriented graphite, zinc acetate and urea in data set D1, D2, D3, D4 respectively.

ligher elements without K_α detectable emissions

In Sections 5.1.1 and 5.1.2, results obtained using the traditional methods for XRPD and XRF, are reported respectively.

5.1.1 Rietveld refinement and Partial or not known crystal structure of XRPD data

In Figure 5.1 the data obtained by using Rietveld refinement are reported for each data set. Each of the above described data sets is associated to a symbol, while a specific composition is associated to a
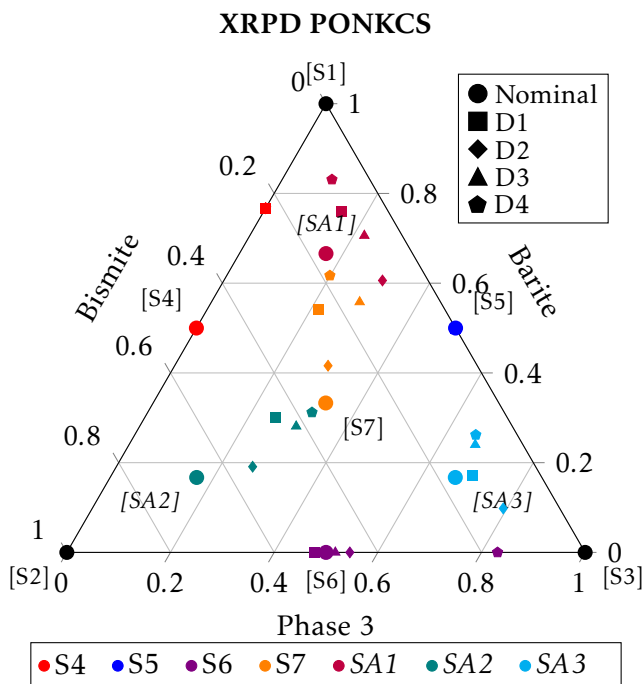
Figure 5.2: Results of the PONKCS analysis reported on the ternary graph representing the mixtures experimental domain. Labelling and color scheme as in Figure 5.1.

color (S1-S7 the mixtures of the simplex-centroid plan, SA1-SA3 the augmented mixtures)[2], as described in Appendix C. The purpose of this representation is to give the reader an idea of the degree of aggregation of the points around the nominal values, indicated by the circle. In this way, the information related to the accuracy of the quantification is immediate. In Figure 5.1, marks belonging to each sample are dispersed and sometimes much distant from the nominal values (circles). At first glance, it can be seen that the marks belonging to the ternary mixtures are all shifted to high values of phase 3. The RR, carried out with a standard approach, greatly overestimates phase 3 of the mixture (the lighter one), in accordance with the aforementioned reasons related to MA. Even in the case of the 50:50

mixture between barite and bismite, both dense materials with high
Z elements, there is an overestimation of the barite (lighter phase) at
76.7%, as bismite is more affected by MA. PO belonging to graphite
(Phase 3 of data set D1 and D2) worsen the Rietveld quantification of
phase 3, as the marks are even more distant from the nominal values.
It should be noted that no fit residues were overlooked, but rather
that the RR produced a model that accurately fitted the patterns, but
with quantification far away from correct values. This means that
the error on the quantification could have been managed only with
a priori knowledge of the system since, for an "as received"sample,
there could have been no clues to an incorrect quantification.

The PONKCS method is the most convenient evolution of the RR
to try to calibrate and correct the microabsorption effects when the
lighter phases of a polycrystalline mixture are overestimated. PONKCS
performs Rietveld refinement on a subset of known phases and uses
an approach similar to the MultiFit one presented in Section 4.1 for
the estimation of the remaining phases, i.e. without known crystal
structure or, as in the present case, with strong problems as PO for
graphite. To calibrate PONKCS and calculate its ZMV value as in eq.
5.2 the mixture at 50% in barite and 50% in phase 3 was used, for
this reason only the nominal value (blue circle in Figure 5.2) is visible
in the diagram. Other attempts using other mixtures for calibration
have been made, but only this is reported because of its best overall
result. As can be seen in Figure 5.2, the dispersion of marks around
the nominal values is less than the one seen in Figure 5.1 for the RR.
Samples appear to be less shifted to high values of phase 3, indicat-
ing that PONKCS is able to compensate for both MA and PO. The
quantification, despite the overall improvement, still lead to elevate
errors, between 10 and 20% in weight for each mixture.

Table 5.2: Results of quantifications by fundamental parameters algorithm within Rigaku NEXQC instrument.

Sample	Nominal values			Results		
-	Ba	Bi	Gr	Ba	Bi	Gr
D1 - SA1	0.666	0.167	0.167	0.706	0.294	0.000
D1 - SA2	0.167	0.666	0.167	0.376	0.624	0.000
D1 - SA3	0.167	0.167	0.666	0.413	0.587	0.000
-	Ba	Bi	Gr	Ba	Bi	Gr
D2 - SA1	0.666	0.167	0.167	0.744	0.266	0.000
D2 - SA2	0.167	0.666	0.167	0.123	0.877	0.000
D2 - SA3	0.167	0.167	0.666	0.333	0.666	0.000
-	Ba	Bi	Zn	Ba	Bi	Zn
D3 - SA1	0.666	0.167	0.167	0.523	0.145	0.332
D3 - SA2	0.167	0.666	0.167	0.152	0.668	0.179
D3 - SA3	0.167	0.167	0.666	0.129	0.165	0.706
-	Ba	Bi	Ur	Ba	Bi	Ur
D4 - SA1	0.666	0.167	0.167	0.750	0.250	0.000
D4 - SA2	0.167	0.666	0.167	0.181	0.819	0.000
D4 - SA3	0.167	0.167	0.666	0.415	0.585	0.000

5.1.2 Fundamental parameters analysis of XRF data

In Table 5.1.2, values obtained for the quantification of the mixtures belonging to the different data sets are reported. For convenience of comparison with the supervised analysis of Section 5.2.2, only the results of the quantitative analysis for the augmented mixtures are reported.

FP method fails to estimate the light phases containing carbon, oxygen, nitrogen and hydrogen, which are associated with phase 3 of data sets D1, D2 and D4. On the contrary, the FP method is able to estimate, with good accuracy, the content of Zinc present in the mixtures of data set D3. The limitation of the FP method lies in the

impossibility of exploiting the entire fluorescence spectrum collected, being linked to the quantification based exclusively on the characteristic X-ray emission of each element. If phase 3 is neglected in data sets D1, D2 and D4, the ratios between barite and bismite are consistent with the results, indicating that the method is not providing an incorrect result, it simply cannot identify a third phase within the mixtures, i.e. the lighter one with elements with $Z < 11$. To overcome this limitation, in some cases the entire fluorescence spectrum is used[9] and a regression is also performed using the intensity of each characteristic peak, including the one belonging Compton effect, but this procedure is not implemented in commercial instruments.

5.2 Multivariate approach

Multivariate analysis was performed at different levels, first as a supervised analysis, as an unsupervised analysis[14] and later as a PCA blind analysis. The first case was carried out by supplying the software the known composition of all the simplex-centroid samples as input and setting the augmented experiments as test set (Experiments SA1, SA2 and SA3). The unsupervised analysis, on the other hand, was performed by providing input only the three pure samples of the simplex-centroid and the remaining seven samples as test sets (Experiments S4-S7, SA1-SA3). A totally different approach was used for blind analysis: while the two first methods are based on the construction of regression models for the quantification of the components of the mixtures, in the case of blind analysis no model is produced and the quantification is carried out calculating the relative distances among the samples projected on the Score Plots obtained by PCA. For the sake of brevity, only the most important results are reported, while the complete results are reported in a dedicated publication submitted to the Journal of Applied Crystallography[15].

The main advantage of the multivariate method consists in not requiring the knowledge of crystal structures, as it is assumed that the

mass fractions of each component are somehow related to the intensi-
ties measured experimentally and the approach is able to recover this
relation. On the other hand, the lack of structural information such
as a scale effect on intensities. Multivariate analysis must therefore
go through a procedure in which the best pre-process combination
of raw data is identified. This data pre-treatment aims to place the
user in the best conditions to extract the information contained in
the data and estimate the scale factor between intensities and weight
fractions.

5.2.1 Pre-process selection

Before starting with the data analysis, a search for the best pre-process
combination was carried out by means of a supervised data analysis.
The calibration is usually carried out automatically by RootProf[14]
by crossing and testing all the available pre-treatments and transfor-
mations. In this case, however, the search for the best combination
of pre-treatments was carried out in part manually, as we wanted
to test transformations that had not yet been integrated within this
software, such as the first derivative of the profiles, the smoothing
Savitzky-Golay and the autoscaling function. The pre-process opti-
mization work was performed using a complete 5-factor factor design,
plus eight additional experiments, for a total of 40 supervised analy-
ses performed on each data set, for both XRPD and XRF data, with a
total of 320 exploratory supervised analyses. The choice of the best
combination of pre-treatments was made using the squared sum of
residuals (SSR) from the expected values for each sample. The details
about all pre-process combinations are reported in the ESI files of the
above cited submitted article.

In addition to finding the best pre-process combinations for quan-
titative analysis, this extended factorial plan was used to identify any
trends in pre-process selection, so that a "standard recipe"could be
created and used by every user facing this type of systems for the

first time, also without a profound knowledge of the pre-processing
routines. This could help the diffusion of such approaches, also in
the industrial world for automatic quality control procedures. Con-
cerning the XRPD data, recurrent pre-processes were identified in all
analyses associated with a low SSR. It has been noted that, concerning
the pre-processes external to RootProf, first derivative and autoscal-
ing are not very efficient, while the Savitzky-Golay smoothing with
polynomial of degree 2 and window of points between 5 and 9 helps
to improve the signal to noise ratio. Concerning the pre-processes
already implemented in RootProf, a small selection of transforma-
tion seemed to be favoured. Supervised analyses associated to a low
SSR used the transformation of the profiles by the logarithm of base
10, the normalization to 1 of the area underlying the profiles, the
absence of a background subtraction and a filtering of the data per-
formed by principal component analysis. In the program input file,
this combination corresponds to the string: preprocess 3 2 0 3. As
for XRF data, the best combination of pre-treatments has a string for
the RootProf input corresponding to: preprocess 3 2 48 3. This
combination is very similar to that identified for XRPD data, with
the addition of a background subtraction, with a window of points
equal to 48. Another difference is that, concerning the external pre-
processes, the autoscaling is preferred in the vast majority of cases
associated to a low SSR. It should be noted that the SSR obtained
for the best quantitative analyses performed on the XRF data is up
to 5 times higher than that obtained for the XRPD data. This is due
to the fact that XRF data are strongly affected by matrix effect and
microabsorption. Furthermore, the use of Compton scattering alone
is not sufficient for a correct estimation of the phases containing only
light atoms, such as graphite and urea.

The best pre-processes, selected for each data set, were used in all
analyses of the following sections.
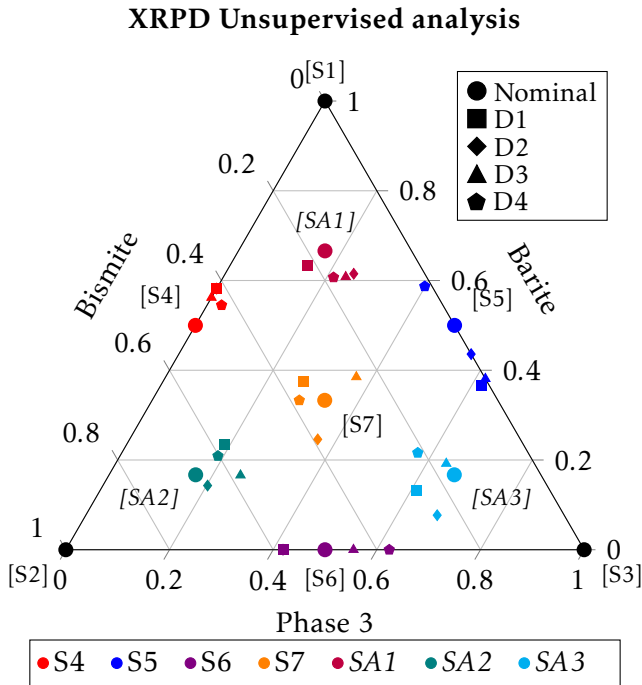
Figure 5.3: Results of the unsupervised analysis reported on the ternary graph representing the mixtures experimental domain. Labelling and color scheme as in Figure 5.1.

5.2.2 Supervised and unsupervised quantitative phase analysis

The quantitative XRPD analysis was performed both supervised and unsupervised. The unsupervised analysis was performed using only pure phases for the construction of the regression models and all the mixtures, both from the basic simplex and from augmented experiments, were used as test set. The only information retained by the supervised analysis is that regarding the best pre-process selected. Figure 5.3 shows the results of the unsupervised analysis. Since they are very similar to the results obtained using the supervised analysis, only results of the unsupervised analysis are reported. The added

Table 5.3: Results of the unsupervised analysis performed on XRPD data by multivariate approach.

XRPD data

data set D1

Chemical	Ba	Bi	Gr	Ba Bi	Ba Gr	Bi Gr	Ba Bi Gr	SA 1	SA 2	SA 3
Ba	1.000	0.000	0.000	0.582 (0.082)	0.367 (-0.133)	0.000 (0.000)	0.374 (0.041)	0.634 (-0.032)	0.235 (0.068)	0.133 (-0.034)
Bi	0.000	1.000	0.000	0.418 (-0.083)	0.014 (0.014)	0.581 (0.081)	0.354 (0.021)	0.215 (0.048)	0.577 (-0.089)	0.257 (0.090)
Gr	0.000	0.000	1.000	0.000 (0.000)	0.618 (0.118)	0.419 (-0.081)	0.271 (-0.062)	0.150 (-0.017)	0.188 (-0.017)	0.610 (-0.056)

data set D2

Chemical	Ba	Bi	Gr	Ba Bi	Ba Gr	Bi Gr	Ba Bi Gr	SA 1	SA 2	SA 3
Ba	1.000	0.000	0.000	0.582 (0.082)	0.436 (-0.064)	0.000 (0.000)	0.246 (-0.087)	0.615 (-0.051)	0.143 (-0.024)	0.077 (-0.090)
Bi	0.000	1.000	0.000	0.418 (-0.082)	0.000 (0.000)	0.580 (0.080)	0.390 (0.057)	0.137 (-0.030)	0.655 (-0.011)	0.244 (0.077)
Gr	0.000	0.000	1.000	0.000 (0.000)	0.564 (0.064)	0.419 (-0.081)	0.363 (0.030)	0.248 (0.081)	0.202 (0.035)	0.678 (0.012)

data set D3

Chemical	Ba	Bi	Zn	Ba Bi	Ba Zn	Bi Zn	Ba Bi Zn	SA 1	SA 2	SA 3
Ba	1.000	0.000	0.000	0.562 (0.062)	0.381 (-0.119)	0.000 (0.000)	0.385 (0.052)	0.608 (-0.058)	0.166 (-0.001)	0.192 (0.025)
Bi	0.000	1.000	0.000	0.438 (-0.062)	0.000 (0.000)	0.444 (-0.056)	0.246 (-0.054)	0.156 (-0.011)	0.580 (-0.086)	0.169 (0.002)
Gr	0.000	0.000	1.000	0.000 (0.000)	0.619 (0.119)	0.555 (0.055)	0.368 (0.035)	0.236 (0.069)	0.254 (0.087)	0.638 (-0.028)

data set D4

Chemical	Ba	Bi	Ur	Ba Bi	Ba Ur	Bi Ur	Ba Bi Ur	SA 1	SA 2	SA 3
Ba	1.000	0.000	0.000	0.587 (0.087)	0.000 (0.000)	0.333 (0.000)		0.607 (-0.059)	0.209 (0.042)	0.216 (0.049)
Bi	0.000	1.000	0.000	0.426 (-0.074)	0.013 (0.013)	0.376 (-0.124)	0.382 (0.049)	0.180 (0.013)	0.601 (-0.065)	0.213 (0.046)
Gr	0.000	0.000	1.000	0.028 (0.028)	0.399 (-0.101)	0.624 (0.124)	0.284 (-0.049)	0.213 (0.046)	0.189 (0.022)	0.571 (-0.096)

XRF Supervised analysis
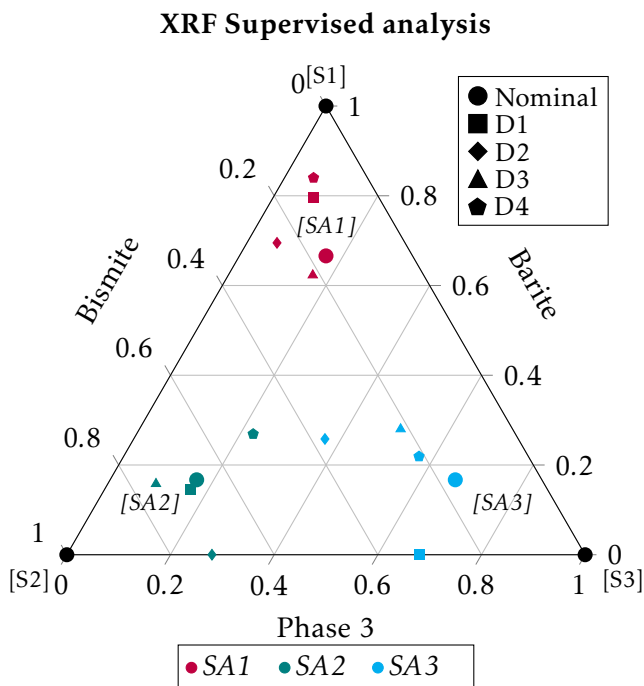
Figure 5.4: Results of the unsupervised analysis reported on the ternary graph representing the mixtures experimental domain. Labelling and color scheme as in Figure 5.1.

value of the results from unsupervised analyses consists its direct association with standard RR and PONKCS methods, which are equally unsupervised methods, if no *ad hoc* calibrations are performed. In Figure 5.3, data are aggregated around the nominal values with a homogeneous dispersion and without a preference towards one of the three phases. The error distributions are normal and zero-centered, a sign that systematic errors are absent, or very limited. Numerical results are reported in Table 5.3 along with the deviation from the nominal values. The error range is comprised between zero and 12.4%, which stands for an overall more accurate quantification than those performed with RR and PONKCS (Figures 5.1 and 5.2).

For XRF data, the supervised analysis only is reported, consisting in

the quantification results of the three augmented experiments (SA1-
SA3). In Figure 5.4, the advantage in using multivariate analysis, if
compared with the results obtained by FP of the instrument reported
in Table 5.1.2, consists in the fact that the light phases can be identi-
fied by exploiting the Compton effect contained in the spectra, which
varies according to the amount of light phase. Unlike the fluorescence
peaks, the Compton effect cannot be attributed to a specific chemical
species, but to a generic phase made up of elements that do not give
a signal that can be read by the instrument. By comparing the data
obtained with MA and the FP method for data set D3, the only one in
which phase 3 presents an XRF signal, it can be concluded that the
total error on the quantification is comparable, with a value of SSR_{FP}
equal to 0.052 and a value of SSR_{MA} equal to 0.058.

5.2.3   Blind PCA analysis

To further challenge the multivariate analysis, a blind analysis was
carried out on the four data sets. The method implies that no compo-
sitional information is provided as input to the software, not even the
pure phases. In this way, the MSA approach must both try to identify
the pure phases of the mixtures and try to perform the quantitative
analysis. This approach differs significantly from those carried out
previously, as the MultiFit approach cannot be used in the absence of
information related to the pure phases. To tackle the problem, PCA is
performed on the matrix containing all the diffraction patterns. The
PCA builds the new reference system based on the explained vari-
ances of each PC, exploiting the intensities at each angle in 2θ of the
patterns contained in the matrix. In general, as reported in Chapter
4.2, for an experimental domain of a mixture of q components, the
PCs generated are $q-1$ and in this new space (Score Plot), the sam-
ples with relative distances linked to the quantitative information
are projected. The results, reported in Figure 5.5 in the form of Score
Plots, show how the multivariate approach was able to reconstruct
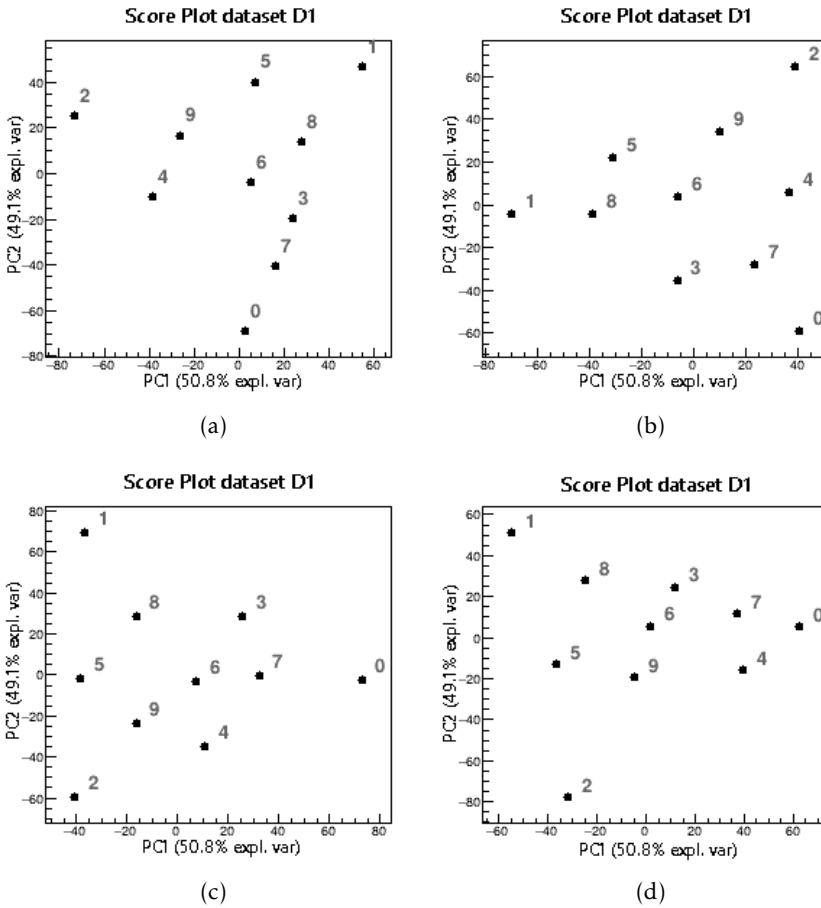
Figure 5.5: Results of the blind analysis are reported in form of score plot for each data set. 5.5(a) - Results of data set D1; 5.5(b) - Results of data set D2; 5.5(c) - Results of data set D3; 5.5(d) - Results of data set D4;

the starting simplexes with great accuracy despite the total absence
of quantitative information and criticalities introduced by us into the
system (PO and MA). Points in the Score Plots, transformed by the
coordinate change algorithm presented in Section 4.2, provide a di-
rect quantification of each mixture. Numerical results, along with
the deviations from the nominal values, are reported in Table 5.4.
Errors from both MultiFit and blind quantification are comparable,
although for some mixtures the error associated to the blind analysis
has errors (e.g. Sample 4 of Data set D4). One important implication
is that the approach used in this section does not involve building a re-
gression model and can be used virtually even in the absence of pure
substances. In fact, in this case the quantification of an unknown
mixture would be based on the relative distance from samples with
known quantities and belonging to the same experimental domain.
Finally, this result can be obtained by analyzing mixtures of compo-
nents whose structure is still unresolved, which cannot be achieved
with traditional methods.

5.3 Conclusions and perspectives

The 4 data sets, analyzed by XRF and XRPD, produced data that were
analysed by traditional methods for quantitative analysis. The data
sets, each with one or more quantification issues (microabsorption
and preferred orientation), have been prepared *ad hoc* to simulate a
typical situation of the industrial world in which samples can not be
prepared to avoid such problems as in the lab environment. Moreover,
they are mixtures with both light and heavy elemental components.
Results were compared with the ones obtained by the multivariate
methods presented in Chapters 2 and 4. The aim of the work is
to test different procedures in a standardized way to highlight their
strengths and weaknesses, with the aim of proposing new methods
or improving existing ones with the development and publication of
easily exploitable recipes for data analysis by the general user in both

Table 5.4: Results of the blind analysis performed by multivariate approach.

data set D1

Chemical	Ba (0)	Bi (1)	Gr (2)	Ba Bi (3)	Ba Gr (4)	Bi Gr (5)	Ba Bi Gr (6)	SA 1 (7)	SA 2 (8)	SA 3 (9)
Ba	0.995 (-0.005)	-0.027 (-0.027)	-0.011 (-0.011)	0.366 (-0.134)	0.563 (0.063)	-0.031 (-0.031)	0.384 (0.051)	0.748 (0.081)	0.133 (-0.034)	0.255 (0.088)
Bi	0.005 (0.005)	1.000 (0.000)	0.012 (0.012)	0.575 (0.075)	0.016 (0.016)	0.384 (-0.116)	0.232 (-0.101)	0.000 (-0.167)	0.575 (-0.091)	0.111 (-0.056)
Gr	0.000 (0.000)	0.027 (0.000)	1.000 (0.000)	0.059 (0.059)	0.421 (-0.079)	0.647 (0.147)	0.384 (0.051)	0.252 (0.085)	0.292 (0.125)	0.634 (-0.032)

data set D2

Chemical	Ba (0)	Bi (1)	Gr (2)	Ba Bi (3)	Ba Gr (4)	Bi Gr (5)	Ba Bi Gr (6)	SA 1 (7)	SA 2 (8)	SA 3 (9)
Ba	1.000 (0.000)	-0.065 (-0.065)	-0.074 (-0.074)	0.621 (0.121)	0.382 (-0.118)	-0.042 (-0.042)	0.376 (0.043)	0.695 (0.029)	0.218 (0.051)	0.090 (-0.077)
Bi	0.000 (0.000)	1.000 (0.000)	0.074 (0.074)	0.368 (-0.132)	0.046 (0.046)	0.546 (0.046)	0.343 (0.010)	0.137 (-0.030)	0.645 (-0.021)	0.233 (-0.100)
Gr	0.000 (0.000)	0.065 (0.000)	1.000 (0.000)	0.011 (0.011)	0.572 (0.072)	0.496 (0.004)	0.281 (-0.115)	0.168 (0.001)	0.137 (-0.030)	0.677 (0.011)

data set D3

Chemical	Ba (0)	Bi (1)	Zn (2)	Ba Bi (3)	Ba Zn (4)	Bi Zn (5)	Ba Bi Zn (6)	SA 1 (7)	SA 2 (8)	SA 3 (9)
Ba	0.847 (-0.153)	-0.087 (-0.087)	0.000 (0.000)	0.468 (0.032)	0.432 (0.068)	-0.050 (-0.050)	0.246 (0.087)	0.500 (-0.166)	0.167 (0.000)	0.111 (-0.056)
Bi	0.000 (0.000)	0.087 (0.087)	1.000 (0.000)	0.445 (-0.055)	0.029 (0.029)	0.482 (-0.018)	0.290 (-0.043)	0.202 (0.035)	0.610 (-0.056)	0.229 (0.062)
Zn	0.153 (0.153)	1.000 (0.000)	0.000 (0.000)	0.087 (0.000)	0.540 (0.040)	0.569 (0.069)	0.465 (0.132)	0.300 (0.133)	0.223 (0.056)	0.660 (-0.006)

data set D4

Chemical	Ba (0)	Bi (1)	Ur (2)	Ba Bi (3)	Ba Ur (4)	Bi Ur (5)	Ba Bi Ur (6)	SA 1 (7)	SA 2 (8)	SA 3 (9)
Ba	0.954 (-0.046)	0.000 (0.000)	0.000 (0.000)	0.453 (-0.047)	0.236 (-0.214)	0.003 (0.003)	0.181 (-0.152)	0.408 (-0.254)	0.091 (0.076)	0.028 (-0.139)
Bi	0.006 (0.006)	0.001 (0.001)	1.000 (0.000)	0.464 (0.036)	0.000 (0.000)	0.429 (0.071)	0.365 (0.065)	0.232 (0.065)	0.667 (0.001)	0.190 (0.023)
Ur	0.040 (0.040)	1.000 (0.000)	0.000 (0.000)	0.084 (0.084)	0.764 (0.264)	0.569 (0.069)	0.454 (0.121)	0.360 (0.193)	0.242 (0.075)	0.783 (0.117)

101

academy and industry.

For XRPD data, the effects due to MA and PO strongly affect the quality of traditional methods for quantification, while this issue is attenuated when using multivariate methods. The errors in the quantification performed by the multivariate methods falls within a range from 0% to 12.4% in weight of components, much lower than those found in the estimates made with by XRPD data with RR and PONKCS.

The XRF data, analyzed with the FP method, show as a result a correct quantification for the phases from which it is possible to read a fluorescence signal, but with the known impossibility of estimating the third phase ($Z < 11$) at all within the mixtures. The problem can be overcome by using the multivariate methods, which are able to recognize the presence of a third light phase within the experimental domain, but with the drawback of a greater imprecision in the estimation of the components that present a characteristic peak of fluorescence. As a future perspective, there is the intention to use additional multivariate methods for data analysis, such as non-negative matrix factorization (NNMF) [16]. This method is based on the principle that negative factor factorizations do not always have physical meaning and that physically significant combinations must be characterized by a combination of additive and never subtractive type. This type of constraint in factoring means that the orthogonality between the individual components is partially lost, but at the same time provides a type of interpretation defined "by parts", compared to a classical holistic approach[17, 18]. A manuscript, complete with all the data on this work, has been submitted to the Journal of Applied Crystallography[15].

BIBLIOGRAPHY

[1]   P. Guccione et al. «Multivariate Analysis Applications in X-ray Diffraction.» In: *Crystals* 11.1 (Dec. 2020), p. 12. DOI: 10.3390/cryst11010012. URL: https://doi.org/10.3390/cryst11010012.

[2]   B. Mangolini et al. «XRF and XRPD data sets in ternary mixtures with high level micro-absorption and/or preferred orientations problems for phase quantification analysis.» In: *Data in Brief* 36 (June 2021), p. 107043. DOI: 10.1016/j.dib.2021.107043. URL: https://doi.org/10.1016/j.dib.2021.107043.

[3]   R. Dinnebier, S. Billinge, and R. S. of Chemistry (Great Britain). *Powder Diffraction: Theory and Practice.* Royal Society of Chemistry, 2008. ISBN: 9780854042319. URL: https://books.google.it/books?id=wmQ%5C_1FIMkFYC.

[4]   R. E. Dinnebier, A. Leineweber, and J. S. Evans. *Rietveld refinement: practical powder diffraction pattern analysis using TOPAS.* Walter de Gruyter GmbH & Co KG, 2018.

[5]   I. C. Madsen et al. «Outcomes of the International Union of Crystallography Commission on powder diffraction round robin on quantitative phase analysis: samples 1a to 1h.» In: *Journal of Applied Crystallography* 34.4 (2001), pp. 409–426.

[6]   N. V. Scarlett et al. «Outcomes of the International Union of Crystallography Commission on Powder Diffraction Round

103

Robin on Quantitative Phase Analysis: samples 2, 3, 4, synthetic bauxite, natural granodiorite and pharmaceuticals.» In: *Journal of Applied Crystallography* 35.4 (2002), pp. 383–400.

[7]   N. V. Y. Scarlett and I. C. Madsen. «Effect of microabsorption on the determination of amorphous content via powder X-ray diffraction.» In: 33.1 (Mar. 2018), pp. 26–37. DOI: 10.1017/s0885715618000052. URL: https://doi.org/10.1017/s0885715618000052.

[8]   N. V. Scarlett and I. Madsen. «Quantification of Phases with Partial or No Known Crystal Structures.» In: *Powder Diffraction - POWDER DIFFR* 21 (Dec. 2006). DOI: 10.1154/1.2362855.

[9]   R. V. Grieken and A. Markowicz, eds. *Handbook of X-Ray Spectrometry*. CRC Press, Nov. 2001. DOI: 10.1201/9780203908709. URL: https://doi.org/10.1201/9780203908709.

[10]   J. W. Criss and L. S. Birks. «Calculation methods for fluorescent x-ray spectrometry. Empirical coefficients versus fundamental parameters.» In: *Analytical Chemistry* 40.7 (1968), pp. 1080–1086. DOI: 10.1021/ac60263a023.

[11]   R. M. Rousseau. «Corrections for matrix effects in X-ray fluorescence analysis—A tutorial.» In: *Spectrochimica Acta Part B: Atomic Spectroscopy* 61.7 (July 2006), pp. 759–777. DOI: 10.1016/j.sab.2006.06.014. URL: https://doi.org/10.1016/j.sab.2006.06.014.

[12]   R. M. Rousseau. «Fundamental algorithm between concentration and intensity in XRF analysis 1—theory.» In: *X-Ray Spectrometry* 13.3 (1984), pp. 115–120. DOI: https://doi.org/10.1002/xrs.1300130306.

[13]   R. M. Rousseau. «Fundamental algorithm between concentration and intensity in XRF analysis 2—practical application.»

In: *X-Ray Spectrometry* 13.3 (1984), pp. 121–125. DOI: https://doi.org/10.1002/xrs.1300130307.

[14] R. Caliandro and D. B. Belviso. «RootProf: software for multivariate analysis of unidimensional profiles.» In: *Journal of Applied Crystallography* 47.3 (2014), pp. 1087–1096.

[15] M. Lopresti et al. «Multivariate vs. traditional quantitative phase analysis of X-ray powder diffraction and fluorescence data by mixtures showing preferred orientation and microabsorption.» In: *Journal of Applied Crystallography* (2022). Submitted.

[16] D. D. Lee and H. S. Seung. «Learning the parts of objects by non-negative matrix factorization.» In: *Nature* 401.6755 (Oct. 1999), pp. 788–791. DOI: 10.1038/44565. URL: https://doi.org/10.1038/44565.

[17] H. S. Geddes et al. «Structural characterisation of amorphous solid dispersions via metropolis matrix factorisation of pair distribution function data.» In: *Chemical Communications* 55.89 (2019), pp. 13346–13349. DOI: 10.1039/c9cc06753a. URL: https://doi.org/10.1039/c9cc06753a.

[18] H. S. Geddes et al. «Extracting interface correlations from the pair distribution function of composite materials.» In: *Nanoscale* 13.31 (2021), pp. 13220–13224. DOI: 10.1039/d1nr01922h. URL: https://doi.org/10.1039/d1nr01922h.

6

DEVELOPMENT OF IMPULSE EXCITATION TECHNIQUE INSTRUMENT FOR A FAST QUALITATIVE ANALYSIS

Am I out of touch? No, it's the children who are wrong.

Skinner, W.S.

In 2020, the COVID-19 pandemic caused by the SARS-CoV-19 virus made access to the university and its equipment impossible. For the same reason, non-destructive testing (NDT) of materials using X-rays was also impossible, not only for lack of portable instruments, but especially for safety rationale. At that juncture, the author of this thesis followed a graduate student as co-supervisor for the first experimental thesis developed completely at his own home. An electronics kit (Arduino Uno and a wide variety of sensors), a latest generation minicomputer (Raspberry Pi 4B +) and a USB condenser microphone were sent directly to the house of the undergraduate, Nazareno Massara, under the supervision of the author of the present

thesis. Following the provided instructions, the student built the first
version of what was later called IETeasy [1]: an instrument for the
impulse analysis of materials according to the Impulse Excitation
Technique method (IET). A second, and final, version for publication
was built by the author of the present thesis. The IET technique has
proved to be particularly suitable for a wide range of analyses, easy
to use and, most importantly, safe to use at home.

The IET is a little known method when compared with others in the
NDT field, but capable of producing data that can be used in mul-
tiple ways, both for the determination of the mechanical properties
of materials, and for a qualitative analysis[2, 3]. The technique is
based on the theory of the Euler-Bernoulli beam with free-free condi-
tions[4], in which the sample, a theoretical beam, is unsupported or
with negligible contact area. The motion of the beam is described by
the following equation[5, 6]:

$$EI\frac{\partial^4 v(x,t)}{\partial x^4} + \rho A \frac{\partial^2 v(x,t)}{\partial t^2 2} = 0 \qquad (6.1)$$

Where E is Young's modulus, I is the inertia of the sectional area, ρ is
the section density and A is the cross-section area of the considered
beam. The solution of the equation, $v(x,t)$, is the transverse deflection
of the beam and can be rewritten by separating it in two functions:
one spatial and one temporal, as it can be described as a stationary
wave:

$$v(x,t) = X(x)T(t) \qquad (6.2)$$

Without going into the details of the resolution of the equations,
which can be found at ref. [7], under free-free boundary conditions
the solution of the spatial part of Eq. 6.2 becomes the transcendental
equation:

$$1 - cosh(k_n L)cos(k_n L) = 0 \qquad (6.3)$$

Where k_n is the wavenumber of the nth oscillation mode and L is
the length of the beam. Eq. 6.3 has infinite solutions and through

k is bound to the elastic modulus of the material and to the circular frequency ω by the characteristic equation:

$$\omega = \sqrt{\frac{EI}{\rho A}} k^2 \qquad (6.4)$$

The equation shown correlate different quantities of interest and can be used in a bijective way. Determining the frequency of the fundamental mode of vibration starting from the elastic modulus of a material is often done in the field of civil engineering, but in one of the cases of application of the IET, the opposite way is pursued [8]. The measurement of the resonant frequency is carried out by sending a pulse on a sample (which must not cause permanent deformation or fracture) and recording the signal produced in response. This signal, which is generally a sound, is analysed in the frequency range where the whole spectrum of vibration can be analysed and where the peaks represent all the recorded vibration modes. Such a use case can be very useful in cases where a tensometer cannot be used as it is necessary to preserve the shape of a sample. Another application for quality control in assembly lines where products with a complex shape can be quickly analysed to determine the presence of macro defects, comparing the frequency obtained with a pre-recorded one on a reference good sample. In the research facilities, the technique finds various applications in the world of ceramics [9–11], where it is used for the research of micro defects and anisotropies, in the geological field [12] for the rapid analysis of found minerals and in the fields of metallurgy [13–15] and materials science, where the knowledge of the Young, shear modulus and Poisson's ratio are a common requirement. It must also be considered that instruments such as linear tensometers are expensive and are hardly suitable for the traction of samples belonging to different classes, such as polymers and steel alloys (where the tensile stresses are orders of magnitude higher). These analyses can be carried out by IET and using a relatively simple setup, of which the previously cited IETeasy is an open-access and

open-hardware version, which has been published in the Hardware
X (Elsevier BV) [1]. The article contains details needed for the au-
tonomous construction of IETeasy, design file for a printable version
with a 3D printer and instructions for use, comprising calibration
to various experimental cases. The technique itself has been known
since 1999 (and the upstream theory since 1773) and there are very
valid commercial tools. What distinguishes IETeasy from the com-
mercial tools is of course the much more lower cost (hundreds instead
of thousands euro) and the direct access to the full data and the high
customization of the tool. An example of this is given by the fact
that commercial instruments generally provide the fundamental res-
onance frequency of a material under analysis, while IETeasy allows
to obtain the entire spectrum, with also the frequencies of the sub-
sequent vibration modes. In addition, the possibility of having an

(a) Score plot PC1-PC2   (b) Score plot PC1-PC3
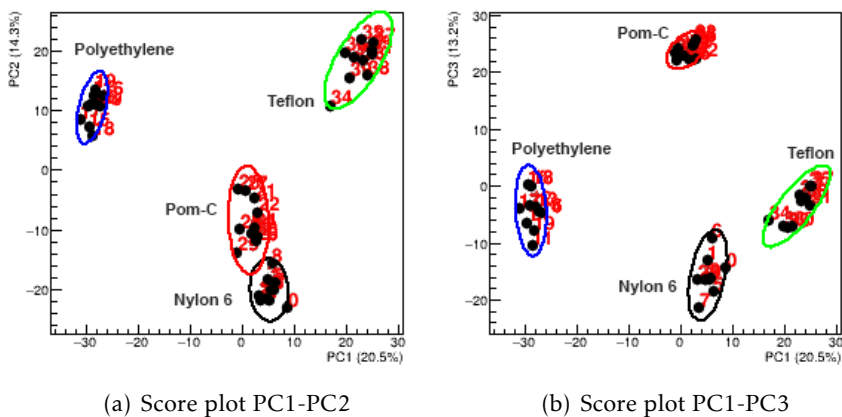
Figure 6.1: Results of the qualitative analysis of the data collected on
different polymeric samples. Figures from ref. [1].

instrument that does not work at a single frequency allows the use
of multivariate techniques for the analysis of the entire spectrum.
Principal Component Analysis (PCA) was used for the first time on
IET data in Section 7 of the published article to demonstrate how,

combining a fully open instrument with multivariate analysis, the user is able to distinguish samples with high accuracy. An example is given in Figure 6.1 taken from ref [1], where the score plots obtained from PCA performed on polymeric samples are shown. Although the characteristic resonance frequencies fall close to each other and that the polymers are not ideal samples for acoustic analysis, but are dampened due to their structure, the classification analysis makes no mistake. In addition, in accordance with the theory presented in Chapter 4, PCA extracts a number of significant PCs equal to the number of sample classes minus one. The groups are then arranged so as to be as far apart as possible from each other in that PC space, in this case a tetrahedron in a three-dimensional space. The complete version of the article, with an in-depth description of all the validation process and data analysis of the data are reported in the Annex II of the present work. Annex III contains a second article published on Data in Brief (Elsevier BV) [1] with the complete explanation of the data collection parameters and the description of each sample collected. The data can also be found in a dedicated database[1] on the Mendeley Data open repository, where deposited data can be exploited open access for calibration and comparison purpose and new data can be uploaded for contribution. The purpose of this database is to collect as much IET data as possible on different materials, in order to constitute the database for the automatic recognition of materials and defects contained in them through machine learning.

---

[1]Dataset for "Impulse excitation technique data set collected on different materials for data analysis methods and quality control procedures development". DOI: 10.17632/srfp7x6wxm.1

B I B L I O G R A P H Y

[1] N. Massara et al. «IETeasy: An open source and low-cost instrument for impulse excitation technique, applied to materials classification by acoustical and mechanical properties assessment.» In: *HardwareX* 10 (Oct. 2021), e00231. DOI: 10.1016/j.ohx.2021.e00231. URL: https://doi.org/10.1016/j.ohx.2021.e00231.

[2] G. Roebben et al. «Impulse excitation apparatus to measure resonant frequencies, elastic moduli, and internal friction at room and high temperature.» In: *Review of Scientific Instruments* 68.12 (1997). cited By 219, pp. 4511–4515. DOI: 10.1063/1.1148422.

[3] G. Roebben et al. «The innovative impulse excitation technique for high-temperature mechanical spectroscopy.» In: *Journal of Alloys and Compounds* 310.1-2 (Sept. 2000), pp. 284–287. DOI: 10.1016/s0925-8388(00)00966-x. URL: https://doi.org/10.1016/s0925-8388(00)00966-x.

[4] S. Timoshenko. *History of Strength of Materials: With a Brief Account of the History of Theory of Elasticity and Theory of Structures*. Dover Civil and Mechanical Engineering Series. Dover Publications, 1983. ISBN: 9780486611877.

[5] J. F. da Silva, L. A. D. do Nascimento, and S. dos Santos Hoefel. «Free vibration analysis of Euler-Bernoulli beams under non-classical boundary conditions.» In: *Anais do IX Congresso Nacional de Engenharia Mecânica*. ABCM Associação Brasileira

de Engenharia e Ciências Mecânicas, 2016. DOI: 10.20906 /cps/con-2016-1053. URL: https://doi.org/10.20906 /cps/con-2016-1053.

[6]   L. Euler. «De motu vibratorio laminarum elasticarum, ubi plures novae vibrationum species hactenus non pertractatae evolvuntur.» In: *Novi Commentarii academiae scientiarum Petropolitanae* (1773).

[7]   W. Shi, X.-F. Li, and K. Y. Lee. «Transverse vibration of free–free beams carrying two unequal end masses.» In: *International Journal of Mechanical Sciences* 90 (Jan. 2015), pp. 251–257. DOI: 10.1016/j.ijmecsci.2014.11.015. URL: https: //doi.org/10.1016/j.ijmecsci.2014.11.015.

[8]   J. Lord and R. Morrell. *Measurement good practice guide no. 98: elastic modulus measurement.* 2006.

[9]   E. Gregorová et al. «Temperature dependence of Young's modulus and damping of partially sintered and dense zirconia ceramics.» In: *Journal of the European Ceramic Society* 40.5 (2020), pp. 2063–2071. ISSN: 0955-2219. DOI: https://doi. org/10.1016/j.jeurceramsoc.2019.12.064. URL: https: //www.sciencedirect.com/science/article/pii/S09552 21919309082.

[10] A. Masini et al. «Elastic properties of multi-layered ceramic systems for SOCs.» In: *International Journal of Applied Ceramic Technology* 15.2 (2018), pp. 370–379. DOI: https://doi. org/10.1111/ijac.12801. eprint: https://ceramics. onlinelibrary.wiley.com/doi/pdf/10.1111/ijac.12801. URL: https://ceramics.onlinelibrary.wiley.com/doi/ abs/10.1111/ijac.12801.

[11] J. Alex et al. «Effect of Sodium on Microstructures and Thermoelastic Properties of Calcium Aluminate Cement-Bonded Refractories.» In: *Journal of the American Ceramic Society* 99.3

(2016), pp. 1079–1085. DOI: https://doi.org/10.1111
/jace.14046. eprint: https://ceramics.onlinelibrary.
wiley.com/doi/pdf/10.1111/jace.14046. URL: https:
//ceramics.onlinelibrary.wiley.com/doi/abs/10.1111
/jace.14046.

[12]   M. Monìk et al. «Rock physics and the circulation of Neolithic
axeheads in Central Europe and the western Mediterranean.»
In: *Wear* 474-475 (2021), p. 203708. ISSN: 0043-1648. DOI:
https://doi.org/10.1016/j.wear.2021.203708. URL:
https://www.sciencedirect.com/science/article/pii/
S0043164821000971.

[13]   M. Richetta and A. Varone. «A Focus on Dynamic Modulus:
Effects of External and Internal Morphological Features.» In:
Metals 11.1 (2021). ISSN: 2075-4701. DOI: 10.3390/met1101
0040. URL: https://www.mdpi.com/2075-4701/11/1/40.

[14]   Y. Li et al. «Modeling of temperature dependent yield strength
for stainless steel considering nonlinear behavior and the ef-
fect of phase transition.» In: *Construction and Building Mate-
rials* 159 (2018), pp. 147–154. ISSN: 0950-0618. DOI: https:
//doi.org/10.1016/j.conbuildmat.2017.10.106. URL:
https://www.sciencedirect.com/science/article/pii/
S095006181732161X.

[15]   I.-C. Jung, D.-G. Kang, and B. C. De Cooman. «Impulse exci-
tation internal friction study of dislocation and point defect
interactions in ultra-low carbon bake-hardenable steel.» In:
Metallurgical and Materials Transactions A 45.4 (2014), pp. 1962–
1978.

EPOXY RESIN COMPOSITES AND INNOVATIVE COATINGS FOR MAGNESIUM ALLOYS

7

Epoxy-based radiodense composites as innovative non-toxic X-ray shielding materials

Convicted of a crime I didn't even commit. Hah! Attempted murder? Now honestly, what is that? Do they give a Nobel Prize for attempted chemistry? Do they?

Roberts, B.

Radiopaque shielding materials have multiple applications, both in the industrial, medical and dental field[1]. The protection of the radiologist technician and the people around him depend not only on the shielding power of the materials that prevent X-rays from escaping from the dedicated areas, but also on the toxicity of the shielding materials themselves[2]. A common issue in the hospital setting is given by the X-rays aprons and lab coats for radiology technicians. In the past, this type of clothing was composed of a double layer of

fabric with thin layers of lead[3, 4] or a lead mesh inside, which made them wearable for a just a short time and with the risk of exposure to the toxic metal or to radiation, if damages are present[5, 6]. Modern lab coats are still made up of a double layer of fabric, but with a soft polymer or gel inside the interspace in which lead particles are dispersed. Similarly, X-rays shielding aprons are often made up by layers of natural or silicone rubber in which lead particles are dispersed[7]. The risk of exposure to lead is, therefore, far from zero and that simple lacerations can cause leaks. In Chapter 1 other uses of radiodense materials are described, along with the state of the art on the materials and what is further required in terms of performances, not only from the point of view of radiopacity to X-rays, but also in terms of mechanical performances, costs and eco-compatibility.

Innovative radiodense materials have been developed by mixing epoxy resins with additive characterized by low or absent toxicity, consisting in high density inorganic powders containing high Z elements. For a proper selection of the materials and design of the best performing mixture, the use of Geant4 as described in Section 2.2 was of fundamental importance. A software for the simulation of the shielding power was programmed with Geant4 libraries, an initial screening of the materials present in scientific literature was carried out only at *in silico* level, in order to identify the additives with the most advantageous performance over costs ratio. This step was necessary as traditional shielding materials have a low cost and are easy to find, therefore to be competitive with them, having similar properties and prices is necessary. Another advantage in using a software based on Geant4 consisted in having the chance to test many different materials in a short time span, avoiding the waste of materials for the initial phase of exploration.

Barite ($BaSO_4$) and bismite (BiO_3), turned out to be the most promising candidates, especially for a combined use, as together they have a synergistic effect for the overall reduction of costs and an increase in shielding power. The first set of samples was prepared by adding

technical grade barite to the epoxy resin until the mixability limit was reached. The limit which was identified with the ratio of 85% in weight of barite and 15% in weight of epoxy resin. Samples obtained were characterized by a multi-technique approach by digital radiography and tomography, X-ray powder diffraction, optical and scanning electron microscopy and thermogravimetry. By the combined use of these techniques, it has been possible to verify that the samples above 60% in weight of additive are not affected by sedimentation effects due to the progressive increase in the viscosity of the mixture. Low additivated samples ($< 50\%$), on the other hand, have a low viscosity and the time required by the resin to polymerize is sufficient for the sedimentation of most of the additive, making the resulting sample anisotropic. For the aforementioned reasons, the successive phase of the experimentation consisted in simulating the performances of ternary mixtures of barite, bismite and epoxy resin with a maximum additive content of 80% in weight. Samples were designed by the means of a $3, 2$-simplex-lattice design as defined in Section 2.3.3.1. The simplex, shown in Figure 7.1, is composed of 6 samples divided in two groups: 3 with a high additive content (black points) and 3 with a high resin content (red points).Simulation results demonstrated that black samples are the most performing in terms of radiopacity, therefore suitable for their integration in industrial radiography applications. Mixtures described by red dots, on the other hand, are suitable for cutting the radiations of the least energetic range (lower than $60 \, \text{keV}$), therefore to be used in the medical and dental fields. For the said reasons, only black samples were produced in laboratory for further analyses. The characterization has shown that the composites obtained are from 5 to 33% more radiodense than steel, with a general weight reduction ranging from 55% to 62%.
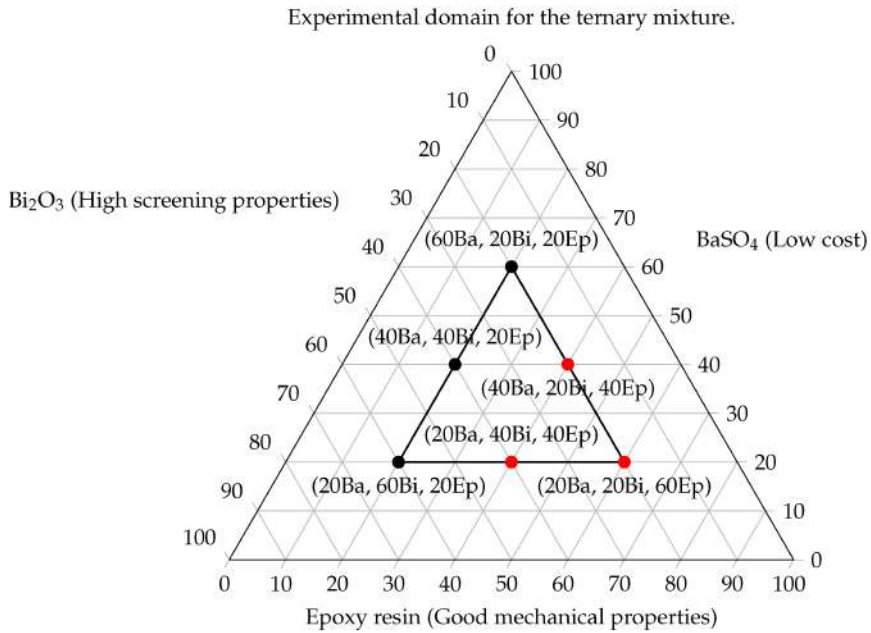
Figure 7.1: The ternary mixture of bismite, barite and epoxy resin was explored by the means of a simplex-lattice design. The simplex is reduced with respect to the experimental domain to not exceed the total of 80% in additives. Red points represent mixtures that were evaluated by simulations as excessively radiotransparent and, therefore were not produced in laboratory. Figure from ref. [8].

Finally, a Life Cycle Assessment (LCA) study was done on the samples to evaluate the environmental performance of the produced samples. The LCA study was done using openLCA 1.9[1] and the ecoinvent 3.5 database[2]. Impacts calculations were performed taking as reference the 20% in $BaSO_4$, 60% in Bi_2O_3, 20% in epoxy resin composite, showing the highest impact on the environment, having a high content in bismite. All the other composites produced and designed by the simplex-lattice design have therefore lower impacts than those of the selected one, as the reference is the highest in bismite content

---

[1]openLCA: https://www.openlca.org
[2]ecoinvent: https://ecoinvent.org
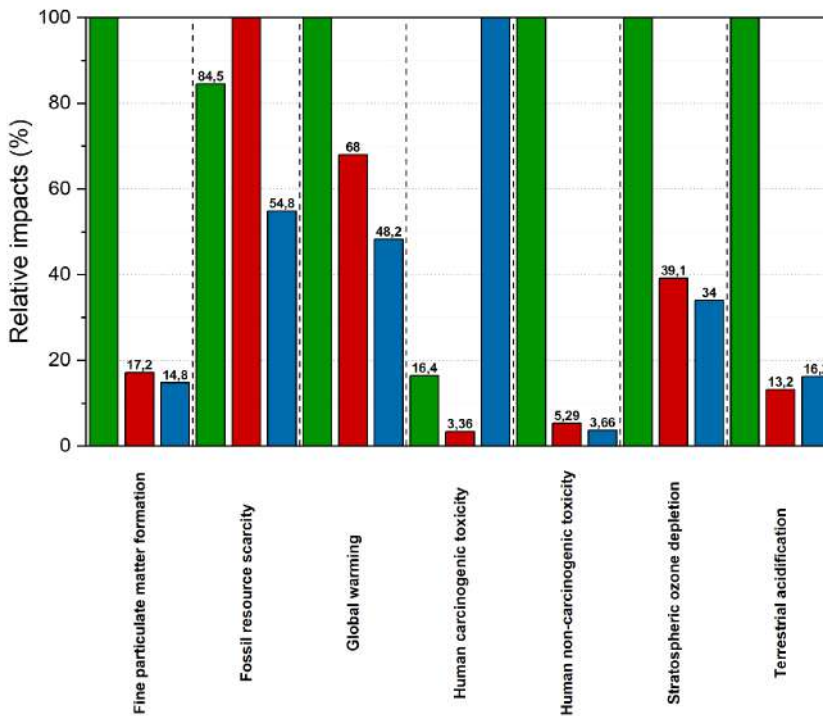
Figure 7.2: Life cycle assessment of produced samples of radiodense composites. Results of the impacts are compared to the ones obtained by traditional screening materials. Green bars represent the relative impacts calculated for lead, red bars for the composite samples and blue bars are referred to steel impacts. Figure from ref. [8].

of the whole set of experiments. In Figure 7.2, results of the most relevant impacts are reported (red bar), with a comparison with the calculated impacts of lead and steel, represented by green and blue bars respectively. Bismite-barite epoxy composites have in general good performances with respect to lead and a reduction of the impact related to human carcirogenicity of 96.64% if compared to steel screens.

Further details of each step of the experimentation and of the characterization process are given in the full version of the study[8], which

is reported in Annex V of the present work.

BIBLIOGRAPHY

[1] S. Nambiar, E. K. Osei, and J. T. W. Yeow. «Polymer nanocomposite-based shielding against diagnostic X-rays.» In: *Journal of Applied Polymer Science* 127.6 (June 2012), pp. 4939–4946. DOI: 10.1002/app.37980. URL: https://doi.org/10.1002/app.37980.

[2] J. P. McCaffrey et al. «Radiation attenuation by lead and non-lead materials used in radiation shielding garments.» In: 34.2 (Jan. 2007), pp. 530–537. DOI: 10.1118/1.2426404. URL: https://doi.org/10.1118/1.2426404.

[3] G. Bartal, A. M. Sailer, and E. Vano. «Should We Keep the Lead in the Aprons?» In: 21.1 (Mar. 2018), pp. 2–6. DOI: 10.1053/j.tvir.2017.12.002. URL: https://doi.org/10.1053/j.tvir.2017.12.002.

[4] R. Roelz and U. Hubbe. «A farewell to lead aprons in spine surgery.» In: (Mar. 2021). DOI: 10.1016/j.spinee.2021.03.019. URL: https://doi.org/10.1016/j.spinee.2021.03.019.

[5] S. E. McKenney, H. J. Otero, and S. T. Fricke. «Lead Apron Inspection Using Infrared Light: A Model Validation Study.» In: 15.2 (Feb. 2018), pp. 313–318. DOI: 10.1016/j.jacr.2017.09.014. URL: https://doi.org/10.1016/j.jacr.2017.09.014.

[6] C. Hayre, H. Bungay, and C. Jeffery. «How effective are lead-rubber aprons in protecting radiosensitive organs from secondary ionizing radiation?» In: 26.4 (Nov. 2020), e264–e269. DOI: 10.1016/j.radi.2020.03.013. URL: https://doi.org/10.1016/j.radi.2020.03.013.

[7] H. Boyle and R. M. Strudwick. «"Do lead rubber aprons pose an infection risk?"» In: 16.4 (Nov. 2010), pp. 297–303. DOI: 10.1016/j.radi.2010.03.002. URL: https://doi.org/10.1016/j.radi.2010.03.002.

[8] M. Lopresti et al. «Light Weight, Easy Formable and Non-Toxic Polymer-Based Composites for Hard X-ray Shielding: A Theoretical and Experimental Study.» In: *International Journal of Molecular Sciences* 21.3 (Jan. 2020), p. 833. DOI: 10.3390/ijms21030833. URL: https://doi.org/10.3390/ijms21030833.

8

MECHANOCHEMICAL FUNCTIONALIZATION OF BARIUM SULFATE ADDITIVES FOR ISOTROPIC RADIODENSE COMPOSITES

...And Harry Potter and all his wizard friends went straight to hell for practicing witchcraft!

Flanders, N., Jr.

In the previous chapter, highly performing radiopaque materials for the replacement of steel and lead in industrial applications were presented. Developed materials, in that context, are mainly dedicated to the safety of the users and surrounding people from highly energetic radiations, with ceilings generally around 350 keV. Medical and dental applications, which exercise at lower energies (40 keV to 70 keV [1]), have been mentioned several times in the previous chapters, in particular referring to the mixtures of the simplex-lattice design with the highest content of epoxy resin (red points in Figure
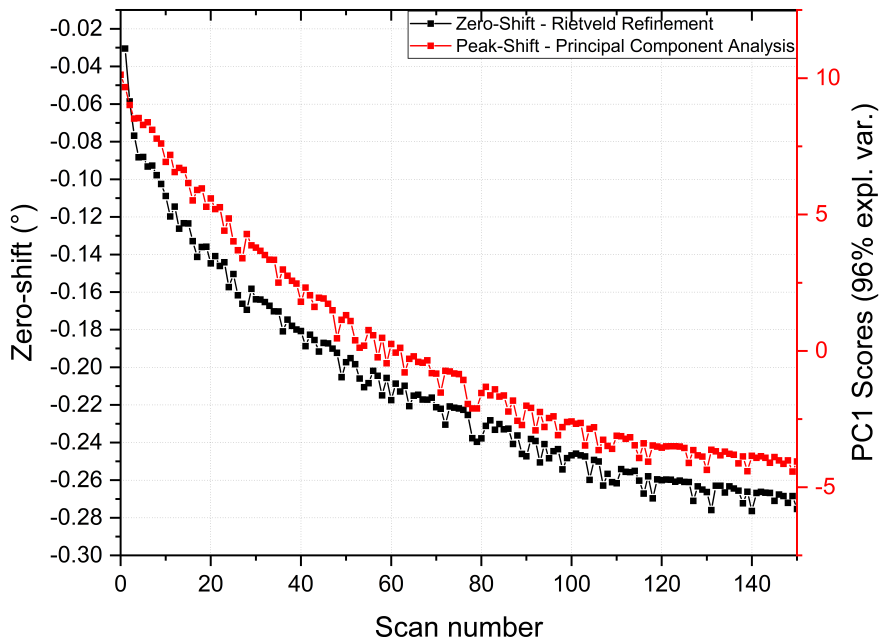
Figure 8.1: Results of the XRPD *in situ* measurement carried out on a 30% in weight of barite sample to monitor sedimentation. The black curve represent the zero-shift error obtain Rietveld Refinement, in red the results of the principal component analysis carried out on the patterns by RootProf.

7.1). Such samples have been identified as suited for medical field due to their high mechanical performances, low weight and good shielding power (total shielding below 60 keV). Radiopaque materials with such performances are useful also for the protection of unused parts of digital radiography detectors, as direct exposure to X radiation drastically shortens its lifespan.

In the study presented in V[2], it was confirmed that samples containing less than 50% in weight of additive show sedimentation due to a synergistic effect between the high density of the additives, low viscosity of the total mixture and scarce interaction at the interface between epoxy resin and additives. The final proof of sedimentation was obtained by a XRPD *in situ* experiment carried out during the

polymerization process on a sample at 30% in weight of barite[1]. The experiment was designed to collect data in a low 2θ range containing the main peaks of barite: between 23.5 and 27 degrees. The measurement, which lasted 8 hours, produced 150 diffraction patterns which were analysed with the principal component analysis using RootProf. A drift in both peaks and intensities was visible within the patterns, but it difficult to analyse or quantify the drifts by naked eye. The use of PCA allowed to observe pattern variations along a new coordinate system and to confirm the downward movement of the additive, a process that slows down over time due to the polymer gelation process (Red curve in Figure 8.1). Data were also analysed by a classical post-measurement Rietveld refinement (Black curve in Figure 8.1) confirming that the progressive drift is due to a zero error and linked to the movement of the barite over time.

Low compatibility between polymeric materials and inorganic additives is a typical phenomenon of composite materials[3–6], in particular when it comes to fiber-reinforced materials[7–9]. In addition to generating anisotropy due to sedimentation, the lack of interaction at the interface causes embrittlement of the specimens and the formation of voids and/or defects. To solve the problem of poor interaction at the interface, the surface functionalization of inorganic particles was considered. Using surfactants and fatty acids, the twofold result of a greater interaction between polymers and lipophilic terminals and the entanglement between the polymeric chains and surfactants was expected. Stearic acid and sodium dodecyl sulfate were selected for barite's surface functionalization, as two common surfactants often used for such purposes[10–13]. Two different qualities of barite were tested:

- Blanc Fixe JM3B (JM3B): barium sulphate powder consisting in spherically shaped primary particles with average size equal to $0.7\,\mu m$;

---

[1]Technical grade barite used for the experiments of Chapter 7 was used.

- Blanc Fixe G (G): barium sulphate with irregular particles and average size of 4 μm.

Surface functionalization was carried out using liquid assisted grinding (LAG). This strategy is a mechanochemical technique in which a small amount of liquid is used to enhance or control a solid state reaction driven by the mechanical action of grinding. LAG approach is more eco-compatible and easy scalable than solvent-based reactions and has been previously applied successfully by some of us in various studies, such as the intercalation of molecules in layered double hydroxides[14–16]. To avoid discontinuous planning of the experiments and, at the same time, an excessive number of samples, mixtures were prepared according to the following scheme:

- A 2^2 factor design having as factors the different types of barite (JM3B and G) and the presence or absence of intensive grinding. In this way, improvement or worsening of the dispersion of the samples due to the sole grinding would have been evaluated.

- Two experiments, one for each type of barite, in which few drops of a hydro-alcoholic solution of sodium hydroxide as in refs. [14, 17] are added during grinding, to have the a reference for effects due to the liquid used for LAG.

- A 2^2 factor design of the two types of barite ground with soda and as a second factor the different type of surfactant: sodium dodecyl sulfate and stearic acid. Surfactants were added in a calculated quantity to completely coat the surface of the particles based the data obtained from the technical data sheets.

- A star design on the best performing surfactant, in order to have a comparison on the influence given by the quantity of surfactant.

The total of 14 samples allowed to optimize the functionalization conditions. Samples were characterized by optical microscopy, SEM and
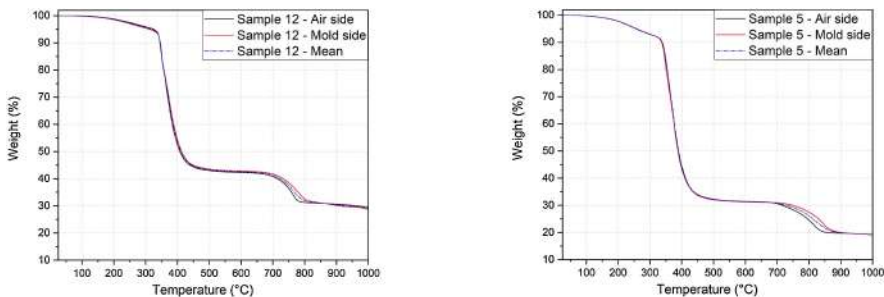
Figure 8.2: Thermogravimetric analysis of samples 5 (0.75g/g of stearic - Blanc Fixe G) and 12 (0.75g/g of stearic - Blanc Fixe JM3B). Thermograms of air and mold side of the samples overlap, leaving the same residue of 30% of the starting weight, which corresponds to the quantitative of $BaSO_4$, and demonstrating that sedimentation does not occur in these samples. Figure and sample from ref. [17]

digital radiography. Results demonstrated that the dispersion of the barite improves considerably, but the use of surfactants introduces air bubbles into the bulk.

Most important improvements in the vertical dispersion of barite were obtained using stearic acid. The best performing samples were further analysed by both XRPD and thermogravimetric analysis (TGA) on the mold and air sides of the samples, to have a quantitative reference on sedimentation. In Figure Figure 8.2 curves corresponding to the thermograms of the air side (black line) and the mold side (red line) of the specimens are overlapped. In the case of sedimentation, the mold side curve settles on values much higher than the reference one (blue line) and, on the contrary, the thermograms of the air side which settles on very low values. In this case TGA shows that the two different sides have no differences in the concentration of additive, which corresponds to an homogeneous dispersion of barite. Full characterization results, with a more in-depth description of all the preparation procedures can be found in the article reported in its original version in Annex VI.

Bibliography

[1]   W. Huda et al. «Optimizing the x-ray photon energy for dig-
      ital radiographic imaging systems.» In: ed. by L. E. Antonuk
      and M. J. Yaffe. SPIE, May 2002. DOI: 10.1117/12.465608.
      URL: https://doi.org/10.1117/12.465608.

[2]   M. Lopresti et al. «Light Weight, Easy Formable and Non-
      Toxic Polymer-Based Composites for Hard X-ray Shielding: A
      Theoretical and Experimental Study.» In: *International Journal
      of Molecular Sciences* 21.3 (Jan. 2020), p. 833. DOI: 10.3390
      /ijms21030833. URL: https://doi.org/10.3390/ijms2103
      0833.

[3]   B. Roy and P. D. Roo. «Vue d'ensemble des conflits de distri-
      bution écologique en Inde.» In: n°75.2 (2019), p. 167. DOI:
      10.3917/mult.075.0167. URL: https://doi.org/10.3917
      /mult.075.0167.

[4]   F. G. Torres, S. Rodriguez, and A. C. Saavedra. «Green Com-
      posite Materials from Biopolymers Reinforced with Agroforestry
      Waste.» In: 27.12 (Sept. 2019), pp. 2651–2673. DOI: 10.100
      7/s10924-019-01561-5. URL: https://doi.org/10.1007
      /s10924-019-01561-5.

[5]   X. Zhang et al. «Interfacial Microstructure and Properties of
      Carbon Fiber Composites Modified with Graphene Oxide.» In:
      4.3 (Mar. 2012), pp. 1543–1552. DOI: 10.1021/am201757v.
      URL: https://doi.org/10.1021/am201757v.

[6] J. Aragón et al. «Development and characterization of a novel bioresorbable and bioactive biomaterial based on polyvinyl acetate, calcium carbonate and coralline hydroxyapatite.» In: 14.1 (Mar. 2011), pp. 25–30. DOI: 10.1590/s1516-14392011 005000012. URL: https://doi.org/10.1590/s1516-14392 011005000012.

[7] N. Hiremath et al. «Low cost textile-grade carbon-fiber epoxy composites for automotive and wind energy applications.» In: 198 (Oct. 2020), p. 108156. DOI: 10.1016/j.compositesb.2 020.108156. URL: https://doi.org/10.1016/j.compositesb. 2020.108156.

[8] Q. Zhang et al. «Dispersion stability of functionalized MWCNT in the epoxy–amine system and its effects on mechanical and interfacial properties of carbon fiber composites.» In: 94 (Mar. 2016), pp. 392–402. DOI: 10.1016/j.matdes.2016.01.062. URL: https://doi.org/10.1016/j.matdes.2016.01.062.

[9] J. Leite et al. «Epoxy/steel fiber composites-A simple model to predict the fiber sedimentation.» In: (2009), NA–NA. DOI: 10.1002/pc.20923. URL: https://doi.org/10.1002/pc.20 923.

[10] Z. Cao et al. «Chemical surface modification of calcium carbonate particles with stearic acid using different treating methods.» In: 378 (Aug. 2016), pp. 320–329. DOI: 10.1016/j. apsusc.2016.03.205. URL: https://doi.org/10.1016 /j.apsusc.2016.03.205.

[11] A. Wołowicz and K. Staszak. «Study of surface properties of aqueous solutions of sodium dodecyl sulfate in the presence of hydrochloric acid and heavy metal ions.» In: 299 (Feb. 2020), p. 112170. DOI: 10.1016/j.molliq.2019.112170. URL: https://doi.org/10.1016/j.molliq.2019.112170.

[12] Y.-J. Yang et al. «Effect of sodium dodecylsulfate monomers and micelles on the stability of aqueous dispersions of titanium dioxide pigment nanoparticles against agglomeration and sedimentation.» In: 450 (July 2015), pp. 434–445. DOI: 10.1016/j.jcis.2015.02.051. URL: https://doi.org/10.1016/j.jcis.2015.02.051.

[13] J. Hu et al. «Stearic acid-coated superhydrophobic Fe2O3/Fe3O4 composite film on N80 steel for corrosion protection.» In: 359 (Feb. 2019), pp. 47–54. DOI: 10.1016/j.surfcoat.2018.12.040. URL: https://doi.org/10.1016/j.surfcoat.2018.12.040.

[14] V. Toson et al. «Facile Intercalation of Organic Molecules into Hydrotalcites by Liquid-Assisted Grinding: Yield Optimization by a Chemometric Approach.» In: 15.11 (Oct. 2015), pp. 5368–5374. DOI: 10.1021/acs.cgd.5b00968. URL: https://doi.org/10.1021/acs.cgd.5b00968.

[15] E. Conterosito et al. «High-Throughput Preparation of New Photoactive Nanocomposites.» In: 9.11 (May 2016), pp. 1279–1289. DOI: 10.1002/cssc.201600325. URL: https://doi.org/10.1002/cssc.201600325.

[16] L. Palin et al. «Understanding the Ion Exchange Process in LDH Nanomaterials by Fast In Situ XRPD and PCA-Assisted Kinetic Analysis.» In: 2019 (Feb. 2019), pp. 1–9. DOI: 10.1155/2019/4612493. URL: https://doi.org/10.1155/2019/4612493.

[17] M. Lopresti et al. «Epoxy resins composites for X-ray shielding materials additivated by coated barium sulfate with improved dispersibility.» In: *Materials Today Communications* 26 (Mar. 2021), p. 101888. DOI: 10.1016/j.mtcomm.2020.101888. URL: https://doi.org/10.1016/j.mtcomm.2020.101888.

9

Development of coatings for magnesium alloys

Ah, you've done grand, laddie. Now you know what you have to do. Burn the house down. Burn them all!

O'Reilly the Leprechaun

The state of the art of magnesium alloys was described in Chapter 1, highlighting how much this type of alloys are prone to corrosion. As an inhibition strategy, coatings are employed to act as barriers against corrosive agents such as oxygen, water and acids. In an our recent study[1], a AM60 magnesium alloy for food contact has been coated using different bio-based coatings and tested in different level of aggressiveness. A polyamide 11 (PA11) based powder coating obtained from renewable resources and commercially known as Rilsan®[2] was used as one of the candidates for the AM60 magnesium alloy coating. The polymer is synthesized from castor oil, which is extracted from plants grown in semi-arid and nutrient-poor environments, which would not be suitable for growing plants intended
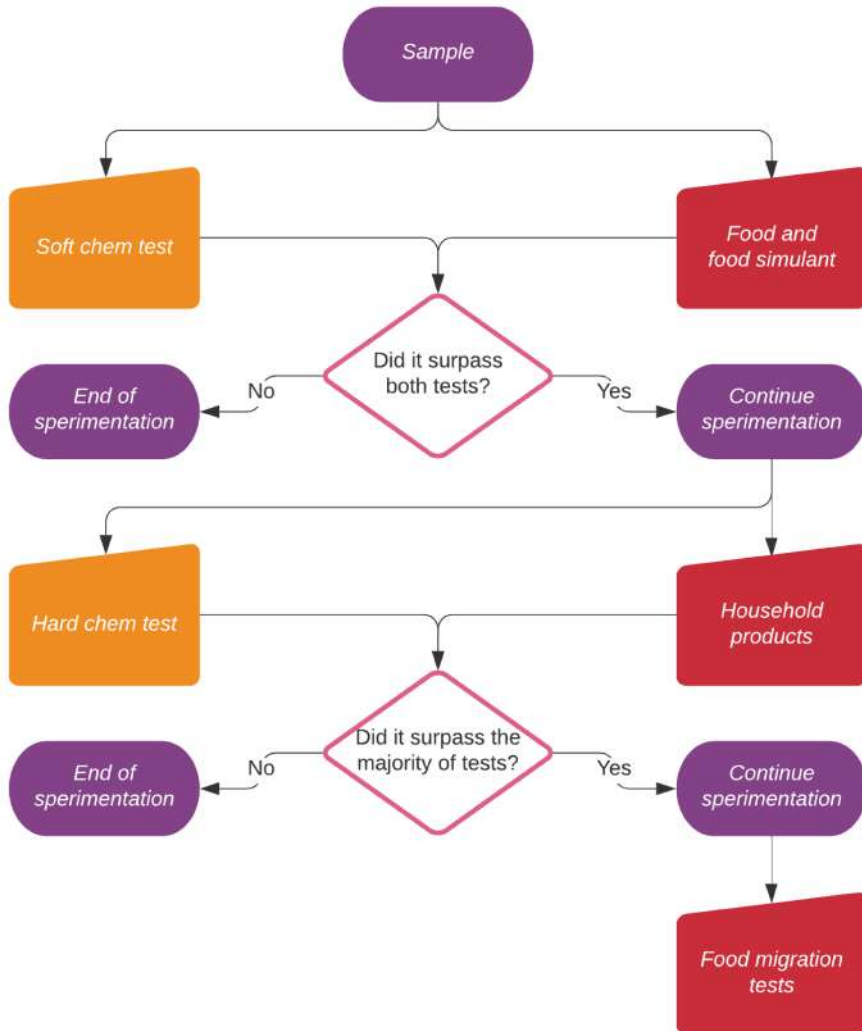
Figure 9.1: Flowchart of the corrosion tests of coatings for AM60 magnesium alloys intended for food contact. In the figure the three different levels of aggressiveness are presented, from the mildest, passing through more aggressive conditions up to harsh conditions. Figure from ref.[1].

for food. Two other coating materials were exploited in the study, both deriving from synthesis: the first silica-based, while the second consisting of polyester-based lacquers. All three materials are known for the protection of steel[3] and aluminum alloys[4], but in this context they are applied for the first time on magnesium alloys.

Specimens, both bare and coated, were exposed to contact conditions with food simulants (Figure 9.1). The first level consisted in exposing the mild conditions, both being chemicals (diluted HCl, NaOH and NaCl) and to food simulants (water, acetic acid, olive oil, ethanol, cola, . . .), the second involved contact with concentrated solutions of the previously used chemicals and household cleaning products (both acidic and basic detergents), while the third level consisted in a migration test, according to the reference standards[5, 6].

A specific drop test was developed to study the behavior of coatings subjected to increasingly aggressive contacts and with ever increasing concentrations of active agents. The procedure is described internally in the article reported in Annex VII. All samples were analyzed using ATR-IR to monitor the state of the coatings using the characteristic infrared bands. In addition, visual analyses by optical and scanning electron microscopy were performed to determine any surface yelding. PA11 was found to be the only coating to have passed all tests, resulting in a promising technology for coating magnesium alloys. PA11 proved to be a winning material even in harsh conditions, which consisted of aggressions by concentrated ionic salts and bases at temperatures of about 70 °C. In addition to coated platelets, real world prototypes have been developed, consisting of espresso cups. Even when deposited on specimens with irregular shapes and welds, the PA11 managed to withstand aggression. In particular, it has been observed that the deposition technique allows the formation of a layer about 120 µm thick, which is sufficient to protect the underlying material from aggression.

All the details regarding the three experimentation steps, the characterization of the samples and the future perspectives of the work

and further observations can be found in the article published on the
International Journal of Molecular Sciences (MDPI) in Annex VII.

Bibliography

[1] B. Mangolini et al. «Low-Cost Biobased Coatings for AM60 Magnesium Alloys for Food Contact and Harsh Environment Applications.» In: *International Journal of Molecular Sciences* 22.9 (May 2021), p. 4915. DOI: 10.3390/ijms22094915. URL: https://doi.org/10.3390/ijms22094915.

[2] P. Borg et al. «Example of industrial valorisation of derivative products of Castor oil.» In: *Oléagineux*, *Corps gras*, *Lipides* 16.4-5-6 (July 2009), pp. 211–214. DOI: 10.1051/ocl.2009.0276. URL: https://doi.org/10.1051/ocl.2009.0276.

[3] J.-L. Pey. «Corrosion protection of pipes, fittings and component pieces of water treatment and pumping stations.» In: 44.2 (1997), pp. 94–99. DOI: 10.1108/00035599710165333.

[4] G. Mirone and R. Pesce. *Photo-crosslinkable multi-coating system having improved gas barrier properties.* US Patent 7,341,791. 2008.

[5] U. E. 1186-1:2003. *Materials and Articles in Contact with Foodstuffs-Plastics-Test Methods for Overall Migration into Aqueous Food Simulants by Total Immersion.* Available online, 2003. URL: http://store.uni.com/catalogo/uni-en-1186-1-2003.

[6] U. E. 1186-3:2003. *Materials and Articles in Contact with Foodstuffs-Plastics-Guide to the Selection of Conditions and Test Methods for Overall Migration.* Available online, 2003. URL: http://store.uni.com/catalogo/uni-en-1186-3-2003.

10

NOVEL APPROACHES IN COATINGS DEVELOPMENT FOR MAGNESIUM ALLOYS

Brothers And Sisters Are Natural Enemies. Like Englishmen And Scots. Or Welshmen And Scots. Or Japanese And Scots. Or Scots And Other Scots. Damn Scots They Ruined Scotland!

MacDougal, W.

In a recent article by Moshynets et al.[1], PA11-based coatings were modified with the aim of creating biocidal and antimicrobial coatings. This type of modification inspired the continuation of the work presented in the previous chapter, whose results are already published[2], paving the way for the improvement of the protective, wear and mechanical properties of PA11 as magnesium alloy coating. At the same time, a new line of research was opened in collaboration with the University of Modena for the use of high-performance coatings on magnesium alloys. Coatings are deposited by using the High

Velocity Oxygen Fuel (HVOF) technique[3, 4] to give alloys exceptional hardness (up to ten times the one of the uncoated magnesium alloy) and resistance to corrosion.

Both projects were launched in the second quarter of 2021 with some delay because of the pandemic, with the planning and execution of the coatings carried out in the third quarter. As a consequence, characterization of the materials is currently underway. For this reason, in this Chapter, experimental planning strategies, development o methods and preliminary results will be reported. However, these data fully demonstrated the power and potentialities of multivariate methods in experiment design and interpretation.

10.1 Functionalized Polyamide 11 for enhanced surface properties

Magnesium samples were coated using PA11 with the addition of different nanomaterials to improve the protective characteristics that had already been verified within the previous test campaign[2]. Nanomaterials chosen for this work belong to the following families:

- POSS (Polyhedral Olygomeric Silsesquioxanes)[5]: nanomaterials consisting of cubic silica cages functionalized with organic groups. These hybrid organic/inorganic materials lend themselves well to the functionalization of polymeric matrices and to the engineering of the latter according to two mechanisms:

    1. choice of the organic group[6]: the greater or lesser chemical affinity of the functionalizing group respectively allows a greater or lesser dispersion of the nanosilica inside the matrix, until crosslinking of the polymeric chains and therefore densification of the host material is obtained. In the case of a chemical non-affinity, the interesting effect

that can be observed is the segregation of the nanomaterial into islands or on the surface of the polymer. This last aspect can be fundamental to obtain a barrier effect;

2. closed-cage and open-cage silsesquioxanse: POSS can be synthesized with the complete cubic cage (Si_8O_{12}), called *closed-cage*, or with the vacancy of a silicon atom (*open-cage*). In the latter case, the structural defect is filled with the formation of three extremely reactive hydroxyl groups. Several scientific studies report the use of open-cage POSS to functionalize the surface of some inorganic materials, for example titanium dioxide[7, 8]. In fact, the surface –OH groups of the TiO_2 particles are involved in condensation reactions with the hydroxyl group of the open-cage POSS, leaving the bulk properties of the particles unchanged. Functionalization has an important effect on the dispersion of the additive[7]. The condensation reaction can be carried out in the laboratory or, as reported in some scientific studies, it can take place directly in the additive phase by exploiting the process heat. This last possibility of *in situ* intervention on the functionalization of inorganic materials with open-cage POSS, suggests the possibility of obtaining positive effects on PA11 matrices in use at an industrial level.

• LDH (Layered Double Hydroxides)[9]: these lamellar nanomaterials, if well dispersed and possibly oriented, can increase the barrier properties to oxidizing agents[10] and act as nanotrap that release intermediate anions and store, through ion exchange, anions relevant for corrosion such as chlorides. As a consequence, LDHs can delay the diffusion of aggressive ions on the surface of the metal substrate.

Coatings are studied with the aim of extrapolating relationships between composition and material properties. For this reason, a Simplex design was adopted as described in Section 2.3.3. A quaternary mixture, as in the case of the considered experimental domain, can be represented as a tetrahedron at the vertices of which the pure substances are present, in the midpoint of the edges the binary mixtures at 50%, in the center of gravity of the faces the ternary mixtures at 33% of each component and at the center of the solid the equi-proportioned quaternary mixture.

The coating tests are carried out in a real world environment of a partner company, then, in order not to keep the production lines busy for too long and not to consume excessive quantities of samples, it was decided to adopt the strategy to keep the quantity of polymer fixed and to vary the quantity additives. By keeping the total percentage of additive (and therefore that of polymer) fixed, the problem is reduced to a ternary experimental domain. This space corresponds to a triangle parallel to the face opposite the vertex of the parameter that has been kept fixed. In Figure 10.1 vertex *A* represents the polymer mass fraction, while the grey cross-sections represent the the three-dimensional experimental domains of the additives. Once the first set of experiments has been carried out (Plane 1 in Figure 10.1), known quantities of polymer and additives are added to each sample in order to pass to the ternary plane directly parallel and to a greater quantity of additive (Plane 2 in Figure 10.1). With small quantities and with a very fast approach (simple addition of pre-weighed quantities of mixtures), it was possible to carry out experiments on three parallel ternary simplexes, analyzing only the vertices. In this way, in addition to the relative quantities among the additives, it is also possible to study their influence on the total quantity with respect to the polymer. This strategy allows, in the post-characterization phase, to choose successive experiments that belong to three-dimensional domains not parallel to the side opposite the vertex representing
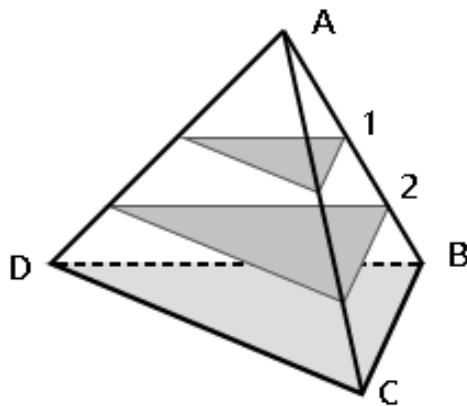
Figure 10.1: Representation of three-dimensional sub-simplexes (1 and 2 cross-sections) in a four-dimensional simplex (tetrahedron).

the polymer, generating inclined cross-sections on which all combinations designed by Simplex-lattice or Simplex-centroid can be explored. The following were chosen as additives: an open-cage POSS (Quantitatives: 0.33%, 0.66%, 1%), a closed-cage POSS (Quantitatives: 0.33%, 0.66%, 1%) and LDH (Quantitatives: 1%, 2%, 3%)[1]. All samples were tested with and without the typical commercial PA11 primer as a substrate between magnesium and PA11 and two extra samples of pure PA11 for reference were produced.

Samples were analysed by optical microscopy and ATR-IR to evaluate the uniformity of the coatings and the effect of nanomaterials on the deposition process. Open-cage POSS improves the uniformity of the surface. The open-cage POSS, however, tends to reticulate: consequently the black aggregates could correspond to denser areas of material. The closed-cage POSS tends to float in the polymers in the liquid or viscous phase and to generate siliceous layers able to increase the barrier effect. This floating effect is also evident in the

---

[1]It can be noted that, due to the quantities chosen, the ternary simplexes are already slightly inclined and are not parallel to the face of the tetrahedron opposite the vertex which represents the quantity of polymer.

application on PA11 to the point that surface aggregations are seen. Observations suggest limiting, in future experiments, the amount of this nanomaterial to lower concentrations. The hydrotalcite, at the concentrations used, is not compatible with rilsan, generates aggregations, limits the melting of the material in the coating phase and, analyzing the specimens under a microscope, both part of the non-dispersed nanoadditive and the formation of some bubbles and craters can be seen within the defect. The possible cause is a thermal decomposition of hydrotalcite or a strong interaction with the polymer matrix.

ATR-IR measurements evidenced that nanomaterials do not modify the IR fingerprint of the polymer. Since the measurement are carried out in reflectance, the primer (between polymer and magnesium alloy) is invisible due to the thickness of the PA11 layer. Surface migration of closed-cage POSS is confirmed again, having a more evident effect in the IR spectrum. Small differences in the CH stretching area at $2900\,\mathrm{cm}^{-1}$ were observed. In general, experimental noise of the spectra increase as the concentration of the POSS increases. However, no characteristic bands of POSS have been observed on spectra. Presence of hydrotalcite signals below $950\,\mathrm{cm}^{-1}$ and at $1350\,\mathrm{cm}^{-1}$ is evident, but the spectrum of PA11 doe not present evident modifications. IR microscopy therefore confirms the non-interaction between hydrotalcite (which aggregates) and PA11.

From the first results it seems that POSS-based nanomaterials, especially at low concentration ratios, have a better dispersion in PA11 and promote their typical effects: cross-linking (open-cage POSS) and surface buoyancy creating a silica barrier layer. LDH, on the other hand, at the used concentrations, would seem not to be compatible with PA11. As a development following the project, POSS-based nanomaterials will be used in a mixture, possibly evaluating concurrent lower concentrations of hydrotalcite.

10.2 High Velocity Oxygen Fuel based coatings for high performances magnesium alloys

HVOF consists of creating a high-speed flow of metal particles in a high-temperature flame. The particles first implant in the substrate (AZ31 Mg alloy) and then accumulate on the surface, growing a homogeneous layer. An Oerlikon-Metco HVOF torch in gas-fuel (H_2/O_2) configuration was used (Figure 10.2). The HVOF system is positioned on a robotic arm that moves along the three axes. Sam-
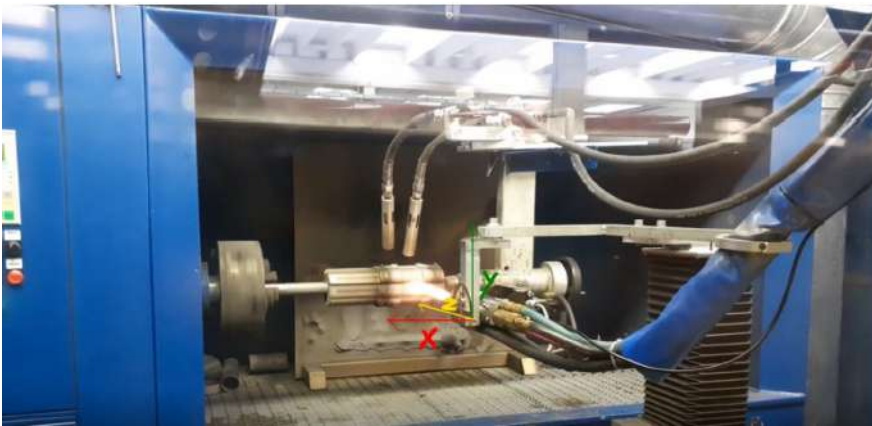
Figure 10.2: HVOF setup used for AZ31 coatings. Coating particles are heated and driven by the torch onto the substrate, sintering once deposited.

ples of AZ31 magnesium alloy are mounted on a rotating spindle thanks to a fixing system (Figure 10.2). The speed of the spindle, in combination with the movement along the horizontal axis (parallel to the spindle rotation axis) determines the process variable called "pitch", which is the distance traveled by the torch while the spindle makes a complete revolution. Several process parameters were then taken into consideration and optimized, such as the number of passes to pre-heat the samples, the distance of the torch, the rotation speed of the spindle. For the first feasibility study, two powder

Run	Coating	Distance (mm)	Pre-Heat (n° of passages)	Sandblasting	Dep. Efficiency (%)
1	WC/CoCr	300	8	N	63.19
2	WC/CoCr	350	8	N	67.92
3	WC/CoCr	350	12	N	66.94
4	WC/CoCr	350	12	Y	65.00
5	WC/CoCr	350	8	Y	63.96
6	WC/CoCr	350	8	Y	65.69
7	CuAl	300	12	Y	57.04
8	CuAl	300	12	Y	49.04
9	CuAl	300	27	Y	58.47
10	CuAl	250	27	Y	62.62
11	CuAl	250	27	N	49.58
12	CuAl	300	27	N	59.26
13	CuAl	300	12	N	59.38

Table 10.1: Some process and pre-treatments optimized during the HVOF procedure. The deposition efficiency was evaluated as the ratio between the weight gain of the sample divided by the weight of used powder.

materials with different properties were used: WC/CoCr and a CuAl bronze. WC/CoCr consists in a tungsten carbide in cobalt-chrome matrix. Peculiarities of this material are high hardness and wear resistance. The CuAl bronze is moderately wear-resistant but has very good anti-corrosive properties. To determine the process parameters, we started from the usual applications on special steels[11]. Considering the AZ31 supports, the deposition distance has been varied, in all cases much greater than the value usually used with this type of torch, generally in the range from 240 mm to 260 mm. Furthermore, the deposition step was modified to control the temperature on the sample; usually, to obtain an overlap of 50%, a doubled pitch is used: in this case, however, the extremes of the horizontal movement of the torch have been set so that the two spirals described by the torch itself with respect to the spindle in the path round trips were staggered by half a step. This allows to maintain the overlap at 50%, thus ensuring the same uniformity of coating, but, at the same time, it allows to
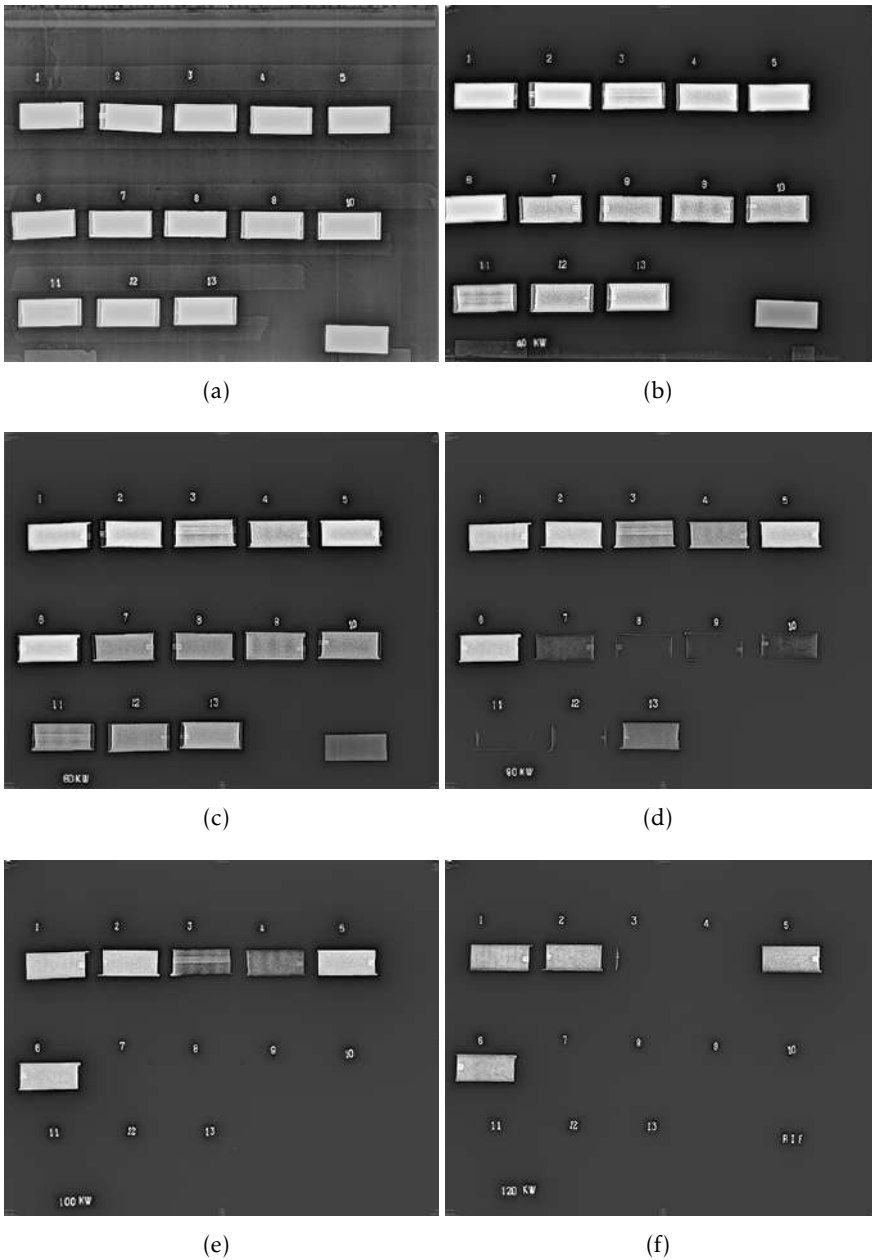
Figure 10.3: Radiographs of samples coated using HVOF. Each radiography is taken in steps of 20 kV in a range from 20 kV to 120 kV.

reduce any problems arising from the concentration of heat in the hit point by increasing the uniformity of distribution on the piece. Efficiency data in terms of mass of powder sprayed, evaluating the mass increase of the samples are reported in Table 10.1 along with other sample parameters. Results of radiographic, X-ray diffraction and optical microscopy analyses are already available, while other tests such as hardness measurement and corrosion resistance tests are currently underway.

One of the main problems of the HVOF deposition method consists in defining the uniformity of the deposited layer and then optimizing the process parameters. Radiographic analysis can help in this, a non-destructive method allowing to quickly evaluate, in addition to the uniformity of the various components of the source material, the presence of defects of various type down to sub-millimeter range, cracks and thickness variations, as described in Chapter 2. The higher the energies of the X-rays sent on the samples, the more transparent samples become, highlighting the uniformity of the coatings. The 13 samples were analysed in a range of the tube spanning from 20 kV to 120 kV with increments of 20 kV each time.

The analysis first showed that the coatings are much denser and less transparent than magnesium, as evidenced by the greater transparency of the naked magnesium, bottom right (not numbered) in the images. Samples 1-6 are less transparent than samples 7-13, which indicates a higher density or/and thickness of WC/CoCr than CuAl. As for the WC/CoCr, samples 1, 2, 5, 6 are thicker and more uniform than the samples 3 and 4. Sample 3, in particular, is not homogeneous and much thinner if compared to the others, to the strip of coating deposited on the lower face is observed. Samples 5 and 1 would appear less thick, but still very uniform. With regard to the CuAl coated samples, the number 13 is the thickest, followed by 7 and 10. Samples 9 and 11 at 60 kV show areas of accumulation and reduction of thickness in alternating bands. Samples 7, 8 and 12,

although thinner, appear more uniform. To obtain quantitative information on the actual radiotransparency an analysis of the grayscale values has been carried out with ImageJ[12], as done in Chapters 7 and 8.

The radiotransparency percentage data were analysed by PCA to-
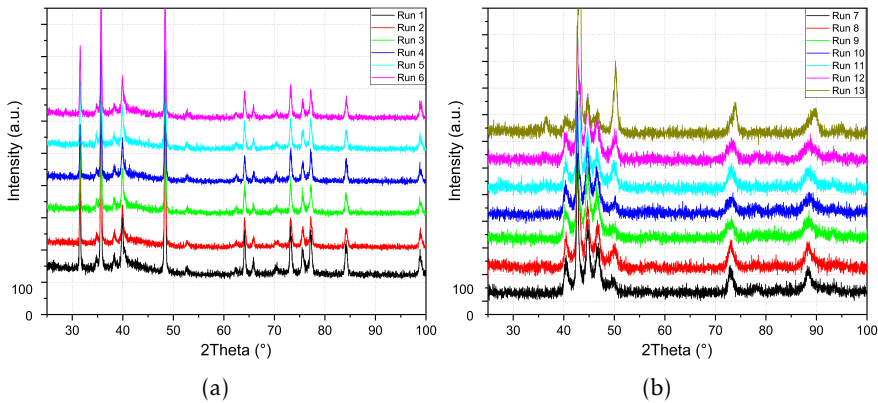
Figure 10.4: XRPD data on HVOF samples. Left: XRPD data collected on WC/CoCr coatings. Right: XRPD data collected on CuAl coatings.

gether with the process variables (flare gas flow, carrier, distance from the sample, ...) and the results obtained on weight gain and efficiency of deposition. In Figure 10.5(a) the Scree Plot indicates that most of the system variance (64.9%) can be explained on a single PC. The second main component has an explained variance value of 13.2%, therefore it was taken into account. Subsequent PCs each bring little contribution and were consequently excluded from the analysis. In the Score Plot of Figure 10.5(b), it can be observed how the samples are positioned in the space of the first two components: along PC1 the types of coating are distinguished (WC/CoCr with PC1 negative and CuAl with PC1 positive). Observing the Loading Plot of Figure 10.5(c), except for the two extremes ($20\,\mathrm{kV}$ and $140\,\mathrm{kV}$), all the radiopacity values closely correlate with the process variables, in particular with the deposition efficiency, with the mass gain, and with

the flux of hydrogen expressed in Standard Liters per Minute (SLPM).
On the contrary, the air flow, the number of coating cycles, and the
pitch, which, if too high, do not provide homogeneous coverage of
the sample, are anti-correlated with a high radiodensity. The num-
ber of preheating cycles and the combustion agent flow of the torch
are instead at negative values of PC2 and only the preheating passes
seem to weigh in part on PC1, a sign that this factor influences the
deposition performance, but not in a clear way. The results obtained
can be useful for an optimization of the torch parameters when it
will pass to a second phase in which a new generation of samples will
be coated. The results are still preliminary and the analyses will be
repeated once more information on the samples is obtained, such as
hardness and corrosion resistance data. Information on the deposited
phases can be obtained from the XRPD measurement, however infor-
mation about the homogeneity of the surface is not obtained. The
XRPD data reported in Figure 10.4 indicate that samples 7, 8 and
11 are very similar, as well as sample 9 showing a similar XRPD pat-
tern to samples 10 and 12, although some differences were observed
with optical microscopy. In particular, the XRPD pattern of sample
10 shows intermediate characteristics compared to those of samples
9 and 12. Sample 13 appears clearly different from the others both
under the optical microscope and as regards the diffraction pattern
since the copper phase is particularly abundant in it. Moreover, an
extraphase peak at 36.5 degrees in 2θ is present. In general, with par-
ticular reference to samples 12 and 13, the prevailing phase is copper.
One minority phase is currently unknown, but the elemental analysis
SEM/EDX indicates the presence of Cu/Al/O, therefore an alumina-
based oxide with copper. XRPD mappings were made on 4x4 dot
grids (Figure 10.6(a)) to identify surface inhomogeneities within the
samples. However, as per previous results, no inhomogeneities were
detected by diffraction. Instead, progressive zero errors have been
identified within some samples and, after an anlysis by PCA on map
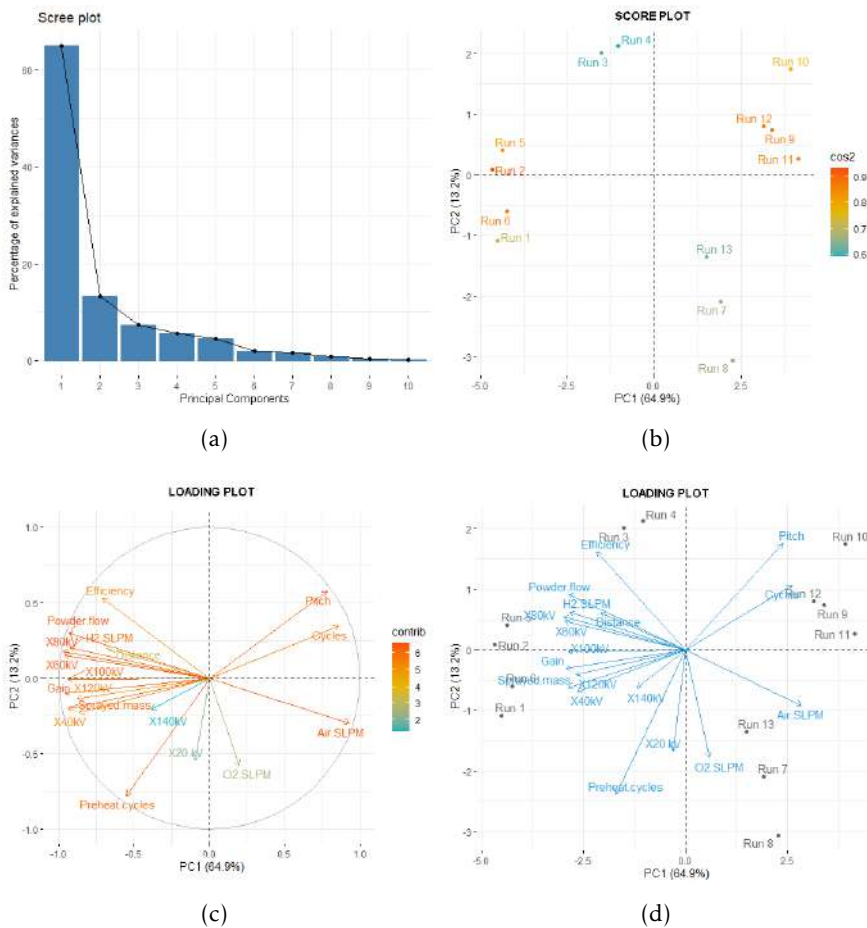
Figure 10.5: Principal components analysis performed on process data an preliminary results on the efficiency of deposition and radio-density data.

data, the score plot (Figure 10.6(b)) presented a peculiar shape in sample disposition. This behavior was associated to the slightly convex shape assumed by the samples when placed in front of the flame. The position of the points in the score plot indicates that the zero error is more pronounced along the x direction (0-3), but it can also be observed that the points of the second and third rows (4-7 and 8-11) are

(a)   (b)
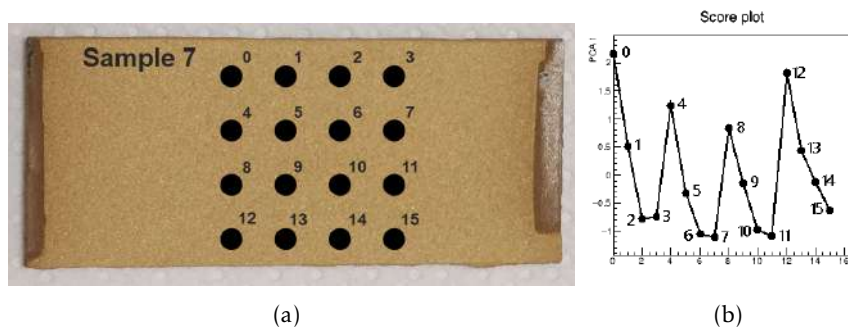
Figure 10.6: Analysis of XRPD maps by multivariate approach. In the score plot, the arrangement of the samples, compared to the position of the points on the map, provides spatial information regarding the directions of curvature of the sample.

at lower values than the corresponding of the first and fourth rows (0-3 and 12-15). This indicates that the samples are convex in both x and y directions, with a less pronounced effect on the y axis. The experiment demonstrates the power of PCA in making data presenting spatial gradients easily visible and interpretable, similarly to what is described in Chapter 8 for the in situ sedimentation experiment (temporal gradient). The same procedure could have been carried out with traditional methods, for instance using the Rietveld refinement for the evaluation of the zero error of each point, but with a much slower procedure, as well as less immediate interpretability.

Bibliography

[1] O. Moshynets et al. «Antibiofilm Activity of Polyamide 11 Modified with Thermally Stable Polymeric Biocide Polyhexamethylene Guanidine 2-Naphtalenesulfonate.» In: *International Journal of Molecular Sciences* 20.2 (Jan. 2019), p. 348. DOI: 10.3390/ijms20020348. URL: https://doi.org/10.3390/ijms20020348.

[2] B. Mangolini et al. «Low-Cost Biobased Coatings for AM60 Magnesium Alloys for Food Contact and Harsh Environment Applications.» In: *International Journal of Molecular Sciences* 22.9 (May 2021), p. 4915. DOI: 10.3390/ijms22094915. URL: https://doi.org/10.3390/ijms22094915.

[3] M. Parco et al. «Investigation of HVOF spraying on magnesium alloys.» In: *Surface and Coatings Technology* 201.6 (Dec. 2006), pp. 3269–3274. DOI: 10.1016/j.surfcoat.2006.06.047. URL: https://doi.org/10.1016/j.surfcoat.2006.06.047.

[4] R. V. Raj, R. S. Unnithan, and G. R. Krishnan. «The characteristics study of HVOF coated AZ91D magnesium alloy with silicon carbide and stainless steel.» In: *AIP Conference Proceedings*. Vol. 2105. 1. AIP Publishing LLC. 2019, p. 020024.

[5] R. H. Baney et al. «Silsesquioxanes.» In: 95.5 (July 1995), pp. 1409–1430. DOI: 10.1021/cr00037a012. URL: https://doi.org/10.1021/cr00037a012.

[6]   S.-W. Kuo and F.-C. Chang. «POSS related polymer nanocomposites.» In: 36.12 (Dec. 2011), pp. 1649–1696. DOI: 10.1016/j.progpolymsci.2011.05.002. URL: https://doi.org/10.1016/j.progpolymsci.2011.05.002.

[7]   P. A. Wheeler et al. «Polyhedral oligomeric silsesquioxane trisilanols as dispersants for titanium oxide nanopowder.» In: 108.4 (2008), pp. 2503–2508. DOI: 10.1002/app.27910. URL: https://doi.org/10.1002/app.27910.

[8]   M. Nowacka, D. Ambrożewicz, and T. Jesionowski. «TiO2-SiO2/Ph-POSS Functional Hybrids: Preparation and Characterisation.» In: 2013 (2013), pp. 1–10. DOI: 10.1155/2013/680821. URL: https://doi.org/10.1155/2013/680821.

[9]   E. Conterosito et al. «Facile preparation methods of hydrotalcite layered materials and their structural characterization by combined techniques.» In: *Inorganica Chimica Acta* 470 (Jan. 2018), pp. 36–50. DOI: 10.1016/j.ica.2017.08.007. URL: https://doi.org/10.1016/j.ica.2017.08.007.

[10] N. M. Larocca, R. B. Filho, and L. A. Pessan. «Influence of layer-by-layer deposition techniques and incorporation of layered double hydroxides (LDH) on the morphology and gas barrier properties of polyelectrolytes multilayer thin films.» In: 349 (Sept. 2018), pp. 1–12. DOI: 10.1016/j.surfcoat.2018.05.030. URL: https://doi.org/10.1016/j.surfcoat.2018.05.030.

[11] P. Sassatelli et al. «Properties of HVOF-sprayed Stellite-6 coatings.» In: *Surface and Coatings Technology* 338 (2018), pp. 45–62.

[12] C. A. Schneider, W. S. Rasband, and K. W. Eliceiri. «NIH Image to ImageJ: 25 years of image analysis.» In: 9.7 (June 2012), pp. 671–675. DOI: 10.1038/nmeth.2089. URL: https://doi.org/10.1038/nmeth.2089.

Multivariate studies of in-situ analysis of evolutionary processes

CHAPTER

11

IMPLEMENTATION OF AN AD HOC *IN SITU* XRPD EXPERIMENTAL SETUP APPLIED TO EUTECTIC FREEZING INVESTIGATION

You look sharp today, sir... You looken sharpen todayen, mein Herr.

Smithers, W.J., Jr

In situ X-ray powder diffraction (XRPD) studies of evolving systems, associated with the use of multivariate methods, has been introduced, from a theoretical viewpoint in Chapter 4. In Chapter 8, the study of the evolution over time of a sample subjected to sedimentation was presented. In that context, principal component analysis (PCA) helped to reconstruct, based on the zero error of the peaks of the diffraction patterns, the hyperbolic trend of the additive motion in the monomer mixture. In Chapter 10, on the other hand, an *in situ* study was carried out in the presence of a spatial gradient on magnesium samples: surfaces of specimens were mapped by XRPD and

then data were processed by PCA. The arrangement of the points in the score plot indicated the presence of a defect in the sample (slight convex shape) due to the coating process that curved the specimen. Both these cases, despite very promising in their developments, does not deal with a real phase transition.

This chapter aims to give space to a third type of *in situ* experiments conduced during the doctoral period, namely those in the presence of temperature gradients, inducing phase transitions and the formation of new phases. Our research team is not new to experiments in the presence of temperature gradients[1–5], but in the past such experiments have mainly been conducted in large scale facilities. Laboratory-scale *in situ* experiments have been optimized only in the last decade. The solidification of a liquid eutectic mixtures was chosen as test case, being a challenging and not usual task in the diffraction field, typically devoted to solid samples. Moreover, the topic is of interest on an industrial collaboration of the group. Two examples are described, showing the power of the combination of *in situ* XRPD and multivariate analysis, which is able to provide results that are easy to interpret are presented. Figure 11.1 shows a picture of the experimental setup optimized for *in situ* experiments with the XRPD instrument at UniUPO: a Bruker D8 Advance with Linxeye XE-T detector. At the center of the picture, the Linkam THM600 ambient chamber, already used in a previous work [6], is positioned on Bruker's UMC compact stage suited for micro-diffraction experiments. Above the chamber, a USB microscope, which has the dual utility of helping the operator to center the sample on the X-ray beam and taking pictures during the measurements, is placed. Linkam ambient chamber works typically in a temperature range from −100 °C to 300 °C and is able to perform ramps at custom speed of heating or cooling. A sample holder suited for liquid samples is also available. The choice in the use (as well as the main advantage) of this type of setup, compared to the one the university has purchased from Bruker, lies in the simplicity of use, in the speed of assembly and in
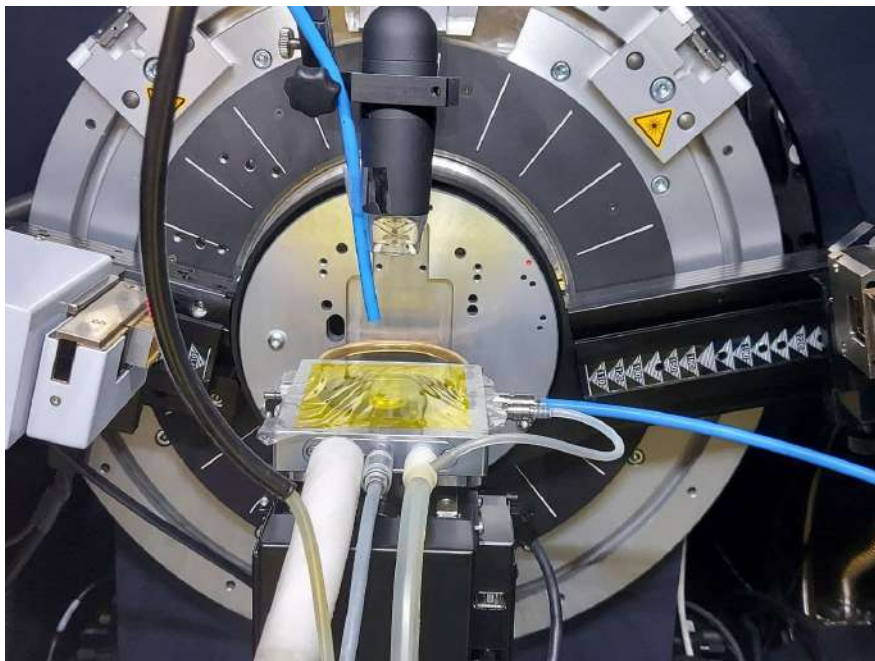
Figure 11.1: Setup for a variable temperature XRPD experiment.

the possibility of monitoring the evolution of the sample through the camera, which becomes very difficult or impossible with the original high temperature chambers, because of a thick, non-transparent Kapton layer.

11.1   Inorganic eutectic mixtures

Two samples of inorganic eutectics, one commercial supplied by a partner company and one prepared in the laboratory, were analyzed by an *in situ* XRPD experiment using the presented setup. The sample supplied by the partner company is certified as a eutectic mixture with a crystallization point at −31 °C. The sample was brought to the temperature of −20 °C degrees and kept at that temperature for ten minutes. A cooling ramp of −1 °C min^{-1} was then set in a range from −20 °C to −50 °C. XRPD measurements were set up to be one

(a)

(b)

(c)

(d)

(e)

(f)

Figure 11.2: Images of the phase transition process of a eutectic. Pictures were taken at the beginning of each measurement, approximately every 43 seconds.

(a)

(b)

(c)

Figure 11.3: On top, data matrices of XRPD data collected during the cooling 11.3(a) and heating 11.3(b). Data were then processed by PCA giving a score plot in which phase transition is showed by the inflection of a sigmoidal curve 11.3(c).

every about 43 s and to take a picture of the sample at the beginning
of each measurement. The pictures obtained during the crystalliza-
tion process are shown in Figure 11.2, where it is possible to observe
that different measurements were collected between the beginning
and the end of the crystallization process. The same procedure was
then repeated in the heating ramp, this time in a range from $-50\,°C$
to $-20\,°C$ with a heating speed of $2\,°C\,min^{-1}$. XRPD data collected
are reported in Figure 11.3. In Figure 11.3(a), it is possible to iden-
tify the beginning of the crystallization by the appearance of XRPD
reflections. On the contrary, the liquefaction is indicated in Figure
11.3(b) by the total disappearance of the peaks. The XRPD patterns
of the two data matrices, processed with PCA, provide the linear
score plots shown in Figure 11.3(c), where it is possible to identify
the melting point indicated by the inflections of the two sigmoidal
curves. By averaging the two inflection points, the resulting tempera-
ture is $\approx -31\,°C$, as reported in the certificate. The sample produced
in the laboratory, with the same composition of the industrial one,
was analyzed using the same temperature range as the previous ex-
periment, but with both ramps of $2\,°C\,min^{-1}$. The result, reported in
Figure 11.4(a), shows a shift of the crystallization point to lower tem-
peratures ($\approx 36.8\,°C$). The result indicates that the real eutectic point
of the mixture is lower than the one achieved at industrial level and
value of $31\,°C$ can be attributed to the presence of additives and im-
purities in the technical grade reactants used in the industrial world
and a higher concentration of salts in the laboratory mixture made
by laboratory grade reactants. Figure 11.4(b) shows the same result
reported in Figure 11.4(a) after calculating the first derivative of the
score profiles. The transformation helps to better identify the crys-
tallization and melting peaks and makes the result comparable to
what can be obtained using a DSC, of course without the information
about the energy exchange. Similar results can not be obtained using
Rietveld refinement, as liquids cannot be refined.
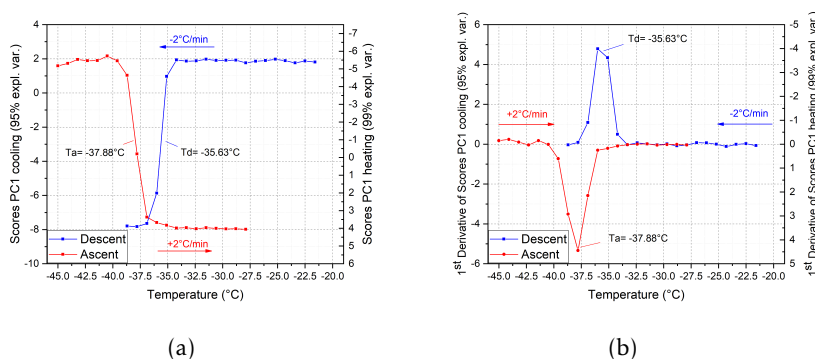
Figure 11.4: Results of the in situ experiment on the eutectic mixture prepared with pure reactants. On the left, the two temperature ramps of cooling and heating, as obtained by PCA. On the right, the first derivative of the two profiles, resembling a DSC-like result.

11.2 Deep Eutectic Solvents

The same approach is currently exploited for the study of innovative eutectic materials known Deep Eutectic Solvents (DES)[7, 8], which have become popular in the last two decades. DES are a subgroup of ionic liquids (ILs) which have a generic composition[8]:

$$Cat^+X^-zY \tag{11.1}$$

Where Cat^+ is an ammonium, phosphonium, or sulfonium cation, X^- is a Lewis base and zY is the number of a Y Brønsted acid. The importance of DES is related to the wide range of potential applications they can have. In particular they have been exploited in the field of component separation, CO_2 sequestration, for the production of nanomaterials and also in the field of genomics. The main characteristic of DES is linked to the very low melting point, generally around room temperature. A choline-based DES was studied with the above presented instrumental setup. The XRPD data were collected on a 2θ range from 21° to 40° and in a temperature range from of 40 °C to 10 °C at the cooling speed of -1 °C min^{-1} so that the crystallization of
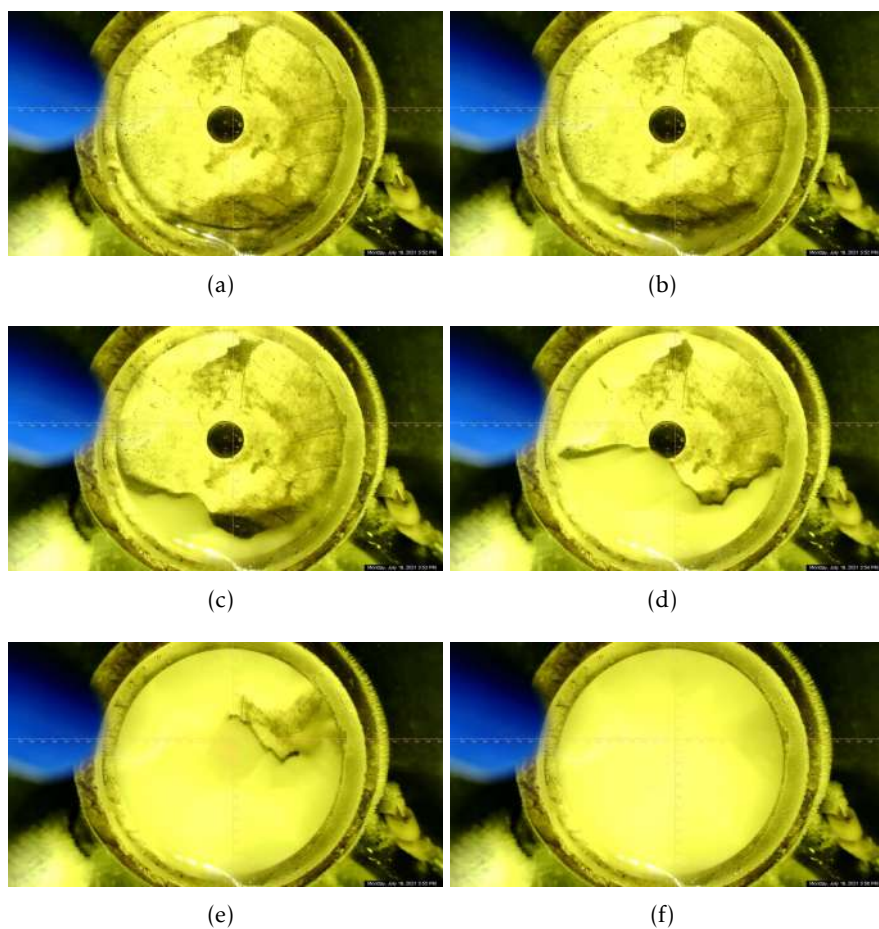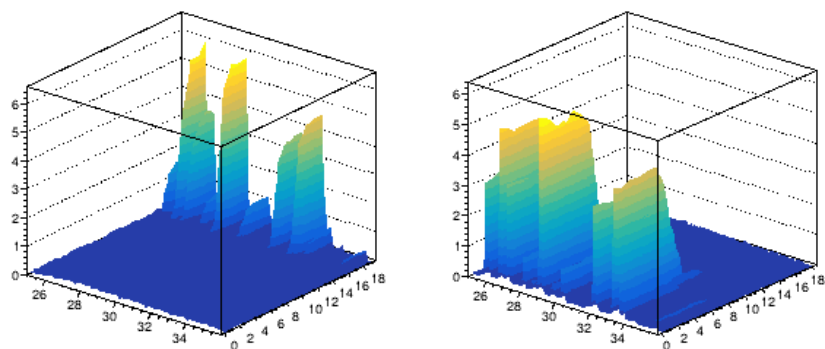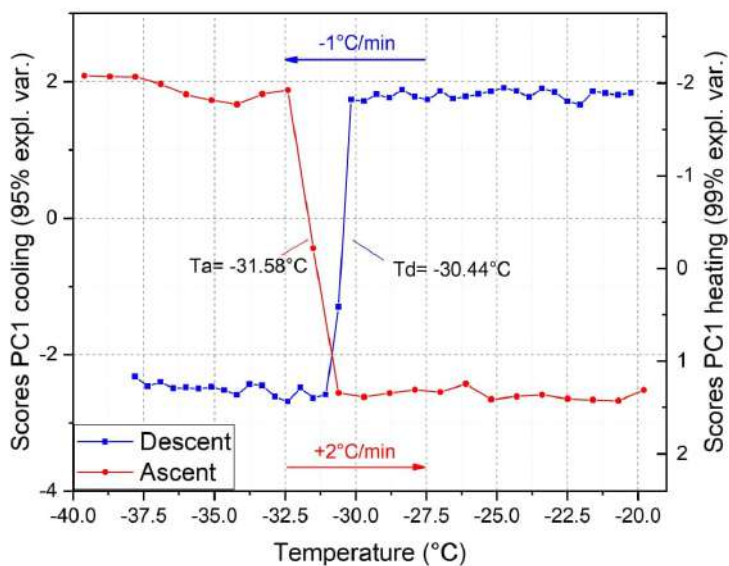
167
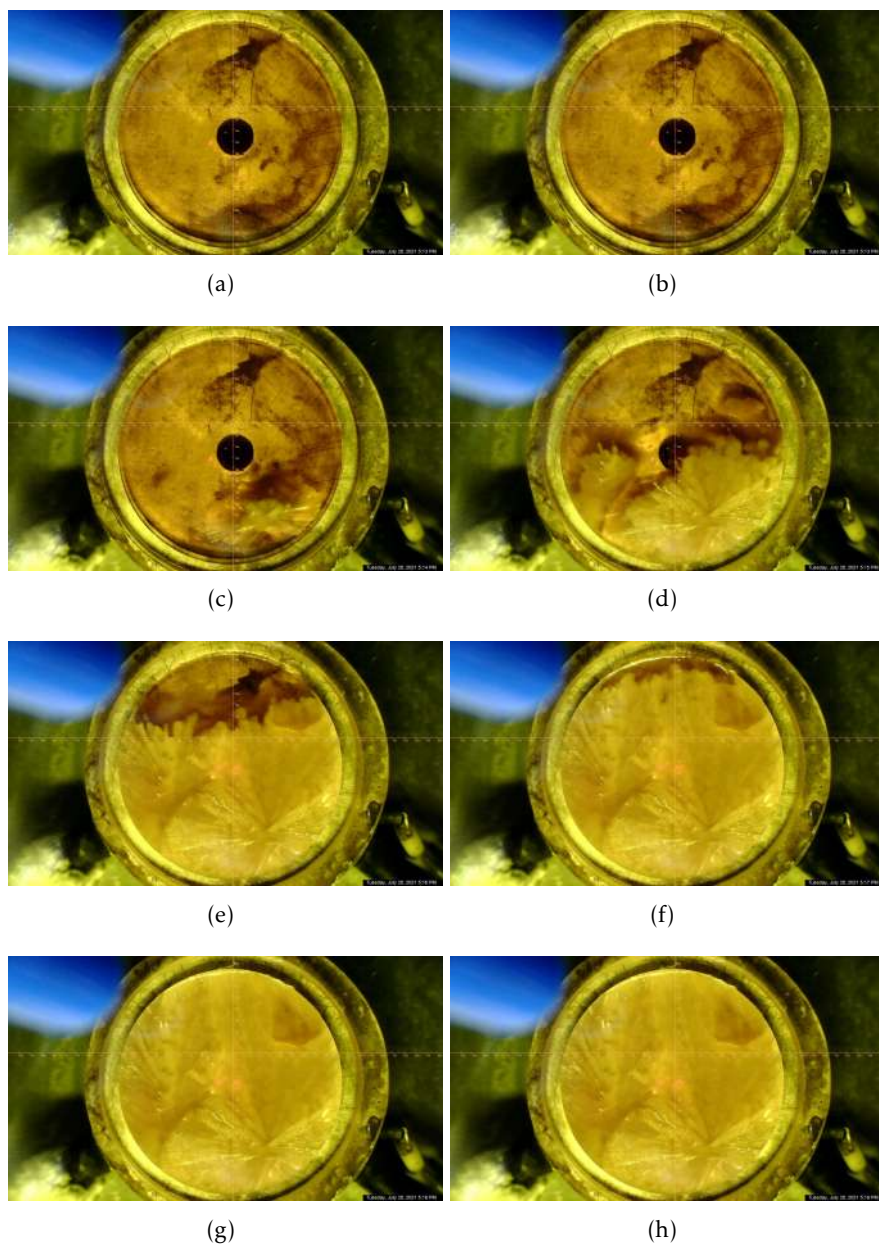
Figure 11.5: Images of the phase transition process of a deep eutectic solvent. Pictures were taken at the beginning of each measurement, approximately every 43 seconds.

the sample could be once again observed. The process of crystallization, slower than that of the eutectic seen above, is shown in a series of eight pictures in Figure 11.5. In this case it is possible to see clearly the evolution of crystallization, starting from a nucleation point that is formed in Figure 11.5(b) and starts to grow. Subsequently, in Figure 11.5(d) two other nucleation points are formed and begin to grow until the complete crystallization of the sample. *In situ* XRPD data were analyzed by PCA using the same approach used before. In Figure 11.6 results of PCA are presented. The scree plot of Figure 11.6(b) shows a variance value explained by the first principal component equal to 99% which explains the appearance of reflections while crystallization occurs. Confirmation of this is given by the Loading Plot of Figure 11.6(c), where the variables have greater weights on the first principal component in correspondence with the characteristic reflections. Finally, in Figure 11.6(d) the PC1 Score Plot shows a trend similar to the one observed in Figure 11.3(c). The difference with respect to inorganic eutectics relies in a more stable sequence of the samples without oscillations and in a longer tail in the sigmoid curve. The crystallization temperature measured at the inflection of the sigmoid curve is equal to 22.13 °C.

The study of thermal gradients is one of the most popular cases of XRPD in situ experiments, together with those in which the evolutionary gradient is represented by time. The results obtained from X-ray diffraction were analyzed thanks to the use of multivariate statistical analysis. The transformation of entire patterns (hundreds or even thousands of variables) into projected points in a lower dimensional space is a winning choice for a simpler global interpretation of the data and for the immediate identification of a phenomenon, as also demonstrated in Chapters 8 and 10. Further experiments, in particular with regard to DES, are currently underway on various formulations, to explore the limitations and the possibilities of this method.

(a)

(b)

(c)

(d)
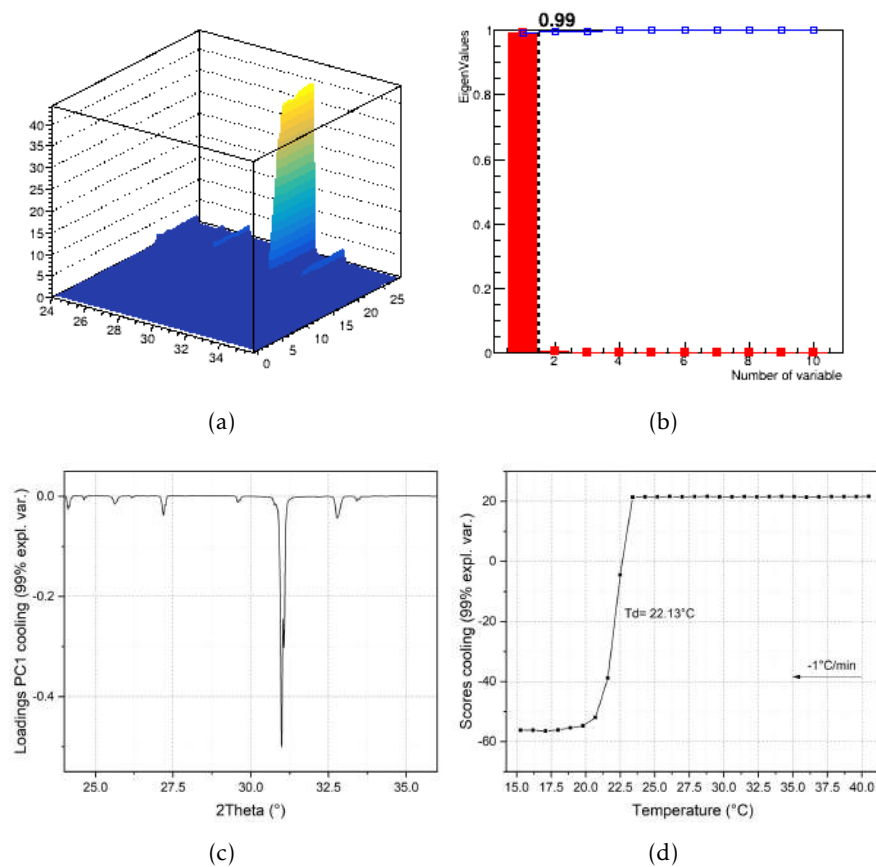
Figure 11.6: Results of PCA analysis performed by RootProf on XRPD
data collected on a choline-based DES sample. 11.6(a): XRPD data
matrix; 11.6(b): Scree plot; 11.6(c): Loadings Plot; 11.6(d): Scores
Plot.

Bibliography

[1] G. Agostini et al. «In Situ XAS and XRPD Parametric Rietveld Refinement To Understand Dealumination of Y Zeolite Catalyst.» In: 132.2 (Dec. 2009), pp. 667–678. DOI: 10.1021/ja907696h. URL: https://doi.org/10.1021/ja907696h.

[2] M. S. del Rio et al. «A combined synchrotron powder diffraction and vibrational study of the thermal treatment of palygorskite–indigo to produce Maya blue.» In: 44.20 (Aug. 2009), pp. 5524–5536. DOI: 10.1007/s10853-009-3772-5. URL: https://doi.org/10.1007/s10853-009-3772-5.

[3] M. Milanesio et al. «Template Burning inside TS-1 and Fe-MFI Molecular Sieves: An in Situ XRPD Study.» In: 125.47 (Nov. 2003), pp. 14549–14558. DOI: 10.1021/ja037229+. URL: https://doi.org/10.1021/ja037229+.

[4] E. Boccaleri et al. «In situsimultaneous Raman/high-resolution X-ray powder diffraction study of transformations occurring in materials at non-ambient conditions.» In: 40.4 (July 2007), pp. 684–693. DOI: 10.1107/s0021889807025113. URL: https://doi.org/10.1107/s0021889807025113.

[5] E. Conterosito, M. Lopresti, and L. Palin. «In Situ X-ray Diffraction Study of Xe and CO2 Adsorption in Y Zeolite: Comparison between Rietveld and PCA-Based Analysis.» In: 10.6 (June 2020), p. 483. DOI: 10.3390/cryst10060483. URL: https://doi.org/10.3390/cryst10060483.

171

[6] R. Caliandro et al. «New Hints on the Maya Blue Formation Process by PCA-Assisted In Situ XRPD/PDF and Optical Spectroscopy.» In: *Chemistry – A European Journal* 25.49 (2019), pp. 11503–11511. DOI: https://doi.org/10.1002/chem.201901932.

[7] B. B. Hansen et al. «Deep Eutectic Solvents: A Review of Fundamentals and Applications.» In: 121.3 (Dec. 2020), pp. 1232–1285. DOI: 10.1021/acs.chemrev.0c00385. URL: https://doi.org/10.1021/acs.chemrev.0c00385.

[8] E. L. Smith, A. P. Abbott, and K. S. Ryder. «Deep Eutectic Solvents (DESs) and Their Applications.» In: 114.21 (Oct. 2014), pp. 11060–11082. DOI: 10.1021/cr300162p. URL: https://doi.org/10.1021/cr300162p.

PART V

DISCUSSION

12

Discussion and future perspectives

Argh not a quarter he'll be dancing for hours!

McCallister, H.P.

The doctoral project was born by the collaboration between Uni-UPO and Bytest, a company specialized in non-destructive testing (NDT) sector, with the aim of developing innovative materials and methods focused on the world of X-ray based NDTs. Within the project, various research lines were born that they are currently under development with interesting perspectives, both on the material science and methods. During the doctoral period, methods and setups were developed for the study of evolutionary events by *in situ* experiments. Innovative materials developed acted as a benchmark for the test of such methods, allowing an in-depth study of data collected in the presence of gradients of different nature (time, temperature, spatial, concentration).

Chapter 1 presented the state of the art of Bytest and UniUPO and

the skills that each of the two entities had before this thesis in the field of NDT. Moreover, the different materials studied in this thesis were presented, with their problems and criticalities. Radiodense materials are essential for the protection of users and the surrounding environment from ionizing radiation and are used in all contexts in which the risks exposure to X-rays are present (in the medical field through shielding clothing and in the industrial case as walls of bunkers and radiographic or tomographic booths). Traditional materials such as lead and steel are still widely used, despite the problems of toxicity (Lead), difficult machinability (Steel) and in general excessive weight. The second topic of intensive study was magnesium alloys, in particular the development of coatings for the prevention of corrosion phenomena. In this case, the development of magnesium surface coating materials has had the dual task of filling the gap in the scientific literature regarding the use on magnesium of bio-compatible materials and high performance coating materials, which are normally applied on steels and other traditional "heavy"alloys. Finally, the eutectic materials and their common uses were briefly presented, being studied for the application of *in situ* diffraction methods developed during the project, also in the context of an industrial partnership not related to the project with Bytest.

In Chapter 2, the theoretical and instrumental methods were presented. Geant4[1–3] and its tools for the study of the interactions between matter and particles were then presented. Analytical chemistry tools, scarcely used in materials science, such as the experimental design methods[4, 5] and multivariate analysis[6, 7] were described, focusing the attention on the used experimental designs and on multivariate techniques for data analysis. Principal Components Analysis (PCA), has been widely used in all topics faced during the thesis. A review article was published on Crystals (MDPI)[7] with my contribution regarding the state of the art of the applications of multivariate methods, in particular PCA, for quantitative phase analysis and the study of data collected by *in situ* experiments.

In Chapter 3 the main goals of the work were outlined.

The efforts done in method developments, necessary to adapt multivariate methods to materials science are described in Chapter 4. In fact, facing real world case studies highlighted limitations of available softwares. In particular, pre-processing methods were lacking and therefore the smoothing algorithm devised by Savitzky and Golay[8] and the possibility of performing multithreading calculations have been successfully integrated into version 16 of the RootProf[9] software, whose updates will soon be presented in a dedicated article. Thanks to these implementations, it is now possible to pre-treat data with derivative smoothing, a transformation that has proved very useful several times in our experience of XRPD data analysis. The collaboration for the improvement and updating of RootProf will continue in the short future with the integration of the algorithm presented in Section 4.2, for the automatic passage from Euclidean coordinates to the barycentric system[10]. The aim is applying the transformation on the PCA results to have a direct quantification of mixtures, as in the work presented in Chapter 5. The version of the 4-dimensional simplex transformation is currently in beta testing. The finalization of the code and its translation to RootProf compliant C++ language are expected in the first half of 2022 and will be useful to exploit PCA analyses for quantification purposes, exploiting XRPD (but not only) data. In the same year, considerable space will be given to testing the Forcefield transformation, the results of which are very promising for applications to systems that evolve over time, both naturally and induced by *in situ* experiments. The algorithm, presented in Section 4.3, was completely conceived, designed, developed and tested by me. Few examples of this novel approach are reported in Appendix B. It has already been demonstrated how, based on the type of gradient present in the data, the response function is different and therefore, as in the case of the autocorrelation of time series, the results can be used to model the different types of evolving phenomena. It represents a very efficient blind approach to unravel the trends and

reaction coordinate in *in situ* data set, complementary to both PCA and traditional methods.

In Chapter 5 a comparison between traditional and multivariate methods for quantification of solid mixtures starting from XRPD and XRF data is presented. The proposed case concerns a situation often occurring in the industrial and academic world, in which the samples are not perfectly distributed in the experimental domain and are prone to present preferential orientations and/or microabsorption. In this situation, which is difficult to deal with by traditional methods based on refinement starting from known crystalline structures, the potential of methods based on multivariate analysis emerges. In fact, not being linked to rigid structural parameters, multivariate methods are able to better model the data and to obtain more accurate results on the quantities of the components in the mixture. Furthermore, it is pointed out that in the total absence of resolved structures, methods such as Rietveld Refinement become inapplicable, whereas multivariate methods only need profiles of the pure components. The results obtained from the use of multivariate methods were as expected, especially the XRPD data for which high accuracy was found. The algorithms developed in Sections 4.1 and 4.2 were exploited. Savitzky-Golay filtering was studied during the pre-process optimization, both as a smoothing method for the reduction of experimental noise in the data. Moreover, first and second derivatives of the data were evaluated as pre-treatment for quantitative analysis. Cornell transformation was used for direct quantification starting from the samples projected in the PCA score plots. This quantification approach, never reported before in the scientific literature, has great potentialities for the quantitative analysis of polyphasic mixtures. An article on this topic has been written and submitted to a scientific journal (Journal of Applied Crystallography).

In recent years, the development of the web has been made available to researchers to create data repositories and make them permanently available to the scientific community (Zenodo, Mendeley Data). In

parallel, scientific journals specialized in collecting information on the data stored in those repositories were born, in order to give scientists a complete and accurate description of the data contained therein. For the first time in the history of the research team, standardized data used for quantitative phase analysis were organized in a database, of which the author of this work is the curator, open to contribution[11] and available for the international community. The database was proposed as a fully open access and open to new contributions complementary to the Round Robins[12–15] proposed by the International Union of Crystallography (IUCr) for methods benchmarking and development for quantitative analysis from polycrystalline mixtures. A second article containing the steps for reproducing the data and an accurate description of the experimental setup was published on Data in Brief (Elsevier BV)[16], and linked to the database.

In the context of the pandemic caused by Covid-19 and the resulting restrictions, it has not been possible to access X-ray-based equipment for a long time. For this reason, IETeasy[17], an open hardware and easily assembled instrument for the impulse excitation technique (IET)[18, 19], was developed and used in home environment and is presented in Chapter 6. The technique involves the acquisition of the acoustic signal produced by a material as a result of a mechanical impulse.The acoustic signals following the impulse can be analysed in the time domain or in the frequency domain, to determine different mechanical properties of the investigated sample, such as the elastic modulus, the Poisson's ratio or damping properties. These are only some of the various applications of IET that can be found in scientific literature[20–22]. The instrument was conceptualized and developed in two different versions, the first one during a bachelor thesis project followed by the author of this work as co-supervisor. IETeasy has been used for data collection on a large variety of materials demonstrating how, in combination with multivariate methods, it is able to provide qualitative analysis of materials with high accuracy

in results and excellent repeatability in measurements. An article, containing construction instructions, validation procedures and instructions for use, was published on HardwareX (Elsevier BV)[17]. Furthermore, the paper contains a section which illustrates how the data collected with IETeasy can be easily analyzed by RootProf to obtain classification analyses, while at the same time extending the field of application of the software. The collected data were organized in an open database[23], making them available to the scientific community, with quality control purposes and the aim of building a database for the automatic recognition of materials with machine learning-based technology. A second article was recently published in Data in Brief (Elsevier BV)[24] in which detailed instructions are given on data collection and how to contribute to the database. Finally, an important result achieved in the development of this project was being able to allow a student to carry out an experimental thesis, under my supervision, in a period in which access to lab facilities and equipment was impossible due to Covid-19 restrictions. The components were delivered directly to the student's home and remote instructions were provided on the assembly of the instrument and on the use of software for data collection and analysis. The development of IETeasy has opened a new line of research that continues today with the study of new materials with different compositions and morphologies. The goal is testing the limits of the technique in combination with multivariate methods, aiming more and more towards automatic recognition systems for materials classification and defects identification.

After describing the methods developed, we enter the field of the development of the materials that have been their testing ground. The work carried out on radiopaque materials, to meet the ecological, health and workability needs that represent limitations in traditional shielding materials, is described in Chapter 7. In scientific literature, different materials and different strategies have been identified[25–28] for the synthesis of innovative materials with high radiodensity

and the choice fell on a approach based on the addition of epoxy resins with high density materials containing high Z elements. The initial screening of the materials was done *in silico* by Geant4. The use of this framework and its tools is still scarcely used outside the fields related to high energy physics and in the scientific literature there are only a few examples of application to materials science. The first utility, conceived and programmed by me, made it possible to evaluate the radiodensity performance of various materials proposed in scientific literature and to select those that were the main object of the research, namely barite and bismite. By the means of experimental design methods, specimens of radiopaque materials obtained additivating barite and/or bismite to an epoxy resin were conceived, developed and finally tested. Characterization with radiography has shown that all samples with a high additive loadings (80% by weight) have a radiodensity higher than steel, with the same thickness and slightly lower than lead. An LCA study was also carried out on these samples, to demonstrate how all the samples are far more ecologically-friendly than lead and, at the same time, how the incidence on human health is drastically lower if compared to the use of steel. Samples with additive quantities greater than 60% by weight also show a homogeneous vertical profile and do not show anisotropy in the shielding power, while for lower additive loadings there are sedimentation effects due to a combined effect of low viscosity, slower gel time of the polymer and high density of both barite and bismite. An article on the topic was published on the International Journal of Molecular Science (MDPI)[29].

The latest observations regarding the vertical homogeneity of the additive specimens within epoxy resin evidenced in ref. [29] inspired the continuation of the research, presented in Chapter 8. The aim is to allow the preparation of specimens with a low barite content for purposes where it is not necessary a high shielding power, but higher mechanical performances are requested, saving material and at the

same time allowing the tunability of the radiodensity of the specimens. To achieve this goal, and reducing the above cited additive sedimentation, it was decided to increase the affinity between additives and polymer by functionalizing the surface of inorganic powders by using surfactants (stearic acid and sodium dodecylsulfate). The procedure was carried out at the solid state exploiting a mechanochemical procedure known as liquid assisted grinding (LAG)[30, 31], which gave positive results with a significant increase in homogeneity in many samples and total isotropy for stearic acid functionalized barite containing samples. The homogeneity of the vertical distribution was verified by the use of different techniques, in particular XRPD and thermogravimetry, performed on the two sides of the specimen (upper side and lower side). In the context of this project, XRPD *in situ* experiments were also conducted on non-functionalized specimens with the aim of observing the migration of the barite towards the bottom of the mold. As a result, a progressive shift of the diffraction pattern reflections at lower angles was observed in 2θ, consistent with an increasing zero error in the samples. The data were analyzed by PCA and Rietveld refinement and the increase of the zero error with the time, due to the sedimentation of the additive, was evidenced. The results of this *in situ* experiment were reported in the aforementioned literature review and a second article published in Materials Today Communications (Elsevier BV)[32] was extracted from the work of optimizing the vertical distribution of additive within the composites.

In Chapter 9 the problem of corrosion of magnesium alloys is addressed by proposing different types of coatings: polyamide 11 (PA11), polyester-based lacquers and silica-based coatings. The magnesium alloy under study was an AM60 alloy, suitable for food contact and for the general industry. The different coatings have been tested with chemical agents (hydrochloric acid, sodium hydroxide, sodium chloride) and food simulants (acetic acid, cola, oil, ...) with increasing aggressiveness. The effects of the aggressions were evaluated

with different techniques: optical and scanning electron microscopy, ATR-IR and ICP-OES, the latter in particular to verify the releases after immersion in milliQ water. It has been verified that PA11 of natural origin is the most performing coating, resisting all types of aggression, even the harshest ones (HCl and NaOH $4M$ at 70 °C). Results of the research were published in a dedicated article on the International Journal of Molecular Science (MDPI)[33].

The results obtained in this first study on magnesium alloys inspired the next phase, currently underway and presented in Chapter 10, of functionalization of PA11 coatings with lamellar materials based on magnesium (Layered double hydroxides - LDH) and polyhedral oligomeric silsesquioxane (POSS). The aim is giving the coatings wear and corrosion resistance, further increase the barrier effect and enhance the resistance to abrasion. The characterization of the materials is currently underway and is expected to be completed in the first months of 2022. In parallel, the study of high-performance coatings used for the first time in the field of magnesium alloys is underway. These coatings, widely used on high performance steels, have the purpose of significantly increase the hardness of the underlying alloy (tungsten carbide) and improving corrosion resistance (aluminum bronze). The coatings are deposited exploiting the high-velocity oxygen fuel (HVOF) method in which the metal alloy particles are sprayed from a high-speed torch onto the substrate alloy, sintering on contact and forming a dense and compact coating. Also in this case, the characterization of the specimens is currently underway and the first characterization phase is expected to be completed in the early months of 2022. However, XRPD measurements *in situ* have already been carried out on the HVOF coated specimens for the evaluation of the homogeneity of the coating. The data, collected by mapping the surface during a *in situ* experiments, were processed by RootProf, resulting in information on the convex shape of the sample, deformed by the torch. The results, made easily interpretable by the multivariate analysis, were reported in this thesis as the application

of multivariate methods in the presence of spatial gradients.

Finally, in Chapter 11, a third example of multivariate analysis combined with the *in situ* study of materials is reported. This experiment transfers the expertise acquired on single crystal to the world of powder diffraction. A paper concerning multivariate analysis applied to in situ experiments under variable temperature conditions has been published in Crystals (MDPI)[34]. The work, concerning the adsorption of CO2 and Xe inside a Y zeolite, laid the foundations for the study of evolutive processes with multivariate analysis. Eutectic mixtures, both traditional and newly developed (Deep Eutectic Solvent - DES), were studied by *in situ* XRPD experiments under variable temperature conditions (thermal gradient) to monitor crystallization and melting of samples. The instrumental setup, optimized by the author of this thesis, made it possible to quickly and easily study samples of eutectic mixtures for the identification of the crystallization temperature in a DSC-like approach. The importance of this type of experiments is that thermodynamic quantities are not used to monitor the phase transition, but only structural information is exploited, allowing a further understanding of the system being analyzed and giving the possibility of recognizing the formation of polymorphs. Further studies exploiting this setup and the methodologies presented will be carried out in the short term in collaboration with the University of Turin on DES.

Bibliography

[1] S. Agostinelli et al. «Geant4—a simulation toolkit.» In: *Nuclear Instruments and Methods in Physics Research Section A: Accelerators, Spectrometers, Detectors and Associated Equipment* 506.3 (July 2003), pp. 250–303. DOI: 10.1016/s0168-9002(03)01368-8. URL: https://doi.org/10.1016/s0168-9002(03)01368-8.

[2] J. Allison et al. «Geant4 developments and applications.» In: *IEEE Transactions on Nuclear Science* 53.1 (Feb. 2006), pp. 270–278. DOI: 10.1109/tns.2006.869826. URL: https://doi.org/10.1109/tns.2006.869826.

[3] J. Allison et al. «Recent developments in Geant4.» In: *Nuclear Instruments and Methods in Physics Research Section A: Accelerators, Spectrometers, Detectors and Associated Equipment* 835 (2016), pp. 186–225. DOI: 10.1016/j.nima.2016.06.125. URL: https://doi.org/10.1016/j.nima.2016.06.125.

[4] G. Box, J. Hunter, and W. Hunter. *Statistics for Experimenters: Design, Innovation, and Discovery*. Wiley Series in Probability and Statistics. Wiley, 2005. ISBN: 9780471718130.

[5] D. Cox and N. Reid. *The Theory of the Design of Experiments*. Chapman & Hall/CRC Monographs on Statistics & Applied Probability. CRC Press, 2000. ISBN: 9781420035834.

[6] I. Jolliffe. «Principal component analysis.» In: *Encyclopedia of statistics in behavioral science* (2005).

[7]   P. Guccione et al. «Multivariate Analysis Applications in X-ray Diffraction.» In: *Crystals* 11.1 (Dec. 2020), p. 12. DOI: 10.3390/cryst11010012. URL: https://doi.org/10.3390/cryst11010012.

[8]   A. Savitzky and M. J. E. Golay. «Smoothing and Differentiation of Data by Simplified Least Squares Procedures.» In: 36.8 (July 1964), pp. 1627–1639. DOI: 10.1021/ac60214a047. URL: https://doi.org/10.1021/ac60214a047.

[9]   R. Caliandro and D. B. Belviso. «RootProf: software for multivariate analysis of unidimensional profiles.» In: *Journal of Applied Crystallography* 47.3 (2014), pp. 1087–1096.

[10] J. A. Cornell. *Experiments with Mixtures*. Wiley, Jan. 2002. DOI: 10.1002/9781118204221. URL: https://doi.org/10.1002/9781118204221.

[11] B. Mangolini et al. *Dataset for "XRF and XRPD data sets in ternary mixtures with high level micro-absorption and/or preferred orientations problems for phase quantification analysis".* 2021. DOI: 10.17632/JS2NZWF5MD.1. URL: https://data.mendeley.com/datasets/js2nzwf5md/1.

[12] I. C. Madsen et al. «Outcomes of the International Union of Crystallography Commission on powder diffraction round robin on quantitative phase analysis: samples 1a to 1h.» In: *Journal of Applied Crystallography* 34.4 (2001), pp. 409–426.

[13] N. V. Scarlett et al. «Outcomes of the International Union of Crystallography Commission on Powder Diffraction Round Robin on Quantitative Phase Analysis: samples 2, 3, 4, synthetic bauxite, natural granodiorite and pharmaceuticals.» In: *Journal of Applied Crystallography* 35.4 (2002), pp. 383–400.

[14] L. León-Reina et al. «Round robin on Rietveld quantitative phase analysis of Portland cements.» In: *Journal of Applied Crystallography* 42.5 (2009), pp. 906–916.

[15]   M. D. Raven and P. G. Self. «Outcomes of 12 years of the
        Reynolds Cup quantitative mineral analysis round robin.» In:
        Clays and Clay Minerals 65.2 (2017), pp. 122–134.

[16]   B. Mangolini et al. «XRF and XRPD data sets in ternary mix-
        tures with high level micro-absorption and/or preferred orien-
        tations problems for phase quantification analysis.» In: *Data
        in Brief* 36 (June 2021), p. 107043. DOI: 10.1016/j.dib.202
        1.107043. URL: https://doi.org/10.1016/j.dib.2021.10
        7043.

[17]   N. Massara et al. «IETeasy: An open source and low-cost
        instrument for impulse excitation technique, applied to ma-
        terials classification by acoustical and mechanical properties
        assessment.» In: *HardwareX* 10 (Oct. 2021), e00231. DOI: 10
        .1016/j.ohx.2021.e00231. URL: https://doi.org/10.101
        6/j.ohx.2021.e00231.

[18]   G. Roebben et al. «Impulse excitation apparatus to measure
        resonant frequencies, elastic moduli, and internal friction at
        room and high temperature.» In: *Review of Scientific Instru-
        ments* 68.12 (1997). cited By 219, pp. 4511–4515. DOI: 10.10
        63/1.1148422.

[19]   G. Roebben et al. «The innovative impulse excitation tech-
        nique for high-temperature mechanical spectroscopy.» In: *Jour-
        nal of Alloys and Compounds* 310.1-2 (Sept. 2000), pp. 284–
        287. DOI: 10.1016/s0925-8388(00)00966-x. URL: https:
        //doi.org/10.1016/s0925-8388(00)00966-x.

[20]   E. Gregorová et al. «Temperature dependence of Young's mod-
        ulus and damping of partially sintered and dense zirconia
        ceramics.» In: *Journal of the European Ceramic Society* 40.5
        (2020), pp. 2063–2071. ISSN: 0955-2219. DOI: https://doi.
        org/10.1016/j.jeurceramsoc.2019.12.064. URL: https:

//www.sciencedirect.com/science/article/pii/S09552
21919309082.

[21] M. Monìk et al. «Rock physics and the circulation of Neolithic axeheads in Central Europe and the western Mediterranean.» In: *Wear* 474-475 (2021), p. 203708. ISSN: 0043-1648. DOI: https://doi.org/10.1016/j.wear.2021.203708. URL: https://www.sciencedirect.com/science/article/pii/S0043164821000971.

[22] I.-C. Jung, D.-G. Kang, and B. C. De Cooman. «Impulse excitation internal friction study of dislocation and point defect interactions in ultra-low carbon bake-hardenable steel.» In: *Metallurgical and Materials Transactions A* 45.4 (2014), pp. 1962–1978.

[23] N. Massara et al. *Dataset for "Impulse excitation technique data set collected on different materials for data analysis methods and quality control procedures development"*. 2021. DOI: 10.17632/SRFP7X6WXM.1. URL: https://data.mendeley.com/datasets/srfp7x6wxm/1.

[24] N. Massara et al. «Impulse excitation technique data set collected on different materials for data analysis methods and quality control procedures development.» In: *Data in Brief* (2021), p. 107503. ISSN: 2352-3409. DOI: https://doi.org/10.1016/j.dib.2021.107503.

[25] V. S. Nisha and R. Joseph. «Preparation and properties of iodine-doped radiopaque natural rubber.» In: *Journal of Applied Polymer Science* 105.2 (2007), pp. 429–434. DOI: 10.1002/app.26040. URL: https://doi.org/10.1002/app.26040.

[26] M. R. Ambika, N. Nagaiah, and S. K. Suman. «Role of bismuth oxide as a reinforcer on gamma shielding ability of unsaturated polyester based polymer composites.» In: *Journal*

of Applied Polymer Science 134.13 (Nov. 2016). DOI: 10.1002 /app.44657. URL: https://doi.org/10.1002/app.44657.

[27] S. Nambiar, E. K. Osei, and J. T. W. Yeow. «Polymer nanocomposite-based shielding against diagnostic X-rays.» In: *Journal of Applied Polymer Science* 127.6 (June 2012), pp. 4939–4946. DOI: 10.1002/app.37980. URL: https://doi.org/10.1002 /app.37980.

[28] S. Suman et al. «Development of highly radiopaque flexible polymer composites for X-ray imaging applications and copolymer architecture-morphology-property correlations.» In: *European Polymer Journal* 95 (Oct. 2017), pp. 41–55. DOI: 10.1016/j.eurpolymj.2017.07.021. URL: https://doi. org/10.1016/j.eurpolymj.2017.07.021.

[29] M. Lopresti et al. «Light Weight, Easy Formable and Non-Toxic Polymer-Based Composites for Hard X-ray Shielding: A Theoretical and Experimental Study.» In: *International Journal of Molecular Sciences* 21.3 (Jan. 2020), p. 833. DOI: 10.3390 /ijms21030833. URL: https://doi.org/10.3390/ijms2103 0833.

[30] E. Conterosito et al. «Facile preparation methods of hydrotalcite layered materials and their structural characterization by combined techniques.» In: *Inorganica Chimica Acta* 470 (Jan. 2018), pp. 36–50. DOI: 10.1016/j.ica.2017.08.007. URL: https://doi.org/10.1016/j.ica.2017.08.007.

[31] V. Toson et al. «Facile Intercalation of Organic Molecules into Hydrotalcites by Liquid-Assisted Grinding: Yield Optimization by a Chemometric Approach.» In: 15.11 (Oct. 2015), pp. 5368–5374. DOI: 10.1021/acs.cgd.5b00968. URL: https://doi.org/10.1021/acs.cgd.5b00968.

[32] M. Lopresti et al. «Epoxy resins composites for X-ray shielding materials additivated by coated barium sulfate with improved

dispersibility.» In: *Materials Today Communications* 26 (Mar. 2021), p. 101888. DOI: 10.1016/j.mtcomm.2020.101888. URL: https://doi.org/10.1016/j.mtcomm.2020.101888.

[33] B. Mangolini et al. «Low-Cost Biobased Coatings for AM60 Magnesium Alloys for Food Contact and Harsh Environment Applications.» In: *International Journal of Molecular Sciences* 22.9 (May 2021), p. 4915. DOI: 10.3390/ijms22094915. URL: https://doi.org/10.3390/ijms22094915.

[34] E. Conterosito, M. Lopresti, and L. Palin. «In Situ X-ray Diffraction Study of Xe and CO2 Adsorption in Y Zeolite: Comparison between Rietveld and PCA-Based Analysis.» In: 10.6 (June 2020), p. 483. DOI: 10.3390/cryst10060483. URL: https://doi.org/10.3390/cryst10060483.

Complete Bibliography

[1] U. E. 1186-1:2003. *Materials and Articles in Contact with Foodstuffs-Plastics-Test Methods for Overall Migration into Aqueous Food Simulants by Total Immersion.* Available online, 2003. URL: http://store.uni.com/catalogo/uni-en-1186-1-2003.

[2] U. E. 1186-3:2003. *Materials and Articles in Contact with Foodstuffs-Plastics-Guide to the Selection of Conditions and Test Methods for Overall Migration.* Available online, 2003. URL: http://store.uni.com/catalogo/uni-en-1186-3-2003.

[3] M. Aceto and E. Calà. «Analytical evidences of the use of iron-gall ink as a pigment on miniature paintings.» In: *Spectrochimica Acta Part A: Molecular and Biomolecular Spectroscopy* 187 (Dec. 2017), pp. 1–8. DOI: 10.1016/j.saa.2017.06.017. URL: https://doi.org/10.1016/j.saa.2017.06.017.

[4] M. Aceto et al. «New evidence of non-traditional Egyptian blue manufacture in the 6th century Ashburnham Pentateuch.» In: *Journal of Archaeological Science: Reports* 33 (Oct. 2020), p. 102487. DOI: 10.1016/j.jasrep.2020.102487. URL: https://doi.org/10.1016/j.jasrep.2020.102487.

[5] S. Agostinelli et al. «Geant4—a simulation toolkit.» In: *Nuclear Instruments and Methods in Physics Research Section A: Accelerators, Spectrometers, Detectors and Associated Equipment* 506.3 (July 2003), pp. 250–303. DOI: 10.1016/s0168-9002(03)01368-8. URL: https://doi.org/10.1016/s0168-9002(03)01368-8.

[6]   G. Agostini et al. «In Situ XAS and XRPD Parametric Rietveld
        Refinement To Understand Dealumination of Y Zeolite Cata-
        lyst.» In: 132.2 (Dec. 2009), pp. 667–678. DOI: 10.1021/ja9
        07696h. URL: https://doi.org/10.1021/ja907696h.

[7]   A. Ahmad and K. Al-Bashaireh. «Provenance Determination
        and Condition Assessment of Archaeological Marble Statues
        from Gerasa Using Non-Destructive Ultrasonic Technique.»
        In: *Studies in Conservation* 66.7 (Dec. 2020), pp. 397–412. DOI:
        10.1080/00393630.2020.1848268. URL: https://doi.org/
        10.1080/00393630.2020.1848268.

[8]   J. Alex et al. «Effect of Sodium on Microstructures and Ther-
        moelastic Properties of Calcium Aluminate Cement-Bonded
        Refractories.» In: *Journal of the American Ceramic Society* 99.3
        (2016), pp. 1079–1085. DOI: https://doi.org/10.1111
        /jace.14046. eprint: https://ceramics.onlinelibrary.
        wiley.com/doi/pdf/10.1111/jace.14046. URL: https:
        //ceramics.onlinelibrary.wiley.com/doi/abs/10.1111
        /jace.14046.

[9]   E. Alizadeh et al. «Measuring systematic changes in invasive
        cancer cell shape using Zernike moments.» In: 8.11 (2016),
        pp. 1183–1193. DOI: 10.1039/c6ib00100a. URL: https:
        //doi.org/10.1039/c6ib00100a.

[10]   J. Allison et al. «Geant4 developments and applications.» In:
        IEEE Transactions on Nuclear Science 53.1 (Feb. 2006), pp. 270–
        278. DOI: 10.1109/tns.2006.869826. URL: https://doi.
        org/10.1109/tns.2006.869826.

[11]   J. Allison et al. «Recent developments in Geant4.» In: *Nuclear
        Instruments and Methods in Physics Research Section A: Accel-
        erators, Spectrometers, Detectors and Associated Equipment* 835
        (2016), pp. 186–225. DOI: 10.1016/j.nima.2016.06.125.
        URL: https://doi.org/10.1016/j.nima.2016.06.125.

[12]   M. R. Ambika, N. Nagaiah, and S. K. Suman. «Role of bismuth oxide as a reinforcer on gamma shielding ability of unsaturated polyester based polymer composites.» In: *Journal of Applied Polymer Science* 134.13 (Nov. 2016). DOI: 10.1002/app.44657. URL: https://doi.org/10.1002/app.44657.

[13]   I. Amenabar, F. Lopez, and A. Mendikute. «In Introductory Review to THz Non-Destructive Testing of Composite Mater.» In: *Journal of Infrared, Millimeter, and Terahertz Waves* 34.2 (Nov. 2012), pp. 152–169. DOI: 10.1007/s10762-012-9949-z. URL: https://doi.org/10.1007/s10762-012-9949-z.

[14]   J. Aragón et al. «Development and characterization of a novel bioresorbable and bioactive biomaterial based on polyvinyl acetate, calcium carbonate and coralline hydroxyapatite.» In: 14.1 (Mar. 2011), pp. 25–30. DOI: 10.1590/s1516-14392011005000012. URL: https://doi.org/10.1590/s1516-14392011005000012.

[15]   C. Artho, K. Havelund, and A. Biere. *High-Level Data Races*. 2003. URL: citeseer.ist.psu.edu/artho03highlevel.html.

[16]   G. Artioli et al. «Correction: Long-distance connections in the Copper Age: New evidence from the Alpine Iceman's copper axe.» In: 12.12 (Dec. 2017), e0189561. DOI: 10.1371/journal.pone.0189561. URL: https://doi.org/10.1371/journal.pone.0189561.

[17]   E. Bagli et al. «Allowing for crystalline structure effects in Geant4.» In: *Nuclear Instruments and Methods in Physics Research Section B: Beam Interactions with Materials and Atoms* 402 (July 2017), pp. 304–307. DOI: 10.1016/j.nimb.2017.03.092. URL: https://doi.org/10.1016/j.nimb.2017.03.092.

[18] A. Bagulya et al. «Recent progress of GEANT4 electromagnetic physics for LHC and other applications.» In: *Journal of Physics: Conference Series* 898 (2017), p. 042032. DOI: 10.108 8/1742-6596/898/4/042032. URL: https://doi.org/10.1 088/1742-6596/898/4/042032.

[19] D. Ballabio and V. Consonni. «Classification tools in chemistry. Part 1: linear models. PLS-DA.» In: *Analytical Methods* 5.16 (2013), p. 3790. DOI: 10.1039/c3ay40582f. URL: https://doi.org/10.1039/c3ay40582f.

[20] R. H. Baney et al. «Silsesquioxanes.» In: 95.5 (July 1995), pp. 1409–1430. DOI: 10.1021/cr00037a012. URL: https://doi.org/10.1021/cr00037a012.

[21] G. Bartal, A. M. Sailer, and E. Vano. «Should We Keep the Lead in the Aprons?» In: 21.1 (Mar. 2018), pp. 2–6. DOI: 10.1053/j.tvir.2017.12.002. URL: https://doi.org/10.1053/j.tvir.2017.12.002.

[22] L. Beck et al. «First use of portable system coupling X-ray diffraction and X-ray fluorescence for in-situ analysis of prehistoric rock art.» In: *Talanta* 129 (2014), pp. 459–464. ISSN: 0039-9140. DOI: https://doi.org/10.1016/j.talanta.2014.04.043.

[23] B. Beckhoff et al. *Handbook of practical X-ray fluorescence analysis*. Springer Science & Business Media, 2007.

[24] R. Behling. *Modern diagnostic x-ray sources: technology, manufacturing, reliability*. CRC Press, 2021.

[25] M. Bhat. «Non-destructive evaluation of defects and damage in composite materials and structures.» In: *Journal of the Indian Institute of Science* 93.4 (2013). cited By 0, pp. 751–766.

[26] S. J. L. Billinge. «The rise of the X-ray atomic pair distribution function method: a series of fortunate events.» In: 377.2147 (Apr. 2019), p. 20180413. DOI: 10.1098/rsta.2018.0413. URL: https://doi.org/10.1098/rsta.2018.0413.

[27] E. Boccaleri et al. «In situsimultaneous Raman/high-resolution X-ray powder diffraction study of transformations occurring in materials at non-ambient conditions.» In: 40.4 (July 2007), pp. 684–693. DOI: 10.1107/s0021889807025113. URL: https://doi.org/10.1107/s0021889807025113.

[28] P. Borg et al. «Example of industrial valorisation of derivative products of Castor oil.» In: *Oléagineux, Corps gras, Lipides* 16.4-5-6 (July 2009), pp. 211–214. DOI: 10.1051/ocl.2009.0276. URL: https://doi.org/10.1051/ocl.2009.0276.

[29] M. Bortolotti, L. Lutterotti, and G. Pepponi. «Combining XRD and XRF analysis in one Rietveld-like fitting.» In: *Powder Diffraction* 32 (2017), pp. 225–230. DOI: 10.1017/S0885715617000276.

[30] A. Bottcher. *Toeplitz matrices, asymptotic linear algebra, and functional analysis.* Basel, Switzerland Boston: Birkhauser, 2000. ISBN: 978-3-0348-8395-5.

[31] G. Box, J. Hunter, and W. Hunter. *Statistics for Experimenters: Design, Innovation, and Discovery.* Wiley Series in Probability and Statistics. Wiley, 2005. ISBN: 9780471718130.

[32] H. Boyle and R. M. Strudwick. «"Do lead rubber aprons pose an infection risk?"» In: 16.4 (Nov. 2010), pp. 297–303. DOI: 10.1016/j.radi.2010.03.002. URL: https://doi.org/10.1016/j.radi.2010.03.002.

[33] R. Brun and F. Rademakers. «ROOT — An object oriented data analysis framework.» In: 389.1-2 (Apr. 1997), pp. 81–86. DOI: 10.1016/s0168-9002(97)00048-x. URL: https://doi.org/10.1016/s0168-9002(97)00048-x.

[34] R. Brun et al. *root-project/root: v6.18/02*. 2019. DOI: 10.5281 /ZENODO.3895860. URL: https://zenodo.org/record/3895 860.

[35] D. Bull et al. «A comparison of multi-scale 3D X-ray tomographic inspection techniques for assessing carbon fibre composite impact damage.» In: 75 (Feb. 2013), pp. 55–61. DOI: 10.1016/j.compscitech.2012.12.006. URL: https://doi. org/10.1016/j.compscitech.2012.12.006.

[36] R. Caliandro. *RootProf - An interactive, general purpose tool for processing unidimensional profiles with specific applications to diffraction and spectroscopic measurements*. 2020. URL: https: //users.ba.cnr.it/ic/crisrc25/RootProf/RootProf%5 C_help.html.

[37] R. Caliandro and D. B. Belviso. «RootProf: software for multivariate analysis of unidimensional profiles.» In: *Journal of Applied Crystallography* 47.3 (2014), pp. 1087–1096.

[38] R. Caliandro et al. «New Hints on the Maya Blue Formation Process by PCA-Assisted In Situ XRPD/PDF and Optical Spectroscopy.» In: *Chemistry – A European Journal* 25.49 (2019), pp. 11503–11511. DOI: https://doi.org/10.1002/chem.20 1901932.

[39] W. Callister and D. Rethwisch. *Materials Science and Engineering*. Wiley, 2014. ISBN: 9781118507070. URL: https: //books.google.it/books?id=8ixEDwAAQBAJ.

[40] Z. Cao et al. «Chemical surface modification of calcium carbonate particles with stearic acid using different treating methods.» In: 378 (Aug. 2016), pp. 320–329. DOI: 10.1016/j. apsusc.2016.03.205. URL: https://doi.org/10.1016 /j.apsusc.2016.03.205.

[41] L. Cartz. *Nondestructive Testing: Radiography, Ultrasonics, Liquid Penetrant, Magnetic Particle, Eddy Current*. ASM International, 1995. ISBN: 9780871705174.

[42] V. Cnudde and M. Boone. «High-resolution X-ray computed tomography in geosciences: A review of the current technology and applications.» In: *Earth-Science Reviews* 123 (Aug. 2013), pp. 1–17. DOI: 10.1016/j.earscirev.2013.04.003. URL: https://doi.org/10.1016/j.earscirev.2013.04.00 3.

[43] E. Confino. «The use of radiography in reproductive medicine.» In: *Infertility and Reproductive Medicine Clinics of North America* 14.2 (2003). cited By 0, pp. 227–240.

[44] E. Conterosito, M. Lopresti, and L. Palin. «In Situ X-ray Diffraction Study of Xe and CO2 Adsorption in Y Zeolite: Comparison between Rietveld and PCA-Based Analysis.» In: 10.6 (June 2020), p. 483. DOI: 10.3390/cryst10060483. URL: https://doi.org/10.3390/cryst10060483.

[45] E. Conterosito et al. «Facile preparation methods of hydrotalcite layered materials and their structural characterization by combined techniques.» In: *Inorganica Chimica Acta* 470 (Jan. 2018), pp. 36–50. DOI: 10.1016/j.ica.2017.08.007. URL: https://doi.org/10.1016/j.ica.2017.08.007.

[46] E. Conterosito et al. «High-Throughput Preparation of New Photoactive Nanocomposites.» In: 9.11 (May 2016), pp. 1279–1289. DOI: 10.1002/cssc.201600325. URL: https://doi.org/10.1002/cssc.201600325.

[47] J. Cornell. *Experiments with Mixtures: Designs, Models, and the Analysis of Mixture Data*. Wiley Series in Probability and Statistics. Wiley, 2011. ISBN: 9781118150498.

[48]   J. A. Cornell. *Experiments with Mixtures*. Wiley, Jan. 2002.
        DOI: 10.1002/9781118204221. URL: https://doi.org/10
        .1002/9781118204221.

[49]   D. Cox and N. Reid. *The Theory of the Design of Experiments*.
        Chapman & Hall/CRC Monographs on Statistics & Applied
        Probability. CRC Press, 2000. ISBN: 9781420035834.

[50]   J. W. Criss and L. S. Birks. «Calculation methods for fluo-
        rescent x-ray spectrometry. Empirical coefficients versus fun-
        damental parameters.» In: *Analytical Chemistry* 40.7 (1968),
        pp. 1080–1086. DOI: 10.1021/ac60263a023.

[51]   P. Diaconis, S. Goel, and S. Holmes. «Horseshoes in multidi-
        mensional scaling and local kernel methods.» In: *Ann. Appl.
        Stat.* 2.3 (2008), pp. 777–807. DOI: 10.1214/08-AOAS165.
        URL: https://doi.org/10.1214/08-AOAS165.

[52]   R. Dinnebier, S. Billinge, and R. S. of Chemistry (Great Britain).
        Powder Diffraction: Theory and Practice. Royal Society of Chem-
        istry, 2008. ISBN: 9780854042319. URL: https://books.
        google.it/books?id=wmQ%5C_lFIMkFYC.

[53]   R. E. Dinnebier, A. Leineweber, and J. S. Evans. *Rietveld refine-
        ment: practical powder diffraction pattern analysis using TOPAS*.
        Walter de Gruyter GmbH & Co KG, 2018.

[54]   K. Eguchi, T. Yamada, and M. Kaneko. «Coronet status of dig-
        ital radiography in chest medicine.» In: *Nihon Kyōbu Shikkan
        Gakkai zasshi* 30 Suppl (1992). cited By 0, pp. 233–239.

[55]   M. Esmaily et al. «Fundamentals and advances in magne-
        sium alloy corrosion.» In: *Progress in Materials Science* 89 (Aug.
        2017), pp. 92–193. DOI: 10.1016/j.pmatsci.2017.04.011.
        URL: https://doi.org/10.1016/j.pmatsci.2017.04.011.

[56]   L. Euler. «De motu vibratorio laminarum elasticarum, ubi plures novae vibrationum species hactenus non pertractatae evolvuntur.» In: *Novi Commentarii academiae scientiarum Petropolitanae* (1773).

[57]   *Eutectic system.* 2021. URL: https://en.wikipedia.org/wiki/Eutectic_system.

[58]   R. Feynman. *The Feynman lectures on physics.* Redwood City, Calif: Addison-Wesley, 1989. ISBN: 978-0-201-02115-8.

[59]   K. Fukunaga. *Introduction to statistical pattern recognition.* Elsevier, 2013.

[60]   D. Gastaldi et al. «In situ tomographic investigation on the early hydration behaviors of cementing systems.» In: 29 (Apr. 2012), pp. 284–290. DOI: 10.1016/j.conbuildmat.2011.10.016. URL: https://doi.org/10.1016/j.conbuildmat.2011.10.016.

[61]   H. S. Geddes et al. «Extracting interface correlations from the pair distribution function of composite materials.» In: *Nanoscale* 13.31 (2021), pp. 13220–13224. DOI: 10.1039/d1nr01922h. URL: https://doi.org/10.1039/d1nr01922h.

[62]   H. S. Geddes et al. «Structural characterisation of amorphous solid dispersions via metropolis matrix factorisation of pair distribution function data.» In: *Chemical Communications* 55.89 (2019), pp. 13346–13349. DOI: 10.1039/c9cc06753a. URL: https://doi.org/10.1039/c9cc06753a.

[63]   C. Giacovazzo et al. *Fundamentals of Crystallography.* IUCr texts on crystallography. Oxford University Press, 2002. ISBN: 9780198509585.

[64]   A. M. Goodpaster and M. A. Kennedy. «Quantification and statistical significance analysis of group separation in NMR-based metabonomics studies.» In: 109.2 (Dec. 2011), pp. 162–

170. DOI: 10.1016/j.chemolab.2011.08.009. URL: https://doi.org/10.1016/j.chemolab.2011.08.009.

[65]   E. Gregorová et al. «Temperature dependence of Young's modulus and damping of partially sintered and dense zirconia ceramics.» In: *Journal of the European Ceramic Society* 40.5 (2020), pp. 2063–2071. ISSN: 0955-2219. DOI: https://doi.org/10.1016/j.jeurceramsoc.2019.12.064. URL: https://www.sciencedirect.com/science/article/pii/S0955221919309082.

[66]   R. V. Grieken and A. Markowicz, eds. *Handbook of X-Ray Spectrometry*. CRC Press, Nov. 2001. DOI: 10.1201/9780203908709. URL: https://doi.org/10.1201/9780203908709.

[67]   P. Guccione et al. «Multivariate Analysis Applications in X-ray Diffraction.» In: *Crystals* 11.1 (Dec. 2020), p. 12. DOI: 10.3390/cryst11010012. URL: https://doi.org/10.3390/cryst11010012.

[68]   P. Guest and P. Guest. *Numerical Methods of Curve Fitting*. Cambridge University Press, 2012. ISBN: 9781107646957. URL: https://books.google.it/books?id=UjnB0FIWv%5C_AC.

[69]   F. Guthrie. «On Eutexia.» In: *Proceedings of the Physical Society of London* 6.1 (Apr. 1884), pp. 124–146. DOI: 10.1088/1478-7814/6/1/312. URL: https://doi.org/10.1088/1478-7814/6/1/312.

[70]   B. B. Hansen et al. «Deep Eutectic Solvents: A Review of Fundamentals and Applications.» In: 121.3 (Dec. 2020), pp. 1232–1285. DOI: 10.1021/acs.chemrev.0c00385. URL: https://doi.org/10.1021/acs.chemrev.0c00385.

[71]   C. Hayre, H. Bungay, and C. Jeffery. «How effective are lead-rubber aprons in protecting radiosensitive organs from secondary ionizing radiation?» In: 26.4 (Nov. 2020), e264–e269.

DOI: 10.1016/j.radi.2020.03.013. URL: https://doi.org/10.1016/j.radi.2020.03.013.

[72] S. Hellberg et al. «The Prediction of Bradykinin Potentiating Potency of Pentapeptides. An Example of a Peptide Quantitative Structure-activity Relationship.» In: *Acta Chemica Scandinavica* 40b (1986), pp. 135–140. DOI: 10.3891/acta.chem.scand.40b-0135. URL: https://doi.org/10.3891/acta.chem.scand.40b-0135.

[73] C. Hellier. *Handbook of Nondestructive Evaluation, 3E.* McGraw-Hill Education, 2020. ISBN: 9781260441444.

[74] F. A. Herzog. «The Potential of a Portable EDXRF Spectrometer for Gemmology.» In: *The Journal of Gemmology* 34.5 (2015), pp. 404–418. DOI: 10.15506/jog.2015.34.5.404. URL: https://doi.org/10.15506/jog.2015.34.5.404.

[75] E. Hille. *Analytic function theory, Volume I.* Vol. 269. American Mathematical Soc., 2012.

[76] N. Hiremath et al. «Low cost textile-grade carbon-fiber epoxy composites for automotive and wind energy applications.» In: 198 (Oct. 2020), p. 108156. DOI: 10.1016/j.compositesb.2020.108156. URL: https://doi.org/10.1016/j.compositesb.2020.108156.

[77] H. Honigsberg et al. «Health Care Workers' Use and Cleaning of X-Ray Aprons and Thyroid Shields.» In: 106.6 (Dec. 2017), pp. 534–546. DOI: 10.1016/j.aorn.2017.10.002. URL: https://doi.org/10.1016/j.aorn.2017.10.002.

[78] H. Hotelling. «Analysis of a complex of statistical variables into principal components.» In: *Journal of Educational Psychology* 24.6 (1933), pp. 417–441. DOI: 10.1037/h0071325. URL: https://doi.org/10.1037/h0071325.

[79]   K. R. Houston et al. «Iodinated polyesters as a versatile plat-
        form for radiopaque biomaterials.» In: *Journal of Polymer Sci-
        ence Part A: Polymer Chemistry* 55.13 (May 2017), pp. 2171–
        2177. DOI: 10.1002/pola.28596. URL: https://doi.org/1
        0.1002/pola.28596.

[80]   J. Hu et al. «Stearic acid-coated superhydrophobic Fe2O3/Fe3O4
        composite film on N80 steel for corrosion protection.» In: 359
        (Feb. 2019), pp. 47–54. DOI: 10.1016/j.surfcoat.2018.12
        .040. URL: https://doi.org/10.1016/j.surfcoat.2018.1
        2.040.

[81]   W. Huda et al. «Optimizing the x-ray photon energy for dig-
        ital radiographic imaging systems.» In: ed. by L. E. Antonuk
        and M. J. Yaffe. SPIE, May 2002. DOI: 10.1117/12.465608.
        URL: https://doi.org/10.1117/12.465608.

[82]   F. James. «MINUIT Function Minimization and Error Analy-
        sis: Reference Manual Version 94.1.» In: (1994).

[83]   I. Jolliffe. «Principal component analysis.» In: *Encyclopedia of
        statistics in behavioral science* (2005).

[84]   A. de Juan, J. Jaumot, and R. Tauler. «Multivariate Curve
        Resolution (MCR). Solving the mixture analysis problem.» In:
        Anal. Methods 6.14 (2014), pp. 4964–4976. DOI: 10.1039/c4
        ay00571f. URL: https://doi.org/10.1039/c4ay00571f.

[85]   I.-C. Jung, D.-G. Kang, and B. C. De Cooman. «Impulse exci-
        tation internal friction study of dislocation and point defect
        interactions in ultra-low carbon bake-hardenable steel.» In:
        Metallurgical and Materials Transactions A 45.4 (2014), pp. 1962–
        1978.

[86]   F. Karavassili et al. «In Quest for Improved Drugs against
        Diabetes: The Added Value of X-ray Powder Diffraction Meth-
        ods.» In: 7.4 (Aug. 2017), p. 63. DOI: 10.3390/biom7030063.
        URL: https://doi.org/10.3390/biom7030063.

[87]   M. Kazempour et al. «Assessment of the radiation attenua-
        tion properties of several lead free composites by Monte Carlo
        simulation.» In: *Journal of biomedical physics & engineering* 5.2
        (2015), p. 67.

[88]   D. A. Keen. «Total scattering and the pair distribution func-
        tion in crystallography.» In: 26.3 (July 2020), pp. 143–201.
        DOI: 10.1080/0889311x.2020.1797708. URL: https://doi.
        org/10.1080/0889311x.2020.1797708.

[89]   K. Kim and W. R. Wagner. «Non-invasive and Non-destructive
        Characterization of Tissue Engineered Constructs Using Ul-
        trasound Imaging Technologies: A Review.» In: *Annals of
        Biomedical Engineering* 44.3 (Oct. 2015), pp. 621–635. DOI:
        10.1007/s10439-015-1495-0. URL: https://doi.org/10
        .1007/s10439-015-1495-0.

[90]   T. Kittelmann and M. Boin. «Polycrystalline neutron scatter-
        ing for Geant4: NXSG4.» In: *Computer Physics Communica-
        tions* 189 (Apr. 2015), pp. 114–118. DOI: 10.1016/j.cpc.20
        14.11.009. URL: https://doi.org/10.1016/j.cpc.2014.1
        1.009.

[91]   M. Koecher and A. Krieg. *Ebene Geometrie*. Springer-Verlag,
        2007.

[92]   S.-W. Kuo and F.-C. Chang. «POSS related polymer nanocom-
        posites.» In: 36.12 (Dec. 2011), pp. 1649–1696. DOI: 10.1016
        /j.progpolymsci.2011.05.002. URL: https://doi.org/10
        .1016/j.progpolymsci.2011.05.002.

[93]   J. Lambert et al. «3D damage characterisation and the role of
        voids in the fatigue of wind turbine blade materials.» In: 72.2
        (2012), pp. 337–343. DOI: 10.1016/j.compscitech.2011.1
        1.023. URL: https://doi.org/10.1016/j.compscitech.20
        11.11.023.

[94]   C. K. Larive and J. V. Sweedler. «Celebrating the 75th Anniversary of the ACS Division of Analytical Chemistry: A Special Collection of the Most Highly Cited Analytical Chemistry Papers Published between 1938 and 2012.» In: 85.9 (May 2013), pp. 4201–4202. DOI: 10.1021/ac401048d. URL: https://doi.org/10.1021/ac401048d.

[95]   N. M. Larocca, R. B. Filho, and L. A. Pessan. «Influence of layer-by-layer deposition techniques and incorporation of layered double hydroxides (LDH) on the morphology and gas barrier properties of polyelectrolytes multilayer thin films.» In: 349 (Sept. 2018), pp. 1–12. DOI: 10.1016/j.surfcoat.2018.05.030. URL: https://doi.org/10.1016/j.surfcoat.2018.05.030.

[96]   B. Le Roux and F. Murtagh. «B. Le Roux and H. Rouanet, Geometric Data Analysis, From Correspondence Analysis to Structured Data Analysis, Dordrecht, Kluwer, 2004, pp. xi + 475.» In: *Journal of Classification* 25 (2008), pp. 137–141. DOI: 10.1007/s00357-008-9007-7.

[97]   D. D. Lee and H. S. Seung. «Learning the parts of objects by non-negative matrix factorization.» In: *Nature* 401.6755 (Oct. 1999), pp. 788–791. DOI: 10.1038/44565. URL: https://doi.org/10.1038/44565.

[98]   J. Leite et al. «Epoxy/steel fiber composites-A simple model to predict the fiber sedimentation.» In: (2009), NA–NA. DOI: 10.1002/pc.20923. URL: https://doi.org/10.1002/pc.20923.

[99]   L. León-Reina et al. «Round robin on Rietveld quantitative phase analysis of Portland cements.» In: *Journal of Applied Crystallography* 42.5 (2009), pp. 906–916.

[100] Y. Li et al. «Modeling of temperature dependent yield strength for stainless steel considering nonlinear behavior and the effect of phase transition.» In: *Construction and Building Materials* 159 (2018), pp. 147–154. ISSN: 0950-0618. DOI: https://doi.org/10.1016/j.conbuildmat.2017.10.106. URL: https://www.sciencedirect.com/science/article/pii/S095006181732161X.

[101] M. Lopresti et al. «Epoxy resins composites for X-ray shielding materials additivated by coated barium sulfate with improved dispersibility.» In: *Materials Today Communications* 26 (Mar. 2021), p. 101888. DOI: 10.1016/j.mtcomm.2020.101888. URL: https://doi.org/10.1016/j.mtcomm.2020.101888.

[102] M. Lopresti et al. «Light Weight, Easy Formable and Non-Toxic Polymer-Based Composites for Hard X-ray Shielding: A Theoretical and Experimental Study.» In: *International Journal of Molecular Sciences* 21.3 (Jan. 2020), p. 833. DOI: 10.3390/ijms21030833. URL: https://doi.org/10.3390/ijms21030833.

[103] M. Lopresti et al. «Multivariate vs. traditional quantitative phase analysis of X-ray powder diffraction and fluorescence data by mixtures showing preferred orientation and microabsorption.» In: *Journal of Applied Crystallography* (2022). Submitted.

[104] J. Lord and R. Morrell. *Measurement good practice guide no. 98: elastic modulus measurement.* 2006.

[105] M. L. D. Lorenzo, A. Longo, and R. Androsch. «Polyamide 11/Poly(butylene succinate) Bio-Based Polymer Blends.» In: *Materials* 12.17 (Sept. 2019), p. 2833. DOI: 10.3390/ma12172833. URL: https://doi.org/10.3390/ma12172833.

[106] L. Luo and N. L. Pierrès. «Innovative Systems for Storage of Thermal Solar Energy in Buildings.» In: *Solar Energy Storage.*

Elsevier, 2015, pp. 27–62. DOI: 10.1016/b978-0-12-409540-3.00003-7. URL: https://doi.org/10.1016/b978-0-12-409540-3.00003-7.

[107]   L. Lutterotti et al. «Combined X-Ray diffraction and fluorescence analysis in the cultural heritage field.» In: *Microchemical Journal* 126 (Dec. 2015). DOI: 10.1016/j.microc.2015.12.031.

[108]   I. C. Madsen et al. «Outcomes of the International Union of Crystallography Commission on powder diffraction round robin on quantitative phase analysis: samples 1a to 1h.» In: *Journal of Applied Crystallography* 34.4 (2001), pp. 409–426.

[109]   J. D. Majumdar et al. «Effect of laser surface melting on corrosion and wear resistance of a commercial magnesium alloy.» In: *Materials Science and Engineering: A* 361.1-2 (Nov. 2003), pp. 119–129. DOI: 10.1016/s0921-5093(03)00519-7. URL: https://doi.org/10.1016/s0921-5093(03)00519-7.

[110]   B. Mangolini et al. *Dataset for "XRF and XRPD data sets in ternary mixtures with high level micro-absorption and/or preferred orientations problems for phase quantification analysis".* 2021. DOI: 10.17632/JS2NZWF5MD.1. URL: https://data.mendeley.com/datasets/js2nzwf5md/1.

[111]   B. Mangolini et al. «Low-Cost Biobased Coatings for AM60 Magnesium Alloys for Food Contact and Harsh Environment Applications.» In: *International Journal of Molecular Sciences* 22.9 (May 2021), p. 4915. DOI: 10.3390/ijms22094915. URL: https://doi.org/10.3390/ijms22094915.

[112]   B. Mangolini et al. «XRF and XRPD data sets in ternary mixtures with high level micro-absorption and/or preferred orientations problems for phase quantification analysis.» In: *Data in Brief* 36 (June 2021), p. 107043. DOI: 10.1016/j.dib.202

1. 107043. URL: https://doi.org/10.1016/j.dib.2021.10
7043.

[113]   D. Mannes et al. «Gemmological Investigations on Pearls and
         Emeralds using Neutron Imaging.» In: *Physics Procedia* 88
         (2017), pp. 134–139. DOI: 10.1016/j.phpro.2017.06.018.
         URL: https://doi.org/10.1016/j.phpro.2017.06.018.

[114]   T. March, S. Chapman, and R. Dendy. «Recurrence plot statis-
         tics and the effect of embedding.» In: 200.1-2 (Jan. 2005),
         pp. 171–184. DOI: 10.1016/j.physd.2004.11.002. URL:
         https://doi.org/10.1016/j.physd.2004.11.002.

[115]   A. Masini et al. «Elastic properties of multi-layered ceramic
         systems for SOCs.» In: *International Journal of Applied Ceramic
         Technology* 15.2 (2018), pp. 370–379. DOI: https://doi.
         org/10.1111/ijac.12801. eprint: https://ceramics.
         onlinelibrary.wiley.com/doi/pdf/10.1111/ijac.12801.
         URL: https://ceramics.onlinelibrary.wiley.com/doi/
         abs/10.1111/ijac.12801.

[116]   N. Massara et al. *Dataset for "Impulse excitation technique data
         set collected on different materials for data analysis methods and
         quality control procedures development"*. 2021. DOI: 10.176
         32/SRFP7X6WXM.1. URL: https://data.mendeley.com/
         datasets/srfp7x6wxm/1.

[117]   N. Massara et al. «IETeasy: An open source and low-cost
         instrument for impulse excitation technique, applied to ma-
         terials classification by acoustical and mechanical properties
         assessment.» In: *HardwareX* 10 (Oct. 2021), e00231. DOI: 10
         .1016/j.ohx.2021.e00231. URL: https://doi.org/10.101
         6/j.ohx.2021.e00231.

[118]   N. Massara et al. «Impulse excitation technique data set col-
         lected on different materials for data analysis methods and
         quality control procedures development.» In: *Data in Brief*

(2021), p. 107503. ISSN: 2352-3409. DOI: https://doi.org/10.1016/j.dib.2021.107503.

[119] J. P. McCaffrey et al. «Radiation attenuation by lead and non-lead materials used in radiation shielding garments.» In: 34.2 (Jan. 2007), pp. 530–537. DOI: 10.1118/1.2426404. URL: https://doi.org/10.1118/1.2426404.

[120] J. Q. McComb et al. «Rapid Screening of Heavy Metals and Trace Elements in Environmental Samples Using Portable X-Ray Fluorescence Spectrometer, A Comparative Study.» In: 225.12 (2014). DOI: 10.1007/s11270-014-2169-5. URL: https://doi.org/10.1007/s11270-014-2169-5.

[121] S. E. McKenney, H. J. Otero, and S. T. Fricke. «Lead Apron Inspection Using Infrared Light: A Model Validation Study.» In: 15.2 (Feb. 2018), pp. 313–318. DOI: 10.1016/j.jacr.2017.09.014. URL: https://doi.org/10.1016/j.jacr.2017.09.014.

[122] E. McMullin. In: 4.1 (Feb. 2002), pp. 13–39. DOI: 10.1007/s00016-002-8357-5. URL: https://doi.org/10.1007/s00016-002-8357-5.

[123] M. Milanesio et al. «Template Burning inside TS-1 and Fe-MFI Molecular Sieves: An in Situ XRPD Study.» In: 125.47 (Nov. 2003), pp. 14549–14558. DOI: 10.1021/ja037229+. URL: https://doi.org/10.1021/ja037229+.

[124] R. Mirji and B. Lobo. «24. Radiation shielding materials: A brief review on methods, scope and significance.» In: *National Conference on 'Advances in VLSI and Microelectronics.'In PC Jabin Science College, Huballi, India*. 2017, pp. 96–100.

[125] G. Mirone and R. Pesce. *Photo-crosslinkable multi-coating system having improved gas barrier properties*. US Patent 7,341,791. 2008.

[126] A. F. Mobius. *Der barycentrische Calcul ein neues Hülfsmittel zur analytischen Behandlung der Geometrie dargestellt und insbesondere auf die Bildung neuer Classen von Aufgaben und die Entwickelung mehrerer Eigenschaften der Kegelschnitte angewendet von August Ferdinand Mobius Professor der Astronomie zu Leipzig.* Verlag von Johann Ambrosius Barth, 1827.

[127] M. Monìk et al. «Rock physics and the circulation of Neolithic axeheads in Central Europe and the western Mediterranean.» In: *Wear* 474-475 (2021), p. 203708. ISSN: 0043-1648. DOI: https://doi.org/10.1016/j.wear.2021.203708. URL: https://www.sciencedirect.com/science/article/pii/S0043164821000971.

[128] J. T. Morton et al. «Uncovering the Horseshoe Effect in Microbial Analyses.» In: *mSystems* 2.1 (2017). Ed. by J. K. Jansson. DOI: 10.1128/mSystems.00166-16. eprint: https://msystems.asm.org/content/2/1/e00166-16.full.pdf. URL: https://msystems.asm.org/content/2/1/e00166-16.

[129] O. Moshynets et al. «Antibiofilm Activity of Polyamide 11 Modified with Thermally Stable Polymeric Biocide Polyhexamethylene Guanidine 2-Naphtalenesulfonate.» In: *International Journal of Molecular Sciences* 20.2 (Jan. 2019), p. 348. DOI: 10.3390/ijms20020348. URL: https://doi.org/10.3390/ijms20020348.

[130] S. Nambiar, E. K. Osei, and J. T. W. Yeow. «Polymer nanocomposite-based shielding against diagnostic X-rays.» In: *Journal of Applied Polymer Science* 127.6 (June 2012), pp. 4939–4946. DOI: 10.1002/app.37980. URL: https://doi.org/10.1002/app.37980.

[131]   V. S. Nisha and R. Joseph. «Preparation and properties of iodine-doped radiopaque natural rubber.» In: *Journal of Applied Polymer Science* 105.2 (2007), pp. 429–434. DOI: 10.1002/app.26040. URL: https://doi.org/10.1002/app.26040.

[132]   M. Nowacka, D. Ambrożewicz, and T. Jesionowski. «TiO2-SiO2/Ph-POSS Functional Hybrids: Preparation and Characterisation.» In: 2013 (2013), pp. 1–10. DOI: 10.1155/2013/680821. URL: https://doi.org/10.1155/2013/680821.

[133]   L. Palin et al. «Understanding the Ion Exchange Process in LDH Nanomaterials by Fast In Situ XRPD and PCA-Assisted Kinetic Analysis.» In: 2019 (Feb. 2019), pp. 1–9. DOI: 10.1155/2019/4612493. URL: https://doi.org/10.1155/2019/4612493.

[134]   L. Pandola, C. Andenna, and B. Caccia. «Validation of the Geant4 simulation of bremsstrahlung from thick targets below 3 MeV.» In: *Nuclear Instruments and Methods in Physics Research Section B: Beam Interactions with Materials and Atoms* 350 (May 2015), pp. 41–48. DOI: 10.1016/j.nimb.2015.03.033. URL: https://doi.org/10.1016/j.nimb.2015.03.033.

[135]   R. Pantola and R. Bahuguna. «Polymorphism: Quality rationalization, mitigation and authentication strategies with respect to regulatory compliances in pharmaceutical industry.» In: *Research Journal of Pharmacy and Technology* 5.10 (2012), pp. 1264–1269.

[136]   M. Parco et al. «Investigation of HVOF spraying on magnesium alloys.» In: *Surface and Coatings Technology* 201.6 (Dec. 2006), pp. 3269–3274. DOI: 10.1016/j.surfcoat.2006.06.047. URL: https://doi.org/10.1016/j.surfcoat.2006.06.047.

[137] K. Pearson. «The law of ancestral heredity.» In: *Biometrika* 2.2 (1903), pp. 211–228.

[138] M. Petrantonaki et al. «Calculating shielding requirements in diagnostic X-ray departments.» In: *The British journal of radiology* 72.854 (1999), pp. 179–185.

[139] J.-L. Pey. «Corrosion protection of pipes, fittings and component pieces of water treatment and pumping stations.» In: 44.2 (1997), pp. 94–99. DOI: 10.1108/00035599710165333.

[140] D. Piparo et al. «Expressing Parallelism with ROOT.» In: 898 (Oct. 2017), p. 072022. DOI: 10.1088/1742-6596/898/7/072022. URL: https://doi.org/10.1088/1742-6596/898/7/072022.

[141] L. V. Prandel et al. «Mineralogical analysis of clays in hardsetting soil horizons, by X-ray fluorescence and X-ray diffraction using Rietveld method.» In: *Radiation Physics and Chemistry* 95 (2014), pp. 65–68. ISSN: 0969-806X. DOI: 10.1016/j.radphyschem.2012.12.017.

[142] G. D. Profio et al. «Bioinspired Synthesis of CaCO3Superstructures through a Novel Hydrogel Composite Membranes Mineralization Platform: A Comprehensive View.» In: *Advanced Materials* 28.4 (Nov. 2015), pp. 610–616. DOI: 10.1002/adma.201504608. URL: https://doi.org/10.1002/adma.201504608.

[143] R. V. Raj, R. S. Unnithan, and G. R. Krishnan. «The characteristics study of HVOF coated AZ91D magnesium alloy with silicon carbide and stainless steel.» In: *AIP Conference Proceedings*. Vol. 2105. 1. AIP Publishing LLC. 2019, p. 020024.

[144] M. D. Raven and P. G. Self. «Outcomes of 12 years of the Reynolds Cup quantitative mineral analysis round robin.» In: *Clays and Clay Minerals* 65.2 (2017), pp. 122–134.

[145]   V. Renda et al. «A multivariate statistical approach of X-ray fluorescence characterization of a large collection of reverse glass paintings.» In: *Spectrochimica Acta Part B: Atomic Spectroscopy* 159 (Sept. 2019), p. 105655. DOI: 10.1016/j.sab.2 019.105655. URL: https://doi.org/10.1016/j.sab.2019 .105655.

[146]   M. Richetta and A. Varone. «A Focus on Dynamic Modulus: Effects of External and Internal Morphological Features.» In: *Metals* 11.1 (2021). ISSN: 2075-4701. DOI: 10.3390/met1101 0040. URL: https://www.mdpi.com/2075-4701/11/1/40.

[147]   M. S. del Rio et al. «A combined synchrotron powder diffraction and vibrational study of the thermal treatment of palygorskite–indigo to produce Maya blue.» In: 44.20 (Aug. 2009), pp. 5524–5536. DOI: 10.1007/s10853-009-3772-5. URL: https://doi.org/10.1007/s10853-009-3772-5.

[148]   J. Riordon, E. Zubritsky, and A. Newman. «Top 10 Articles.» In: 72.9 (May 2000), 324 A–329 A. DOI: 10.1021/ac002801q. URL: https://doi.org/10.1021/ac002801q.

[149]   G. Roebben et al. «The innovative impulse excitation technique for high-temperature mechanical spectroscopy.» In: *Journal of Alloys and Compounds* 310.1-2 (Sept. 2000), pp. 284–287. DOI: 10.1016/s0925-8388(00)00966-x. URL: https://doi.org/10.1016/s0925-8388(00)00966-x.

[150]   G. Roebben et al. «Impulse excitation apparatus to measure resonant frequencies, elastic moduli, and internal friction at room and high temperature.» In: *Review of Scientific Instruments* 68.12 (1997). cited By 219, pp. 4511–4515. DOI: 10.10 63/1.1148422.

[151]   R. Roelz and U. Hubbe. «A farewell to lead aprons in spine surgery.» In: (Mar. 2021). DOI: 10.1016/j.spinee.2021.03

.019. URL: https://doi.org/10.1016/j.spinee.2021.03
.019.

[152]   R. M. Rousseau. «Corrections for matrix effects in X-ray flu-
        orescence analysis—A tutorial.» In: *Spectrochimica Acta Part
        B: Atomic Spectroscopy* 61.7 (July 2006), pp. 759–777. DOI:
        10.1016/j.sab.2006.06.014. URL: https://doi.org/10.1
        016/j.sab.2006.06.014.

[153]   R. M. Rousseau. «Fundamental algorithm between concentra-
        tion and intensity in XRF analysis 1—theory.» In: *X-Ray Spec-
        trometry* 13.3 (1984), pp. 115–120. DOI: https://doi.org/1
        0.1002/xrs.1300130306.

[154]   R. M. Rousseau. «Fundamental algorithm between concentra-
        tion and intensity in XRF analysis 2—practical application.»
        In: *X-Ray Spectrometry* 13.3 (1984), pp. 121–125. DOI: https:
        //doi.org/10.1002/xrs.1300130307.

[155]   B. Roy and P. D. Roo. «Vue d'ensemble des conflits de distri-
        bution écologique en Inde.» In: n°75.2 (2019), p. 167. DOI:
        10.3917/mult.075.0167. URL: https://doi.org/10.3917
        /mult.075.0167.

[156]   P. Russo. *Handbook of X-ray imaging: physics and technology*.
        CRC press, 2017.

[157]   P. Sassatelli et al. «Properties of HVOF-sprayed Stellite-6 coat-
        ings.» In: *Surface and Coatings Technology* 338 (2018), pp. 45–
        62.

[158]   A. Savitzky and M. J. E. Golay. «Smoothing and Differenti-
        ation of Data by Simplified Least Squares Procedures.» In:
        36.8 (July 1964), pp. 1627–1639. DOI: 10.1021/ac60214a047.
        URL: https://doi.org/10.1021/ac60214a047.

[159] T. Scagliarini et al. *Quantifying high-order interdependencies on individual patterns via the local O-information: theory and applications to music analysis.* 2021. eprint: arXiv:2108.1162 5.

[160] N. V. Y. Scarlett and I. C. Madsen. «Effect of microabsorption on the determination of amorphous content via powder X-ray diffraction.» In: 33.1 (Mar. 2018), pp. 26–37. DOI: 10.1017 /s0885715618000052. URL: https://doi.org/10.1017/s08 85715618000052.

[161] N. V. Scarlett and I. Madsen. «Quantification of Phases with Partial or No Known Crystal Structures.» In: *Powder Diffraction - POWDER DIFFR* 21 (Dec. 2006). DOI: 10.1154/1.2362 855.

[162] N. V. Scarlett et al. «Outcomes of the International Union of Crystallography Commission on Powder Diffraction Round Robin on Quantitative Phase Analysis: samples 2, 3, 4, synthetic bauxite, natural granodiorite and pharmaceuticals.» In: *Journal of Applied Crystallography* 35.4 (2002), pp. 383–400.

[163] H. Scheffé. «Experiments with Mixtures.» In: *Journal of the Royal Statistical Society: Series B (Methodological)* 20.2 (July 1958), pp. 344–360. DOI: 10.1111/j.2517-6161.1958.tb00 299.x. URL: https://doi.org/10.1111/j.2517-6161.195 8.tb00299.x.

[164] H. Scheffé. «The Simplex-Centroid Design for Experiments with Mixtures.» In: *Journal of the Royal Statistical Society: Series B (Methodological)* 25.2 (July 1963), pp. 235–251. DOI: 10.1111/j.2517-6161.1963.tb00506.x. URL: https: //doi.org/10.1111/j.2517-6161.1963.tb00506.x.

[165] C. A. Schneider, W. S. Rasband, and K. W. Eliceiri. «NIH Image to ImageJ: 25 years of image analysis.» In: 9.7 (June

2012), pp. 671–675. DOI: 10.1038/nmeth.2089. URL: https://doi.org/10.1038/nmeth.2089.

[166] M. B. Seasholtz and B. Kowalski. «The parsimony principle applied to multivariate calibration.» In: *Analytica Chimica Acta* 277.2 (May 1993), pp. 165–177. DOI: 10.1016/0003-2670(93)80430-s. URL: https://doi.org/10.1016/0003-2670(93)80430-s.

[167] E. Seeram. *Computed Tomography-E-Book: Physical Principles, Clinical Applications, and Quality Control*. Elsevier Health Sciences, 2015.

[168] W. Shi, X.-F. Li, and K. Y. Lee. «Transverse vibration of free–free beams carrying two unequal end masses.» In: *International Journal of Mechanical Sciences* 90 (Jan. 2015), pp. 251–257. DOI: 10.1016/j.ijmecsci.2014.11.015. URL: https://doi.org/10.1016/j.ijmecsci.2014.11.015.

[169] D. F. Silva, V. M. D. Souza, and G. E. Batista. «Time Series Classification Using Compression Distance of Recurrence Plots.» In: IEEE, Dec. 2013. DOI: 10.1109/icdm.2013.128. URL: https://doi.org/10.1109/icdm.2013.128.

[170] J. F. da Silva, L. A. D. do Nascimento, and S. dos Santos Hoefel. «Free vibration analysis of Euler-Bernoulli beams under non-classical boundary conditions.» In: *Anais do IX Congresso Nacional de Engenharia Mecânica*. ABCM Associação Brasileira de Engenharia e Ciências Mecânicas, 2016. DOI: 10.20906/cps/con-2016-1053. URL: https://doi.org/10.20906/cps/con-2016-1053.

[171] E. L. Smith, A. P. Abbott, and K. S. Ryder. «Deep Eutectic Solvents (DESs) and Their Applications.» In: 114.21 (Oct. 2014), pp. 11060–11082. DOI: 10.1021/cr300162p. URL: https://doi.org/10.1021/cr300162p.

[172] G. Song. «Recent Progress in Corrosion and Protection of Magnesium Alloys.» In: *Advanced Engineering Materials* 7.7 (July 2005), pp. 563–586. DOI: 10.1002/adem.200500013. URL: https://doi.org/10.1002/adem.200500013.

[173] G. L. Song and A. Atrens. «Corrosion Mechanisms of Magnesium Alloys.» In: *Advanced Engineering Materials* 1.1 (Sept. 1999), pp. 11–33. DOI: 10.1002/(sici)1527–2648(199909)1:1<11::aid–adem11>3.0.co;2–n. URL: https://doi.org/10.1002/(sici)1527–2648(199909)1:1%3C11::aid-adem11%3E3.0.co;2-n.

[174] P. van der Stelt. «Improved diagnosis with digital radiography.» In: *Current opinion in dentistry* 2 (1992). cited By 10, pp. 1–6.

[175] S. Suman et al. «Development of highly radiopaque flexible polymer composites for X-ray imaging applications and copolymer architecture-morphology-property correlations.» In: *European Polymer Journal* 95 (Oct. 2017), pp. 41–55. DOI: 10.1016/j.eurpolymj.2017.07.021. URL: https://doi.org/10.1016/j.eurpolymj.2017.07.021.

[176] *Test Method for Corrosion Testing of Decorative Electrodeposited Coatings by the Corrodkote Procedure.* DOI: 10.1520/b0380–97. URL: https://doi.org/10.1520/b0380–97.

[177] D. Thickett et al. «Using non-invasive non-destructive techniques to monitor cultural heritage objects.» In: *Insight - Non-Destructive Testing and Condition Monitoring* 59.5 (May 2017), pp. 230–234. DOI: 10.1784/insi.2017.59.5.230. URL: https://doi.org/10.1784/insi.2017.59.5.230.

[178] M. L. Thomas, I. S. Butler, and J. A. Kozinski. «In situ synchrotron-based X-ray powder diffraction and micro-Raman study of biomass and residue model compounds at hydrothermal conditions.» In: *Energy Science & Engineering* 3.3 (Mar. 2015),

pp. 189–195. DOI: 10.1002/ese3.68. URL: https://doi.org/10.1002/ese3.68.

[179] S. Timoshenko. *History of Strength of Materials: With a Brief Account of the History of Theory of Elasticity and Theory of Structures*. Dover Civil and Mechanical Engineering Series. Dover Publications, 1983. ISBN: 9780486611877.

[180] F. G. Torres, S. Rodriguez, and A. C. Saavedra. «Green Composite Materials from Biopolymers Reinforced with Agroforestry Waste.» In: 27.12 (Sept. 2019), pp. 2651–2673. DOI: 10.1007/s10924-019-01561-5. URL: https://doi.org/10.1007/s10924-019-01561-5.

[181] V. Toson et al. «Facile Intercalation of Organic Molecules into Hydrotalcites by Liquid-Assisted Grinding: Yield Optimization by a Chemometric Approach.» In: 15.11 (Oct. 2015), pp. 5368–5374. DOI: 10.1021/acs.cgd.5b00968. URL: https://doi.org/10.1021/acs.cgd.5b00968.

[182] R. S. Al-Umairi et al. «COVID-19 Associated Pneumonia.» In: *Sultan Qaboos University Medical Journal [SQUMJ]* 21.1 (Mar. 2021), e4–11. DOI: 10.18295/squmj.2021.21.01.002. URL: https://doi.org/10.18295/squmj.2021.21.01.002.

[183] M. Vadrucci et al. «Analysis of Roman Imperial coins by combined PIXE, HE-PIXE and μ-XRF.» In: *Applied Radiation and Isotopes* 143 (Jan. 2019), pp. 35–40. DOI: 10.1016/j.apradiso.2018.10.016. URL: https://doi.org/10.1016/j.apradiso.2018.10.016.

[184] R. Van Grieken and A. Markowicz. *Handbook of X-ray Spectrometry*. CRC press, 2001.

[185] B. Wang et al. «Non-destructive testing and evaluation of composite materials/structures: A state-of-the-art review.» In: *Advances in Mechanical Engineering* 12.4 (Apr. 2020), p. 168781402091376.

DOI: 10.1177/1687814020913761. URL: https://doi.org/1
0.1177/1687814020913761.

[186] W. Wang et al. «Development of X-ray opaque poly(lactic acid) end-capped by triiodobenzoic acid towards non-invasive micro-CT imaging biodegradable embolic microspheres.» In: *European Polymer Journal* 108 (Nov. 2018), pp. 337–347. DOI: 10.1016/j.eurpolymj.2018.09.018. URL: https://doi.org/10.1016/j.eurpolymj.2018.09.018.

[187] P. A. Wheeler et al. «Polyhedral oligomeric silsesquioxane trisilanols as dispersants for titanium oxide nanopowder.» In: 108.4 (2008), pp. 2503–2508. DOI: 10.1002/app.27910. URL: https://doi.org/10.1002/app.27910.

[188] S. Wold, M. Sjöström, and L. Eriksson. «PLS-regression: a basic tool of chemometrics.» In: *Chemometrics and Intelligent Laboratory Systems* 58.2 (Oct. 2001), pp. 109–130. DOI: 10.1016/s0169-7439(01)00155-1. URL: https://doi.org/10.1016/s0169-7439(01)00155-1.

[189] A. Wołowicz and K. Staszak. «Study of surface properties of aqueous solutions of sodium dodecyl sulfate in the presence of hydrochloric acid and heavy metal ions.» In: 299 (Feb. 2020), p. 112170. DOI: 10.1016/j.molliq.2019.112170. URL: https://doi.org/10.1016/j.molliq.2019.112170.

[190] Y.-J. Yang et al. «Effect of sodium dodecylsulfate monomers and micelles on the stability of aqueous dispersions of titanium dioxide pigment nanoparticles against agglomeration and sedimentation.» In: 450 (July 2015), pp. 434–445. DOI: 10.1016/j.jcis.2015.02.051. URL: https://doi.org/10.1016/j.jcis.2015.02.051.

[191] L. Yu et al. «Lightweight Bismuth Titanate (Bi4Ti3O12) Nanoparticle-Epoxy Composite for Advanced Lead-Free X-ray Radiation

Shielding.» In: *ACS Applied Nano Materials* 4.7 (2021), pp. 7471–7478.

[192]   G. U. Yule. «On the Theory of Correlation.» In: *Journal of the Royal Statistical Society* 60.4 (Dec. 1897), p. 812. DOI: 10.2307/2979746. URL: https://doi.org/10.2307/2979746.

[193]   K. Zhang et al. «Electrophoretic deposition of graphene oxide on NiTi alloy for corrosion prevention.» In: *Vacuum* 161 (Mar. 2019), pp. 276–282. DOI: 10.1016/j.vacuum.2018.12.032. URL: https://doi.org/10.1016/j.vacuum.2018.12.032.

[194]   Q. Zhang et al. «Deep eutectic solvents: syntheses, properties and applications.» In: *Chemical Society Reviews* 41.21 (2012), pp. 7108–7146.

[195]   Q. Zhang et al. «Dispersion stability of functionalized MWCNT in the epoxy–amine system and its effects on mechanical and interfacial properties of carbon fiber composites.» In: 94 (Mar. 2016), pp. 392–402. DOI: 10.1016/j.matdes.2016.01.062. URL: https://doi.org/10.1016/j.matdes.2016.01.062.

[196]   X. Zhang et al. «Interfacial Microstructure and Properties of Carbon Fiber Composites Modified with Graphene Oxide.» In: 4.3 (Mar. 2012), pp. 1543–1552. DOI: 10.1021/am201757v. URL: https://doi.org/10.1021/am201757v.

Cornell transformation in R

If I wrote down everything you told me to write down, I'd have no time for punching.

Jones, J.

In Chapter 4 the workflow of the algorithm for transforming points from Euclidean space to a barycentric coordinate system was presented. At the state of the art, the code written for this algorithm allows only the projection of the points of with two coordinates in the space of a three-dimensional mixture, as in the results presented in chapter 5. This section shows a working example in R of the developed code. The installation and loading of some R libraries are necessary for the correct functioning of both the following code and the one presented in Appendix B:

```
1  library(ape)
2  library(ggplot2)
3  library(xlsx)
4  library(dplyr)
5  library(RcppArmadillo)
6  library(tidyr)
```

```
7  library(prospectr)
8  library(corrplot)
9  library(stringr)
10 library(foreach)
11 library(parallel)
12 library(doParallel)
13 library(iterators)
14 library(pls)
15 library(plsgenomics)
16 library(signal)
17 library(ptw)
18 library(dtw)
19 library(plotly)
20 library(plot3D)
```

Listing A.1: Suggested R packages

Starting from two arrays named PC1 and PC2 containing respectively the x and y coordinates of the samples projected on the score plot, this code can be run to find the projection of those points into a ternary space diagram. This procedure is based on what reported in appendix 3A of John Cornell's "Experiments with Mixtures"[48]. While in the example reported in the book the ternary mixture space, represented by a triangle, has one vertex in $(0,0)$ coordinates of the Cartesian axes, in this situation the triangle projected in the score plot can be positioned in any way and have any inclination. This leads to a translation procedure, until it has the closest vertex in the origin of the axes and then an iterated rotation until the other two vertices have defined coordinates: $(0.366, 1.366)$ and $(1.366, 0.366)$.

```
1  #### Conversion from two vectors to matrix
2  PCs <- as.matrix(data.frame(PC1, PC2))
3
4  #### Calculation of dimensionality
5  dimensionality <- ncol(PCs)
6
7  #### Range scaling function
8  range_scaling <- function(x){
9    (x-min(x))/(max(x)-min(x))
```

```r
10 }
11
12 #### Range scaling function in the space of the q components
13 q <- 1 + (1 / (1 + ((dimensionality+1)^(1/2))))
14 range_scaling_q <- function(x){
15   (x-min(x))/(max(x)-min(x))*q
16 }
17
18 #### Range scaling and centering
19 for(i in 1:dimensionality){
20 PCs[,i] <- range_scaling(PCs[,i])    #Scaling [0,1]
21 PCs[,i] <- PCs[,i] - PCs[1,i]        #Centering
22 }
23
24 #### Simplex matrix rotation
25 max_phi <- 90
26 min_phi <- -90
27 phi <- 0
28 x <- 1
29 while(abs(x) > 10^-10){
30   phi_rad <- phi * pi / 180
31   rot_vector <- c(cos(phi_rad), sin(phi_rad), -sin(phi_rad), cos(phi_
      ↪ rad))
32   rot_matrix <- matrix(as.numeric(rot_vector),ncol=dimensionality)
33   rotated_PCs_temp <- PCs%*%rot_matrix
34   cornell_PCs_temp <- range_scaling_q(rotated_PCs_temp)
35   x <- abs(cornell_PCs_temp[2,1]) - abs(cornell_PCs_temp[3,2])
36
37   if(x < 0){
38     min_phi <- phi
39     phi <- (max_phi + min_phi)/2
40   }
41
42   if(x > 0){
43     max_phi <- phi
44     phi <- (max_phi + min_phi)/2
45   }
46 }
47
48 #### Cornell scaling
```

223

```r
49 cornell_PCs <- cornell_PCs_temp
50 t_cornell_PCs <- t(cornell_PCs)
51
52 #### Rotation matrix for the q components
53 cornell_vector <- c(q, q-1, q-1, q)
54 cornell_matrix <- matrix(as.numeric(cornell_vector), ncol =
        ↪ dimensionality)
55 cornell_matrix_inverted <- solve(cornell_matrix)
56 quantitatives <- cornell_matrix_inverted\%*\%t_cornell_PCs
57
58
59 #### Range scaling and centering
60 for(i in 1:dimensionality){
61   quantitatives[i,] <- range_scaling(quantitatives[i,])
62 }
63
64 #### Calculation of the q-th component
65 nth <- dimensionality + 1
66 quantitatives <- rbind(quantitatives,1)
67 for(i in 1:dimensionality){
68   quantitatives[nth,] <- quantitatives[nth,] - quantitatives[i,]
69   }
70
71 results <- t(quantitatives)
72 results
```

Listing A.2: Cornell transformation

B

FORCEFIELD ALGORITHM

I had a lot of internal conflicts about becoming a bully. My folks always told me to do unto others at they would do to you. But then I remembered... I was stronger than most people, so they can't do unto my anything!

Starbeam, D.

In Section 4.3, Forcefield transformation was presented under the mathematical point of view. In this Appendix, a more applicative description of the transformation is given, with both *ad hoc*-built and experimental examples. To run the transformation function presented below, packages `foreach`, `parallel`, `doParallel` and `iterators` from Appendix A are required. To speed up calculations for large matrices, a small cluster using one's PC cores is suggested. For instance, the author of this thesis uses a cluster of 4 cores by giving the following command:

```
1 cl <- makeCluster(4)
2 registerDoParallel(cl)
3 on.exit(stopCluster(cl))
```

Listing B.1: Four-core cluster

Once loaded the packages, the following function can be inserted in the R project:

```r
force.field <- function(Mat){
  #Function of euclidean distances
  euc.dist <- function(P1, P2) sqrt(sum((P1 - P2) ^ 2))
  #Calculation of forcefield
  n <- nrow(Mat)
  x <- foreach(i=1:n, .combine='rbind') %:%
    foreach(j=1:n, .combine='c') %dopar% {
      cor(Mat[i,],Mat[j,]) / (euc.dist(Mat[i,],Mat[j,]))^2
    }
  #Substituting zeros and Infinite on the diagonal
  for(i in 1:n){
    for(j in 1:n){
      if(i == j){
        x[i,j] <- 1
      }
    }
  }
  return(x)
}
```

Listing B.2: Forcefield transformation function in R

B.1 Use of Forcefield transformation on data matrices of non-evolutionary samples

For this example, a $\mathbf{X}_{(n,p)}$ experimental matrix with $n = 100$ and $p = 200$ is generated and filled with random data within the range $[-1 : 1]$. The code in Listing B.2 is then used on the data matrix $\mathbf{X}_{(n,p)}$ and the Forcefield-transformed matrix $\mathbf{F}_{(n,n)}$ is obtained. Original data and the heat map representation of $\mathbf{F}_{(n,n)}$ are reported in Figures 4.4(a) and 4.4(c) respectively. The spectral decomposition is applied on $\mathbf{F}_{(n,n)}$, by using the Singular Value Decomposition (SVD) as described in the review article in Annex I. The decomposition creates a new coordinate system (orthonormal basis), which is convenient for

a simplified view of the Forcefield-transformed data. In fact, as in a PCA-like approach, only few coordinates of the new orthonormal basis can be selected for a dimensionality reduction. In this context, the projection of samples in the new space (Score matrix in PCA) and the projection of the variables (Loadings matrix in PCA) are identical, as the $\mathbf{F}_{(n,n)}$ is symmetric. The eigenvalues are all equal to 1 as the only information on the system retained after the Forcefield transformation concerns the spatial distribution of the samples. For convenience of explanation, from now on the matrix of the projection of the samples in the space of the new coordinates is called Scores matrix as in the case of the PCA. In Figure B.1, scores obtained from the matrix $\mathbf{F}_{(n,n)}$ can be observed. In Figure B.1(a), samples are projected in a three-dimensional space built by the first three eigenvectors (PCs). The data appears as a homogeneous cloud of points with no particular patterns. The heat map of the scores matrix does not suggest particular spatial patterns, as expected from uncorrelated samples.

Data collected on thirty samples of natural extracts by the means of voltammetry were analyzed with the same approach. Samples, coming from plants of different nature and origin, were dissolved in hydroalcoholic solutions and measured to observe the oxidation profiles. Obtained voltammograms, consisting in x, y profiles, were organized in matrix form and transformed into a $\mathbf{F}_{(n,n)}$ matrix. The expected result from this transformation consists in a random distribution of the samples in space, as each sample is characterized by its own electrochemical profile and no gradient is present within the samples. Although some samples are very similar to each other, there is no type of evolution in the samples (increasing concentrations, decompositions of characteristic molecules over time, ...). Consequently, the Forcefield transformation has the sole purpose of projecting the samples into a space where each point has its own position, without having any particular correlation with the others surrounding it. To better observe this effect, SVD was performed on the $\mathbf{F}_{(n,n)}$ matrix.
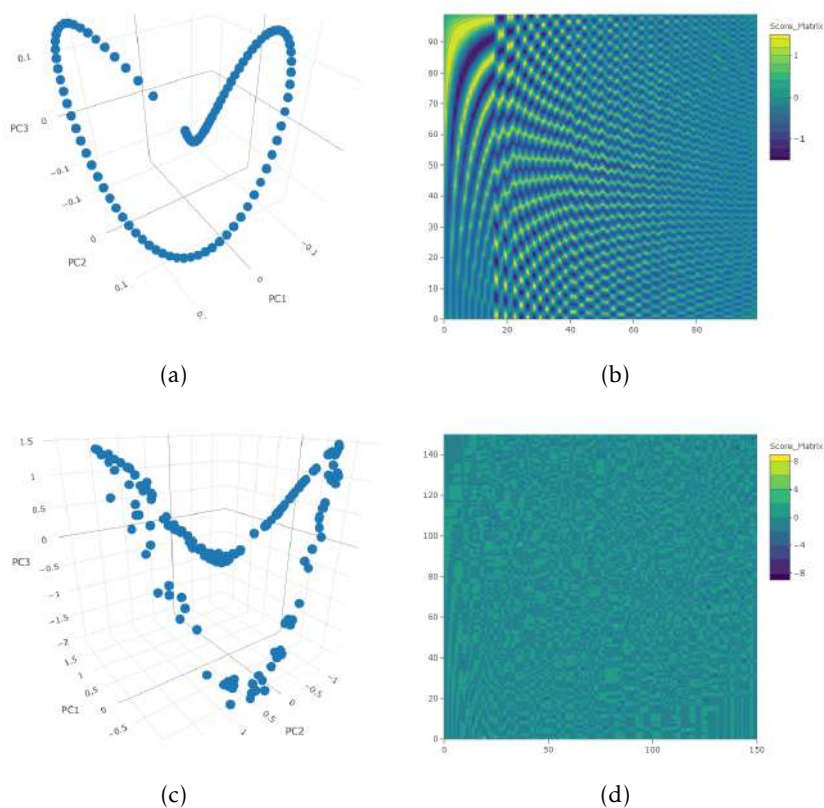
(a)

(b)

(c)

(d)
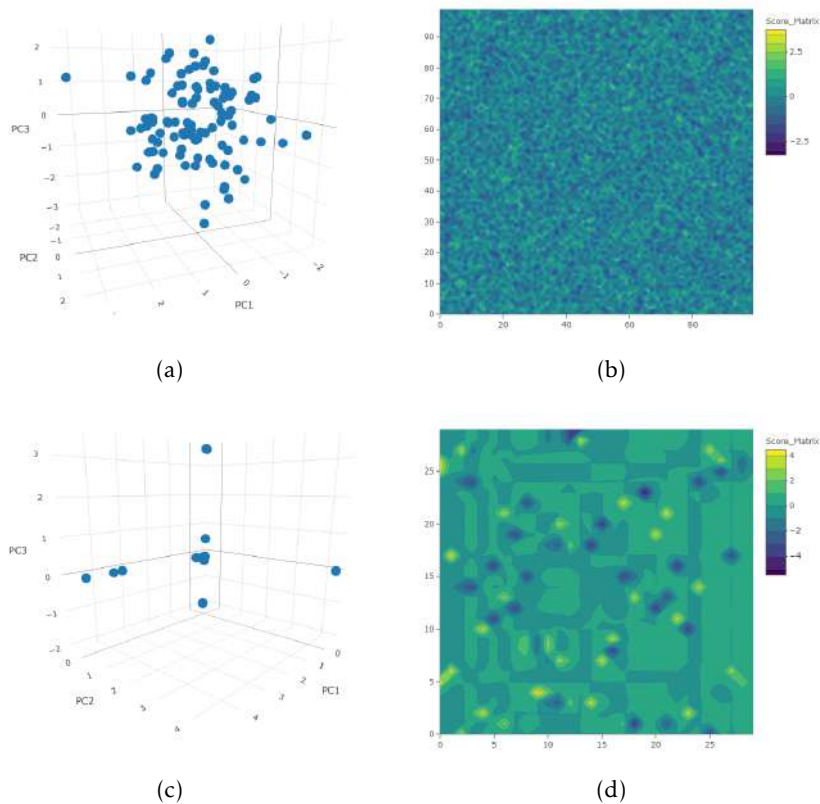
Figure B.1: Scores of uncorrelated Forcefield-transformed samples. B.1(a): samples projected in the space of the first three PCs; B.1(b): contour map of the scores matrix obtained on random samples; B.1(c): natural extracts samples projected in the space of the first three PCs; B.1(c): contour map of the scores matrix obtained on natural extracts.

Results can be observed in Figures B.1(c) and B.1(d), where data appear as distributed in clusters of points in the space (Figure B.1(a)). Samples of the cluster have no similarities of both origin, nature and content, therefore the distribution has no particular meaning. The heat map of the score matrix of Figure B.1(b) has the same random distribution of high and low values, as expected.

B.2 Use of Forcefield transformation on data matrices of evolutionary samples

A different behavior is observed when analyzing samples of evolutionary experiments. In this section, two different data sets are presented to observe the effect of Forcefield transformation on the data. The first dataset consists in a *ad hoc* created gradient, in order to give the reader a reference on samples that present a perfect evolution over time. The second dataset, on the other hand, consists in the XRPD data presented in Chapter 8, in which the presence of a temporal gradient linked to the progressive sedimentation of the dispersed barite within a mixture of monomers during the polymerization time was demonstrated.

For the first data set, a linear gradient is added to matrix $\mathbf{X}_{(n,p)}$ of the previous example along the rows of the matrix: the variables can assume higher and higher values as the sample number increases (first sample has random numbers in the range $[-1; 1]$, the second sample in the range $[-2; 2]$ and so on). The distribution of the data and the shape of the matrix $\mathbf{F}_{(n,n)}$ are reported in Figures 4.4(b) and 4.4(d) of section 4.3. Using the same procedure performed on the randomly distributed data, the matrix of the scores for evolving data is constructed. Results can be seen in Figures B.2(a) and B.2(b): samples in the three-dimensional space are organized on a perfect sequence which, observed on the PC1-PC2 score plot, would assume the typical horseshoe shape of the Guttmann effect[128].

(a)

(b)

(c)

(d)

Figure B.2: Scores of evolutive Forcefield-transformed samples. B.1(a): samples projected in the space of the first three PCs; B.1(b): contour map of the scores matrix obtained on evolutive samples; B.1(c): sedimentation XRPD patterns projected in the space of the first three PCs; B.1(c): contour map of the scores matrix obtained on sedimentation XRPD patterns.

XRPD data collected during the *in situ* experiment presented in Chapter 8, were transformed into a $\mathbf{F}_{(n,n)}$ matrix and subsequently decomposed by SVD. Samples projected in the new 3D-space, reported in Figure B.2(c), show that samples are arranged as in Figure B.2(a), albeit in a less precise way. However, the same pattern in the heat map of Figure B.2(b) is not clearly visible in the equivalent map calculated on the XRPD data, even if the left and the bottom part are very similar to the one in Figure B.2(b). This may be due to various factors, including the noise of the instrumental measurement, or to samples, which are not perfectly equidistant in space: the monitored sedimentation process is not a linear evolution over time, but of a hyperbolic form, such as shown in Figure 8.1 of Chapter 8.

Further implementations of the algorithm and its testing are currently underway. Some implementations concern the modeling of evolutionary processes starting from the results obtained from the SVD and the correlation of experiments in the presence of gradients with theoretical incremental sequences.

XRPD and XRF data sets

Fixing the church should be our top priority! I say this as a teenager, and the parent of a teenager.

Zzyzwicz, K. Sr.

The data used in Chapter 5, for the comparison between traditional methods and multivariate methods with the aim of carrying out quantitative phase analysis, were collected on specially prepared samples in order to have problems that could not be avoided in the preparation phase of the samples. These issues, which consist of preferential orientations and micro-absorption, are problems that can be found in the industrial world, can heavily affect the quality control process and still present themselves today as enormous obstacles for the traditional methods known in literature. The samples were prepared following a simplex-centroid augmented experimental design by mixing organic and inorganic phases, with each group

characterized by the presence of one or more problems for quantification. The four data sets, a collection of ten samples each, were produced by mixing barite ($BaSO_4$) and bismite (Bi_2O_3), with a third rotating substance that was chosen specifically for each data set. Barite and bismite are phases characterized by high density ($4.5\,g\,cm^{-3}$ and $8.9\,g\,cm^{-3}$ respectively), with high Z elements, therefore rich in electrons and, consequently, with higher scattering power for X-rays, but also with a high microabsorption. In data sets D1 and D2, graphite was selected as the third phase of the mixture: in the first data set only sieved graphite with a diameter of less than $90\,\mu m$ was used, in order to reduce the effect of preferential orientations, while in the second case, a 30% of larger graphite (diameter greater than $90\,\mu m$)was added to the sieved one, to introduce a greater contribution given by preferred orientations. In data set D3, zinc acetate ($C_4H_6O_4Zn$) was used as the third phase in order to have an organic compound that could be detectable by XRF due to the presence of a metal with Z greater than 11 (sodium). In this data set the main problem lies in microabsorption alone, since no effects of preferred orientation had been observed. In the last data set, D4, the third phase is urea (CH_4N_2O) which, as in the case of graphite, is invisible to XRF due to the light elements, shows preferred orientations (slighter than graphite) and has larger average particle size. The preparation of the samples and their characteristics are extensively described in a dedicated article published on Data in Brief and were made available to the scientific community in a free online repository, which was subsequently converted into an open database for data from XRPD and XRF. The database can therefore be freely used by the scientific community for benchmarking new methods for QPA. In Annex IV, the full version of the article published on Data in Brief (Elsevier) is reported [112], while the data repository can be found on Mendeley Data[110].

D

IETeasy data set

I like to cry at the ocean, because only there do my tears seem small.

Muntz, N.M.

In Chapter 6, IETeasy was presented as an open hardware tool for the acoustic analysis of materials. The instrument is very simple to use and an analysis only takes a few seconds[117]. For this reason, during Nazareno Massara's thesis project, a large variety of materials was sampled and their acoustic profiles were collected with ten repetition each. Analyzed materials were more than thirty and belonging to different classes: metal alloys, polymers, ceramics, materials of natural origin and composites.

Within the thesis work, each material was analyzed by IETeasy and all the results were presented, demonstrating measurement repeatability and sensitivity, in particular when combined with multivariate analysis.

Afterwards, a selection of materials (for which both the composition was known and there was a technical data sheet) was used to create an open database for the collection of acoustic analysis data carried

out by IET. Original audio files, acoustic data in textual format and .txt data processed with Fast Fourier Transformed were uploaded to a dedicated online repository[116], and are available to the scientific community for future uses. Such a database will be implemented with data belonging to more materials to be used for both quality control as base for machine learning.

The process of data collection and conversion has been accurately described in a specific article published in Data in Brief (Elsevier BV)[118], in which the acoustic profile characteristics of each class of materials are also described. The full version of the article is presented in Annex III of this thesis work.

MULTIVARIATE ANALYSIS
APPLICATIONS IN X-RAY DIFFRACTION

See, statements like that are why people think we're gay.

Carlson, C. Jr.

Review

Multivariate Analysis Applications in X-ray Diffraction

Pietro Guccione [1], Mattia Lopresti [2], Marco Milanesio [2] and Rocco Caliandro [3,*]

[1] Dipartimento di Ingegneria Elettrica e dell'Informazione, Politecnico di Bari, via Orabona 4, 70125 Bari, Italy; pietro.guccione@gmail.com

[2] Dipartimento di Scienze e Innovazione Tecnologica, Università del Piemonte Orientale, viale T. Michel 11, 15121 Alessandria, Italy; mattia.lopresti@uniupo.it (M.L.); marco.milanesio@uniupo.it (M.M.)

[3] Institute of Crystallography, CNR, via Amendola, 122/o, 70126 Bari, Italy

* Correspondence: rocco.caliandro@ic.cnr.it; Tel.: +39-080-592-9150

Abstract: Multivariate analysis (MA) is becoming a fundamental tool for processing in an efficient way the large amount of data collected in X-ray diffraction experiments. Multi-wedge data collections can increase the data quality in case of tiny protein crystals; in situ or operando setups allow investigating changes on powder samples occurring during repeated fast measurements; pump and probe experiments at X-ray free-electron laser (XFEL) sources supply structural characterization of fast photo-excitation processes. In all these cases, MA can facilitate the extraction of relevant information hidden in data, disclosing the possibility of automatic data processing even in absence of a priori structural knowledge. MA methods recently used in the field of X-ray diffraction are here reviewed and described, giving hints about theoretical background and possible applications. The use of MA in the framework of the modulated enhanced diffraction technique is described in detail.

Keywords: multivariate analysis; chemometrics; principal component analysis; partial least square; X-ray powder diffraction; X-ray single crystal diffraction

Publisher's Note: MDPI stays neutral with regard to jurisdictional claims in published maps and institutional affiliations.

1. Introduction

Multivariate analysis (MA) consists of the application of a set of mathematical tools to problems involving more than one variable in large datasets, often combining data from different sources to find hidden structures. MA provides decomposition in simpler components and makes predictions based on models or recovers signals buried in data noise.

Analysis of dependency of data in more dimensions (or variables) can be derived from the former work of Gauss on linear regression (LR) and successively generalized to more than one predictor by Yule and Pearson, who reformulated the linear relation between explanatory and response variables in a joint context [1,2].

The need to solve problems of data decomposition into simpler components and simplify the multivariate regression using few, representative explanatory variables brought towards the advent of the principal component analysis (PCA) by Pearson and, later, by Hotelling [3,4] in the first years of the 20th century. Since then, PCA has been considered a great step towards data analysis exploration because the idea of data decomposition into its principal axes (analogies with mechanics and physics were noted by the authors) allows the data to be explained into a new multidimensional space, where directions are orthogonal to each other (i.e., the new variables are uncorrelated) and each successive direction is decreasing in importance and, therefore, in explained variance. This paved the way to the concept of dimensionality reduction [5] that is crucially important in many research areas such as chemometrics.

Chemometrics involves primarily the use of statistical tools in analytical chemistry [6] and, for this reason, it is as aged as MA. It is also for this reason that the two disciplines started to talk since the late 1960s, initially concerning the use of factor analysis (FA) in

chromatography [7]. FA is a different way to see the same problem faced by PCA, as in FA data are explained by hidden variables (latent variables or factors) by using different conditions for factor extraction [8], while in PCA components are extracted by using the variance maximization as unique criterion. Since then, chemometrics and MA have contaminated each other drawing both advantages [9].

Multivariate curve resolution (MCR) [10] is a recent development consisting in the separation of multicomponent systems and able to provide a scientifically meaningful bilinear model of pure contributions from the information of the mixed measurements. Another data modeling tool is the partial least square (PLS) [11], a regression method that avoids the bad conditioning intrinsic of LR by projecting the explanatory variables onto a new space where the variables are uncorrelated each other, but maximally correlated with the dependent variable. PLS has been successfully applied in problems such as quantitative structure-activity vs. quantitative structure-property of dataset of peptides [12] or in the analysis of relation of crystallite shapes in synthesis of super-structures of $CaCO_3$ through a hydrogel membrane platform [13].

Moreover, classification methods have been adopted in chemometrics since the beginning, mainly for pattern recognition, i.e., classification of objects in groups according to structures dictated by variables. Discriminant analysis (DA), PLS-DA [14], support vector machines (SM) [15] have been used for problems such as classification of food quality or adulteration on the basis of sensitive crystallization [16], toxicity of sediment samples [17] or in classification of biomarkers [18], gene data expression or proteomics [19] just to mention few examples.

MA has been also used to improve the signal-to-noise ratio in measurements. Methods such as phase sensitive detection (PSD) have been developed and implemented for technical applications as in the lock-in amplifier, which amplifies only signals in phase with an internal reference signal. PSD has found a large applications in chemometrics connected to excitation enhanced spectroscopy, where it has been used to highlight excitation-response correlations in chemical systems [20]. Summarizing, although widely used in analytical chemistry, MA is less diffused in materials science and certainly under-exploited in crystallography, where much wider applications are forecast in the next decade.

The main multivariate methods, grouped according to their main field of application, are outlined in Figure 1. In the following, they are critically compared each other, with particular attention on the specificity of chemometric problems and applications to crystallography. In detail, the bad conditioning due to the high dimensionality and the concept of overfitting is analyzed and the needs and advantages in reducing the problem of dimensionality are discussed (Section 2.1); then, similar methods are put in comparison in the successive subsections: PCA vs. FA vs. MCR for dimensionality reduction (Section 2.2), with particular attention to X-ray diffraction applications. In Section 3 we describe a new technique, called modulated enhanced diffraction (MED), which allows the extraction of signals from single components from complex crystal systems monitored by X-ray diffraction experiment, showing the convergence of PSD (a Fourier deconvolution approach) with standard and constrained (OCCR) PCA approaches. PCA, MCR and FA applications to the investigation of powder samples and single-crystal samples by X-ray diffraction are reviewed in Sections 4 and 5, respectively. In detail, Section 4 is devoted to the main applications to kinetic (Section 4.1) and quantitative analysis (Section 4.2). Examples of these two main applications are given to highlight the wide potentialities of MA-based approaches. Section 5 describes the results and perspectives in single crystal diffraction, in details in solving the phase problem (Section 5.1) merging datasets (Section 5.2) and crystal monitoring (Section 5.3), exploiting the capability of MA methods in general and PCA in particular to highlight dynamic phenomena.
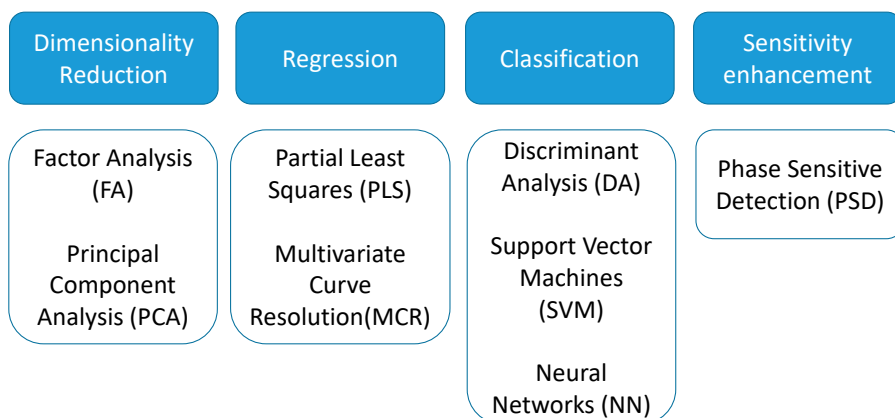
Figure 1. Schematic view showing main multivariate methods grouped according to their field of application.

2. Multivariate Methods

2.1. High Dimension and Overfitting

MA provides answers for prediction, data structure, parameter estimations. In facing these problems, we can think at data collected from experiments as objects of an unknown manifold in a hyperspace of many dimensions [21]. In the context of X-ray diffraction, experimental data are constituted by diffraction patterns in case of single crystals or diffraction profiles in case of powder samples. Diffraction patterns, after indexing, are constituted by a set of reflections, each identified by three integers (the Miller indices) and an intensity value, while diffraction profiles are formed by 2ϑ values as independent variable and intensity values as dependent variable. The data dimensionality depends on the number of reflections or on the number of 2ϑ values included in the dataset. Thus, high-resolution data contain more information about the crystal system under investigation, but have also higher dimensionality.

In this powerful and suggestive representation, prediction, parameter estimation, finding latent variables or structure in data (such as classify or clustering) are all different aspects of the same problem: model the data, i.e., retrieve the characteristics of such a complex hypersurface plunged within a hyperspace, by using just a sampling of it. Sometimes, few other properties can be added to aid the construction of the model, such as the smoothness of the manifold (the hypersurface) that represents the physical model underlying the data. Mathematically speaking, this means that the hypersurface is locally homeomorphic to a Euclidean space and can be useful to make derivatives, finding local minimum in optimization and so on.

In MA, it is common to consider balanced a problem in which the number of variables involved is significantly fewer than the number of samples. In such situations, the sampling of the manifold is adequate and statistical methods to infer its model are robust enough to make predictions, structuring and so on. Unfortunately, in chemometrics it is common to face problems in which the number of dimensions is much higher than the number of samples. Some notable examples involve diffraction/scattering profiles, but other cases can be found in bioinformatics, in study for gene expression in DNA microarray [22,23]. Getting high resolution data is considered a good result in Crystallography. However, this implies a larger number of variables describing a dataset: (more reflections in case of single-crystal data or higher 2ϑ values in case of powder data). Consequently, it makes more complicated the application of MA.

When the dimensionality increases, the volume of the space increases so fast that the available data become sparse on the hypersurface, making it difficult to infer any trend in data. In other words, the sparsity becomes rapidly problematic for any method that

requires statistical significance. In principle, to keep the same amount of information (i.e., to support the results) the number of samples should grow exponentially with the dimension of the problem.

A drawback of having a so much high number of dimensions is the risk of overfitting. Overfitting is an excessive adjustment of the model to data. When a model is built, it must account for an adequate number of parameters in order to explain the data. However, this should not be done too precisely, so to keep the right amount of generality in explaining another set of data that would be extracted from the same experiment or population. This feature is commonly known as model's robustness. Adapting a model to the data too tightly introduces spurious parameters that explain the residuals and natural oscillations of data commonly imputed to noise. This known problem was named by Bellman the "curse of dimensionality" [5], but it has other names (e.g., the Hughes phenomenon in classification). A way to partially mitigate such impairment is to reduce the number of dimensions of the problem, giving up to some characteristic of the data structure.

The dimensionality reduction can be performed by following two different strategies: selection of variables or transformation of variables. In the literature, the methods are known as feature selection and feature extraction [24].

Formally, if we model each variate of the problem as a random variable X_i, the selection of variables is the process of selecting a subset of relevant variables to be used for model construction. This selection requires some optimality criterion, i.e., it is performed according to an agreed method of judgement. Problems to which feature selection methods can be applied are the ones where one of the variables, Y, has the role of 'response', i.e., it has some degree of dependency from the remaining variables. The optimality criterion is then based on the maximization of a performance figure, achieved by combining a subset of variables and the response. In this way, each variable is judged by its level of relevance or redundancy compared to the others, to explain Y. An example of such a figure of performance is the information gain (*IG*) [25], which resorts from the concept of entropy, developed in the information theory. *IG* is a measure of the gain in information achieved by the response variable (Y) when a new variable (X_i) is introduced into the measure. Formally:

$$IG(Y, X_i) = H(Y) - H(Y|X_i) \tag{1}$$

being $H()$ the entropy of the random variable. High value of *IG* means that the second term $H(Y|X_i)$ is little compared to the first one, $H(Y)$, i.e., that when the new variable X_i is introduced, it explains well the response Y and the corresponding entropy becomes low. The highest values of *IG* are used to decide which variables are relevant for the response prediction. If the response variable is discrete (i.e., used to classify), another successful method is Relief [26], which is based on the idea that the ranking of features can be decided on the basis of weights coming from the measured distance of each sample (of a given class) from nearby samples of different classes and the distance of the same sample measured from nearby samples of the same class. The highest weights provide the most relevant features, able to make the best prediction of the response.

Such methods have found application in the analysis of DNA microarray data, where the number of variables (up to tenths of thousands) is much higher than the number of samples (few hundreds), to select the genes responsible for the expression of some relevant characteristic, as in the presence of a genetic disease [27]. Another relevant application can be found in proteomics [28], where the number of different proteins under study or retrieved in a particular experimental environment is not comparable with the bigger number of protein features, so that reduction of data through the identification of the relevant feature becomes essential to discern the most important ones [29].

Feature extraction methods, instead, are based on the idea of transforming the variables set into another set of reduced size. Using a simple and general mathematical formulation, we have:

$$[Y_1, \ldots, Y_m]^T = f\left([X_1, \ldots, X_n]^T\right), \quad m \ll n \tag{2}$$

with the output set $[Y_1, \ldots ,Y_m]$ a completely different set of features from the input $[X_1, \ldots ,X_n]$, but achieved from them. Common feature-extraction methods are based on linear transformation, i.e.,

$$\boldsymbol{Y} = A\boldsymbol{X}, \quad m \ll n \tag{3}$$

where the variables are transformed losing their original meaning to get new characteristics that may reveal some hidden structure in data.

Among these methods, PCA is based on the transformation in a space where variables are all uncorrelated each other and sorted by decreasing variance. Independent Component Analysis (ICA), instead, transforms variables in a space where they are all independent each other and maximally not-Gaussian, apart for one, which represents the unexplained part of the model, typically noise. Other methods, such as MCR, solve the problem by applying more complicated conditions such as the positivity of the values in the new set of variables or similar, so that the physical meaning of the data is still preserved. A critical review of dimensionality reduction feature extraction methods is in Section 2.2.

PCA and MCR have an important application in solving mixing problems or in decomposing powder diffraction profiles of mixtures in pure-phase components. In such decomposition, the first principal components (or contributions, in MCR terminology) usually include the pure-phase profiles or have a high correlation with these.

2.2. Dimensionality Reduction Methods

In Section 2.1, the importance of applying dimensionality reduction to simplify the problem view and reveal underlying model within data was underlined. One of the most common method to make dimensionality reduction is principal component analysis.

PCA is a method to decompose a data matrix finding new variables orthogonal each other (i.e., uncorrelated), while preserving the maximum variance (see Figure 2). These new uncorrelated variables are named principal components (PCs).
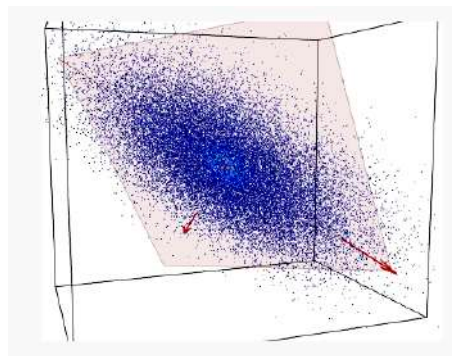
Figure 2. A set of data (blue dots) of three variables is represented into a 3D space. Data are mostly spread on the orange plane, with little departure from it. Principle component analysis (PCA) identifies the plane and the directions of maximum variability of data within it.

PCA is then an orthogonal linear transformation that transforms data from the current space of variables to a new space of the same dimension (in this sense, no reduction of dimension is applied), but so that the greatest variance lies on the first coordinate, the second greatest variance on the second coordinate and so on. From a mathematical viewpoint, said X the dataset, of size $N \times P$ (N being the number of samples, P that of the variates), PCA decomposes it so that

$$\boldsymbol{X} = \boldsymbol{T}\boldsymbol{W}^{'} \tag{4}$$

with T (of size $N \times P$) the matrix of the principal components (called also *scores*), which are the transformed variable values corresponding to each sample and with W (of size $P \times P$) the matrix of the *loadings*, corresponding to the weights by which each original variable must be multiplied to get the component scores. The matrix W is composed by orthogonal columns that are the eigenvectors of the diagonalization [30] of the sample covariance matrix of X:

$$X'X = W'\Lambda W \tag{5}$$

In Equation (5), Λ is a diagonal matrix containing the eigenvalues of the sample covariance matrix of X, i.e., $X'X$. Since a covariance matrix is always semi-definite positive, the eigenvalues are all real and positive or null and correspond to the explained variance of each principal component. The main idea behind PCA is that in making such decomposition, often occurs that not all the directions are equally important. Rather, the number of directions preserving most of the explained variance (i.e., energy) of the data are few, often the first 1–3 principal components (PC). Dimensionality reduction is then a lossy process, in which data are reconstructed by an acceptable approximation that uses just the first few principal components, while the remaining are neglected:

$$\hat{X} \approx T_{(1:s)} W'_{(1:s)} \tag{6}$$

With s the retained components (i.e., the first s columns of both the matrices) and $s \ll P$.

Diagonalization of the covariance matrix of data is the heart of PCA and it is achieved by resorting to singular value decomposition (SVD), a basic methodology in linear algebra. SVD should not be confused with PCA, the main difference being the meaning given to the results. In SVD the input matrix is decomposed into the product a left matrix of eigenvectors U, a diagonal matrix of eigenvalues Λ and a right matrix of eigenvectors V, reading the decomposition from left to right:

$$Y = U\Lambda V' \tag{7}$$

SVD may provide decomposition also of rectangular matrices. PCA, instead, uses SVD for diagonalization of the data covariance matrix $X'X$, which is square and semi-definite positive. Therefore, left and right eigenvector matrices are the same, and the diagonal matrix is square and with real and positive value included. The choice of the most important eigenvalues allows the choice of the components to retain, a step that is missing from SVD meaning.

Factor analysis is a method based on the same concept of PCA: a dataset is explained by a linear combination of hidden factors, which are uncorrelated each other, apart for a residual error:

$$X = l_1 F_1 + \dots l_n F_n + \varepsilon \tag{8}$$

FA is a more elaborated version of PCA in which factors are supposed (usually) to be known in number and, although orthogonal each other (as in PCA), they can be achieved adopting external conditions to the problem. A common way to extract factors in FA is by using a depletion method in which the dataset X is subjected to an iterative extraction of factors that can be analyzed time by time: $X^{(k)} = X^{(k-1)} - l_k F_k$. In FA, there is the clear intent to find physical causes of the model in the linear combination. For this reason, their number is fixed and independency of the factors with the residual ε is imposed too. It can be considered, then, a supervised deconvolution of original dataset in which independent and fixed number of factors must be found. PCA, instead, explores uncorrelated directions without any intent of fixing the number of the most important ones.

FA has been applied as an alternative to PCA in reducing the number of parameters and various structural descriptors for different molecules in chromatographic datasets [31]. Moreover, developments of the original concepts have been achieved by introducing a certain degree of complexity such as the shifting of factors [32] (factors can have a certain

degree of misalignment in the time direction, such as in the time profile for X-ray powder diffraction data) or the shifting and warping (i.e., a time stretching) [33].

Exploring more complete linear decomposition methods, MCR [8] has found some success as a family of methods that solve the mixture analysis problem, i.e., the problem of finding the pure-phase contribution and the amount of mixing into a data matrix including only the mixed measurements. A typical paradigm for MCR, as well as for PCA, is represented by spectroscopic or X-ray diffraction data. In this context, each row of the data matrix represents a different profile, where the columns are the spectral channels or diffraction/scattering angles, and the different rows are the different spectra or profiles recorded during the change of an external condition during time.

In MCR analysis, the dataset is described as the contribution coming from reference components (or profiles), weighted by coefficients that vary their action through time:

$$X_i \approx c_i S'_i \qquad (9)$$

With c_i the vector of weights (the profile of change of the i-th profile through time) and S_i the pure-phase i-th reference profile. The approximation sign is since MCR leaves some degree of uncertainty in the model. In a compact form we have:

$$X = CS' + E \qquad (10)$$

MCR shares the same mathematical model of PCA, apart for the inclusion of a residual contribution E that represents the part of the model we give up explaining. The algorithm that solves the mixture problem in the MCR approach, however, is quite different from the one used in PCA. While PCA is mainly based on the singular value decomposition (i.e., basically the diagonalization of its sample covariance matrix), MCR is based on the alternating least square (ALS) algorithm, an iterative method that tries to solve conditioned minimum square problems of the form:

$$\{C, S\}_{opt} = argmin_{C,S}\left\{\sum_{i,j}\left(x_{i,j} - c_i S'_j\right)^2 + \lambda\left(\sum_i \parallel c_i \parallel^2 + \sum_j \parallel s_j \parallel^2\right)\right\} \qquad (11)$$

The previous problem is a least square problem with a regularization term properly weighted by a Lagrange parameter λ. The regularization term, quite common in optimization problems, is used to drive the solution so that it owns some characteristics. The L_2-norm of the columns of S or C, as reported in the Equation (11), is used to minimize the energy of the residual and it is the most common way to solve ALS. However, other regularizations exist, such as L_1-norm to get more sparse solutions [34] or imposing positivity of the elements of S and C. Usually, the solution to Equation (11) is provided by iterative methods, where initial guesses of the decomposition matrices S or C are substituted iteratively by alternating the solution of the least-square problem and the application of the constraints. In MCR, the condition of positivity of elements in both S or C is fundamental to give physical meaning to matrices that represent profile intensity and mixing amounts, respectively.

The MCR solution does not provide the direction of maximum variability as PCA. PCA makes no assumption on data; the principal components and particularly the first one, try to catch the main trend of variability through time (or samples). MCR imposes external conditions (such as the positivity), it is more powerful, but also more computationally intensive. Moreover, for quite complicated data structures, such as the ones modeling the evolution of crystalline phases through time [35,36], it could be quite difficult to impose constraints into the regularization term, making the iterative search unstable if not properly set [37,38]. Another important difference between MCR and PCA is in the model selection: in MCR the number of latent variables (i.e., the number of profiles in which decomposition must be done) must be known and set in advance; in PCA, instead, while there are some criterion of selection of the number of significative PC such as the Malinowski

indicator function (MIF) [39,40] or the average eigenvalue criterion (AEC) [41,42], it can also be inferred by simply looking at the trend of the eigenvalues, which is typical of an unsupervised approach. The most informative principal components are the ones with highest values.

For simple mathematical models, it will be shown in practical cases taken from X-ray diffraction that PCA is able to optimally identify the components without external constraints. In other cases, when the model is more complicated, we successfully experimented a variation of PCA called orthogonal constrained component rotation (OCCR) [43]. In OCCR, a post-processing is applied after PCA aimed at revealing the directions of the first few principal components that can satisfy external constraints, given by the model. The components, this way, are no longer required to keep the orthogonality. OCCR is then an optimization method in which the selected principal components of the model are let free to explore their subspace until a condition imposed by the data model is optimized. OCCR has been shown to give results that are better than traditional PCA, even when PCA produces already satisfactory results. A practical example (see Section 3) is the decomposition of the MED dataset in pure-phase profiles, where PCA scores, proportional to profiles, may be related each other with specific equations.

Smoothed principal component analysis or (SPCA) is a modification of common PCA suited for complex data matrices coming from single or multi-technique approaches where the time is a variable, in which sampling is a continuous, such as *in situ* experiment or kinetic studies. The *ratio* behind the algorithm proposed by Silvermann [44] is that data without noise should be smooth. For this reason, in continuous data, such as profiles or time-resolved data, the eigenvector that describes the variance of data should be also smooth [45]. Within these assumptions, a function called "roughness function" is inserted within the PCA algorithm for searching the eigenvectors along the directions of maximum variance. The aim of the procedure is reducing the noise in the data by promoting the smoothness between the eigenvectors and discouraging more discrete and less continuous data. SPCA had been successfully applied to crystallographic data in solution-mediated kinetic studies of polymorphs, such as L-glutamic acid from α to β form by Dharmayat et al. [46] or p-Aminobenzoic acid from α to β form by Turner and colleagues [47].

3. Modulated Enhanced Diffraction

The Modulated Enhanced Diffraction (MED) technique has been conceived to achieve chemical selectivity in X-ray diffraction. Series of measurements from *in situ* or *operando* X-ray diffraction experiments, where the sample is subjected to a varying external stimulus, can be processed by MA to extract information about active atoms, i.e., atoms of the sample responding to the applied stimulus. This approach has the great advantage of not requiring preliminary structural information, so it can be applied to complex systems, such as composite materials, quasi-amorphous samples, multi-component solid-state processes, with the aim to characterize the (simpler) sub-structure comprising active atoms. The main steps involved in a MED experiment are sketched in Figure 3. During data collection of X-ray diffraction data, the crystal sample is perturbed by applying an external stimulus that can be controlled in its shape and duration. The stimulus determines a variation of structural parameters of the crystallized molecule and/or of the crystal lattice itself. These changes represent the response of the crystal, which is usually unknown. Repeated X-ray diffraction measurements allow to collect diffraction patterns at different times, thus sampling the effect of the external perturbation. In principle, the set of collected diffraction patterns can be used to detect the diffraction response to the stimulus. Offline data analysis based on MA methods must be applied to implement the deconvolution step, i.e., to process time-dependent diffraction intensities I_h measured for each reflection h to recover the time evolution of the parameters for each atom j of the crystal structure, such as occupancy (n_j), atomic scattering factor (f_j) and atomic position (r_j). It is worth noting that in X-ray diffraction the measured intensities (I_h), representing the detected variable, depend on the square of the structure factors F_h, embedding the actual response of the system.
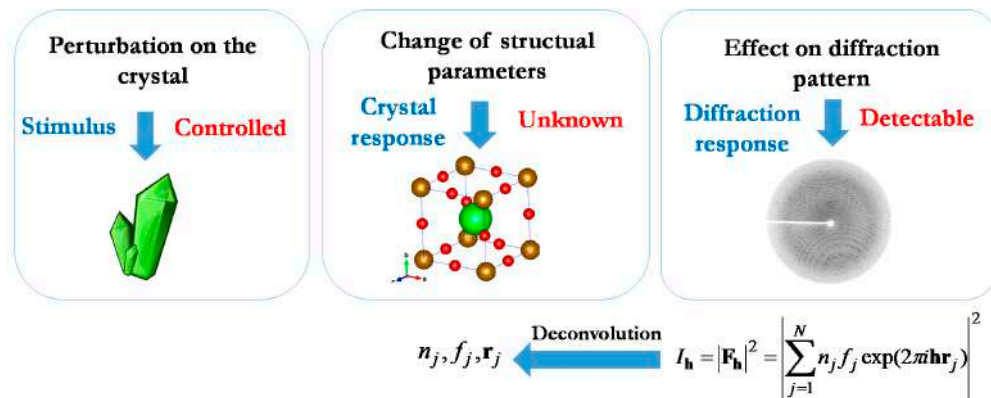
Figure 3. Main steps involved in a MED experiment. A perturbation is applied in a controlled way on a crystal sample, which responds by changing the crystal structural parameters in unknown way. Repeated X-ray diffraction measurements allow detecting the diffraction response, which can be properly analyzed through an offline process called deconvolution, to determine the variations in main structural parameters.

Applications of MED are twofold: on one hand, the active atoms sub-structure can be recovered, so disclosing information at atomic scale about the part of the system changing with the stimulus, on the other hand the kinetic of changes occurring in the sample can be immediately captured, even ignoring the nature of such changes.

To achieve both these goals, MA tools have been developed and successfully applied to crystallographic case studies. These methods, which will be surveyed in the next paragraph, implement the so-called data deconvolution, i.e., they allow extracting a single MED profile out of the data matrix comprising the set of measurements.

Deconvolution Methods

The first deconvolution method applied to MED technique was sensitive phase detection (SPD). SPD is a MA approach widely applied since decades to spectroscopic data (modulation enhanced spectroscopy—MES), which can be applied to systems linearly responding to periodic stimuli. SPD projects the system response from time domain to phase domain by using a reference periodic-typically sinusoidal-signal, through the following equation:

$$p(x, \varphi) = \frac{2}{N} \sum_{i=0}^{N} y_i(x) sin\left(\frac{2K\pi}{N} i + \varphi \right) \tag{12}$$

where φ *is* the SPD phase angle, $y_i(x)$ are the n measurements collected at the time i, and k is the order of the demodulation. The variable x can be the angular variable 2ϑ in case of X-ray powder diffraction measurements or the reflection h in case of single-crystal diffraction data. Equation (12) represents a *demodulation* in the frequency space of the system response, collected in the time space. Demodulation at $k = 1$, i.e., at the lower frequency of the reference signal, allows the extraction of kinetic features, involving both active and silent atoms; demodulation at $k = 2$, i.e., at double the lower frequency of the reference signal, allow to single out contribution from only active atoms. This was demonstrated in [35] and comes from the unique property of X-ray diffraction that the measured intensities I_h depends on the square of the structure factors F_h. A pictorial way to deduce this property is given in Figure 4: silent and active atoms respond in a different way to the external stimulus applied to the crystal. This can be parameterized by assigning different time dependences to their structure factors, respectively F_S and F_A. For sake of simplicity, we can assume that silent atoms do not respond at all to the stimulus, thus F_S remain constant during the experiment, while active atoms respond elastically, thus F_A has the same time dependence of that of the stimulus applied (supposed sinusoidal in Figure 4). In these

hypotheses, the diffraction response can be divided in three terms, the first being constant, the second having the same time dependence of the stimulus, the third having a doubled frequency with respect to that of the stimulus and representing the contribution of active atoms only. PSD performed incredibly well for the first case study considered, where the adsorption of Xe atoms in an MFI zeolite was monitored in situ by X-ray diffraction, by using pressure or temperature variations as external stimulus [48,49]. However, it was immediately clear that this approach had very limited applications, since very few systems, only in particular conditions, have a linear response -mandatory to apply PSD for the demodulation- to periodic stimuli, and it is easier to apply non-periodic stimuli.
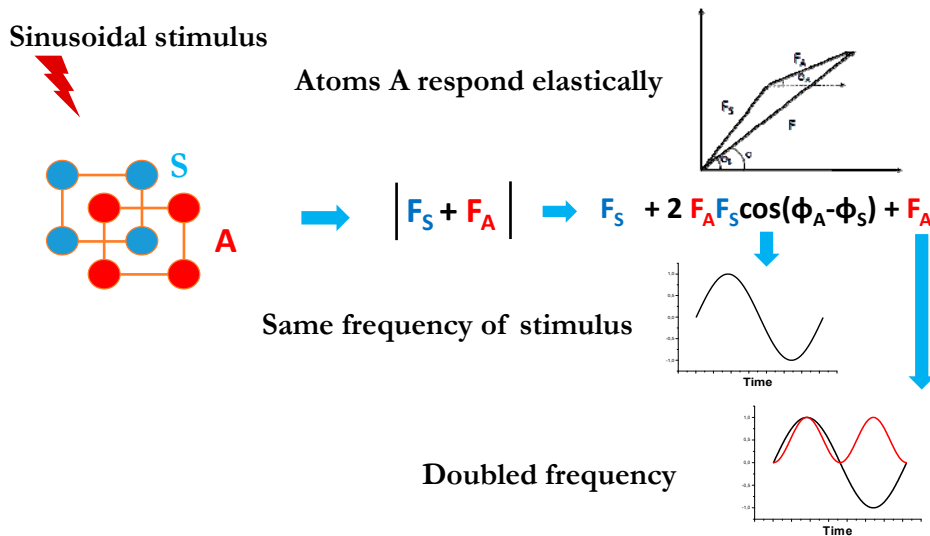
Figure 4. Pictorial demonstration of the possibility to extract information of active atoms only in a MED experiment. The crystal system is divided in silent (**S**) and active (**A**) atoms, depending on how they respond to an external stimulus applied. The diffraction response measured on the X-ray detector can be divided in two contributions from S and A atoms. This give rise to three terms, the first being constant in time, the second having the same time-dependence of the stimulus, the third varying with double the frequency of the stimulus and representing the contribution of active atoms only.

A more general approach would allow coping with non-periodic stimuli and non-linear system responses. To this aim, PCA was applied to MED data, with the underlying idea that in simple cases, the first principal component (PC1) should capture changes due to active and silent atoms, the second principal component (PC2) should instead capture changes due to active atoms only. In fact, if the time-dependence of the contribution from active atoms can be separated, i.e., $F_A(t) = F_A * g(t)$, then the MED demodulation shown in Figure 4 can be written in a matrix form:

$$I_h = \begin{pmatrix} 1 & g(t) & g(t)^2 \end{pmatrix} * \begin{pmatrix} F_S{}^2 \\ 2F_A F_S cos(\varphi_A - \varphi_S) \\ F_A{}^2 \end{pmatrix} \tag{13}$$

By comparing Equation (13) with Equation (12) it can be inferred that PCA scores should capture the time-dependence of the stimulus, while PCA loadings should capture the dependence from the 2ϑ or h variable of the diffraction pattern. In particular, we expect two significant principal component, the first having $T_1 = g(t)$ and $W_1 = 2F_A F_S cos(\varphi_A - \varphi_S)$, the second having $T_2 = g(t)^2$ and $W_2 = F_A{}^2$. Notably, constant terms are excluded by PCA processing, since in PCA it is assumed zero-mean of the data matrix columns. An example of deconvolution carried out by PCA, which is more properly

referred to as *decomposition* of the system response, is shown in Figure 5, considering in situ X-ray powder diffraction data. The PC1 scores reproduce the time dependence of the applied stimulus, whereas PC2 scores have a doubled frequency. PC1 loadings have positive and negative peaks, depending on the values of the phase angles φ_A and φ_S, while PC2 loadings have only positive peaks, representing the diffraction pattern from active atoms only.
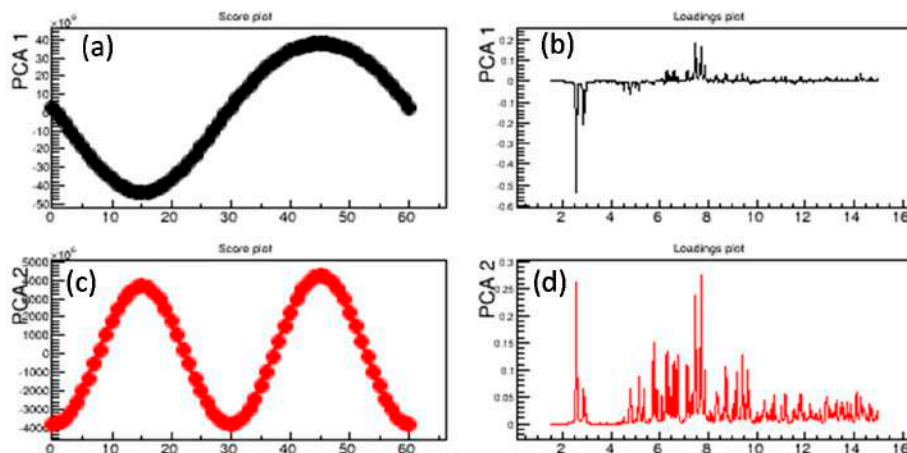
Figure 5. Example of PCA decomposition applied to in situ X-ray powder diffraction data. Scores (**a**) and loadings (**b**) of the first principal component (PC1); scores (**c**) and loadings (**d**) of the second principal component (PC2). A sinusoidal stimulus was applied during the *in situ* experiment.

In this framework, a rationale can be figured out, where the PC1 term is like the $k = 1$ PSD term and the PC2 term is like the $k = 2$ PSD term. This correspondence is strict for systems responding linearly to periodic stimuli, while for more general systems PCA is the only way to perform decomposition. This new approach was successfully applied to different case studies [50,51] outperforming the PSD method.

Another important advancement in MED development was to introduce adapted variants of existing MA methods. In fact, PCA decomposition cannot be accomplished as outlined above for complex systems, where several parts (sub-structures) vary with different time trends, each of them captured by specific components. A signature for failure of the standard PCA approach is a high number of principal components describing non-negligible data variability, and failure to satisfy two conditions for PC1 and PC2, descending from the above-mentioned squared dependence of measured intensity from structure factors. In the standard PCA case, PC2 loadings, which describe the data variability across reflections (or 2ϑ axis in case of powder samples), are expected to be positive, given the proportionality with squared structure factors of only active atoms. Moreover, PC1 and PC2 scores, which describe the data variability across measurements, are expected to follow the relation:

$$T_2 = (T_1)^2 \qquad (14)$$

as changes for active atoms vary with a frequency doubled with respect to that of the stimulus.

A MA approach adapted to MED analysis has been developed, where constraints on PC2 loadings and on PC1/PC2 scores according to Equation (14) are included in the PCA decomposition. This gave rise to a new MA method, called orthogonal constrained component rotation (OCCR), which aims at finding the best rotations of the principal components determined by PCA, driven by figure of merits based on the two MED constraints. The OCCR approach allows overcoming the main limitation of PCA, i.e., to blind searching

components that are mutually orthogonal. It has been successfully applied to characterize water-splitting processes catalyzed by spinel compounds [43] or to locate Xe atoms in the MFI zeolite to an unprecedented precision [50].

A further advancement in the route of routinely applying PCA to MED was done in [51,52], where the output of PCA was analytically derived, and expected contribution to scores and loadings to specific changes in crystallographic parameters have been listed. This would make easier the interpretation of the results of PCA decomposition.

4. Applications in Powder X-ray Diffraction

X-ray powder diffraction (XRPD) offers the advantage of very fast measurements, as many crystals are in diffracting orientation under the X-ray beam at the same time. A complete diffraction pattern at reasonable statistics can be acquired in seconds, even with lab equipment and such high measurement rates enable the possibility to perform *in situ* experiments, where repeated measurements are made on the same sample, while varying some external variable, the most simple one being time [53]. On the other hand, the contemporary diffraction from many crystals makes it difficult to retrieve structural information about the average crystal structure by using phasing methods. In this context, MA has great potential, since it allows extracting relevant information from raw data, which could be used to carry out the crystal structure determination process on subset of atoms, or to characterize the system under study without any prior structural knowledge. Some specific applications of MA on powder X-ray diffraction are reviewed in the following sections. The two main fields of applications are the extraction of dynamic data (Section 4.1) in a temporal gradient and qualitative and quantitative analysis (Section 4.2) in presence of concentration gradients.

4.1. Kinetic Studies by Single or Multi-Probe Experiments

The advent of MA has also revolutionized kinetic studies based on in situ powder X-ray diffraction measurements. Several works have used MA to extract efficiently the reaction coordinate from raw measurements [54–56]. Moreover, in a recent study of solid-state reactions of organic compounds, the classical approach of fitting the reaction coordinate by several kinetic models has been replaced by a new approach, which embeds kinetic models within the PCA decomposition [57,58]. The discrimination of the best kinetic model is enhanced by the fact that it produces both the best estimate of the reaction coordinate and the best agreement with the theoretical model. MCR-ALS is another decomposition method that had been employed in the last few years in several kinetic studies on chemical reactions [59–61].

MA is even more powerful when applied to datasets acquired in multi-technique experiments, where X-ray diffraction is complemented by one or more other techniques. The MA approach allows, in these cases, to extract at best the information by the different instruments, probing complementary features. In fact, the complete characterization of an evolving system is nowadays achieved by complex in situ experiments that adopt multi-probe measurements, where X-ray measurements are combined with spectroscopic probes, such as Raman FT-IR or UV-vis spectroscopy. In this context, covariance maps have been used to identify correlated features present in diffraction and spectroscopic profiles. Examples include investigations of temperature-induced phase changes in spin crossover materials by XRPD/Raman [36] perovskites by combining XRPD and pair distribution function (PDF) measurements [62], characterization of hybrid composite material known as Maya Blue performed by XRPD/UV-Vis [63] and metabolite-crystalline phase correlation in wine leaves by XRPD coupled with mass spectrometry and nuclear magnetic resonance [64].

To highlight the potentialities of the application of PCA to unravel dynamics from in situ X-ray diffraction studies, a recently published case study [52] is briefly described. In this paper, the sedimentation of barium sulfate additive inside an oligomeric mixture was studied during polymerization by repeated XRPD measurements with a scan rate of 1°/min. The kinetic behavior of the sedimentation process was investigated by processing

the high number (150) of XRPD patterns with PCA, without using any prior structural knowledge. The trend in data can hardly be observed by visual inspection of the data matrix (Figure 6a), as the peak intensity does not change with a clear trend and their positions drift to lower 2ϑ values during the data collection. PCA processes the whole data matrix in seconds, obtaining a PC that explains the 89% of the system's variance (Figure 6b). The loadings associated to this PC resemble the first derivative of an XRPD profile (Figure 6c), suggesting that this PC captured the changes in data due to barite peak shift toward lower 2ϑ values. In fact, PCA, looking for the maximum variance in the data, basically extract from the data and highlight the variations of the signal through time. PCA scores, which characterize in the time domain the variations in data highlighted by loadings, indicate a decreasing trend (Figure 6d). In fact, the peak shift is strongly evident at the beginning of the reaction, with an asymptotic trend at the end of the experiment. Scores in Figure 6d can thus be interpreted as the reaction coordinate of the sedimentation process. In ref. [52], the comparison of PCA scores with the zero-error obtained by Rietveld refinement confirmed that the dynamic trend extracted by PCA is consistent with that derived from the traditional approach. However, the time for data processing (few seconds with MA, few hours with Rietveld Refinement) makes PCA a very useful complementary tool to extract dynamic and kinetic data while executing the experiment, to check data quality and monitor the results without *a priori* information.
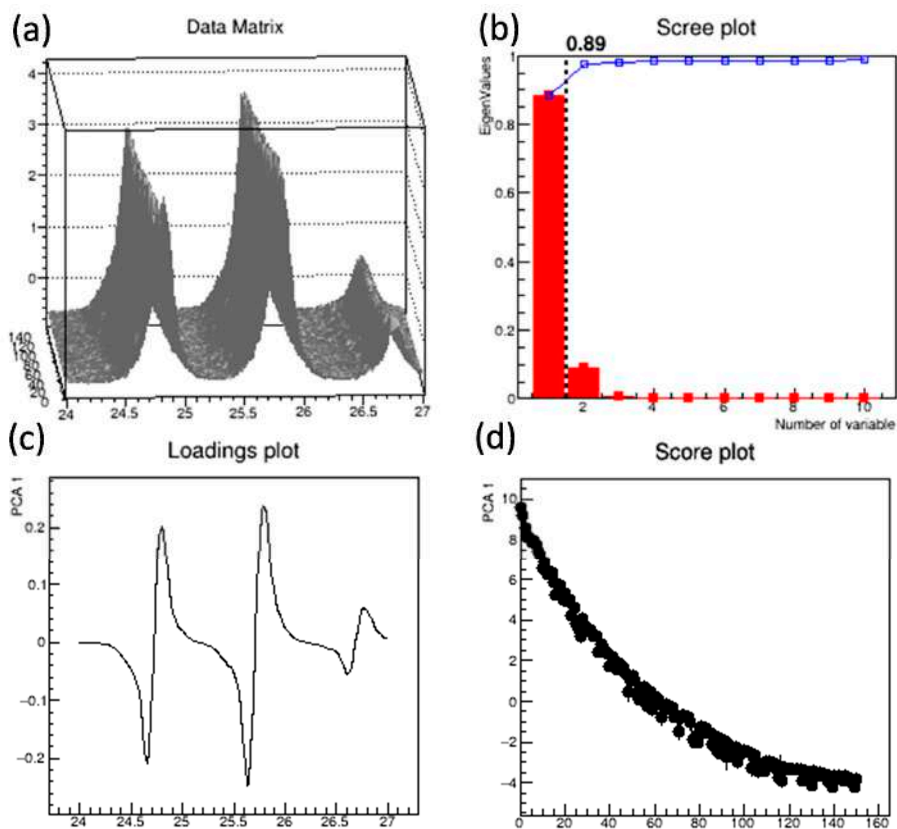
Figure 6. In situ analysis of sedimentation data for barite additive in an oligomeric mixture during gelation time; 150 measurements were collected during the experiment, covering the angular range of the three more intense peaks of barium sulfate XRPD profile; (**a**) Analyzed data matrix; (**b**) scree plot; (**c**) loadings plot; (**d**) score plot.

4.2. Qualitative and Quantitative Studies

Having prompt hints about main trends in data is beneficial in many applications and can facilitate subsequent structural analysis. Qualitative and/or quantitative analysis on sets from X-ray powder diffraction profiles can be achieved by both FA [65,66] and PCA, particularly from the score values of the main components. This approach is common in the -omics sciences in the analytical chemistry field. Euclidean distances in PC score plots can be calculated to obtain also a semi-quantitative estimation between groups or clusters [67,68]. In fact, the arrangement of representative points in the scores plot can be used to guess the composition of the mixture. An example of application of this approach is given in Figure 7. Figure 7a reports the original X-ray diffraction data collected on pure phases (A, B, C), the binary mixtures (AB, BC, AC) 50:50 weight and ternary mixture ABC prepared by properly mixing calcium carbonate (A), acetylsalicylic acid (B) and sodium citrate (C). PCA analysis was carried out and the corresponding PC scores (Figure 7b) and loadings (Figure 7c) are reported. It is evident that the PCA scores are sensible to %weight of the samples since they form a triangle with the monophasic datasets (A, B, C) at the vertices, the binary mixtures (AB, BC, AC) in the middle of the edges and the ternary mixture ABC in its center. All the possible mixtures are within the triangle, in the typical representation of a ternary mixture experimental domain. PCA recognizes the single-phase contributions by the PC loadings, containing the XRPD pattern features, highlighted in Figure 7c. PC1 loadings have positive peaks corresponding to phases B and C, and negative ones to phase A. PC2 loadings show positive peaks corresponding to phase B and negative ones to phase C, while phase A has a very moderate negative contribution, being located close to 0 along the PC2 axis in Figure 7b.

PCA scores in Figure 7b can be exploited to perform a semi-quantitative analysis, since the above described dependence of the topology of data points in the scores plot is related to the composition. The procedure is easy for binary and ternary mixtures where a 2D plot (Figure 7b) can be exploited to calculate Euclidean distances (Figure 7d) and thus compositions (Table 1). For instance, the A phase amount within the ABC mixture, identified by the F score in Figure 7d, is given by the ratio AJ/AC. Given any score in the triangle, the corresponding phase amounts can be calculated accordingly. The comparison between compositions (Table 1) from PC scores (not requiring *a priori* information) and multilinear regression, exploiting the knowledge of profiles of the pure phases, is impressive and very promising for wide applications in quality control where solid mixtures are involved. Quantification errors can occur if data are not perfectly positioned in the triangle, such as the AC mixture in Figure 7b that is slightly out of the polygon. In such case, the sum of the estimated phase amounts can exceed or in general be different from 1 as a result of the unrealistic negative quantification of the third phase B. Deviations from unity of the sum of estimated phase amounts can be used as indicator of systematic errors, due for example to the presence of amorphous content in the samples, phases with different X-ray absorption properties or missing phases in the model [69].
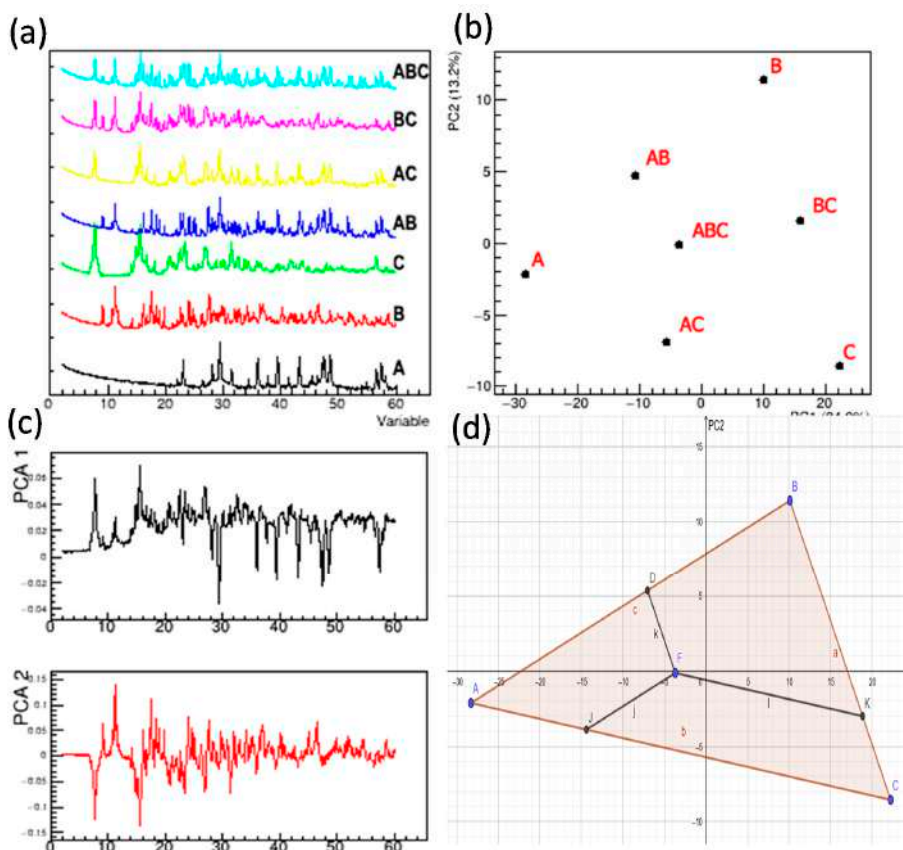
Figure 7. Original data (**a**), PC scores (**b**), PC loading (**c**) and calculation of Euclidean distances from PC scores (**d**) from X-ray powder diffraction data by ternary mixtures. Data points A, B, and C correspond to powder diffraction profiles from monophasic mixtures, data points AB, AC and BC to binary mixtures and ABC to a mixture containing an equal amount of the three crystal phases.

Table 1. Results of the quantification of the phases in polycrystalline mixtures represented in Figure 6 by PCA scores and multilinear regression.

Sample	Geometric Estimation from PC Scores			Regression		
	Phase 1	**Phase 2**	**Phase 3**	**Phase 1**	**Phase 2**	**Phase 3**
0	1.00	0.00	0.00	1.000	0.000	0.000
1	0.00	1.00	0.00	0.000	1.000	0.000
2	0.00	0.00	1.00	0.000	0.000	1.000
3	0.53	0.49	0.00	0.538	0.462	0.000
4	0.58	0.00	0.53	0.507	0.000	0.493
5	0.00	0.51	0.49	0.000	0.522	0.478
6	0.45	0.28	0.27	0.425	0.301	0.274

The approach can be extended to more than 3 phases. With four phases, the analysis can still be carried out graphically, even if a 3D plot is necessary, with increased difficulties in its representation and analysis. The graphical approach is of course impossible to represent without simplification or projections with 5 or more phases. In these cases, a non-graphic and general matrix-based approach can be used, as proposed by Cornell [70].

Quantitative analysis from raw data (Figure 6a) can be carried out exploiting a different approach, i.e., using least-squares calculations. Each individual experimental pattern is fitted by using a linear regression model:

$$y(x) = \sum_{i=1}^{N} a_i y_i(x) + b(x) \tag{15}$$

where $i = 1, \ldots, n$ runs for all the crystal phases present in the sample, $y_i(x)$ is the experimental profiles of the i-th pure crystal phases and $b(x)$ is the background estimated from the experimental pattern.

The weight fraction can be derived from the coefficients a_i estimated from the fitting procedures. This approach is followed by the RootProf program, where it can be also used in combination with a preliminary PCA step aiming at filtering the experimental patterns to highlight their common properties [69]. Results obtained by the PCA + least squares approach have been compared with those obtained by supervised analysis based on PLS for a case study of quaternary carbamazepine-saccharin mixtures monitored by X-ray diffraction and infrared spectroscopy [71].

As a final note concerning recent developments in this field, the deep-learning technique based on Convolutional Neural Network (CNN) models has been applied for phase identification in multiphase inorganic compounds [72]. The network has been trained using synthetic XRPD patterns, and the approach has been validated on real experimental XRPD data, showing an accuracy of nearly 100% for phase identification and 86% for phase-fraction quantification. The drawback of this approach is the large computational effort necessary for preliminary operations. In fact, a training set of more than 1.5×10^6 synthetic XRPD profiles was necessary, even for a limited chemical space of 170 inorganic compounds belonging to the Sr-Li-Al-O quaternary compositional pool used in ref [72].

5. Applications in Single-Crystal X-ray Diffraction

Single-crystal diffraction data are much more informative than X-ray powder diffraction data as highlighted by Conterosito et al. [52], as they contain information about the intensity of each diffraction direction (reflection), which is usually enough to obtain the average crystal structure by phasing methods. By contrast, the measurement is longer than for powder X-ray diffraction, since the crystal must be rotated during the measurement to obtain diffraction conditions from all reflections. For this reason, radiation damage issues can be very important for single-crystal X-ray diffraction, and in fact this prevents carrying out in situ studies on radiation-sensitive molecules, as often observed in organic and bio-macromolecular systems. MA can still be useful for single crystal diffraction data, since it helps in solving specific aspects that will be highlighted in the following paragraphs. Regarding MED applications, it is worth mentioning that single-crystal X-ray diffraction has an intrinsic advantage over powder X-ray diffraction, related to the effect of lattice distortions during measurements: in a powder diffraction pattern a change of crystal cell parameters manifest itself in a shift in peak positions, which is usually combined with changes in peak shape and height due to variations of the average crystal structure. The combined effect of lattice distortions and structural changes makes difficult to interpret MA results. In a single-crystal pattern, the intensity of individual reflections is not affected by crystal lattice distortions, and crystal cell parameters are determined by indexing individual patterns measured at different times, so that they are not convoluted with structural variations.

5.1. Multivariate Approaches to Solve the Phase Problem

As noticed by Pannu et al. [73], multivariate distributions emerged in crystallography with the milestone work by Hauptman and Karle [74], dealing with the phase problem solution. The phase problem is "multivariate" by definition because the phases of the reflections, needed to solve a crystal structure, are in general complex numbers depending

on the coordinate of all atoms. In other words, the atomic positions are the random variables related to the multivariate normal distribution of structure factors. After these considerations, statistical methods like joint probability distribution functions were of paramount importance in crystallography in general [75] developing direct methods, used for decades, until today, for crystal structure solution [76]. Despite these premises, the methods more diffused in analytical chemistry such as PCA were rarely exploited to solve the phase problems. The more closely related approach is that of maximum likelihood, exploited to carry out the structure solution and heavy-atom refinement. In the framework of the isomorphous replacement approach [77] the native and derivative structure factors are all highly correlated: to eliminate this correlation, covariance is minimized [73,78,79]. PCA in a stricter sense was used to monitor protein dynamics in theoretical molecular dynamics [80] and in experimental in situ SAXS studies [81] and recently in *in situ* single crystal diffraction data [51]. Even if much less applications of PCA to *in situ* X-ray single crystal with respect to powder diffraction data can be found, a huge potential of application also in *in situ* single crystal diffraction is envisaged in the next decades.

5.2. Merging of Single-Crystal Datasets

A common problem in protein crystallography is to combine X-ray diffraction datasets taken from different crystals grown in the same conditions. This operation is required since only partial datasets can be taken from single crystals before they get damaged by X-ray irradiation. Thus, a complete dataset (sampling the whole crystal lattice in the reciprocal space) can be recovered by merging partial datasets from different crystals. However, this can be only accomplished if merged crystals have similar properties, i.e., comparable crystal cell dimensions and average crystal structures. To select such crystals, clustering protocols have been implemented to identify isomorphous clusters that may be scaled and merged to form a more complete multi-crystal dataset [82,83]. MA applications in this field have a great potential, since protein crystallography experiments at X-ray free-electron laser (XFEL) sources are even more demanding in terms of dataset merging. Here thousands to millions of partial datasets from very tiny crystals are acquired in few seconds, which needs to be efficiently merged before further processing may get structural information [84].

5.3. Crystal Monitoring

Crystal recognition is a key step in high-throughput Protein Crystallography initiatives, where high-throughput crystallization screening is implemented, which demand for the systematic analysis of crystallization results. 42 diffraction datasets related to protein crystals grown under diffusion mass-transport controlled regime have been analyzed by PCA to determine possible trends in quality indicators [85]. In reference [86] neural networks were used to assess crystal quality directly from diffraction images, i.e., without using quality indicators. More recently, CNN has been used to efficiently and automatically classify crystallization outputs by processing optical images [87]. The training has been accomplished by using nearly half a million of experiments across a large range of conditions stored in the framework of the machine recognition of crystallization outcomes (MARCO) initiative from different proteins and crystallization conditions. The resulting machine-learning scheme was able to recapitulate the labels of more than 94% of a test set, which represents a benchmark for actual attainable accuracy for uncured datasets. The MA performances could be enhanced by complementing optical microscopy with UV measurements or second-order nonlinear optical imaging of chiral crystals (SONICC), or by using time course information, as each crystallization experiment records a series of images taken over times [88]. Moreover, the possibility of classifying crystallization images in terms of crystals, precipitate and clear drop can be used to identify pathways for optimization [89]. The application of this approach to large libraries of historical data may therefore reveal patterns that guide future crystallization strategies, including novel chemical screens and mutagenesis programs.

6. Conclusions and Perspectives

Multivariate methods in general and PCA approach in particular are widely used in analytical chemistry, but less diffused in materials science and rarely used in X-ray diffraction, even if their possible applications have been envisaged already in the 50s of the last century [74], in relation to the phase problem solution. More systematic MA applications in Crystallography started appearing in the literature since about 2000 on and in the last two decades some groups started working with a more systematic approach to explore potentialities and limitations of multivariate methods applications in crystallography, focusing the efforts mainly in powder diffraction data analysis. Among the various approaches, multilinear regression and PCA are the main methods showing huge potentialities in this context.

Two main fields of application are envisaged: e.g., fast on-site kinetic analysis and qualitative/semi-quantitative analysis from in situ X-ray powder diffraction data. In details, MA has the ability to extract the dynamics in time series (i.e., in measurements monitoring the time evolution of a crystal system) or qualitative and quantitative information in concentration gradients (i.e., in samples showing different composition). Typically, the presented methods have the advantages, with respect to traditional methods, of needing no or much less *a priori* information about the crystal structure and being so efficient and fast to be applied on site during experiment execution. The main drawbacks of MA approaches lie on the fact that they exploit data-driven methods and do not claim to provide physical meaning to the obtained results. Outputs from PCA, MCR or FA, if not properly driven or interpreted may lead to wrong or unreasonable results.

Applications in single crystal diffraction started appearing in the last years and huge potentialities are foreseen, especially in serial crystallography experiments where the data amount is very large and unfeasible for the traditional approaches. Crystal monitoring and dataset merging are the more promising approaches in single crystal diffraction, where huge potentialities are envisaged. Kinetic analysis in singles crystal diffraction is also envisaged as a possible breakthrough field of applications, since the evolution of source and detectors suggest for the next decade a huge growth, as seen for *in situ* powder diffraction in the last decades of the 20th century. MA methods can for sure play a key role, because the huge amount of data make the traditional approaches unfeasible.

This review is centered on PCA, MCR, FA and PSD since they are the approaches employed in X-ray diffraction data analysis in the last decade. However, also other MA approaches have many potentialities in the field and wait to be tested on X-ray diffraction data. Statistical methods have revolutionized the field in the past, producing disrupting advances in the crystal structure determination of small molecules and biological macromolecules. We expect to be close to a similar turning point regarding applications of artificial intelligence to solve complex problems related to basic crystallography, such as merging thousands of datasets from different crystals or finding phase values to diffraction amplitudes starting from random values. Neural networks have a great potential to tackle these problems and accomplish the non-linear deconvolution of multivariate data, provided a proper training is given.

The spread of use of MA methods is intimately connected with availability of software with friendly graphic interfaces available to scientific community. Programs like Root-Prof [90] or MCR-ALS 2.0 toolbox [91] have contributed to this goal, making MA available to scientists carrying out X-ray diffraction studies.

The possibility of exploiting automated processes—highly demanding in terms of computational resources, but very fast and with minimal user intervention—is highly attractive both for industrial applications, where X-ray diffraction is used for quality control and monitoring of production processes, and in fundamental research applications, where extremely fast data analysis tools are required to cope with very bright X-ray sources and detectors with fast readouts.

References

1. Pearson, K.; Yule, G.U.; Blanchard, N.; Lee, A. The Law of Ancestral Heredity. *Biometrika* **1903**, *2*, 211–236. [CrossRef]
2. Yule, G.U. On the Theory of Correlation. *J. R. Stat. Soc.* **1897**, *60*, 812–854. [CrossRef]
3. Hotelling, H. Analysis of a complex of statistical variables into principal components. *J. Educ. Psychol.* **1933**, *24*, 417. [CrossRef]
4. Jolliffe, I.T. *Principal Components Analysis*, 2nd ed.; Springer: Berlin, Germany, 2002.
5. Bellman, R.E. *Dynamic Programming*; Princeton University Press: Princeton, NJ, USA, 1957.
6. Brereton, R.G. The evolution of chemometrics. *Anal. Methods* **2013**, *5*, 3785–3789. [CrossRef]
7. Massart, D.L. The use of information theory for evaluating the quality of thin-layer chromatographic separations. *J. Chromatogr. A* **1973**, *79*, 157–163. [CrossRef]
8. Child, D. *The Essentials of Factor Analysis*, 3rd ed.; Bloomsbury Academic Press: London, UK, 2006.
9. Bro, R.; Smilde, A.K. Principal Component Analysis. *Anal. Methods* **2014**, *6*, 2812–2831. [CrossRef]
10. De Juan, A.; Jaumot, J.; Tauler, R. Multivariate Curve Resolution (MCR). Solving the mixture analysis problem. *Anal. Methods* **2014**, *6*, 4964–4976. [CrossRef]
11. Wold, S.; Sjöström, M.; Eriksson, L. PLS-regression: A basic tool of chemometrics. *Chemom. Intell. Lab. Syst.* **2001**, *58*, 109–130. [CrossRef]
12. Hellberg, S.; Sjöström, M.; Wold, S. The prediction of bradykinin potentiating potency of pentapeptides, an example of a peptide quantitative structure–activity relationship. *Acta Chem. Scand. B* **1986**, *40*, 135–140. [CrossRef]
13. Di Profio, G.; Salehi, S.M.; Caliandro, R.; Guccione, P. Bioinspired Synthesis of $CaCO_3$ Superstructures through a Novel Hydrogel Composite Membranes Mineralization Platform: A Comprehensive View. *Adv. Mater.* **2015**, *28*, 610–616. [CrossRef]
14. Ballabio, D.; Consonni, V. Classification tools in chemistry: Part 1: Linear models. PLS-DA. *Anal. Methods* **2013**, *5*, 3790–3798. [CrossRef]
15. Xu, Y.; Zomer, S.; Brereton, R. Support vector machines: A recent method for classification in chemometrics. *Crit. Rev. Anal. Chem.* **2006**, *36*, 177–188. [CrossRef]
16. Ellis, D.L.; Brewster, V.L.; Dunn, W.B.; Allwood, J.W.; Golovanov, A.P.; Goodacrea, R. Fingerprinting food: Current technologies for the detection of food adulteration and contamination. *Chem. Soc. Rev.* **2012**, *41*, 5706–5727. [CrossRef] [PubMed]
17. Alvarez-Guerra, M.; Ballabio, D.; Amigo, J.M.; Viguri, J.R.; Bro, R. A chemometric approach to the environmental problem of predicting toxicity in contaminated sediments. *J. Chemom.* **2009**, *24*, 379–386. [CrossRef]
18. Heinemann, J.; Mazurie, A.; Lukaszewska, M.T.; Beilman, G.L.; Bothner, B. Application of support vector machines to metabolomics experiments with limited replicates. *Metabolomics* **2014**, *10*, 1121–1128. [CrossRef]
19. Huang, S.; Cai, N.; Pacheco, P.P.; Narandes, S.; Wang, Y.; Xu, W. Applications of SVM Learning Cancer Genomics. *Cancer Genom. Proteom.* **2018**, *15*, 41–51.
20. Schwaighofer, A.; Ferfuson-Miller, S.; Naumann, R.L.; Knoll, W.; Nowak, C. Phase-sensitive detection in modulation excitation spectroscopy applied to potential induced electron transfer in crytochrome c oxidase. *Appl. Spectrosc.* **2014**, *68*, 5–13. [CrossRef]
21. Izenmann, A.J. Introduction to Manifold Learning. *WIREs Comput. Stat.* **2012**, *4*, 439–446. [CrossRef]
22. Jaumot, J.; Tauler, R.; Gargallo, R. Exploratory data analysis of DNA microarrays by multivariate curve resolution. *Anal. Biochem.* **2006**, *358*, 76–89. [CrossRef]
23. Culhane, A.C.; Thioulouse, J.; Perrière, G.; Higgins, D.G. MADE4: An R package for multivariate analysis of gene expression data. *Bioinformatics* **2005**, *21*, 2789–2790. [CrossRef]
24. James, G.; Witten, D.; Hastie, T.; Tibshirani, R. *An Introduction to Statistical Learning*, 8th ed.; Casella, G., Fienberg, S., Olkin, I., Eds.; Springer: Berlin/Heidelberg, Germany, 2013; p. 204.
25. Quinlan, J.R. Induction of Decision Trees. *Mach. Learn.* **1986**, *1*, 81–106. [CrossRef]
26. Kira, K.; Rendell, L. A Practical Approach to Feature Selection. In Proceedings of the Ninth International Workshop on Machine Learning, Aberdeen, UK, 1–3 July 1992; pp. 249–256.
27. Kumar, A.P.; Valsala, P. Feature Selection for high Dimensional DNA Microarray data using hybrid approaches. *Bioinformation* **2013**, *9*, 824–828. [CrossRef]
28. Giannopoulou, E.G.; Garbis, S.D.; Vlahou, A.; Kossida, S.; Lepouras, G.; Manolakos, E.S. Proteomic feature maps: A new visualization approach in proteomics analysis. *J. Biomed. Inform.* **2009**, *42*, 644–653. [CrossRef] [PubMed]
29. Lualdi, M.; Fasano, M. Statistical analysis of proteomics data: A review on feature selection. *J. Proteom.* **2019**, *198*, 18–26. [CrossRef] [PubMed]
30. Anton, H.; Rorres, C. *Elementary Linear Algebra (Applications Version)*, 8th ed.; John Wiley & Sons: Hoboken, NJ, USA, 2000.

31. Stasiak, J.; Koba, M.; Gackowski, M.; Baczek, T. Chemometric Analysis for the Classification of some Groups of Drugs with Divergent Pharmacological Activity on the Basis of some Chromatographic and Molecular Modeling Parameters. *Comb. Chem. High Throughput Screen.* **2018**, *21*, 125–137. [CrossRef] [PubMed]
32. Harshman, R.A.; Hong, S.; Lundy, M.E. Shifted factor analysis—Part I: Models and properties. *J. Chemometr.* **2003**, *17*, 363–378. [CrossRef]
33. Hong, S. Warped factor analysis. *J. Chemom.* **2009**, *23*, 371–384. [CrossRef]
34. Zhou, Y.; Wilkinson, D.; Schreiber, R.; Pan, R. Large-Scale Parallel Collaborative Filtering for the Netflix Prize. In *Algorithmic Aspects in Information and Management*; Springer: Berlin/Heidelberg, Germany, 2008; pp. 337–348.
35. Chernyshov, D.; Van Beek, W.; Emerich, H.; Milanesio, M.; Urakawa, A.; Viterbo, D.; Palin, L.; Caliandro, R. Kinematic diffraction on a structure with periodically varying scattering function. *Acta Cryst. A* **2011**, *67*, 327–335. [CrossRef]
36. Urakawa, A.; Van Beek, W.; Monrabal-Capilla, M.; Galán-Mascarós, J.R.; Palin, L.; Milanesio, M. Combined, Modulation Enhanced X-ray Powder Diffraction and Raman Spectroscopic Study of Structural Transitions in the Spin Crossover Material [Fe(Htrz)2(trz)](BF4)]. *J. Phys. Chem. C* **2011**, *115*, 1323–1329. [CrossRef]
37. Uschmajew, A. Local Convergence of the Alternating Least Square Algorithm for Canonical Tensor Approximation. *J. Matrix Anal. Appl.* **2012**, *33*, 639–652. [CrossRef]
38. Comona, P.; Luciania, X.; De Almeida, A.L.F. Tensor decompositions, alternating least squares and other tales. *J. Chemom.* **2009**, *23*, 393–405. [CrossRef]
39. Malinowski, E.R. Theory of the distribution of error eigenvalues resulting from principal component analysis with applications to spectroscopic data. *J. Chemom.* **1987**, *1*, 33–40. [CrossRef]
40. Malinowski, E.R. Statistical F-tests for abstract factor analysis and target testing. *J. Chemom.* **1989**, *3*, 49–60. [CrossRef]
41. Guttman, L. Some necessary conditions for common factor analysis. *Psychometrika* **1954**, *19*, 149–161. [CrossRef]
42. Kaiser, H.F. The application of electronic computers to factor analysis. *Educ. Psychol. Meas.* **1960**, *20*, 141–151. [CrossRef]
43. Caliandro, R.; Guccione, P.; Nico, G.; Tutuncu, G.; Hanson, J.C. Tailored Multivariate Analysis for Modulated Enhanced Diffraction. *J. Appl. Cryst.* **2015**, *48*, 1679–1691. [CrossRef]
44. Silverman, B.W. Smoothed functional principal components analysis by choice of norm. *Ann. Stat.* **1996**, *24*, 1–24. [CrossRef]
45. Chen, Z.-P.; Liang, Y.-Z.; Jiang, J.-H.; Li, Y.; Qian, J.-Y.; Yu, R.-Q. Determination of the number of components in mixtures using a new approach incorporating chemical information. *J. Chemom.* **1999**, *13*, 15–30. [CrossRef]
46. Dharmayat, S.; Hammond, R.B.; Lai, X.; Ma, C.; Purba, E.; Roberts, K.J.; Chen, Z.-P.; Martin, E.; Morris, J.; Bytheway, R. An Examination of the Kinetics of the Solution-Mediated Polymorphic Phase Transformation between α- and β-Forms of l-Glutamic Acid as Determined Using Online Powder X-ray Diffraction. *Cryst. Growth Des.* **2008**, *8*, 2205–2216. [CrossRef]
47. Turner, T.D.; Caddick, S.; Hammond, R.B.; Roberts, K.J.; Lai, X. Kinetics of the Aqueous-Ethanol Solution Mediated Transformation between the Beta and Alpha Polymorphs of p-Aminobenzoic Acid. *Cryst. Growth Des.* **2018**, *18*, 1117–1125. [CrossRef]
48. Caliandro, R.; Chernyshov, D.; Emerich, H.; Milanesio, M.; Palin, L.; Urakawa, A.; Van Beek, W.; Viterbo, D. Patterson selectivity by modulation-enhanced diffraction. *J. Appl. Cryst.* **2012**, *45*, 458–470. [CrossRef]
49. Palin, L.; Caliandro, R.; Viterbo, D.; Milanesio, M. Chemical selectivity in structure determination by the time dependent analysis of in situ XRPD data: A clear view of Xe thermal behavior inside a MFI zeolite. *Phys. Chem. Chem. Phys.* **2015**, *17*, 17480–17493. [CrossRef] [PubMed]
50. Guccione, P.; Palin, L.; Milanesio, M.; Belviso, B.D.; Caliandro, R. Improved multivariate analysis for fast and selective monitoring of structural dynamics by in situ X-ray powder diffraction. *Phys. Chem. Chem. Phys.* **2018**, *20*, 2175–2187. [CrossRef] [PubMed]
51. Chernyshov, D.; Dovgaliuk, I.; Dyadkin, V.; Van Beek, W. Principal Component Analysis (PCA) for Powder Diffraction Data: Towards Unblinded Applications. *Crystals* **2020**, *10*, 581. [CrossRef]
52. Conterosito, E.; Palin, L.; Caliandro, R.; Van Beek, W.; Chernyshov, D.; Milanesio, M. CO2 adsorption in Y zeolite: A structural and dynamic view by a novel principal-component-analysis-assisted in situ single-crystal X-ray diffraction experiment. *Acta Cryst. A* **2019**, *75*, 214–222. [CrossRef] [PubMed]
53. Lopresti, M.; Palin, L.; Alberto, G.; Cantamessa, S.; Milanesio, M. Epoxy resins composites for X-ray shielding materials additivated by coated barium sulfate with improved dispersibility. *Mater. Today Commun.* **2020**, *20*, 101888. [CrossRef]
54. Palin, L.; Milanesio, M.; Van Beek, W.; Conterosito, E. Understanding the Ion Exchange Process in LDH Nanomaterials by Fast In Situ XRPD and PCA-Assisted Kinetic Analysis. *J. Nanomater.* **2019**, *2019*, 4612493. [CrossRef]
55. Kumar, S.; Carniato, F.; Arrais, A.; Croce, G.; Boccaleri, E.; Palin, L.; Van Beek, W.; Milanesio, M. Investigating Surface vs Bulk Kinetics in the Formation of a Molecular Complex via Solid-State Reaction by Simultaneous Raman/X-ray Powder Diffraction. *Cryst. Growth Des.* **2009**, *9*, 3396–3404. [CrossRef]
56. Matos, C.R.S.; Xavier, M.J.; Barreto, L.S.; Costa, N.B.; Gimenez, I.F. Principal Component Analysis of X-Ray Diffraction Patterns to Yield Morphological Classification of Brucite Particles. *Anal. Chem.* **2007**, *75*, 2091–2095. [CrossRef]
57. Guccione, P.; Palin, L.; Belviso, B.D.; Milanesio, M.; Caliandro, R. Principal component analysis for automatic extraction of solid-state kinetics from combined in situ experiments. *Phys. Chem. Chem. Phys.* **2018**, *20*, 19560–19571. [CrossRef]
58. Conterosito, E.; Lopresti, M.; Palin, L. In Situ X-Ray Diffraction Study of Xe and CO2 Adsorption in Y Zeolite: Comparison between Rietveld and PCA-Based Analysis. *Crystals* **2020**, *10*, 483. [CrossRef]
59. Rodriguez, M.A.; Keenan, M.R.; Nagasubramanian, G. In situ X-ray diffraction analysis of (CFx)n batteries: Signal extraction by multivariate analysis. *J. Appl. Cryst.* **2007**, *40*, 1097–1104. [CrossRef]

60. Taris, A.; Grosso, M.; Brundu, M.; Guida, V.; Viani, A. Reaction Monitoring of Cementing Materials through Multivariate Techniques Applied to In Situ Synchrotron X-Ray Diffraction Data. *Comput. Aided Chem. Eng.* **2015**, *37*, 1535–1540.
61. Taris, A.; Grosso, M.; Brundu, M.; Guida, V.; Viani, A. Application of combined multivariate techniques for the description of time-resolved powder X-ray diffraction data. *J. Appl. Cryst.* **2017**, *50*, 451–461. [CrossRef]
62. Caliandro, R.; Altamura, D.; Belviso, B.D.; Rizzo, A.; Masi, S.; Giannini, C. Investigating temperature-induced structural changes of lead halide perovskites by in situ X-ray powder diffraction. *J. Appl. Cryst.* **2019**, *52*, 1104–1118. [CrossRef]
63. Caliandro, R.; Toson, V.; Palin, L.; Conterosito, E.; Aceto, M.; Boccaleri, E.; Gianotti, V.; Dooryhee, E.; Milanesio, M. New hints on Maya Blue formation process by PCA-assisted in situ XRPD/PDF and optical spectroscopy. *Chem. Eur. J.* **2019**, *25*, 11503–11511. [CrossRef]
64. Rizzuti, A.; Caliandro, R.; Gallo, V.; Mastrorilli, P.; Chita, G.; Latronico, M. A combined approach for characterisation of fresh and brined vine leaves by X-ray powder diffraction, NMR spectroscopy and direct infusion high resolution mass spectrometry. *Food Chem.* **2013**, *141*, 1908–1915. [CrossRef] [PubMed]
65. Fomina, E.; Kozlov, E.; Bazai, A. Factor Analysis of XRF and XRPD Data on the Example of the Rocks of the Kontozero Carbonatite Complex (NW Russia). Part I: Algorithm. *Crystals* **2020**, *10*, 874. [CrossRef]
66. Kozlov, E.; Fomina, E.; Khvorov, P. Factor Analysis of XRF and XRPD Data on the Example of the Rocks of the Kontozero Carbonatite Complex (NW Russia). Part II: Geological Interpretation. *Crystals* **2020**, *10*, 873. [CrossRef]
67. Goodpaster, A.M.; Kennedy, M.A. Quantification and statistical significance analysis of group separation in NMR-based metabonomics studies. *Chemom. Intell. Lab. Syst.* **2011**, *109*, 162–170. [CrossRef]
68. Worley, B.; Halouska, S.; Powers, R. Utilities for Quantifying Separation in PCA/PLS-DA Scores Plots. *Anal. Biochem.* **2013**, *433*, 102–104. [CrossRef] [PubMed]
69. Caliandro, R.; Belviso, B.D. RootProf: Software for multivariate analysis of unidimensional profiles. *J. Appl. Cryst.* **2014**, *47*, 1087–1096. [CrossRef]
70. Cornell, J.A. *Experiments with Mixtures: Designs, Models, and the Analysis of Mixture Data*, 3rd ed.; John Wiley & Sons: Hoboken, NJ, USA, 2002.
71. Caliandro, R.; Di Profio, G.; Nicolotti, O. Multivariate analysis of quaternary carbamazepine-saccharin mixtures by X-ray diffraction and infrared spectroscopy. *J. Pharm. Biomed. Anal.* **2013**, *78–79*, 269–279. [CrossRef] [PubMed]
72. Lee, J.-W.; Park, W.B.; Lee, J.H.; Sing, S.P.; Sohn, K.-S. A deep-learning technique for phase identification in multiphase inorganic compounds using synthetic XRD powder patterns. *Nat. Commun.* **2020**, *11*, 86. [CrossRef] [PubMed]
73. Pannu, N.S.; McCoy, A.J.; Read, R.J. Application of the complex multivariate normal distribution to crystallographic methods with insights into multiple isomorphous replacement phasing. *Acta Cryst. D* **2003**, *59*, 1801–1808. [CrossRef] [PubMed]
74. Hauptman, H.; Karle, J. *The Solution of the Phase Problem. I: The Centrosymmetric Crystal*; ACA Monograph No. 3; American Crystallographic Association: New York, NY, USA, 1953.
75. Shmueli, U.; Weiss, G.H. Probabilistic Methods in Crystal Structure Analysis. *J. Am. Stat. Assoc.* **1990**, *85*, 6–19. [CrossRef]
76. Giacovazzo, C. *Direct Methods in Crystallography*; Oxford University Press: Oxford, UK, 1980.
77. Giacovazzo, C. *Phasing in Crystallography*; Oxford University Press: Oxford, UK, 2013.
78. Skubák, P.; Murshudov, G.N.; Pannu, N.S. Direct incorporation of experimental phase information in model refinement. *Acta Cryst. D* **2004**, *60*, 2196–2201. [CrossRef]
79. Read, R.J. Pushing the boundaries of molecular replacement with maximum likelihood. *Acta Cryst. D* **2001**, *57*, 1373–1382. [CrossRef]
80. David, C.C.; Jacobs, D.J. Principal component analysis: A method for determining the essential dynamics of proteins. *Methods Mol. Biol.* **2014**, *1084*, 193–226.
81. Herranz-Trillo, F.; Groenning, M.; Van Maarschalkerweerd, A.; Tauler, R.; Vestergaard, B.; Bernardò, P. Structural Analysis of Multi-component Amyloid Systems by Chemometric SAXS Data Decomposition. *Structure* **2017**, *25*, 5–15. [CrossRef]
82. Foadi, J.; Aller, P.; Alguel, Y.; Cameron, A.; Axford, D.; Owen, R.L.; Armour, W.; Waterman, D.G.; Iwata, S.; Evans, G. Clustering procedures for the optimal selection of data sets from multiple crystals in macromolecular crystallography. *Acta Cryst. D* **2013**, *69*, 1617–1632. [CrossRef]
83. Winter, G.; Waterman, D.G.; Parkhurst, J.M.; Brewster, A.S.; Gildea, R.J.; Gerstel, M.; Fuentes-Montero, L.; Vollmar, M.; Michels-Clark, T.; Young, I.D.; et al. DIALS: Implementation and evaluation of a new integration package. *Acta Cryst. D* **2018**, *74*, 85–97. [CrossRef] [PubMed]
84. Beilsten-Edmands, J.; Winter, G.; Gildea, R.; Parkhurst, J.; Waterman, D.; Evans, G. Scaling diffraction data in the DIALS software package: Algorithms and new approaches for multi-crystal scaling. *Acta Cryst. D* **2020**, *76*, 385–399. [CrossRef] [PubMed]
85. Gavira, J.A.; Otálora, F.; González-Ramírez, L.A.; Melero, E.; Driessche, A.E.; García-Ruíz, J.M. On the Quality of Protein Crystals Grown under Diffusion Mass-transport Controlled Regime (I). *Crystals* **2020**, *10*, 68. [CrossRef]
86. Berntson, A.; Stojanoff, V.; Takai, H. Application of a neural network in high-throughput protein crystallography. *J. Synchrotron Radiat.* **2003**, *10*, 445–449. [CrossRef] [PubMed]
87. Bruno, A.E.; Charbonneau, P.; Newman, J.; Snell, E.H.; So, D.R.; Vanhoucke, V.; Watkins, C.J.; Williams, S.; Wilson, J. Classification of crystallization outcomes using deep convolutional neural networks. *PLoS ONE* **2018**, *13*, e0198883. [CrossRef]
88. Mele, K.; Lekamge, B.M.T.; Fazio, V.J.; Newman, J. Using Time Courses to Enrich the Information Obtained from Images of Crystallization Trials. *Cryst. Growth Des.* **2014**, *14*, 261–269. [CrossRef]

89. Snell, E.H.; Nagel, R.M.; Wojtaszcyk, A.; O'Neill, H.; Wolfley, J.L.; Luft, J.R. The application and use of chemical space mapping to interpret crystallization screening results. *Acta Cryst. D* **2008**, *64*, 1240–1249. [CrossRef]
90. Available online: http://www.ba.ic.cnr.it/softwareic/rootprof/ (accessed on 24 December 2020).
91. Available online: https://mcrals.wordpress.com/download/mcr-als-2-0-toolbox/ (accessed on 24 December 2020).

IETeasy: An open source and low-cost instrument for impulse excitation technique, applied to materials classification by acoustical and mechanical properties assessment

Sorry, Homer. I was born a snake handler, and I'll die a snake handler.

Szyslak, M.

IETeasy: An open source and low-cost instrument for impulse excitation technique, applied to materials classification by acoustical and mechanical properties assessment.

Nazareno Massara [a], Enrico Boccaleri [a], Marco Milanesio [a], Mattia Lopresti [a,*]

[a] Università del Piemonte Orientale, Dipartimento di Scienze e Innovazione Tecnologica, Viale T. Michel 11, 15121 Alessandria, Italy

ARTICLE INFO

ABSTRACT

In the past twenty years, impulse excitation technique (IET) has become a widely diffused non-destructive technique in metal industry field. This success resides in its capability to determine with high precision and accuracy some elastic properties of materials, such as Young's modulus, shear modulus and Poisson's ratio. The technique, which is very fast and non-destructive, consists in exciting a sample by a mechanical input and registering the acoustic output that, once analyzed by Fast Fourier-Transformation (FFT), provides the resonant frequencies of the sample, with a fast data analysis procedure. The approach is thus very easy to be applied to most materials and cost and time effective. Despite these many advantages, IET is still an under exploited technique in academic research centres, that mainly rely on traditional destructive methods for the evaluation of such properties, for instance by the measurement of strain-stress curves. Commercial IET instruments, similarly to traditional ones, have costs spanning from many hundreds to thousands of dollars, limiting their diffusion in academic world but also in small companies with limited R&D or quality control expenses. Non-professional instruments can also give very precise results and can be successfully used in basic research and in quality control even if not certified as commercial ones. Moreover they can be easily customized according to specific user needs and sample features. Since no examples of low cost IET designs can still be found in the scientific literature, we fill the gap in this paper, giving instructions for a self-assembled instrument for IET analysis, with a cost in the range of 70–85 USD. Moreover, the collected calibration data are analyzed to prove that the instrument can be used for other purposes than the common elastic properties determination, but also for a fast and cheap material characterization exploiting a multivariate analysis approach. Calibration results show that IETeasy can be used in both academic and industrial field for quality control purposes as a low-cost, fast and efficient alternative to tensometers. Principal component analysis, applied in this paper for the first time to IET data analysis, was able to distinguish and classify steel from Al or Cu alloys from polymers, but also different steel grades, demonstrating its potential in massive and eventually automatic IET data analysis. Calculated mechanical properties fitted with good approximation the ranges expected for each sample.

© 2021 The Authors. Published by Elsevier Ltd. This is an open access article under the CC BY-NC-ND license (http://creativecommons.org/licenses/by-nc-nd/4.0/).

Hardware name	IETeasy
Subject area	• Engineering and Material Science
	• Educational Tools and Open Source Alternatives to Existing Infrastructure
Hardware type	• Measuring physical properties and in-lab sensors
	• Mechanical engineering and materials science
Open source license	CC-BY 4.0
Cost of hardware	Approximately 70 USD for the home-made version, approximately 85 USD for the material and additional 50 USD of machine time for the 3D-Printed version.
Source file repository	https://doi.org/10.17632/c8sxdwds5x.1

1. Hardware in context

In the last years of the 1990s, [1,2] Impulse Excitation Technique (IET) was proposed as an easily applicable method for the measurement of resonant frequencies of materials, which can be exploited to calculate elastic properties, such as Young's modulus, shear ratio and Poisson's coefficient. The approach can be thought of as playing a percussion instrument, which consists in generating a mechanical impulse in a sample, using a mallet or a projectile, and collecting the audible output sound-wave. The data collection can be performed by different sensors depending on the availability: microphones, accelerometers, piezoelectric sensors, or laser vibrometers. Then, data are processed usually by FFT, which converts the sound-wave signals in the time domain to spectral data in the frequency domain. In the obtained spectra, natural resonant frequencies of the samples are identified by the peak positions and, by applying Euler-Bernoulli beam theory for Free-Free boundary conditions [3], elastic properties of materials can be determined. Despite being a relatively simple approach, the accuracy of the technique is very high, and the uncertainty on the calculated moduli can be lowered to 0.1% [4]. IET is also very versatile and can be used in a wide range of temperatures (from $-50\,°C$ to $1700\,°C$ [2]) and in presence of different gases or in vacuum, depending on which sensor is equipped on the instrument (laser vibrometers is necessary for vacuum measurements). In the 2000s, the industrial world implemented this approach in the quality control processes, while regulatory bodies [5–7] provided technical standards for IET procedures. Despite its capability to provide precise and accurate results in a very short time, IET initially remained mainly confined in the industrial world and used for quality control purposes. However, even in this field, other expensive complementary techniques had been preferred to IET, such as the ultrasounds analysis, radiography and tomography [8], which are still the most used non-destructive techniques (NDT) for quality control and certification. In the last years, many notable academic research examples began to spread in the fields of the metallurgy [9–11], geology [12] and the science of ceramic materials [13–15]. Even if IET data are rich in information content, the main application of the technique consists in the measurement of elastic properties of materials, such as Young's modulus, shear modulus and Poisson's coefficient [16]. In some research articles, IET is used on samples to detect and study the nature of defects [17,11], stress [18] and voids [19]. The technique can be used, not only for the elastic characteristics of a material and its damping properties, but also for material classification and qualitative analysis of samples. For these purposes, multivariate statistical analysis can cover a key role with many unexplored and promising applications, with the most common pattern recognition and classification methods (Cluster analysis, principal component analysis, linear discriminant analysis) being used for sample identification. In more complex and wider data collections, machine learning can be also used to build an automated recognition system. These applications are still scarce in the scientific literature and this can be ascribed to two concurrent causes. On one hand, many professional instruments are often rather costly, especially the portable ones and do not allow the full analysis of the collected impulses due to factory settings or lacks of suitable algorithms. In particular, some instruments are designed to give the Young's module of sampled materials as output, which is only one of the responses that can be extracted by a complete analysis of the impulse. Academic research requires a direct control and handling of raw data. On the other hand, despite being known as a technique that does not require a professional equipment, in scientific literature, no examples of low-cost and/or open source instruments for IET can be found. To overcome these obstacles hindering a wider diffusion in academic world, but also in small companies not able to afford a professional instrument, a self-built instrument for IET analysis (IETeasy) is presented in two different versions: one built in spruce wood and another one, identical in shape but in polylactic acid (PLA), made by 3D-Printing. The main difference between the two setups resides in their aesthetic, with the 3D-printed version being more elegant than the spruce wood one. However, the 3D-printed version, can be reproduced more easily in many identical exemplars. Some samples of different materials were then analyzed with the IETeasy and both raw and processed data are provided in an online Mendeley Data repository [20] and described in the respective data article [21]. Descriptive statistics on the collected data and a demonstration of the capability in materials recognition are provided in Section 7. Young's moduli for these materials were calculated and compared to the expected ones reported in literature or in technical data sheets. Finally, the potentialities of principal component analysis (PCA) in fast, efficient and eventually automatic analysis of very large data set by IET spectroscopy is demonstrated, since PCA can be a con-

venient complementary or alternative approach to Fourier transform based methods, as demonstrated in crystallography field by some of us [22].

2. Hardware description

IETeasy is an instrument very simple in its design, composed by two separate parts: a sample-holding frame and a mallet support. The first part is a frame with two taut nylon strings with diameter of 0.5mm. The strings have the task of supporting the sample and, at the same time, implementing Free-Free boundary conditions as well as possible by placing them along the nodal lines of the desired vibration mode. Inside the frame, a passing bar is placed with a centimeter scale, used to measure the distance between the two strings and guarantee that all the data collections are done in the same conditions. The centimeter scale is, not only convenient to guarantee that data are collected in the same conditions, but also to place the strings along the nodal lines. Moreover, the central bar has the task of supporting the strings, in order to avoid distortion effects that can be caused the string vibrations against flat surfaces of the frame. The mallet support consists in a xylophone mallet mounted on a wooden standing support which has the task of preventing differences in the exciting impulse strength. Being only gravity-based, the hitting strength of the mallet is always the same, which guarantees that the measurement as reproducible as possible. A USB condenser microphone connected to a PC is used as acquisition setup. The head of the microphone is positioned above the sample and directed toward its upper side, as displayed in Fig. 1. An average acquisition spans between 8 and 12s, depending on how much damped is the sound produced by the sample.

2.1. Traditional data analysis methods

The collected raw data are in the time domain and they can be used for the calculation of the damping parameter of the investigated samples, which gives an estimation of the material's behavior in response to an induced oscillation. It has to be considered that the calculation of the acoustic insulation can not be accurate with this setup, as the air viscosity it's usually not negligible. Vacuum chamber and a laser vibrometer (or another non-acoustic sensor) are required for a precise measurement. Traditional analysis can be carried out on both time or frequency domain. The calculation can be done by refining the damped sound wave with an exponentially damped sine function in time domain in the form [23]:

$$s_t = Ae^{-kt}sin(2\pi f_r t + \phi) \tag{1}$$

where:

1. s_t is the collected sound wave in the time domain;
2. A is a scale coefficient that have to be refined;
3. k is the decrease parameter due to the damping;
4. t is the time;
5. f_r is the frequency of the fundamental flexion vibration mode;
6. ϕ is the wave phase.

Often, such refinements are not easy to perform due to the superposition of several modes. The time domain data are then processed by FFT to transform the signal in the frequency domain and extract the resonant frequencies, which can be used for qualitative analysis or to calculate the mechanical properties, or even to determine if a sample has structural defects. For mechanical properties, on rectangular samples (the ones for which this instrument is designed), Young's modulus (E) of rectangular samples can be calculated as [5,7,6]:

(a)   (b)
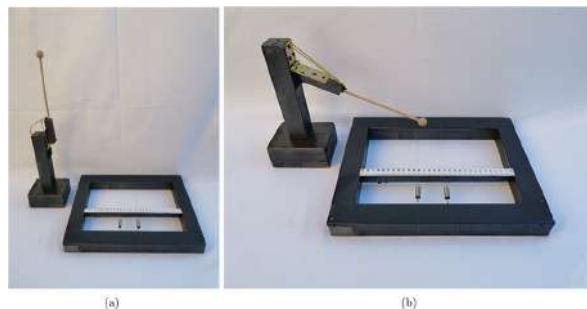
Fig. 1. One of the wooden self-built version of IETeasy instrument.

$$E = 0.9465 \left(\frac{m^2 f_r^2}{w} \right) \left(\frac{l^3}{t^3} \right) C \tag{2}$$

Where:

1. m is the mass in kilograms of the sample;
2. f_r is the frequency of the fundamental flexion vibration mode;
3. w is the width in metres of the sample;
4. l is the length in metres of the sample;
5. t is the thickness in metres of the sample;
6. C is the correction factor defined as:

$$C = 1 + 6.585 \left(\frac{t}{l} \right)^2 \tag{3}$$

The correction factor should be used only when $l/t \geqslant 20$.

2.2. Multivariate data analysis as a fast and efficient approach to IET data

Multivariate analysis allows a precise qualitative analysis and, differently from traditional data analysis, can be performed for classification purposes on both time domain and FFT-processed frequency data. In other fields, it resulted a very efficient alternative or complementary technique to FFT based method, as demonstrated by some of us in crystallography [22,24]. One of the main advantages of using a multivariate approach consists in the reduction of dimensionality, in which useful information is extracted from a large set of variables and rewritten in a few "easy to interpret" variables. More important is its capability of easily, fastly and very efficiently analysing very large dataset also in an automatic fashion. In this paper we demonstrated PCA huge potentialities in IETeasy data analysis, and in general, on IET data. Consequently, a fast data analysis coupled to a tool that can produce a huge amount of data in a short time is suitable for on-line analysis (i.e. waste disposal centres). Of course no direct advantage is evident in the small training set used in this paper, but PCA can be easily applied to thousands of data set in a few time and also in an automatic fashion, differently from traditional analysis methods, using mostly (or only) the fundamental frequency. An example of this approach is given in Section 7.3 with the principal component analysis applied to the validation of the data. Also, by measuring series of samples with the same size and shape, it is possible to determine whether defectivity or deviation from conformity is present in a sample or not, making an automatic version of this instrument a good candidate for an on-line quality control.

- Mechanical properties can be determined with high precision and accuracy on materials of different natures;
- Classification analysis can be performed by using both time domain and frequency domain data. Samples can be very well distinguished in the corresponding classes with a highly precise approach;
- By calculating the damping coefficient, a rough estimation of the acoustic insulation of the material can be performed. The use of a vacuum chamber and a laser vibrometer might improve the precision of the calculation, but such approach is beyond the scope of the present contribution.

3. Design files

For the wood version of the IETeasy, detailed building instructions and illustrations are reported in Section 5, therefore no design files were produced. For the 3D-Printed version of the instrument, the required .stl files can be found as Supplementary material of the present article. All files are detailed in the following table.

3.1. Design files summary

Design filename	File type	Open source license	Location of the file
angle a	stl 3D file	CC BY-NC-ND 4.0	Available within the repository
angle b	stl 3D file	CC BY-NC-ND 4.0	Available within the repository
base a	stl 3D file	CC BY-NC-ND 4.0	Available within the repository
base b	stl 3D file	CC BY-NC-ND 4.0	Available within the repository
central bar	stl 3D file	CC BY-NC-ND 4.0	Available within the repository
canti	stl 3D file	CC BY-NC-ND 4.0	Available within the repository
pin a	stl 3D file	CC BY-NC-ND 4.0	Available within the repository
pin b	stl 3D file	CC BY-NC-ND 4.0	Available within the repository

4. Bill of materials

4.1. Bill of the wood structure

Designator	Number	Cost per unit currency	Total cost	Source of materials	Material type
Wood strip 40 mm × 40 mm × 1 m	3	4.04 USD per piece	12.12 USD	Leroy Merlin	Spruce wood
Wood strip 20 mm × 20 mm × 1 m	1	2.49 USD per piece	2.49 USD	Leroy Merlin	Spruce wood
Vinyl glue	1	2.40 USD per 225 g	2.40 USD	Leroy Merlin	Vinyl glue
Wood screw 6 mm × 4 mm	7	14.70 USD per kg	0.25 USD	Leroy Merlin	Bronzed steel

4.2. Bill of the 3D-Printed structure

Designator	Number	Cost per unit currency	Total cost	Source of materials	Material type
angle a	2	35.69 USD per kg	11.64 USD	Aliexpress	PLA filament, ϕ = 1.75 mm
angle b	2	35.69 USD per kg	11.64 USD	Aliexpress	PLA filament, ϕ = 1.75 mm
base a	1	35.69 USD per kg	4.39 USD	Aliexpress	PLA filament, ϕ = 1.75 mm
base b	1	35.69 USD per kg	2.74 USD	Aliexpress	PLA filament, ϕ = 1.75 mm
central bar	1	35.69 USD per kg	1.64 USD	Aliexpress	PLA filament, ϕ = 1.75 mm
canti	1	35.69 USD per kg	0.36 USD	Aliexpress	PLA filament, ϕ = 1.75 mm
pin a	3	35.69 USD per kg	0.86 USD	Aliexpress	PLA filament, ϕ = 1.75 mm
pin a	4	35.69 USD per kg	0.22 USD	Aliexpress	PLA filament, ϕ = 1.75 mm

For the 3D-printed version of the frame and the mallet support, the required total estimated time is of ≈100 h of machine time. For an average 3D-printer, the electric consumption is about 70W for an hour, using a heated bed temperature of 60°C and an hotend temperature of 205°C. Therefore, the costs of the 3D-printing process can not be ignored and are estimated as 50 USD, depending on the cost of 1 kWh and common maintenance costs.

4.3. Bill of the essentials

Designator	Number	Cost per unit currency	Total cost	Source of materials	Material type
Nylon wire 0.5 mm × 100 m	1	5.91 USD per 100 m	5.91 USD	Leroy Merlin	Nylon
Electrician clamp	2	2.77 USD 12 pieces	0.46 USD	Amazon	Plastic and brass clamps
Xylophone mallet	1	9.15 USD 4 pieces	2.29 USD	Amazon	Wood mallet
USB condenser microphone	1	40.23 USD per piece	40.23 USD	Amazon	Composite
Flat hinge 25 mm	1	2.59 USD per piece	2.59 USD	Amazon	Steel

5. Build instructions

The dimensions and materials of the instrument have been arbitrarily chosen by the authors, based on the size of the samples that are usually analyzed in the laboratory work scale. Other materials and sizes can be chosen as needed. In particular, the mallet support is an optional component of the instrument as it was observed in the testing phase that even free-hand data impulses have excellent reproducibility on the position of the resonant frequencies. Mallet support has been incorporated into the basic design of the instrument as it helps standardize the intensities of spectral signals, which would otherwise be subject to high variability.

5.1. Frame and sample-holding strings

In this section, the "made in wood" IETeasy building instructions are reported. Concerning the corresponding PLA 3D-Printed version, the single pieces have unequivocal interlocks, thus no specific instructions are needed for assembling the PLA frame and the mallet support. Once the PLA frame is built, the operations for mounting the wires are the same of the wood version, therefore only instructions from point 4 onward are required for the 3D-Printed IETeasy version.

1. Two square stripes of spruce wood, one larger with section size of 4 cm, and one smaller with section size of 2 cm were cut to obtain the four frame pieces and the passing central bar that will hold the wires in tension as showed in Fig. 2(a). The larger strips are cut 40 cm in length, while the smaller strip is cut 32 cm long.
2. To avoid wood fissuring along its natural venatures, pre-holes for wood screws were made on the four corners before screwing together the four strips of the frame as shown in Fig. 2(b). The pre-holes were made using a battery drill with a 3.5 mm in diameter drill bit. The central bar was fixed with wood screws inserted in pre-holes as shown in Fig. 2(c). Every surface irregularity can be removed by using sandpaper for a better aesthetic result.
3. On the central bar a centimetre scale was glued (Fig. 2(d)) in order to have a reference of the distance between the sample-holding wires. It is not important that the centimetre scale is positioned at the beginning of the central bar, because it's unlikely that wires will be separated more than 20 centimetres due to possible collisions between the sample and the frame. If wanted, rubber feet can be attached to the lower part of the frame to keep all the instrument suspended from the underneath table for a better aesthetic result. As spruce wood is soft, the wire can indent the surface, metal plaque can be added to preserve the structure as displayed in Fig. 1.
4. Two pieces of 1 m each of nylon wire with diameter 0.5 mm was cut to make the sample holder. The wires are passed around both the central bar and the opposite side of the frame, as shown in Fig. 2(f). In the version showed in Fig. 2, wires are passed through two holes at the desired measurement distance. Optionally, the wires can be kept in tension using two steel springs, as shown in Fig. 1, which let wires to be custom-positioned at each measurement.
5. The two wires are then taut and kept in position by using electrician clamps. The wire tension can be checked by using a guitar tuner. In this case, an A_4 note was used to accord the wires, but this specific note is not necessary to obtain reproducible measurement: the important check is conversely having both wires equally taut and giving the same note, in order to avoid undesired damping effects on the sample.

5.2. Mallet support

Similarly to what stated for the frame, the 3D-Printed version of the mallet support does not require instructions as interlocks are unequivocal. Only flat hinge and mallet instructions have to be read, from the following point 3 onward.

1. Three pieces 12 cm long and 4 cm wide are glued together using vinyl glue in order to obtain a squared piece that will act as the base of the mallet support. Once the glue is set, surface irregularities can be removed by using sandpaper (Fig. 3(a)).
2. A strip 25 cm long and 4 cm wide and a strip 7 cm long and 2 cm wide are cut and will be used as stand part and mallet support respectively.
3. A pre-hole is made at the center of the base and a strip in order to fix by using a screw the 25 cm long piece as shown in Fig. 3(b). To avoid rotations of the vertical part, applying some glue is suggested.
4. A hole 1 cm deep, with a diameter slightly smaller than the one of the mallet strip is made on the flat part of the support as displayed in Fig. 3(c). The piece is fixed to the vertical mallet support with the hinge in order to have a semicircular movement toward the bottom. The mallet is glued and fixed in the proper hole as shown in Fig. 3(d).
5. A rubber band is used to keep the mallet suspended after the impulse is given. There is no particular indication about the rubber band, because it has to be evaluated by the user depending on the setup positioning. The authors used a standard commercial rubber band with a section of 1 mm $\times$ 5 mm and a diameter of 42 mm.

(a)   (b)   (c)

(d)   (e)   (f)
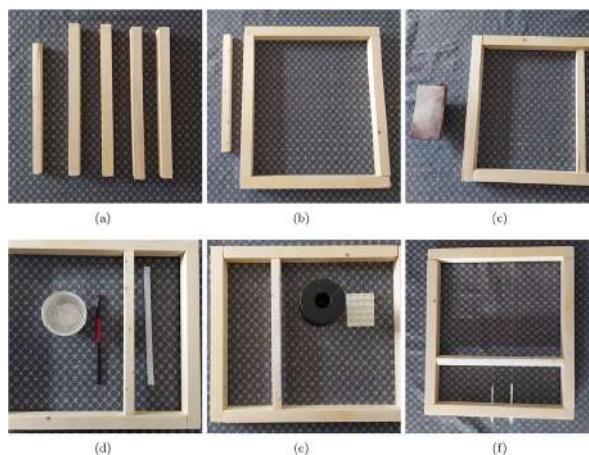
Fig. 2. Visual building instructions of the sample-holding frame.
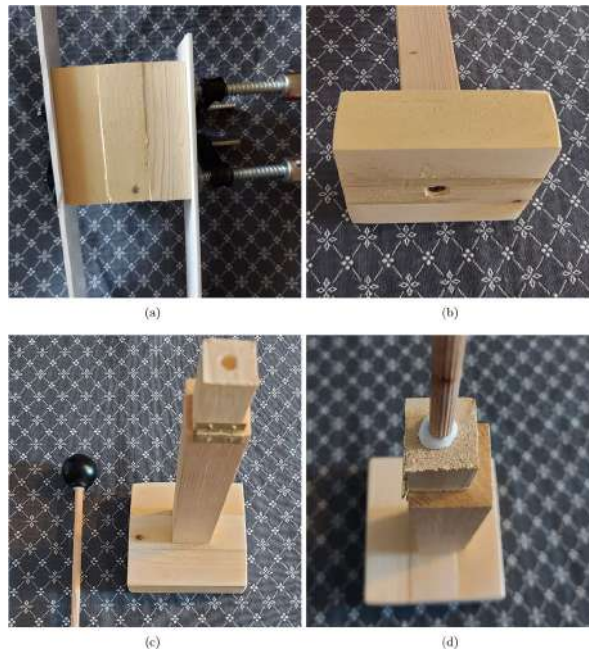
Fig. 3. Visual building instructions of the mallet support.

6. Operation instructions

- Place the instrument on a flat stable surface, with the microphone positioned as shown in Fig. 4. Check the distances between the frame and the mallet support and be sure that the mallet can hit the sample correctly once positioned.
- Connect the USB microphone to the PC used to record the impulse. Open the recording software and check that the USB microphone is default input device and that the audio signal is correctly read by the PC. In this paper, Audacity 2.4.2 [25] was used to manage sound sampling.
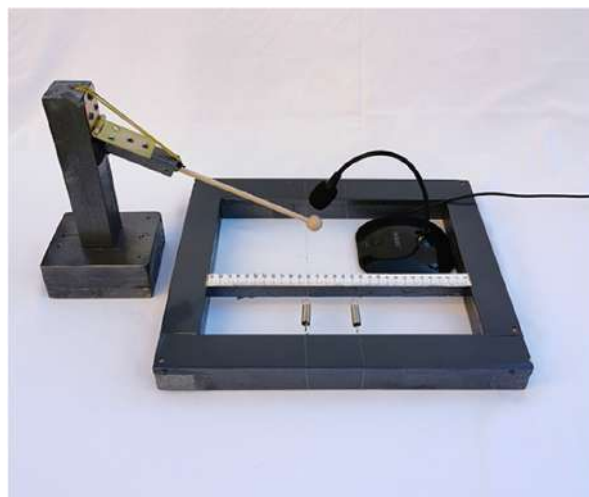
Fig. 4. Acquisition setup. The sample is positioned on the sample-holding strings and the mallet is released, giving the mechanical excitation to the material. The produced sound wave is collected by the microphone positioned over the sample and then is processed for further analyses.

- Check the correct distancing between the sample-holding strings. In this paper, standard distance is 5 cm as samples are about 10 cm long.
- Place the sample on the supporting strings and check that the microphone is correctly positioned over it as shown in Fig. 4.
- Start recording and, after few seconds, release the mallet.
- Stop recording after 5–6 s after the impulse production, when the damping is finished.

7. Validation and characterization

The IETeasy hardware was tested initially in its different components and with different purposes: at first, the uncertainty due to the microphone was tested (Subsection 7.1) by collecting notes generated at given frequencies. Then, real-world samples of fifteen different materials were measured by using IETeasy ten times each, in order to obtain descriptive statistics on the natural resonant frequencies of the materials, using an traditional univariate approach (Subsection 7.2). In this section, Young's moduli had been calculated and compared to the tabulated values on the corresponding technical data sheets for each material. In subSection 7.3, the whole frequency spectra were analyzed with a multivariate approach by using Principal Component Analysis (PCA) to demonstrate its capability in their classification and the potentialities of such an approach when dealing with thousand data files. For the validation of the hardware construction procedure, two different IETeasy instruments were built by two different users (NM and ML) and then massively used, thus suggesting that multiple IETeasy can easily be assembled and used for materials analysis and classification with good reproducibility.

7.1. Microphone distortion

The accuracy of the microphone was tested by putting it in front of a speaker and generating sound waves corresponding to the seven notes on nine octaves, from A_0 to B_8. Then, those sounds were recorded and processed with FFT to transform the time-domain signals in frequency-domain signals. In Table 1, the generated frequencies and the acquired ones are reported.

As can be seen in Table 1, the errors relative to the acquisition setup are very small and affecting the last one or two significant figures, therefore it can be assumed that the intrinsic overall error is less than the 0.01%, with respect to the measurement itself.

7.2. Characteristic resonant frequencies

Samples of different materials (metals and polymers), were then measured with ten repetitions each, and the collected data were processed by FFT to further analyses reported in Tables 2 and 3. Details on both the samples and the data collection and FFT algorithm are given in the related data article [21]. Obtained spectra were analyzed with the `pick.peaks` function of the `ChemometricsWithR` package in R, in order to extract the principal resonant frequencies. The results are very precise for alloys but then become more noisy for polymers, as their internal structure is very different, not only due to the long polymeric chains that have more degree of freedom, and a consequent less efficient phononic propagation, but also because of their amorphous structure, which causes an internal damping effect. When plotting the original sound-waves, it can be noticed that the acquisition time of polymers is far shorter than those from the alloys, simply because of the different damping of the materials.

By looking at the descriptive statistics in Table 4, calculated on the resonant frequencies of Tables 2 and 3, it can be observed that alloys samples best perform as reproducibility of the method, with a coefficient of variation of $10^{-3} - 10^{-4}$ percent. Polymers, due to their molecular structures, characterized by long interconnected chains and amorphous (or less crystalline) phases, have a greater variation coefficient, about 100 times greater than the ones obtained for metals. Despite this, the coefficient of variation of this material is still very low, being only 0.56%.

Table 1
Musical notes from A_0 to B_8. For each note the $_{read}$ value is the value obtained by processing by FFT the collected data, while the $_{gen}$ is the note produced by a frequency generator. All data are in Hz.

Octave	C_{read}	C_{gen}	D_{read}	D_{gen}	E_{read}	E_{gen}	F_{read}	F_{gen}	G_{read}	G_{gen}	A_{read}	A_{gen}	B_{read}	B_{gen}
0	–	–	–	–	–	–	–	–	–	–	27.480	27.500	30.879	30.868
1	32.705	32.703	36.722	36.708	41.209	41.203	43.639	43.654	49.014	48.999	55.006	55.000	61.727	61.735
2	65.405	65.406	73.416	73.416	82.435	82.407	87.336	87.307	97.999	97.999	110.02	110.00	123.47	123.47
3	130.86	130.81	146.84	146.83	164.79	164.81	174.60	174.61	196.02	196.00	220.00	220.00	246.95	246.94
4	261.70	261.63	293.75	293.67	329.65	329.63	349.32	349.23	392.03	392.00	440.05	440.00	493.88	493.88
5	523.28	523.25	587.41	587.33	659.30	659.23	698.49	698.46	784.04	783.99	880.14	880.00	987.92	987.77
6	1046.6	1046.5	1174.8	1174.7	1318.6	1318.5	1397.0	1396.9	1568.1	1568.0	1760.3	1760.0	1975.7	1975.5
7	2093.2	2093.0	2349.6	2349.3	2637.4	2637.0	2794.2	2793.8	3136.4	3136.0	3520.4	3520.0	3951.6	3951.0
8	4186.5	4186.0	4699.2	4698.6	5274.7	5274.0	5588.3	5587.7	6272.6	6271.9	7040.8	7240.0	7903.1	7902.1

Table 2

Frequencies of the fundamental flexion vibration mode in Hz for each sampled material. For each sample, 10 impulses were collected.

Sample #	AISI 304 steel	AISI 316 steel	Aluminum 6082	B10 bronze	B12 bronze	BrAl alloy	C45E steel
1	3845.167	4953.186	5171.082	4170.651	4487.253	2892.7	5045.326
2	3845.242	4953.369	5171.082	4170.583	4487.288	2892.654	5045.331
3	3845.200	4953.323	5171.082	4170.607	4487.262	2892.654	5045.390
4	3845.158	4953.278	5171.082	4170.714	4487.337	2892.609	5045.420
5	3845.233	4953.278	5171.082	4170.680	4487.334	2892.609	5045.444
6	3845.104	4953.186	5171.082	4170.622	4487.334	2892.609	5045.374
7	3845.164	4953.278	5171.173	4170.559	4487.361	2892.609	5045.371
8	3845.237	4953.278	5171.127	4170.637	4487.300	2892.609	5045.336
9	3845.153	4953.278	5171.036	4170.652	4487.277	2892.609	5045.406
10	3845.174	4953.278	5171.082	4170.697	4487.312	2892.609	5045.429

Table 3

Frequencies of the fundamental flexion vibration mode in Hz for each sampled material. For each sample, 10 impulses were collected.

Sample #	Copper	CW614 brass	Fe37 drawn	HDPE	Nylon 6	Pom-C	Teflon	X150 steel
1	3635.632	3072.876	4236.647	1520.05	1893.813	1814.667	840.150	5100.128
2	3635.591	3072.922	4236.590	1520.035	1921.683	1812.744	840.857	5100.128
3	3635.602	3072.922	4236.632	1519.958	1904.682	1815.308	839.649	5100.128
4	3635.535	3072.876	4236.697	1520.05	1917.503	1811.92	839.877	5100.128
5	3635.514	3072.876	4236.680	1519.684	1927.536	1811.462	839.375	5100.037
6	3635.520	3072.876	4236.646	1524.628	1907.469	1812.012	841.883	5100.128
7	3635.597	3072.876	4236.635	1522.293	1921.683	1810.822	839.945	5100.128
8	3635.492	3072.876	4236.641	1523.163	1917.503	1811.188	840.629	5100.128
9	3635.514	3072.876	4236.642	1523.071	1928.372	1811.646	841.884	5100.128
10	3635.512	3072.876	4236.679	1519.409	1917.503	1812.469	841.883	5100.137

Table 4

Descriptive statistics of the collected resonant frequencies.

Sample	Mean	Median	Range	Std.Dev.	Coef.Var.
AISI 304 steel	3845.183	3845.171	0.138	0.044284	0.001152
AISI 316 steel	4953.273	4953.278	0.183	0.054776	0.001106
Aluminum 6082	5171.091	5171.082	0.137	0.035920	0.000695
B10 bronze	4170.640	4170.644	0.155	0.049241	0.001181
B12 bronze	4487.306	4487.306	0.108	0.035801	0.000798
BrAl alloy	2892.627	2892.609	0.091	0.031719	0.001097
C45E steel	5045.383	5045.382	0.118	0.042387	0.000840
Copper	3635.551	3635.528	0.14	0.049256	0.00136
CW614 brass	3072.885	3072.876	0.046	0.019395	0.000631
Fe37 drawn	4236.649	4236.644	0.107	0.030289	0.000715
Nylon 6	1915.775	1917.503	34.559	10.801986	0.563844
HDPE	1521.234	1520.05	5.219	1.866040	0.122666
Pom-C	1812.424	1811.966	4.486	1.472017	0.081218
Teflon	840.6132	840.3895	2.509	0.975587	0.116057
X150 steel	5100.120	5100.128	0.1	0.029230	0.000573

Young's moduli of the analyzed materials were determined using Eq. 2. All calculated values are compared to the corresponding average values in Table 5. The reported tabulated values are taken from literature [26] or from specialized websites, as no experimental data were reported in technical data sheets given by the supplier. Stainless steel reported values that are about 30 GPa lower than the expected value, while for other materials the difference between the calculated and the expected data is very low.

As a final note on the reproducibility during IETeasy usage and on the stability of the whole hardware and its components, it must be pointed out that the two built instruments were massively used in preliminary analyses and in the campaign to obtain the data described in the Data in Brief article [21]. Hundreds measurements were carried out and resulted reproducible within time, without progressive drifts in the measurements and without changes in the experimental error, also comparing data by the two above-mentioned different instruments.

7.3. Multivariate analysis

PCA is a common method for pattern recognition analysis, which is often used to explore relationships between samples and variables. A detailed description of the method applied to xy data and the interpretation of its results is reported in a

Table 5

Calculated Young's moduli for the analyzed materials. The obtained values are compared to tabulated values from collections of technical data sheets.

Sample	Calculated Young's modulus	Tabulated Young's modulus
AISI 304 steel	166 GPa	193 GPa [26]
AISI 316 steel	170 GPa	193 GPa [26]
Aluminum 6082	69 GPa	67.0 GPa to 70.0 GPa [27,28]
B10 bronze	92.5 GPa	90 GPa to 110 GPa [29]
B12 bronze	93.9 GPa	90 GPa to 110 GPa [30]
BrAl alloy	119 GPa	125 GPa [31]
C45E steel	184 GPa	190 GPa [32]
Copper	132 GPa	118 GPa to 132 GPa [33]
CW614	107 GPa	105 GPa [34]
Fe37 drawn	201 GPa	200 GPa [35]
HDPE	2.16 GPa	0.65 GPa to 4.30 GPa [36]
Nylon 6	4.08 GPa	1.30 GPa to 4.20 GPa [37]
Pom-C	4.29 GPa	0.59 GPa to 11.7 GPa [38]
Teflon	1.19 GPa	0.39 GPa to 2.25 GPa [39]
X150 steel	181 GPa	190 GPa [40]

recent review published by some of us [24], in the field of powder crystallography. The same approach and concepts are here applied to IETeasy data to give an example on how a large collection of samples can be analyzed in a fast and efficient way to obtain a classification. The analysis was performed by using RootProf [41], a software developed at CNR of Bari and based on CERN's ROOT framework.

Collected data were processed by FFT and the resulting sound spectra were sub-sampled and analyzed by RootProf to test the capability in sample recognition for qualitative analysis purposes. Samples and data pre-processing are described in the corresponding article [21]. The sub-sampling consisted in arbitrarily dividing the whole data set in three different batches with different homogeneity concerning sample features. The subset are described as follows in order to submit to the software groups of data with increasingly difficulty in sample recognition and classification:

- Group 1 – full mixture: AISI 304 steel, aluminum 6082, copper and Teflon. This group is the most heterogeneous and simple to analyze, as the analyzed materials are very different one from another, with large differences in both number of peaks, intensities and peak broadening; the target is recognizing polymer from pure metals and alloys.
- Group 2 – Fe-based metals: AISI 304 steel, AISI 316 steel, C45E steel, Fe37 drawn, X150 steel. All these materials are iron-based alloys and have very similar compositions, that vary only for the ligands; the target is to distinguish the different steel grades.
- Group 3: nylon 6, high-density polyethylene (HDPE), pom-c and Teflon. All the analyzed materials are polymer-based. Even if the molecular structures are very different one from another, three of these samples (HDPE, pom-c and Teflon) have the fundamental resonant frequency in a range of 300Hz, with a noisy spectrum and broader peaks, if compared to the other analyzed materials; the target is to distinguish the polymers.

Before proceeding with the analysis, the only pre-processing that was carried out on the data was a normalization to reduce scale effects that could affect the analysis, as described on RootProf documentation [42]. As well, the range of frequencies that were analyzed spans from 0 Hz to 8000 Hz. No other pre-treatments were used in order to analyze the data with a blind approach, without using prior knowledge on the systems. However, along with the interpretation of the results, detailed suggestions on how to better analyze the results are given. The results of the analysis for the first group of samples can be observed in Fig. 5. The scree plot (Fig. 5(a)) shows that the first three principal components, the ones that the software considers reliable, explain the 62% of the total variance of the system. The explained variance in this situation can be increased by reducing the range of analysis and the variables in which no signals are present. Three PCs were selected by the algorithm also because the software automatically recognized four groups of samples very different one from the other. In this situation, PCA positions the n clusters on the vertices of an n-dimensional solid, for the representation of which $n - 1$-dimensions are required. Therefore, in this case, the four groups are on the vertices of a tetrahedron in a three dimensional space. In Fig. 5(b) and (c) this is confirmed by the projections of the samples in the principal component space (Score plot): PC1, PC2 and PC3 can be seen as the new x,y, and z axis, and the position of the samples are the projection of a tetrahedron on the two PC1-PC2 and PC1-PC3 planes. The four clusters are highlighted by the four coloured circles on the score plot, which are calculated by the software by using a hierarchical clusterization approach (Euclidean distances with group average method). In Fig. 5(d) is reported a colour map that represents the distances between the samples. The four different clusters are highlighted by the four blue squares along the diagonal of the matrix, which represent that the ten elements of each cluster have very little distances one from another, while they have greater distances between one group and another. This approach can be without effort extended to the analysis of thousand of data and, in a quality control vision, the result automatically analyzed to identify sample not conform to a defined standard and/or outliers. In Fig. 6 the results of the analysis performed on Group 2 and 3 are reported. Results of the analysis of Group 3 are very similar to the previous ones, with a
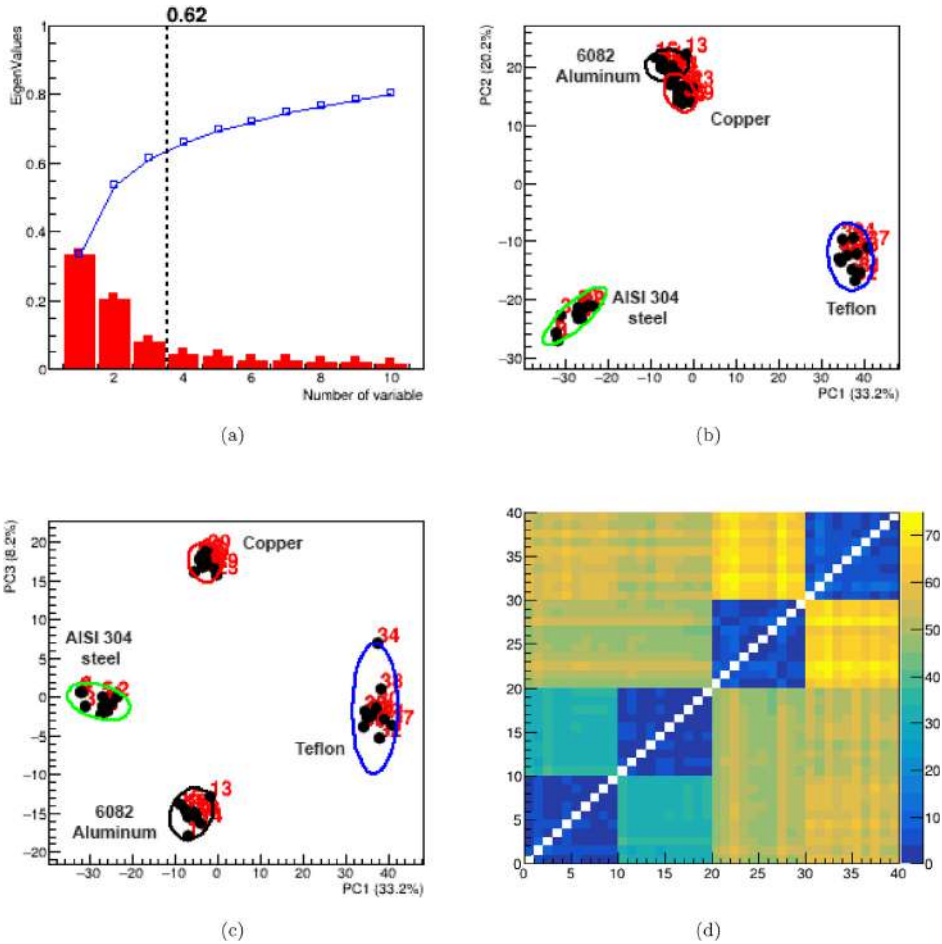
Fig. 5. Results of the qualitative analysis of the data group 1. (a): scree plot. (b): score plot of PC1 vs PC2. (c): score plot of PC1 vs PC3. (d): coloured map as representation of the distance matrix used for clusterization.

number of significant principal components which is equal to the number of samples minus one for a total explained variance of 54%. In the score plot of Fig. 6(a), samples 10–19 and samples 20–29 seem superimposed because of the projection of the data in a two-dimensional spaces, but by looking at Fig. 6(b), the two sample groups are well separated. The analysis on Group 3 samples, despite the noisy spectra recorded on the polymeric samples (showing broad peaks) gave satisfactory results, and the samples can be distinguished one from another, as shown in Fig. 6(d). The cumulative explained variance of the significant principal components is 48%. This value is rather smaller than previous three groups and is due to the noisy data. However, it must be noted that the raw data were analyzed and the explained variance (and thus the amount of extracted information, can be increased by pre-processing spectral data using pre-treatments and variable selection, commonly used in chemometrics.

- The IETeasy data collection is non-destructive, reproducible and accurate, making it suited for mechanical properties analysis. As shown at the beginning of this section, the coefficient of variation is very low ($\approx 0.001\%$ on metals and $\approx 1\%$ on polymers), demonstrating that the approach is excellent for the measurement of the properties of the materials and their classification.
- The PCA-cluster analysis, used for the first time on IET data, demonstrated that the instrument is suitable for in situ and ex situ qualitative analyses. The instrument, combined with any software for multivariate analysis is capable to recognize and classify different kinds of materials, spanning from hard materials such as alloys to soft ones such as polymers. many other materials, also of biological origin can be analyzed with the same approach.
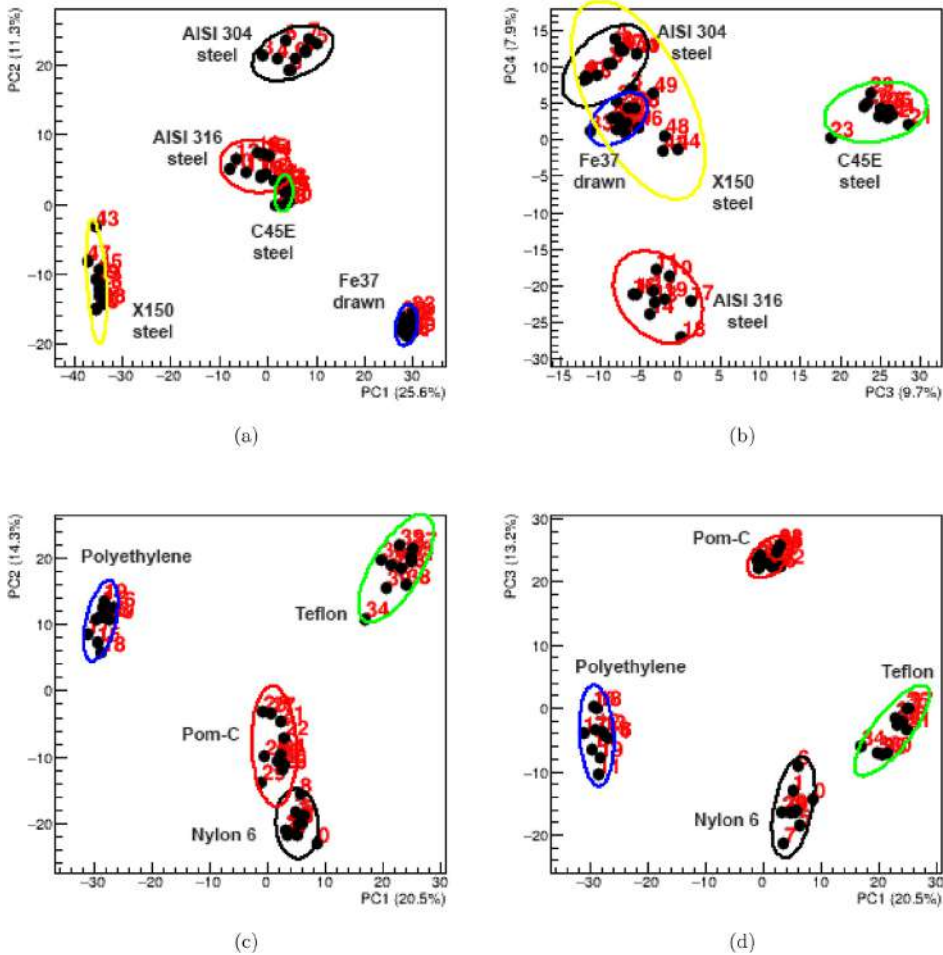
Fig. 6. Results of the qualitative analysis of the data Groups 2 (top) and 3 (bottom). (a): Score plot PC1-PC2. (b): Score plot PC3-PC4. (c): Score plot PC1-PC2. (d): Score plot PC1-PC3.

- Ellipses in score plots of Figs. 5 and 6 can be used to identify anomalies, as samples falling inside the ellipses are identified as "conform" and samples not included are "doubt" or "defective". This approach can be further investigated as a perspective of the present work, in the quality control philosophy of detecting problems (i.e. all samples not falling within the ellipses of Figs. 5 and 6) and thus reducing scraps.
- Data collected by IETeasy can be used for classification purposes even with different methods, that can be based on Linear Discriminant Analysis which uses the single frequencies or exploiting a machine learning approach that takes as an input the whole sound profiles or the frequency spectra of the samples.
- The power of multivariate approach of PCA applied to the whole spectra analysis, demonstrated in the present paper, can be winning when handling hundreds to thousands (or even more) data file, a typical situation in quality control procedures; moreover PCA allows obtaining more information with a reduced uncertainty with respect to traditional OVAT approaches, in a much shorter time, and eventually also in an automatic way; samples not conform to a defined standard can be easily (an also automatically) identified.

Authors' contribution

The instrument in Figure 1 was assembled by NM during his bachelor thesis under the guidance of ML. A second instrument was built by ML. Data collection was performed by NM and ML. Multivariate analysis was carried out by NM and ML. All the authors participated to data interpretation, edited the manuscript and approved its final version.

Declaration of Competing Interest

The authors declare that they have no known competing financial interests or personal relationships that could have appeared to influence the work reported in this paper.

Acknowledgements

Appendix A. Supplementary data

Supplementary data associated with this article can be found, in the online version, at https://doi.org/10.1016/j.ohx.2021. e00231.

References

[1] Gert Roebben, Bikramjit Basu, Jozef Vleugels, Jan Van Humbeeck, Omer Van der Biest, Impulse excitation apparatus to measure resonant frequencies, elastic moduli, and internal friction at room and high temperature, Rev. Sci. Instrum. 68 (12) (1997) 4511–4515.

[2] Gert Roebben, Bikramjit Basu, Jozef Vleugels, Jan Van Humbeeck, Omer Van der Biest, The innovative impulse excitation technique for high-temperature mechanical spectroscopy, J. Alloys Compd. 310 (1) (2000) 284–287, Intern. Conf. Internal Friction and Ultrasonic Attenuation in Solids (ICIFUAS-12).

[3] Stephen Timoshenko, History of strength of materials: with a brief account of the history of theory of elasticity and theory of structures, Courier Corporation (1983).

[4] J.D. Lord, R. Morrell, Measurement good practice guide no. 98: elastic modulus measurement, National Physical Lab. Report (2006) 41–65.

[5] Advanced technical ceramics – mechanical properties of monolithic ceramics at room temperature – part 2: Determination of young's modulus, shear modulus and poisson's ratio; german version en 843-2:2006. Accessed on: 2021-06-23.

[6] Methods of test for refractory products – part 1: Determination of dynamic young's modulus (moe) by impulse excitation of vibration. Accessed on: 2021-06-23.

[7] Test method for dynamic youngs modulus, shear modulus, and poissons ratio by impulse excitation of vibration. Accessed on: 2021-06-23.

[8] Mattia Lopresti, Luca Palin, Gabriele Alberto, Simone Cantamessa, Marco Milanesio, Epoxy resins composites for x-ray shielding materials additivated by coated barium sulfate with improved dispersibility, Mater. Today Commun. 26 (2021) 101888.

[9] Maria Richetta, Alessandra Varone, A focus on dynamic modulus: effects of external and internal morphological features, Metals 11 (1) (2021).

[10] Ying Li, Weiguo Li, Xianhe Zhang, Jianzuo Ma, Jiaxing Shao, Haibo Kou, Yong Deng, Modeling of temperature dependent yield strength for stainless steel considering nonlinear behavior and the effect of phase transition, Constr. Build. Mater. 159 (2018) 147–154.

[11] Il-Chan Jung, Deok-Gu Kang, Bruno C. De Cooman, Impulse excitation internal friction study of dislocation and point defect interactions in ultra-low carbon bake-hardenable steel, Metall. Mater. Trans. A 45 (4) (2014) 1962–1978.

[12] Martin Monìk, Selina Delgado-Raack, Hynek Hadraba, David Jech, Roberto Risch, Rock physics and the circulation of neolithic axeheads in central europe and the western mediterranean, Wear 474–475 (2021) 203708.

[13] Eva Gregorová, Vojtech Necina, Sona Hríbalová, Willi Pabst, Temperature dependence of young's modulus and damping of partially sintered and dense zirconia ceramics, J. Eur. Ceram. Soc. 40 (5) (2020) 2063–2071.

[14] Alessia Masini, Filip Šiška, Oldrich Ševecek, Zdenek Chlup, Ivo Dlouhý, Elastic properties of multi-layered ceramic systems for socs, Int. J. Appl. Ceram. Technol. 15 (2) (2018) 370–379.

[15] Jennifer Alex, Luc Vandeperre, William E. Lee, Bruno Touzo, Chris Parr, Effect of sodium on microstructures and thermoelastic properties of calcium aluminate cement-bonded refractories, J. Am. Ceram. Soc. 99 (3) (2016) 1079–1085.

[16] Joern Werner, Christos G. Aneziris, The influence of pyrolysis temperature on young's modulus of carbon-bonded alumina at temperatures up to 1450 c, Ceram. Int. 42(2, Part B) (2016) 3460–3464.

[17] Il-Chan Jung, Deok-Gu Kang, Bruno C. De Cooman, Impulse excitation internal friction study of dislocation and point defect interactions in ultra-low carbon bake-hardenable steel, Metall. Mater. Trans. A 45 (4) (2014) 1962–1978.

[18] Nicolas Traon, Thorsten Tonnesen, Rainer Telle, Estimation of damage in refractory materials after progressive thermal shocks with resonant frequency damping analysis, J. Ceram. Sci. Technol. 7 (2016) 165–172.

[19] Amina Sidi Mammar, Dietmar Gruber, Harald Harmuth, Shengli Jin, Tensile creep measurements of ordinary ceramic refractories at service related loads including setup, creep law, testing and evaluation procedures, Ceram. Int. 42 (6) (2016) 6791–6799.

[20] Nazareno Massara, Enrico Boccaleri, Marco Milanesio, Mattia Lopresti, Dataset for impulse excitation technique data set collected on different materials for data analysis methods and quality control procedures development, 2021.

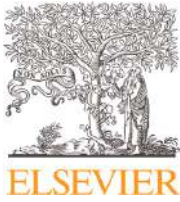[21] Nazareno Massara, Enrico Boccaleri, Marco Milanesio, Mattia Lopresti, Impulse excitation technique data set collected on different materials for data analysis methods and quality control procedures development, Data Brief (2021).

[22] Luca Palin, Rocco Caliandro, Davide Viterbo, Marco Milanesio, Chemical selectivity in structure determination by the time dependent analysis of in situ xrpd data: a clear view of xe thermal behavior inside a MFI zeolite, PCCP 17 (26) (2015) 17480–17493.

[23] Douglas C. Giancoli, Physics for Scientists & Engineers with Modern Physics, Addison-Wesley, fourth ed., 2008.

[24] Pietro Guccione, Mattia Lopresti, Marco Milanesio, Rocco Caliandro, Multivariate analysis applications in x-ray diffraction, Crystals 11 (1) (2021) 12.

[25] Audacity. URL: https://www.audacityteam.org/, 2020. Accessed: 2021-06-23.

[26] William D. Callister, David G. Rethwisch, Materials science and engineering, volume 5, John wiley & Sons NY (2011).

[27] Alimex 6082 t651 aluminum alloy rolled. URL: http://www.matweb.com/search/DataSheet.aspx?MatGUID=39d199eebf034c3cb424caaee9d4be08. Accessed: 2021-06-23.

[28] 6082-t6 aluminum. URL: https://www.makeitfrom.com/material-properties/6082-T6-Aluminum. Accessed: 2021-06-23.

[29] Cusn10-c - gs - gebr. kemper gmbh + co. kg. URL: https://www.kemper-olpe.de/oc/business-units/cast-products/material/special-bronze/cusn10-c-gs/?L=0. Accessed: 2021-06-23.

[30] Cusn12-c - gs - gebr. kemper gmbh + co. kg. URL: https://www.kemper-olpe.de/oc/business-units/cast-products/material/special-bronze/cusn12-c-gs/?L=0. Accessed: 2021-06-23.

[31] Guide to nickel aluminium bronze for engineers. URL: http://copperalliance.it/uploads/2018/03/pub-222-nickel-al-bronze-guide-engineers-1.pdf. Accessed: 2021-06-23.

[32] Normalized and tempered (+nt) 1.1191 steel. URL: https://www.makeitfrom.com/material-properties/Normalized-and-Tempered-NT-1.1191-Steel. Accessed: 2021-06-23.

[33] High conductivity copper for electrical engineering. URL: http://copperalliance.it/uploads/2018/02/pub-122-hicon-copper-for-electrical-engineering.pdf. Accessed: 2021-06-23.

[34] Data sheet: 39pb3 cw614n. URL: http://www.almag.it/en/pdf/39PB3-CW614N-TN-EN.pdf. Accessed: 2021-06-23.

[35] En 1.0038 high manganese carbon steel. URL: http://www.matweb.com/search/datasheet.aspx?matguid=fc28725f7a4546698c890b5ab3eb09e2&ckck=1. Accessed: 2021-06-23.

[36] Overview of materials for high density polyethylene (hdpe), blow molding grade. URL: http://www.matweb.com/search/DataSheet.aspx?MatGUID=4f13f71f5f904fa19874597dd53fd754. Accessed: 2021-06-23.

[37] Overview of materials for nylon 6, cast. URL: http://www.matweb.com/search/DataSheet.aspx?MatGUID=8d78f3cfcb6f49d595896ce6ce6a2ef1. Accessed: 2021-06-23.

[38] Overview of materials for acetal copolymer, unreinforced. URL: http://www.matweb.com/search/DataSheet.aspx?MatGUID=c3039ef87c9245448cdebe961b19a54c. Accessed: 2021-06-23.

[39] Overview of materials for polytetrafluoroethylene (ptfe), molded. URL: http://www.matweb.com/search/DataSheet.aspx?MatGUID=4d14eac958e5401a8fd152e1261b6843. Accessed: 2021-06-23.

[40] Annealed d2 tool steel. URL: https://www.makeitfrom.com/material-properties/Annealed-D2-Tool-Steel. Accessed: 2021-06-23.

[41] Rocco Caliandro, Danilo Benny Belviso, Rootprof: software for multivariate analysis of unidimensional profiles, J. Appl. Crystallogr. 47 (3) (2014) 1087–1096.

[42] Rootprof documentation. URL: https://users.ba.cnr.it/ic/crisrc25/RootProf/RootProf_help.html, 2014. Accessed: 2021-06-23.

Born in Borgosesia (VC, Italy) on February 14th, 1997. Obtained his degree in materials science in December 2020 with the experimental thesis entitled "Complete self-construction of a microcomputer-based instrument for the study of materials through impulse analysis", under the supervision of prof. Enrico Boccaleri, prof. Marco Milanesio and mr. Mattia Lopresti at the University of Eastern Piedmont.

Born in Alessandria (AL, Italy) on January 31st,1973. Obtained his degree in chemistry "cum laude" in 1996 with the experimental thesis entitled "Solid-gas Reactivity of organometallic complexes of transition metals", under the supervision of prof. Roberto Gobetto and Prof. Enrico Sappa. In March 2001 he defends his PhD thesis in Chemical Sciences at the University of Turin, Department of Inorganic, Physical and Materials Chemistry. The thesis, titled "Correlation spectroscopic properties-structure: vibrational patterns applied to polyatomic systems" was written under the supervision of prof. P.L. Stanghellini. Associate professor at the University of Eastern Piedmont. Co-author of 58 articles in international scientific journals, 1 chapter in scientific volumes, 2 European patents, one patent and one Italian national patent application. Supervisor of 32 bachelor and master theses and three Ph.D. theses.

Born in Savigliano (CN, Italy) on November 25th, 1971. Degree in Chemistry in 1996 and Ph.D. in Chemistry by the University of Torino in 2001. Since October 2001 researcher and since August 2017 Associate professor in Physical Chemistry at the University of Piemonte Orientale. Recipient of the "Young Italian Crystallographer" award in 2003 and member of the teaching staff several AIC schools and organizers or chair of various international crystallographic events. Coordinator of several research projects and of a long term project (code CH-2234) at the ESRF (Grenoble, France) to develop a new instrumental setup to carry out simultaneous X-ray Diffraction and Raman experiments at non-ambient conditions. Invited lecturer at several national and international congresses. Author of more than 90 original publications on international journals, more than 50 communications to international and national congresses as main author, and 3 ITA and one EU patents. My main research interests are the study of the molecular and crystal structure of chemical compounds and materials, together with the characterization of their physical-chemical properties. Single-Crystal and Powder X-ray Diffraction, using both conventional and synchrotron radiation sources, also combined with Raman and/ or UV-vis spectroscopy, are the employed experimental techniques, also at in situ non-ambient conditions. In the last years the development of new method of data analysis in crystallography have been carried out, exploiting Principal Component Analysis for the analysis of large in situ X-ray diffraction datasets. The studied compounds are in the fields of additives for polymers and inorganic binders, of porous and layered systems for gas/molecules adsorption, transport, degradation or sequestration and of phototactive materials for photovoltaic applications.

Born in Galliate (NO, Italy) on March 17th, 1991. Obtained his bachelor's degree in materials science in 2014 and his master's degree in chemistry in 2017. From 2018 Ph.D. student in chemistry under the supervision of professor Milanesio at the University of Eastern Piedmont (Italy). His research concerns the integration of multivariate statistical analysis in the crystallographic area, especially for the quantitative analysis of powder mixtures. His Ph.D. topic is the theoretical and experimental development of lightweight X-Ray shielding materials. His work also regards coating development for ultralight magnesium alloys for everyday purposes and the analysis of plant polyphenolic extracts as adjuvants for wines and winemaking products. The red thread that connects each of these areas of interest is the passion for both crystallography and chemometric techniques.

III

Impulse excitation technique data set collected on different materials for data analysis methods and quality control procedures development

Ah, yes. I'm looking for a friend of mine, last name is Jass, first name Hugh.

Simpson. B.J.

Data Article

Impulse excitation technique data set collected on different materials for data analysis methods and quality control procedures development☆

Nazareno Massara, Enrico Boccaleri, Marco Milanesio, Mattia Lopresti*

Universitá del Piemonte Orientale, Dipartimento di Scienze e Innovazione Tecnologica, Viale T. Michel 11, Alessandria 15121, Italy

A R T I C L E   I N F O

A B S T R A C T

Mechanical properties such as the Young modulus, shear modulus and Poisson's coefficient are very important to define different materials applications, for basic research and for quality control procedures. Impulse excitation technique (IET) is a non-destructive, easy and fast method for characterization of elastic and acoustic properties of materials. The technique consists in sending a mechanical impulse in a sample and measuring the output sound wave. Commercial instruments are widely spread in metal industry, but they are not diffused in academic research centres. Such instruments can be easily self-built at low cost, allowing a much wider diffusion and exploitation in many fields involving materials characterization, since they guarantee high precision and high data reproducibility. For a proper acoustic characterization, necessary to obtain reliable mechanical data, a calibration of the instrument must be performed, for a proper association of the acoustic response to the features of each specific material. In this data article, a data set of impulses, collected on different materials by a self-built instrument

https://doi.org/10.1016/j.dib.2021.107503

for IET, named IETeasy, is provided for mechanical properties characterization by a self-built IET tool, and multivariate statistical analysis purposes. The aim is double in the short term: on one hand, providing a verified data set useful to develop, test and verify methods of analysis and tailor the IETeasy instrument on the needs of each specific user; on the other hand, giving a benchmark for any one designing, building and testing his IET home-made instrument. In the long term, since the data base is open, any contribution consisting in data collected by similar self-made or commercial instruments can be added to the data base, with the aim of building a large collection of data, useful for automatic recognition of sound outputs by machine learning or other multivariate or monovariate data analysis approaches, and for instrument performance comparison and alignment.

Specifications Table

Subject	Engineering and materials science
Specific subject area	Materials characterization by acoustic analysis
Type of data	Text files
	.mp3 files
How data were acquired	IETeasy
Data format	Raw .mp3
	Analyzed .txt
Parameters for data collection	Strings distance: 5 cm
	Collection interval: 8 s to 14 s
Description of data collection	Impulses were collected from the IETeasy instrument, suspending the sample on PA6 strings with a distance of 5 cm and a collection interval of 8 s to 14 s. Audio signals were collected using Audacity software on a Raspberry Pi 4 with a Raspbian OS 5.4.51.
Data source location	Institution: Universitá del Piemonte Orientale
	City/Town/Region: Alessandria
	Country: Italy
Data accessibility	Repository name: Mendeley Data
	Data identification number: https://doi.org/10.17632/srfp7x6wxm.1
	Direct URL to data: https://data.mendeley.com/datasets/srfp7x6wxm

Value of the Data

- The data set is a collection of replicated impulses sampled on fifteen different materials, spanning from pure metals, to alloys, to polymers. Data are provided in three different formats: .mp3 audio file for direct wave data processing, two-column .txt files for monovariate or multivariate data analysis and the values of magnitude of .txt files processed by Fast-Fourier Transform (FFT) for the analysis of the resonance frequencies of the materials. These data can be used with multiple purposes: instrumental precision evaluation, accuracy of outputs with a comparison with data reported in scientific literature (collected using professional instruments [1–5]) and multivariate analysis for classification.
- Data can be used for developing new quality control methods, or to make the existing ones more robust, for a fast and easy on-line analysis in productive processes and in research laboratories.
- Analyzing these data can promote the spread of open-source and cheap self-assembled IET instruments, that can result in two principal advantages: the expansion of the present data set, which reflects in more robust analyses and potentialities in machine learning, and the

evolution of this technology in the open source model. Widespread in-situ quality control can help reducing scraps in production, help reducing environmental impacts, while improving the value of the production itself.

1. Data Description

The present data set was gathered by collecting ten measurements on each of the analyzed material. It can be found in the repository on Mendeley Data linked in the specification table, and it is organized as described in the following tree diagram:

```
root/
├── Audio data
│   ├── AISI 304 steel
│   ├── AISI 316 steel
│   ├── Aluminium 6082
│   ├── B10 bronze
│   ├── B12 bronze
│   ├── BrAl alloy
│   ├── C45E steel
│   ├── Copper
│   ├── CW614 brass
│   ├── Fe37 drawn
│   ├── Nylon 6
│   ├── Polizene
│   ├── Pom-C
│   ├── Teflon
│   └── X150 steel
├── Text data
│   ├── AISI 304 steel
│   ├── AISI 316 steel
│   ├── Aluminium 6082
│   ├── B10 bronze
│   ├── B12 bronze
│   ├── BrAl alloy
│   ├── C45E steel
│   ├── Copper
│   ├── CW614 brass
│   ├── Fe37 drawn
│   ├── Nylon 6
│   ├── Polizene
│   ├── Pom-C
│   ├── Teflon
│   └── X150 steel
└── Fourier-transformed data
    ├── AISI 304 steel
    ├── AISI 316 steel
    ├── Aluminium 6082
    ├── B10 bronze
    ├── B12 bronze
    ├── BrAl alloy
    ├── C45E steel
    ├── Copper
    ├── CW614 brass
    ├── Fe37 drawn
    ├── Nylon 6
    ├── Polizene
    ├── Pom-C
    ├── Teflon
    └── X150 steel
```

Table 1
Analyzed materials and sample parameters.

Sample	Length (cm)	Depth (cm)	Thickness (cm)	Mass (g)
6082 aluminium	9.900	5.985	0.985	157
AISI 304 steel	9.900	10.050	0.820	636
AISI 316 steel	10.045	5.000	1.035	400
Fe37 steel	9.900	7.990	0.795	488
X150 steel	9.950	10.225	1.065	826
B10 bronze	10.000	8.250	1.250	905
B12 bronze	10.000	8.325	1.345	996
BrAl	9.855	6.460	0.680	319
C45E steel	10.010	9.230	1.015	735
Copper	10.650	9.200	1.010	824
CW614 brass	9.825	7.600	0.810	507
Nylon 6	10.245	10.350	1.035	120
Polizene	10.195	7.7650	1.015	75
Pom-C	10.315	10.150	1.065	154
Teflon	10.290	10.235	1.115	230

Each level-2 directory indicates the file format contained in children folders: .mp3 audio files, .txt raw files, .txt FFT pre-processed files. Each level-3 directory, instead, indicates the corresponding analyzed material, which is described by Table 1 in the following section. Audio files are 8 s to 14 s long with IET pulses placed at about half-length, in order to collect the whole acoustic signal. Quality settings of the audio file are MONO 32-bit float with sampling rate of 48,000 Hz. In Figs. 1–3, measurements on the materials are reported as both wave form and FFT processed profiles. Due to the high on number of data (fifteen different samples and ten measurements for each sample), only the first measurement for each sample is reported in the graphs. In Fig. 1(a) the average spectra calculated on the ten measurements for each sample are reported for comparison. All polymeric samples show absolute sound intensities that are up to twenty times lower than those belonging to metal samples. Moreover, no important peaks are present above 10,000 Hz. In panels Fig. 1(b)–(f), different steels are showed. Shape and duration of the sound wave in the figures are very different for each material, in particular between Fe37 steel and X150 steel, that both have a pulse duration of about 1 s, but a very different damping shape. The characteristic frequencies and magnitudes are different as well from one sample to another. AISI 304 steel and AISI 316 steel, which are very similar in composition, being both part of the AISI 300 steel series, show very different profiles, with the AISI 304 being richer in peaks and with a natural resonant frequency at lower values than AISI 316 steel. In Fig. 2 data collected on other alloys are reported. In these data, a longer sound wave than steels can be observed, with BrAl alloy, lasting more than two seconds. Differences are also marked in the frequency domain with a large variety in peak number and positions. B10 and B12 bronzes show very similar patterns, with a shift of peaks at higher frequencies for B2 bronze. In Fig. 3 the sound waves and the spectra of four polymers are reported. As previously observed, the magnitudes are lower than those belonging to metallic samples. Profiles also tends to be much more noisy. Differences can also be observed in the waves of the miniatures, which are much shorter and irregular than those showed in Figs. 1 and 2. For each of the analyzed samples, length, depth, thickness and mass are reported in the following section, as required for the calculation of some properties such as Young modulus.
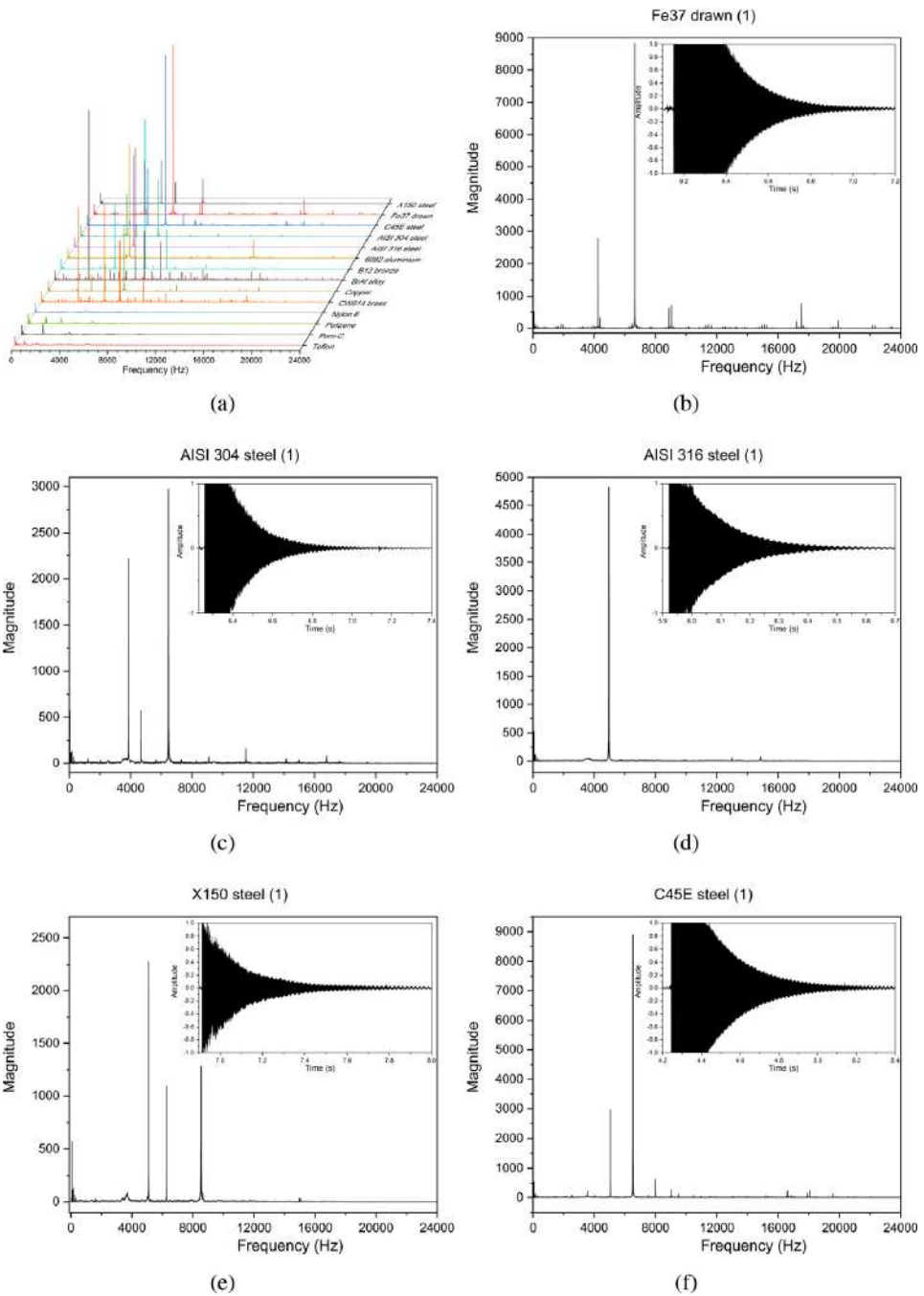
Fig. 1. In Fig. 1(a) the collection of the average spectra of the fifteen analyzed materials is reported. The reported spectra were calculated on the ten measurements for each sample. In Fig. 1(b)–(f) each sound wave (shown in the inset) and the corresponding frequency pattern are reported for different steel alloys.
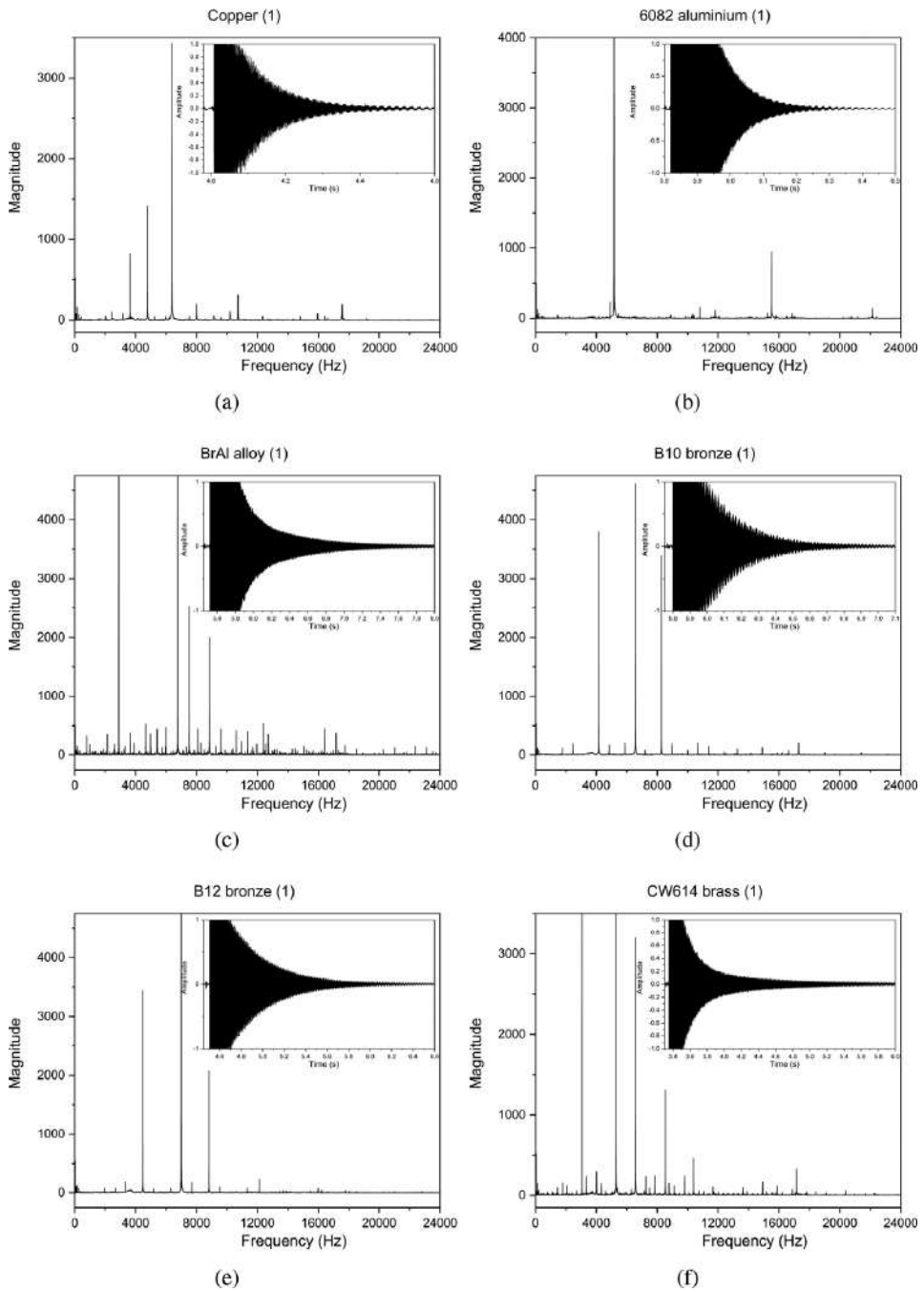
Fig. 2. The reported spectra were calculated on the ten measurements for each sample. In Fig. 2(a)–(f) each sound wave (shown in the inset) and the corresponding frequency pattern are reported for different copper or aluminium-based alloys.
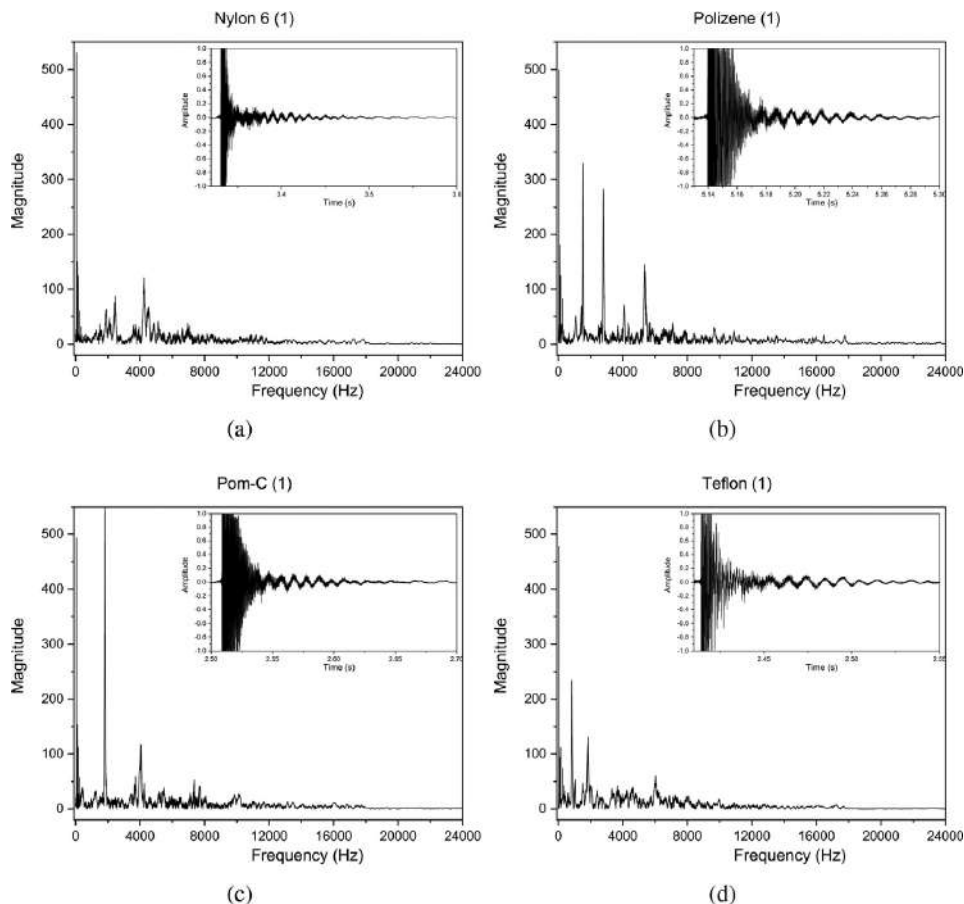
Fig. 3. The reported spectra were calculated on the ten measurements for each sample. In Fig. 3(a)–(d) each sound wave (shown in the inset) and the corresponding frequency pattern are reported for different polymers.

2. Experimental Design, Materials and Methods

2.1. Materials

Analyzed materials were purchased by HobbyMetal, (Giulianova, Italy) which provided samples with mass and dimensions as described in Table 1.

2.2. Data collection

Data were collected by the IETeasy instrument [6] placing the sample on the strings distanced by 5 cm and releasing the percussion mallet. The acoustic output is collected by a microphone that faces the top of the sample, as detailed in the supporting article. The whole setup was connected to a Raspberry Pi 4 which uses Raspbian 5.4.51 as operating system. Audio .mp3 files were recorded using Audacity 2.4.2 [7] open-source software and then converted in .txt raw files with SoX [8]. Raw files were then processed by fast Fourier-transformed on Origin 2020 [9] to obtain the signal in the frequency domain. Two column data (frequency vs. magnitude) were then exported in .txt files.

CRediT Author Statement

The instrument was assembled by NM and ML. Data collection was performed by NM. All the authors analyzed the data, edited the manuscript and approved its final version.

Declaration of Competing Interest

The authors declare that they have no known competing financial interests or personal relationships which have, or could be perceived to have, influenced the work reported in this article.

CRediT Author Statement

Nazareno Massara: Data curation, Methodology, Writing – original draft, Writing – review & editing; **Enrico Boccaleri:** Conceptualization, Writing – original draft, Writing – review & editing; **Marco Milanesio:** Formal analysis, Funding acquisition, Supervision, Validation, Writing – original draft, Writing – review & editing; **Mattia Lopresti:** Conceptualization, Data curation, Formal analysis, Methodology, Software, Writing – original draft, Writing – review & editing.

Acknowledgements

References

[1] G. Roebben, B. Bollen, A. Brebels, J. Van Humbeeck, O. Van der Biest, Impulse excitation apparatus to measure resonant frequencies, elastic moduli, and internal friction at room and high temperature, Rev. Sci. Instrum. 68 (12) (1997) 4511–4515, doi:10.1063/1.1148422.

[2] G. Roebben, B. Basu, J. Vleugels, J. Van Humbeeck, O. Van der Biest, The innovative impulse excitation technique for high-temperature mechanical spectroscopy, J. Alloy. Compd. 310 (1) (2000) 284–287, doi:10.1016/S0925-8388(00)00966-X. Intern. Conf. Internal Friction and Ultrasonic Attentuation in Solids (ICIFUAS-12)

[3] N. Traon, T. Tonnesen, R. Telle, Estimation of damage in refractory materials after progressive thermal shocks with resonant frequency damping analysis, J. Ceram. Sci. Technol. 7 (2016) 165–172, doi:10.4416/JCST2015-00080.

[4] E. Gregorová, V. Nečina, S. Hříbalová, W. Pabst, Temperature dependence of Young's modulus and damping of partially sintered and dense zirconia ceramics, J. Eur. Ceram. Soc. 40 (5) (2020) 2063–2071, doi:10.1016/j.jeurceramsoc.2019.12.064.

[5] I.-C. Jung, D.-G. Kang, B.C. De Cooman, Impulse excitation internal friction study of dislocation and point defect interactions in ultra-low carbon bake-hardenable steel, Metall. Mater. Trans. A 45 (4) (2014) 1962–1978.

[6] N. Massara, E. Boccaleri, M. Milanesio, M. Lopresti, IETeasy: an open source and low-cost instrument for impulse excitation technique, applied to materials characterization, Hardware X 10 (2021) e00231 ISSN 2468-0672, doi:10.1016/j.ohx.2021.e00231.

[7] Audacity. (2020). https://www.audacityteam.org/. Accessed February 25, 2021.

[8] Sox - sound exchange. (2015). http://sox.sourceforge.net/. Accessed February 25, 2021.

[9] Apache Software Foundation (2020). Origin 2020. https://www.originlab.com/. Accessed February 25, 2021.

XRF AND XRPD DATA SETS IN TERNARY MIXTURES WITH HIGH LEVEL MICRO-ABSORPTION AND/OR PREFERRED ORIENTATIONS PROBLEMS FOR PHASE QUANTIFICATION ANALYSIS

Don't cry for me, I'm already dead.

Gumble, B. A. Sr.

Data Article

XRF and XRPD data sets in ternary mixtures with high level micro-absorption and/or preferred orientations problems for phase quantification analysis[☆],[☆☆]

Beatrice Mangolini [a],[1], Luca Palin [a],[b],[2], Marco Milanesio [a],[3], Mattia Lopresti [a],[4],*

[a] Universitá del Piemonte Orientale, Dipartimento di Scienze e Innovazione Tecnologica, Viale T. Michel 11, Alessandria 15121, Italy
[b] Nova Res s.r.l., Via D. Bello 3, Novara 28100, Italy

ARTICLE INFO

ABSTRACT

Micro-absorption (MA) and/or preferred orientations (PO) are two among the major problems affecting quantitative phase analysis (QPA) by X-ray Powder Diffraction Data (XRPD) in industrial samples such as minerals and ores, additives, cements, friction materials, coal combustion by-products. Typically XRPD data are coupled to elemental analysis by X-ray Fluorescence (XRF) to facilitate phase recognition and quantification when elements heavier than sodium are present. Graphite and urea are typical examples of large production industrial commodities showing such analytical problems. The present article provides a recipe to produce sets of data of increasing difficulty to test the performances of different approaches and/or software's for QPA by XRPD in graphite, zinc acetate and urea containing samples. Graphite, due to its

platelet morphology, can exhibit orientation and was chosen because it is possible to control its PO degree by sieving. Simplex-centroid design augmented was used for the design of the experiments to select the mixtures with the more possible homogeneous exploration of the ternary experimental domains, from pure phase to equal-weighted mixtures. The different data sets collected on the four experimental domains by XRF and XRPD are provided and stored as a repository on Mendeley Data. Using the same approach, additional data sets sets with different composition and/or experimental setup can be added by us or any other contributor with the same DoE approach to create a wide open access data set of standardized X-ray powder diffraction and X-ray fluorescence data.

Specifications Table

Subject	Materials science
Specific subject area	Quantitative phase analysis by XRF and XRPD
Type of data	Text files
How data were acquired	X-ray fluorescence
	X-ray powder diffraction
Data format	Raw
Parameters for data collection	XRF and XRPD raw profiles were collected on four different sample groups of mixtures, designed by the simplex-centroid augmented scheme with increasing effects of micro-absorption and/or preferred orientations.
Description of data collection	XRF data were collected in air condition on a Rigaku NEX QC with the X-ray tube at 20 kV and 200 μA. XRPD data were collected by a Bruker D8 Advance in the 2θ range of 10° to 120° with the X-ray tube ad 40 kV electric potential and 40 mA filament current in standard Bragg-Brentano conditions.
Data source location	Institution: Universitá del Piemonte Orientale City/Town/Region: Alessandria Country: Italy
Data accessibility	Repository name: Mendeley Data
	Data identification number: https://doi.org/10.17632/js2nzwf5md.2
	Direct URL to data: https://doi.org/10.17632/js2nzwf5md.2

Value of the Data

- Chemists, earth and materials scientists, engineers by both industrial and academic fields, interested in solid-state matter analysis can benefit of these data to test and improve the performances and explore the potentialities and limitations of the analytical methods of solid samples. Improving quality control process in commodity production can improve materials usages and reduce wastes and resource consumption. These data will benefit researchers in developing and improving methods, and software and/or analytical approaches can be benchmarked and ranked on the same sets of data to have a clearer view of their accuracy and limitations for quantitative phase analysis in complex samples.
- The data sets available in the literature are natural samples or mixtures prepared with concentrations suitable to reflect real sample compositions [1–7]. Conversely, the data set D1-4 are the first available XRF/XRPD data sets designed using the DoE theory, therefore by a method-centred approach. A simplex-centroid augmented experimental plan for mixture was used: in this way, the mixture concentrations do not mimic real samples but are optimised

to properly sample the experimental domain. This allow the best possible precision in evaluating and comparing methods and/or software used for XRPD/XRF data analysis.

- Methods for phase analysis by X-ray powder diffraction data in presence of preferred orientation and micro-absorption are needed in many industrial applications for the quality control of raw and refined materials. This data set was built measuring samples containing urea and graphite which suffer of such problems and can hardly be quantified with traditional methods of analysis by XRF and XRPD data. The provided data set was built analyzing samples and substances showing different degrees of micro-absorption and preferred orientations, in order to produce standard data set on which different methods can be used for quantification purposes. Patterns and spectra of the pure phases are provided, giving all the necessary tools for both supervised and unsupervised analysis.
- The provided data set is open source and open access and new XRPD/XRF data sets built with the same simplex-centroid design approach but with different samples and/or experimental setup can be added by us or any other contributor. In this way, a wide standardized database of experimental data will be available to carefully test and compare the performances, limitations and possibilities of assessed or new methods of analysis.

1. Data Description

The actual (v.4) version of the repository on Mendeley Data is a collection of 80 raw files organized as described in the following directory tree diagram:

```
root/
├── D1
│   ├── D1 - XRF data
│   └── D1 - XRPD data
├── D2
│   ├── D2 - XRF data
│   └── D2 - XRPD data
├── D3
│   ├── D3 - XRF data
│   └── D3 - XRPD data
└── D4
    ├── D4 - XRF data
    └── D4 - XRPD data
```
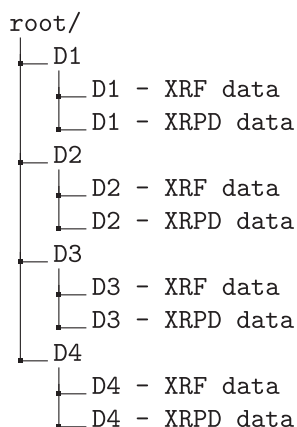
Each level-1 directory (D1, D2, D3 and D4) has the name of the corresponding mixture experimental domain, which is accurately described in the next section. The data set consists in a couple of measurements (one XRF spectrum and one XRPD pattern) collected on each sample of the four sets of experiments. XRF data are provided in two-columns `.txt` files: intensity (a.u.) vs. energy (keV). XRPD data are instead provided three-column `.xye` files, in which are reported the intensity (a.u.), the 2θ angles (degrees) and the error associated to the measurement (a.u.). Both XRF and XRPD sets were not pre-processed and are given as obtained by the instruments. Each set of data was collected on mixture samples designed with a simplex-centroid augmented design on four different ternary mixture spaces. The approach, based on DoE, guarantees a full and homogeneous exploration of such experimental domains. The data on experimental set D1 (composed by $BaSO_4$, Bi_2O_3 and graphite with diameter lower than 90 µm) are reported in Fig. 1. For readability purposes, XRF data are plotted from 0 keV to 25 keV to better show the principal signals belonging to each pure phase. In the database, data are provided in the full collection range, from 0 keV to 50 keV, although almost no signal is present above 25 keV. As can be seen in Fig. 1, both samples *D1-Ba* and *D1-Bi*, belonging to the pure phases of respectively $BaSO_4$ and Bi_2O_3, show the signals of the detectable atoms with this techniques: barium, sulfur and bismuth. However, since the measurement were performed at 20 kV of electric potential (which is
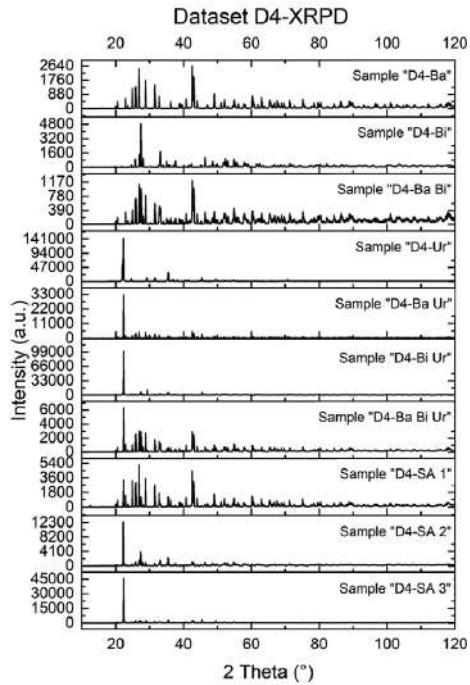
(a)

(b)

(c)

(d)
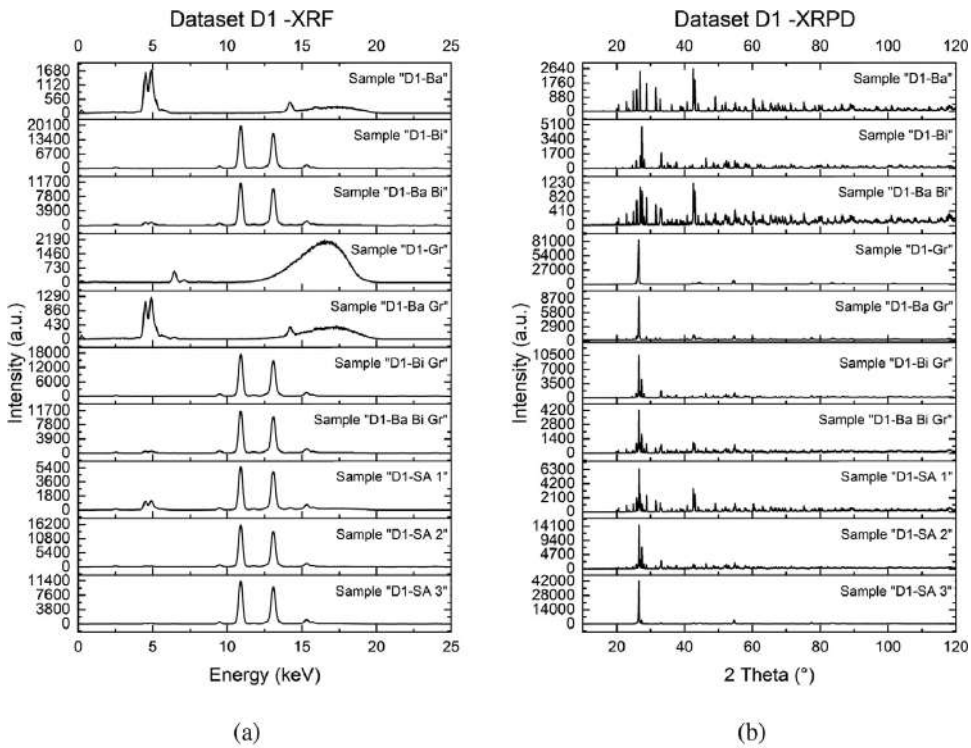
Fig. 1. Raw data of experiment set D1 (and) and D2 (and). Figures on the left report XRF data, while figures on the right show XRPD data.

the optimal condition for mixtures containing medium and high Z elements) the signal of the sulfur appears very small. The 20 kV measurement condition was chosen to also allow comparison of XRF data with a 20 kV SEM/EDX measurement. SEM/EDX data are not present in this dataset because EDX is not competitive with XRF concerning both analysis duration/complexity and accuracy in quantification, it was used to assess the morphology of mixture components. Sample *D1-Gr*, belonging to graphite, shows Compton scattering only, except for a small signal near 6 keV which was attributed to small impurities of iron that appeared after sieving the powders ($K_{\alpha_1 Fe} = 6.404$ keV, $K_{\alpha_2 Fe} = 6.391$ keV, $K_{\beta_1 Fe} = 7.057$ keV). The physical laws that regulate the signal intensity are not linear combinations of the signal of the pure phases, which is one of the principal obstacles of quantification by XRF. In Fig. diffraction patterns of the same samples are shown. Data were collected in the 2θ range of 10° to 120°, since there were no signals below 10° and peaks belonging to the heavy phases were well visible until very high angles. Samples *D1-Ba* and *D1-Bi* both have patterns very rich in signals with principal peaks intensities in the order of magnitude of 10^3. Those many signals cause peak superposition, resulting in very complex XRPD pattern such as the one in mixture *D1-Ba Bi*. Sample *D1-Gr* shows a very intense peak and few other signals that are about two orders of magnitude lower, which is typical of oriented samples. Effects of micro-absorption can be observed by looking and the differences in the signal intensities: in principle the scattering power increases with increasing Z numbers of the element in each phase. However, the high density of barite and bismite, especially in the case of bismite showing large crystallites, cause and increase absorption of X-ray and net reduced diffraction efficiency. However, barite and bismite both have high densities, which result in crystals where the absorption of the incident X-ray is higher. Data set D2 shows data very similar to data set D1, but in this second collection of data, graphite contains a 30% of large particles (diameters greater than 90 μm) resulting in a much more oriented system with large PO effects. In fact, XRPD data of sample *D2-Gr* show an intense peak which is an order of magnitude greater than the one in sample *D1-Gr*. The effects of preferred orientation and of the micro-absorption are more evident, as the intensities of the peaks in mixtures shows complex features without any clear mathematical relation to those belonging to the pure phases. Data set D3 was collected on an experiment set of mixtures in which graphite was substituted by zinc acetate, therefore a salt with a metallic element which can produce a XRF signal. In Fig. 2(a), in addition to the previously described signals of barite and bismite, the XRF spectrum of zinc acetate can be observed (*D3-Zn*), with two characteristic signals corresponding to its K_β and K_β ($K_{\alpha_1 Zn} = 8.639$ keV, $K_{\alpha_2 Zn} = 8.616$ keV, $K_{\beta_1 Zn} = 9.572$ keV). Zinc acetate, pure and in mixture, is characterized by a principal peak (Fig. 2(b)), 10 to 100 times more intense than the others, which flatten all the other peaks in the pattern. The effect of PO is comparable to the one that affect data set D2. Data set D4 was collected on a ternary mixture experimental domain composed by barium sulfate, bismuth oxide and urea. XRF spectrum of sample *D4-Ur* does not show peaks except for a large band between 14 keV to 19 keV, which is related to the Compton scattering of carbon, nitrogen and oxygen, which do not have an XRF detectable signal. In XRPD data plotted in Fig. 2(d), urea shows a behaviour very similar to zinc acetate and graphite, with a very intense characteristic peak that is two orders of magnitude greater than the most intense peaks of barium sulfate and bismuth oxide.

2. Experimental Design, Materials and Methods

2.1. Simplex-centroid design augmented

Design of experiments (DoE) is a practice following the "parsimony principle", consisting in using the smallest number of samples able to give the greatest possible amount of information. This can be done designing experiments homogeneously within the experimental domain, avoiding lined up samples and empty unexplored areas. Most common approaches such as D-optimal, K-optimal, Box-Behnken and Doelhert designs [8] are not suitable for the exploration of a space
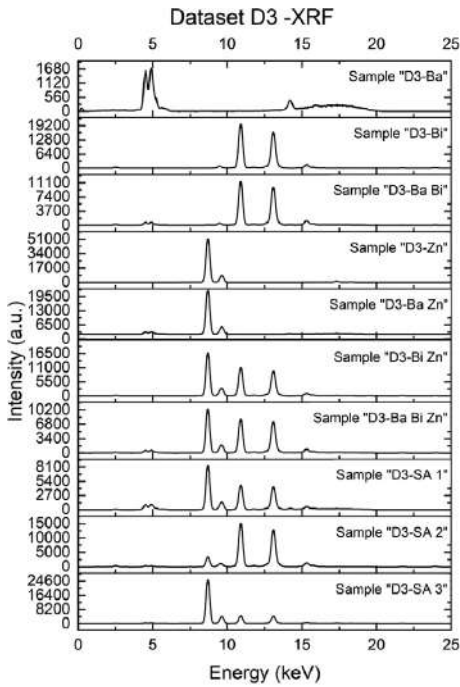
(a)
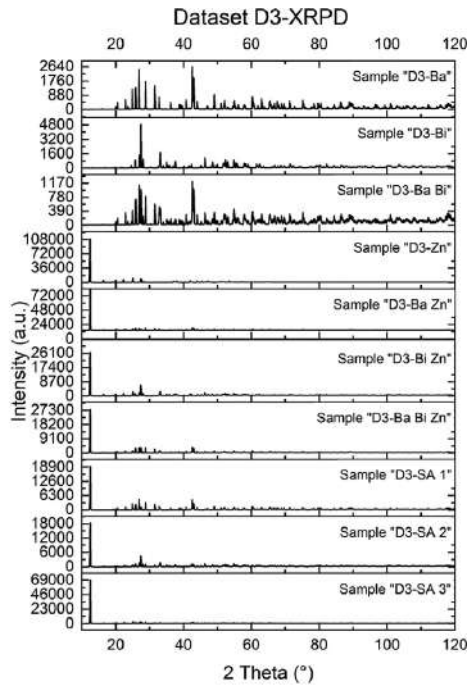
(b)
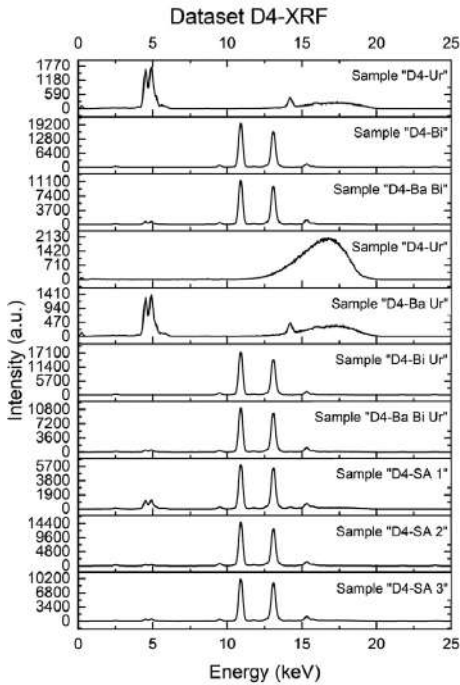
(c)

(d)

Fig. 2. Raw data of experiment set D3 (and) and D4 (and). Figures on the left report XRF data, while figures on the right show XRPD data.

in which variables cannot be fully independent [9]. Indeed, in mixtures, a fundamental relation states that the sum of every weight fraction x_i of all the q components has to be equal to 1, clearly stating the impossibility of the independence principle:

$$\sum_{i=1}^{q} x_i = 1 \tag{1}$$

For this reason, the choice of best DoE approach for mixtures must consider designs appositely made for systems showing such a dependency [9,10]. Among the many existing solutions (such as simplex-lattice design [11], axial design, ...) simplex-centroid design augmented was chosen because of the low number of experiments required to have a full homogeneous exploration of the mixture space spanning from pure phases to equal-weighted mixtures. Simplex-centroid design is a component-independent experimental design for mixtures in which experiments are generated by the equation:

$$n = 2^q - 1 \tag{2}$$

Where n is the number of experiments and q is the maximum number of components of the mixture (corresponding to the dimensionality of the mixture space). While the number of the experiments is defined by Eq. 2, the composition of each mixture is defined by the generic binomial coefficient $\binom{q}{m}$, where m represents the number of desired components in the mixture. This means:

$$
\begin{aligned}
&\text{for } m = 1, \binom{q}{1} \text{ pure components, permutations of } (1, 0, 0, \ldots, 0)\\
&\text{for } m = 2, \binom{q}{2} \text{ mixtures, permutations of } (1/2, 1/2, 0, \ldots, 0)\\
&\text{for } m = 3, \binom{q}{3} \text{ mixtures, permutations of } (1/3, 1/3, 1/3, \ldots, 0)\\
&\cdots\\
&\text{for } m = q, \binom{q}{q} \text{ mixture of the } q \text{ components } (\tfrac{1}{q}, \tfrac{1}{q}, \tfrac{1}{q}, \ldots, \tfrac{1}{q})
\end{aligned} \tag{3}
$$

A graphical representation of this experimental design applied to a three-components system, for a generic mixture $\{A, B, C\}$ can be seen in Fig. 3, represented by the black dots. Pure components are positioned on the vertices of an equilateral triangle, two-component mixtures are positioned in the midpoint of each side and the ternary mixture is positioned in the center of gravity of the triangle. The red points in the ternary graph represent the "augmented" experiments of the simplex-centroid design [9], which is a set of additional experiments which give the possibility to obtain more precise information on the curvature of the response surface inside the experimental domain. With an equal number of experiments, another DoE (such as simplex-lattice design {3,2} [11]) would give more information about the perimeter of the experimental domain, neglecting the central zone of the mixture space. This set of experiments is commonly used for model validation and testing, but can also be used to build more robust models. The set of augmented experiments is obtained by the q permutations of the $(\tfrac{q+1}{2q}, \tfrac{1}{2q}, \tfrac{1}{2q}, \ldots, \tfrac{1}{2q})$ mixture, which results in three additional experiment for a three-component mixture domain.

2.2. Materials

Blanc Fixe G barium sulfate (>99% w/w, MM = 137.327 g mol^{-1}, $\rho = 4.48$ g cm^{-3}) were given by Universal Services S.r.l. (Milano, Italy) and produced by Solvay (Massa, Italy). Bi_2O_3 (>99% w/w, MM = 208.980 g mol^{-1}, $\rho = 8.93$ g cm^{-3}) was purchased by Thermo Fischer (Kandel, Germany). Zinc acetate (>99% w/w, MM = 219.528 g mol^{-1}, $\rho = 1.74$ g cm^{-3}) and urea (>99% w/w, MM = 60.06 g mol^{-1}, $\rho = 1.32$ g cm^{-3}) were purchased by Merck KGaA (Darmstadt, Germany). Graphite (>99% w/w, MM = 12.01 g mol^{-1} $\rho = 2.23$ g cm^{-3}) was given by Itaprochim (Milan, Italy).
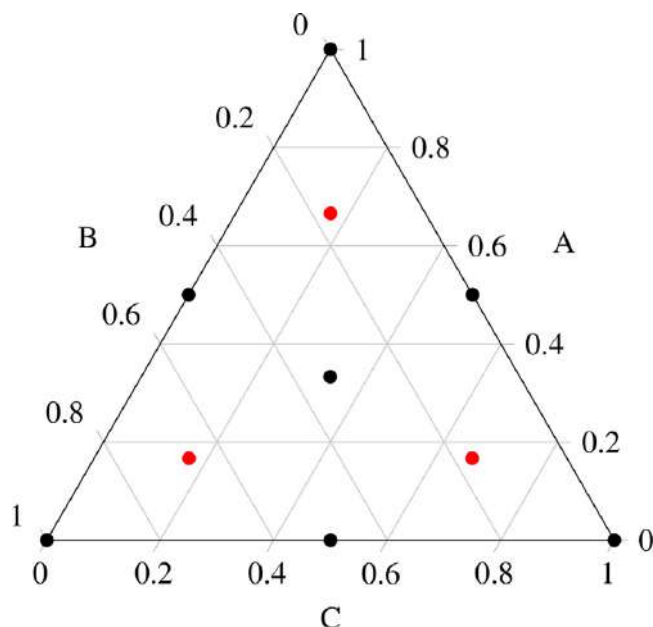
Fig. 3. Simplex-centroid design augmented for ternary systems. In black, the $2^q + 1 = 7$ points representing the seven mixtures designed from the sole Simplex-Centroid design. In red, the $q = 3$ augmented experiments, for model testing and validation. (For interpretation of the references to colour in this figure legend, the reader is referred to the web version of this article.)

2.3. Data collection

A Rigaku NEX QC with the X-ray tube at 20 kV in electric potential and 200 μA in current was used for XRF measurement in air condition. Rigaku's filter A was used during the measurements. A Bruker D8 Advance with a Lynxeye XE-T detector and a Cu source ($\lambda = 1.54$ Å) was used for XRPD pattern collection in the 2θ range of 10° to 120°). The instrument was equipped with an auto-sampler with nine positions and an air scatter knife. On both the primary and secondary optics Soller slits 2.5° opening were positioned and automatic divergence slits were used with a fixed sample illumination of 10 mm length. Goniometer radius was 280 mm. Analyses were run without sample rotation as in preliminary measurements it was observed to negatively affect the quality of data. In fact, the large differences in density cause a segregation during rotation because heavy and light phases are concentrated in the bottom and top parts of the sample holder respectively. Such phenomenon could be avoided by pressing the sample in a pellet but this would cause an increased and not controllable degree of PO. The tube was set at 40 mA in current and 40 kV in electric potential. Powders were observed with a STEMI 508 microscope with a 2x frontal optic equipped with Zeiss fiber optics halogen bulbs and a LED ring for illumination. Digital high resolution images of the powders were collected with a 20 MPx SONY sensor camera. A Hitachi FLEXSEM 1000 equipped with AZtecOne Oxford EDS, was used for electron microscopy analysis and elemental analysis, in order to evaluate samples' features. The source of the electrons was a tungsten filament at 20 kV. Powders were measured without coatings.

2.4. Sample preparation

Substances were only manually ground prior measurement in an agate mortar to simulate an industrial content in which simple and fast measurements are preferred (i.e. avoid Mc Crone grinding prior XRPD measurement). Graphite, the compound showing layered morphology and
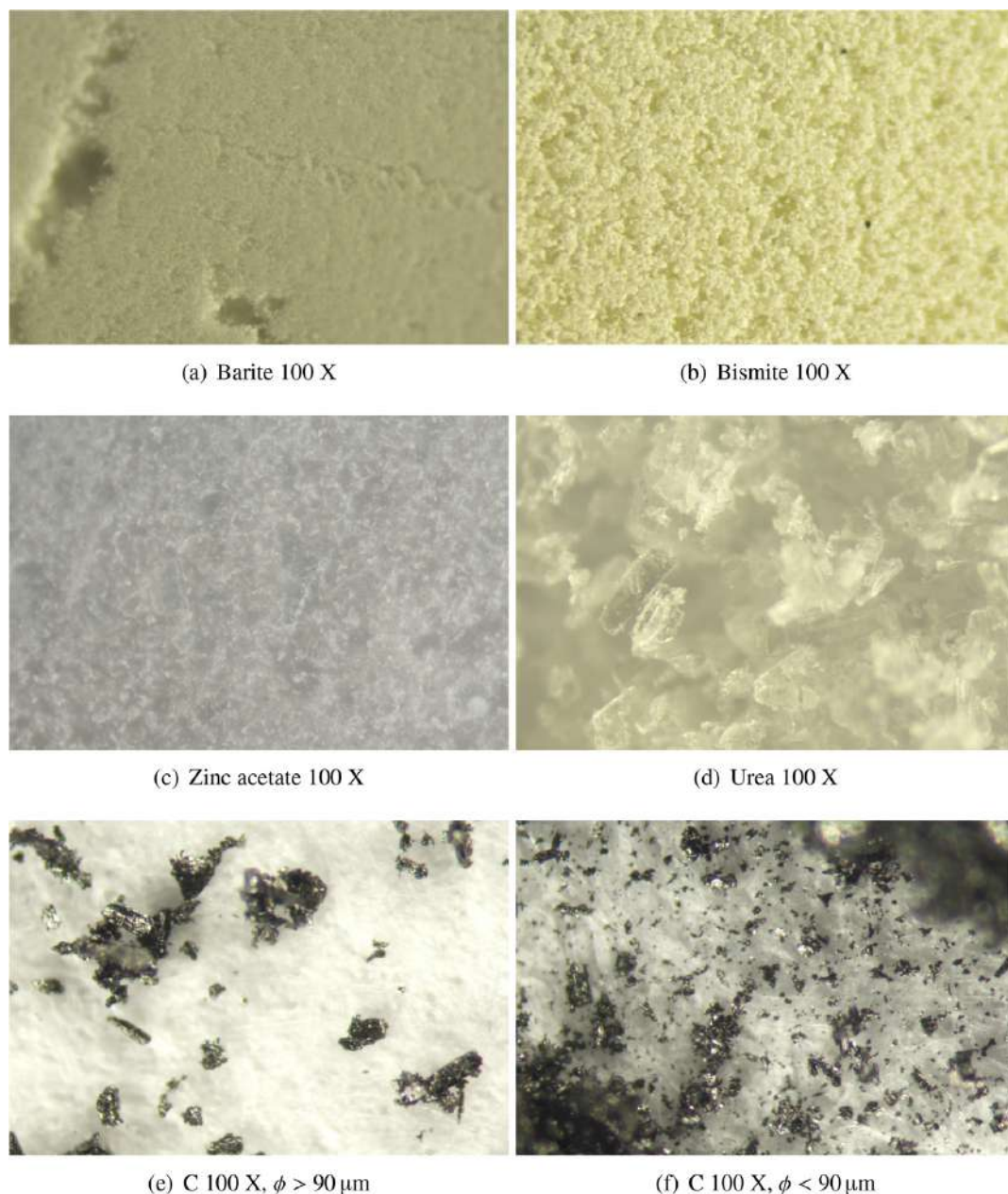
Fig. 4. Optical microscope images of pure phases used in all the experimental designs. Particle size are very different from one substance to another promoting micro-absorption effects. Graphite is divided in two batches due to sieving, as shown in figures.

thus more prone to PO, was then sieved (90 μm mesh diameter) and both the finer and the larger fractions were retained with the scope of preparing samples with different but controlled presence of PO. Images of pure phases, collected with a STEMI 508 microscope with a 2x frontal optic, are shown in Fig. 4. 4.5 g of each sample were prepared. The quantity was chosen accordingly to the UNI EN 15309:2007 Italian standard methodology for the determination of elemental by X-ray fluorescence [12] as there are no particular requirements for XRPD.

Mixtures sets, whose compositions are detailed in Table 1, were prepared according to a Simplex-centroid design augmented and characterized by the following: four sets of samples

Table 1

Compositions and ID of every produced sample. The four experimental design are ordered in an increasing degree of influence of the micro-absorption and PO effect. Graphite quantities in experiments set D2 are reported as total weight fraction outside the brackets and in relative quantities of the larger and smaller fractions inside the brackets.

Sample ID	$BaSO_4$ (% w/w)	Bi_2O_3 (% w/w)	$Zn(CH_3COO)_2(H_2O)_2$ (% w/w)	CH_2N_2O (% w/w)	C $(C_{or.} - C_{n.or.})^a$ (% w/w)
			Experiments set D1		
D1-Ba	1.000	0.000	-	-	0.000 (0-0)
D1-Bi	0.000	1.000	-	-	0.000 (0-0)
D1-Gr	0.000	0.000	-	-	1.000 (0–1.000)
D1-Ba Bi	0.500	0.500	-	-	0.000 (0-0)
D1-Ba Gr	0.500	0.000	-	-	0.500 (0-0.500)
D1-Bi Gr	0.000	0.500	-	-	0.500 (0-0.500)
D1-Ba Bi Gr	0.333	0.333	-	-	0.333 (0-0.333)
D1-SA 1	0.666	0.167	-	-	0.167 (0-0.167)
D1-SA 2	0.167	0.666	-	-	0.167 (0-0.167)
D1-SA 3	0.167	0.167	-	-	0.666 (0-0.666)
			Experiments set D2		
D2-Ba	1.000	0.000	-	-	0.000 (0-0)
D2-Bi	0.000	1.000	-	-	0.000 (0-0)
D2-Gr	0.000	0.000	-	-	1.000 (0.310-0.690)
D2-Ba Bi	0.500	0.500	-	-	0.000 (0-0)
D2-Ba Gr	0.500	0.000	-	-	0.500 (0.155-0.345)
D2-Bi Gr	0.000	0.500	-	-	0.500 (0.155-0.345)
D2-Ba Bi Gr	0.333	0.333	-	-	0.333 (0.103-0.230)
D2-SA 1	0.666	0.167	-	-	0.167 (0.052-0.115)
D2-SA 2	0.167	0.666	-	-	0.167 (0.052-0.115)
D2-SA 3	0.167	0.167	-	-	0.666 (0.206-0.460)
			Experiments set D3		
D3-Ba	1.000	0.000	0.000	-	-
D3-Bi	0.000	1.000	0.000	-	-
D3-Zn	0.000	0.000	1.000	-	-
D3-Ba Bi	0.500	0.500	0.000	-	-
D3-Ba Zn	0.500	0.000	0.500	-	-
D3-Bi Zn	0.000	0.500	0.500	-	-
D3-Ba Bi Zn	0.333	0.333	0.333	-	-
D3-SA 1	0.666	0.167	0.167	-	-
D3-SA 2	0.167	0.666	0.167	-	-
D3-SA 3	0.167	0.167	0.666	-	-
			Experiments set D4		
D4-Ba	1.000	0.000	-	0.000	-
D4-Bi	0.000	1.000	-	0.000	-
D4-Ur	0.000	0.000	-	1.000	-
D4-Ba Bi	0.500	0.500	-	0.000	-
D4-Ba Ur	0.500	0.000	-	0.500	-
D4-Bi Ur	0.000	0.500	-	0.500	-
D4-Ba Bi Ur	0.333	0.333	-	0.333	-
D4-SA 1	0.666	0.167	-	0.167	-
D4-SA 2	0.167	0.666	-	0.167	-
D4-SA 3	0.167	0.167	-	0.666	-

^{a}Quantities of oriented graphite ($C_{or.}$, $\phi > 90\,\mu m$) and non-oriented graphite ($C_{n.or.}$, $\phi < 90\,\mu m$).

were then produced, in order to simulate an equal number of different systems with different typical obstacles for the quantitative phase analysis: complexity of the mixture by the increasing peak superposition, preferred orientations and high differences in density and particle size of the phases are also present, to enhance the effects of micro-absorption. The 4 data sets have been built with the following features:

- Experiments set D1: the three components are barite, bismite and the sieved graphite ($\phi < 90\,\mu m$), showing a limited PO effect. The main issues related to this data set are the large
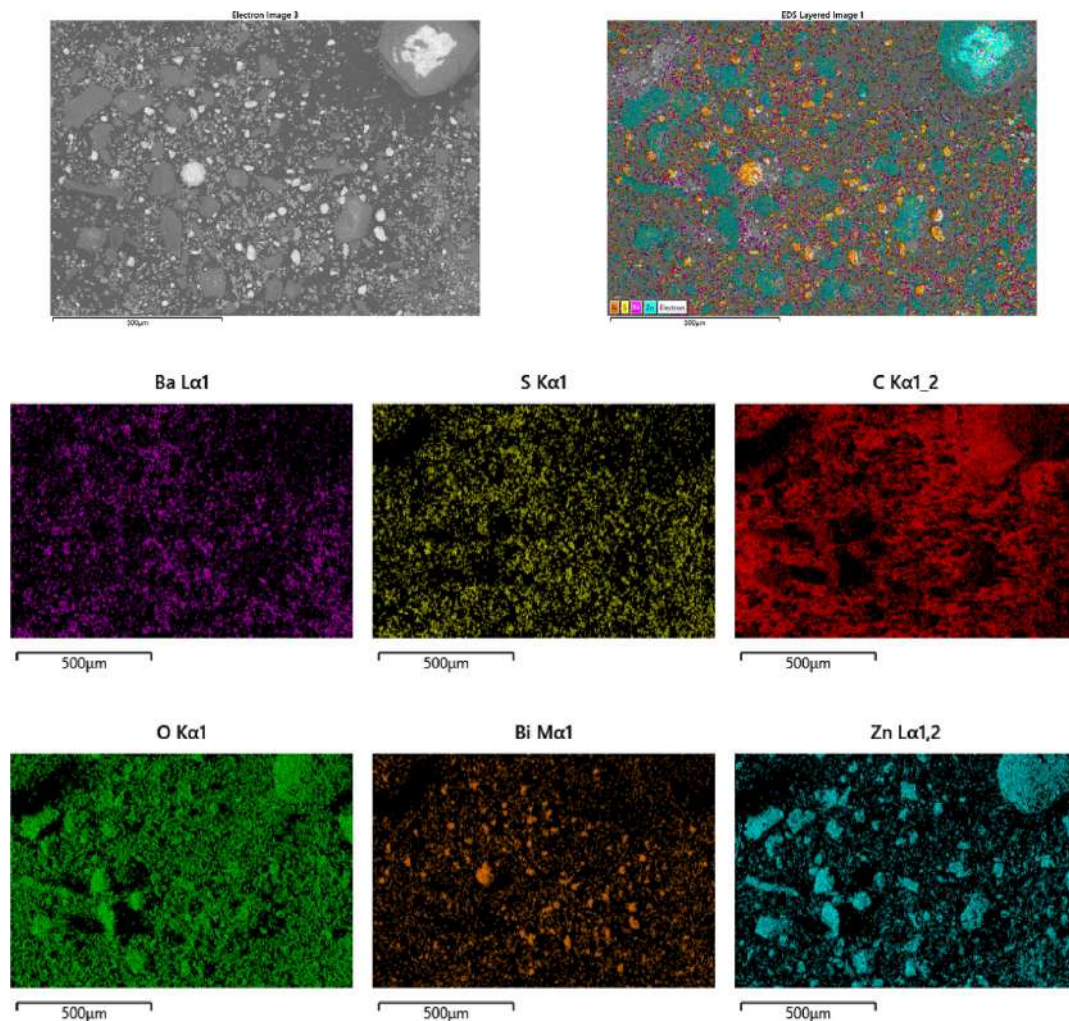
Fig. 5. SEM-EDS images of sample *D3-Ba Bi Zn*. Although being accurately dispersed, large differences in particle size of each powder is clearly visible. A large agglomerate of zinc acetate can be observed in the top-right area of the pictures.

differences in density and in the particle size of the three pure phases and the presence of a phase (graphite) which does not have a characteristic XRF signal.

- Experiments set D2: identical to experimental set D1, but 30% in weight of the used graphite belonged the fraction with diameter larger than 90 μm after sieving. As a result, an important PO effect in addition to the previously described issues of experiment set D1 is introduced in experiment set D2.
- Experiments set D3: graphite is substituted by zinc acetate, which possesses an XRF signal ($K_{\alpha Zn} = 8.63$ keV, $K_{\beta Zn} = 9.57$ keV), shows PO and has a lower density, which enhances the micro-absorption effects and a larger unit cell, increasing peak superposition effects.
- Experiments set D4: in this set, the third component is urea, which once again does not possesses a XRF signal, has a slight PO effect, has larger particles (as can be seen in Fig. 4) and has a lower density than zinc acetate, with increased with in micro-absorption effects due to density difference with respect to barite and bismite.

SEM-EDS analysis was used for electron microscopy analysis and elemental analysis, in order to evaluate samples' correct dispersion and differences in particle size. In this paper, an example of the distribution of the mixtures prepared is reported in Fig. 5, where the dispersion of the

three phases (barium sulfate, bismuth oxide and zinc acetate) can be observed. Although being accurately mixed, the differences in the average particle size of the pure substances affect the homogeneity of the powder mixture. In particular, a large agglomerate of almost 300 μm can be observed on the top-right corner of the figures.

Open Database Rules

Any one can add a XRPD data set provided that:

- XRPD data and instrumental conditions are provided to the corresponding author to produce a new updated version of the Mendeley Data repository;
- the simplex-centroid augmented approach must be used to produce ten XRPD patterns and, if possible, the ten corresponding XRF spectra for each proposed dataset;
- all the instrumental data set to both reproduce the experiments and using parametric approach for data refinement and/or analysis must be provided.

Authors' Contribution

Mixtures were prepared by BM. XRF and XRPD analysis was performed by BM. Materials characterization by optical microscopy, SEM and EDS was performed by both BM and LP. All the authors analyzed the data, edited the manuscript and approved its final version.

Declaration of Competing Interest

The authors declare that they have no known competing financial interests or personal relationships which have, or could be perceived to have, influenced the work reported in this article.

Acknowledgments

References

[1] I. Madsen, N. Scarlett, L. Cranswick, T. Lwin, Outcomes of the international union of crystallography commission on powder diffraction round robin on quantitative phase analysis: samples 1a to 1h, J. Appl. Crystallogr. 34 (4) (2001) 409–426, doi:10.1107/S0021889801007476. Cited By 152

[2] R. Kleeberg, State-of-the-art and trends in quantitative phase analysis of geological and raw materials, Zeitschrift fur Kristallographie, Supplement (30) (2009) 47–52, doi:10.1524/zksu.2009.0007. Cited By 6

[3] L. León-Reina, A. De La Torre, J. Porras-Väzquez, M. Cruz, L. Ordonez, X. Alcobé, F. Gispert-Guirado, A. Larrañaga-Varga, M. Paul, T. Fuellmann, R. Schmidt, M. Aranda, Round robin on rietveld quantitative phase analysis of portland cements, J. Appl. Crystallogr. 42 (5) (2009) 906–916, doi:10.1107/S0021889809028374. Cited By 41

[4] M.D. Raven, P.G. Self, Outcomes of 12 years of the reynolds cup quantitative mineral analysis round robin, Clays Clay Miner. 65 (2) (2017) 122–134.

[5] M. Bortolotti, L. Lutterotti, G. Pepponi, Combining XRD and XRF analysis in one rietveld-like fitting, Powder Diffr. 32 (2017) 225–230, doi:10.1017/S0885715617000276.

[6] B.M. Pederson, R.M. Gonzalez, R.S. Winburn, Minimization of microabsorption effects in complex mixtures, Adv. X-Ray Anal. 46 (2003) 68–73.

[7] N.V. Scarlett, I.C. Madsen, Effect of microabsorption on the determination of amorphous content via powder x-ray diffraction, Powder Diffr. 33 (1) (2018) 26.

[8] D.R. Cox, N. Reid, The theory of the design of experiments, CRC Press, 2000.

[9] J.A. Cornell, Experiments with mixtures: Designs, models, and the analysis of mixture data, volume 403, John Wiley & Sons, 2011.

[10] H. Scheffé, Experiments with mixtures, Journal of the Royal Statistical Society: Series B (Methodological) 20 (2) (1958) 344–360.

[11] M. Lopresti, G. Alberto, S. Cantamessa, G. Cantino, E. Conterosito, L. Palin, M. Milanesio, Light weight, easy formable and non-toxic polymer-based composites for hard x-ray shielding: a theoretical and experimental study, Int. J. Mol. Sci. 21 (3) (2020) 833.

[12] UNI, Characterization of waste and soil - determination of elemental composition by x-ray fluorescence, 2007, Accessed: 2021-01-15, http://store.uni.com/catalogo/uni-en-15309-2007.

Light Weight, Easy Formable and Non-Toxic Polymer-Based Composites for Hard X-ray Shielding: A Theoretical and Experimental Study

They think they're better than us because their performance review reflects it!

Leonard, L.

Article

Light Weight, Easy Formable and Non-Toxic Polymer-Based Composites for Hard X-ray Shielding: A Theoretical and Experimental Study

Mattia Lopresti [1] , **Gabriele Alberto** [2] , **Simone Cantamessa** [1] , **Giorgio Cantino** [1] ,
Eleonora Conterosito [1] , **Luca Palin** [1] **and Marco Milanesio** [1,*]

[1] Dipartimento di Scienze e Innovazione Tecnologica, Università degli Studi del Piemonte Orientale,
     viale T. Michel, 11-15121 Alessandria, Italy; mattia.lopresti@uniupo.it (M.L.);
     simone.cantamessa@uniupo.it (S.C.); giorgio.cantino@uniupo.it (G.C.);
     eleonora.conterosito@uniupo.it (E.C.); luca.palin@uniupo.it (L.P.)
[2] Bytest s.r.l.-TÜV SÜD Group, Research Center, via Pisa 12, 10088 Volpiano, Italy; gabriele.alberto@tuv.it
[*] Correspondence: marco.milanesio@uniupo.it

check for
updates

Abstract: Composite lightweight materials for X-ray shielding applications were studied and developed with the goal of replacing traditional screens made of lead and steel, with innovative materials with similar shielding properties, but lighter, more easily formed and workable, with lower impact on the environment and reduced toxicity for human health. New epoxy based composites additivated with barium sulfate and bismuth oxide were designed through simulations performed with softwares based on Geant4. Then, they were prepared and characterized using different techniques starting from digital radiography in order to test the radiopacity of the composites, in comparison with traditional materials. The lower environmental impact and toxicity of these innovative screens were quantified by Life Cycle Assessment (LCA) calculation based on the ecoinvent database, within the openLCA framework. Optimized mixtures are (i) 20% epoxy/60% bismuth oxide/20% barite, which guarantees the best performance in X-ray shielding, largely overcoming steel, but higher in costs and a weight reduction of *circa* 60%; (ii) 20% epoxy/40% bismuth oxide/40% barite which has slightly lower performances in shielding, but it is lighter and cheaper than the first one and (iii) the 20% epoxy/20% bismuth oxide/60% barite which is the cheapest material, still maintaining the X-ray shielding of steel. Depending on cost/efficiency request of the specific application (industrial radiography, aerospace, medical analysis), the final user can choose among the proposed solutions.

1. Introduction

X-ray shielding is particularly interesting for many applications, from the industrial field of non destructive control techniques (radiography and tomography), airport scanners and control [1] to the medical field (radiology and dentistry) [2,3]. Nowadays the most common shields for X-rays are still made of lead and steel. While lead has excellent shielding properties, its mechanical features are very poor, being very soft and malleable. Steel, instead, has sufficient shielding properties and excellent mechanical performances but high costs and limited workability for the realization of shielding masks by machining. These materials have complementary advantages in the quality of the shielding, soft X-rays cutting and good mechanical properties, but the drawbacks are objects weight, human health hazards and environment pollution. The principal solutions given

in the specialized literature are based on three different types of materials: inorganic, organic and composites. The most common alternative to the traditional shielding is the use of inorganic materials: a compressed slab of minerals like barium sulfate ($BaSO_4$), calcium sulfate ($CaSO_4$) or calcium carbonate ($CaCO_3$). This kind of solution is easy to obtain but the objects have very poor mechanical properties, with low tensile strength and tendency to crumble. Furthermore, the weight gain is not so convenient. The second solution is represented by organic materials in which the number of electrons by volume unit is increased by adding iodine atoms to polymeric chains: mostly, isoprenic rubber is synthesized with monomers that have iodine atoms covalently bound. Examples of these monomers are iopanoic acid 3-(3-amino-2,4,6-triiodophenyl)-2-ethyl propanoic acid and iothalamic acid (5-acetamido-2,4,6-triiodo-N-methyl iso-phthalamic acid) and 2,4,6-triiodobenzoic acid [4–6]. Resulting materials have sufficient radiopacity and good mechanical performances. Also, as the iodine is covalently bound, the chances of leaks are low. However, these kinds of shields are unfit for industrial radiography, where the photon energies are larger than 150 keV. In this region, because of the dilution of iodine into the polymer, the shielding power is very low. The last class is that of composite materials, attempting at joining the qualities of minerals (high shielding and no or low toxicity) with those of metals (good mechanical properties), adding an improved workability and lower cost. Composites are divided in two sub-classes:

- metal powders embedded in the polymeric matrices. Some of these solutions are already in commerce, e.g., tungsten-loaded polylactic acid for 3D-Printing [7];
- minerals included in polymeric matrices, typically high density oxides such as zinc oxide (ZnO), tin oxide (SnO_2) or bismuth oxide (Bi_2O_3) [2,8–10] and compounds of materials of the sixth period of the periodic table such as barium sulphate ($BaSO_4$) [11].

A critical factor for composite materials is dispersion and adhesion of the solid materials to the polymer, in order to avoid both fractures and leakage of heavy transition/post-transition metals. Another critical issue resides in the homogeneous distribution of the additive in the whole volume of the sample, as evidenced by Prolongo et al. [12]. The sedimentation of the powder on the bottom side of the sample, may bring to three effects:

- reduction of the effective thickness of the shielding material, which causes the reduction of the overall shielding performance;
- different mechanical properties in the same sample based only on which side is considered, a chance that could bring to fracture or lower the overall resistance;
- anisotropic shielding yields.

In this paper, we focus on developing low-cost lightweight shielding composite materials that can be easily processed, formed in complex shapes and produced. Materials from scientific literature were simulated with Geant4 to test their screening performances. Commercial epoxidic resins were chosen because of their low cost, easy formability and workability. Barium sulphate and bismuth oxide were chosen because of their good balance of low cost, radiopacity, low environmental impact and absent or low toxicity. Different composite formulations were then predicted with a Simplex-lattice experimental design and developed in laboratory. Materials were fully characterized using XRPD, optic and electronic microscopy, computed radiography and tensile strength test. The overall environmental impacts of the samples were examined through an LCA study "from the cradle to the gate" and compared to the same calculations for the traditional screens of lead and steel. It was thus possible to develop composite formulations able to assure the best performances in term of shielding, weight and low cost depending on final user requests.

2. Results

2.1. Geant4 Simulations

The first batch of simulations was made with a software based on Geant4 which simulates the interaction between electromagnetic radiation and matter; the interaction of pure materials selected from the scientific literature with monochromatic beams of X-rays was then studied adopting successive steps of energy in the range 0–350 keV, as described in Appendix B. This approach can be defined a *"soft simulation"* because of its approximation, since in industrial radiography the incident beam is a spectrum, more specifically the Bremsstrahlung spectrum plus the characteristic emissions of the anti cathode of the X-ray tube. The aim is estimating which materials were the best fitted for shields that have to be not only radiopaque, but also economically affordable and mechanically resistant. As showed in Figure 1a, the three principal additives from scientific literature, $BaSO_4$, Bi_2O_3 and ZnO, over-perform the stainless steel in the range 75–240 keV, which is also the main energy of photons of standard X-ray tubes for radiography. Also, simulated samples of composites epoxy resin—$BaSO_4$ were compared to steel in order to evaluate the effect that would be obtained by adding this inorganic additive into the epoxy resin (Figure 1b). After this analysis, ZnO was discarded because its shielding properties are similar to those of barium sulfate, but its cost is about 100 times higher. Samples predicted from the Simplex-lattice experimental design for a ternary mixture were simulated in a second time with a second application built with Geant4, which allowed a more accurate approach to the problem. This new simulation setup featured a thin tungsten solid between the beam source and the sample. Incident particles were also changed from X-rays to electrons, so that from the first impact with the anti cathode, a characteristic Bremsstrahlung spectrum of X-rays of W would be generated and focused on the sample, as described in Figure A1 in Appendix B. Figure 2a–d show the simulated behavior of each sample compared to steel. In the range 30 keV–80 keV some spikes are evident, and are the characteristic emissions of the tungsten target ($K_{\beta_1} = 67.24$ keV, $K_{\beta_2} = 69.10$ keV) or effects of absorption-emission from the heavy atoms in the screens (Barium $K_{\alpha_1} = 31.81$ keV, Barium $K_{\alpha_2} = 32.19$ keV, Bismuth $K_{\alpha_1} = 74.82$ keV, Bismuth $K_{\alpha_2} = 77.11$ keV). Results of this simulation set can be seen in Figure 2. The large noise in the simulation results is due to the high rate in absorption from the material; on the other hand, a fit of the resulting data would lead to a loss of information about the K_α and K_β riemissions from the heavy metals in the simulated samples. Studied samples all perform better than steel, in particular sample of Figure 2d.
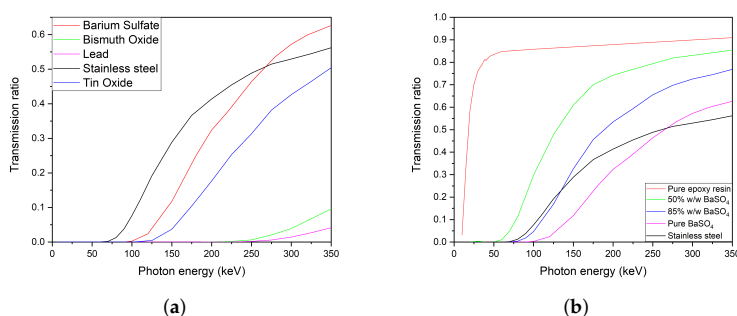
Figure 1. First generation of simulations. These data are referred to 1 cm cubes irradiated with a monochromatic beam of X-rays at successive steps of photon energies, from 0 to 350 keV. In (**a**) common shielding materials from scientific literature are compared. In (**b**) samples of mixture between epoxy resin and $BaSO_4$ are simulated and compared to stainless steel. (**a**) Pure materials; (**b**) $BaSO_4$ samples.

(**a**)

(**b**)

(**c**)

(**d**)
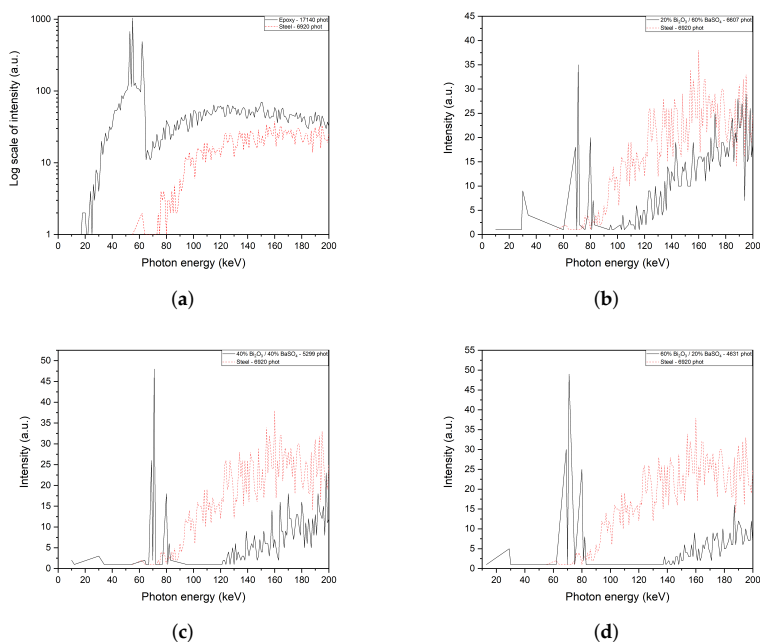
Figure 2. Simulations of the transmitted spectrum of Bremsstrahlung of a tungsten target of 300 μm through a sample of a 1 cm-sided cube of different mixtures compared to the same solid of stainless steel. (**a**) shows the transmitted spectrum through a sample of pure epoxy resin with no additive; the log scale was set due to the high rate of transmitted photons that crossed the polymeric materials. (**a**) Pure epoxy resin; (**b**) 60% $BaSO_4$, 20% Bi_2O_3, 20% Epoxy; (**c**) 40% $BaSO_4$, 40% Bi_2O_3, 20% Epoxy; (**d**) 20% $BaSO_4$, 60% Bi_2O_3, 20% Epoxy.

2.2. Setup and Optimization of Sample Preparation Methods

The inorganic additives were analyzed with X-ray Powder Diffraction to evaluate the purity of the minerals before being added to the polymeric matrix. The XRPD patterns of barium sulfate by Itaprochim and Universal Services S.r.l. and of bismuth oxide by Thermo Fischer (Kandel, Germany) were collected. After identifying the impurities by peak matching using QualX [13], Rietveld refinement was performed on the XRPD patterns using structures from the Crystallographic Information Files retrieved from the Crystallographic Open Database and TOPAS Academic V5 [14]. Identified in the first barium sulfate batch (Itaprochim) some impurities: calcite ($CaCO_3$), and dolomite ($CaMg(CO_3)_2$) 0.8 and 13.6% *w/w* respectively. Blanc fixe barium sulfate (Universal Services S.r.l.) and Bi_2O_3 showed a purity of 99.5% and no relevant impurities were found by XRPD analysis.

Nine samples (Table 1) were produced with epoxy resin and an increasing mass fraction of $BaSO_4$ (Itaprochim), from 30% *w/w* to 85% *w/w* according to the procedure described in Section 5 and shown in Appendix C; 85% *w/w* was observed to be the upper limit of wettability of the powders and, consequently, the limit of mixability between powders and liquid precursors of the epoxy resin. XRPD was also used to characterize this same batch of nine barite samples. After their curing, they were analyzed on both sides: the one exposed to the air and the one in contact with the mold. The samples showed different behaviors depending on the sides and the quantity of inorganic additive.

Table 1. Samples of BaSO₄—Epoxy composites to assess additive amount effect.

BaSO₄ Samples		
Sample Name	BaSO₄ Weight %	Epoxy Weight %
1	0	100
2	30	70
3	40	60
4	50	50
5	60	40
6	70	30
7	80	20
8	80	20
9	85	15

In Figure 3, bottom graph, in sample 2 the broad band of the amorphous epoxy polymer is evident, suggesting that most of the inorganic moved down in the sample during the curing. On the bottom side of the sample (Mold in Figure 3), the barium sulfate pattern is dominant, confirming the sedimentation of the additive. Rietveld refinement of all datasets indicated a different behaviour of barite and of dolomite impurities. Because of their different density and size, up to sample 5 the sedimentation of barite is larger with an increasing amount in the mold side with respect to dolomite. Conversely in samples 6, 7 and 8 this behavior is not observed and the trend is inverted with a smaller barite percentage in the mold side. This trend can be explained because samples 6, 7 and 8 were already rather viscous before curing and therefore the sedimentation effect was limited (Figure 4). In samples 7 and 8 the amorphous band is not visible and the intensity of air side and mold side patterns are very similar. The refined peak shift confirms the sedimentation hypothesis. A peak shift is observed but it is a combination of the sedimentation and of sample imperfections (bubbles and rugosity), causing a misalignment of the sample. XRPD evidenced a progressive sedimentation process, occurring during the time of gelification of the resin. The phenomenon is more evident in samples with an inorganic fraction smaller than 60% w/w, as the viscosity is low and the powders encounters little resistance to the deposition process.
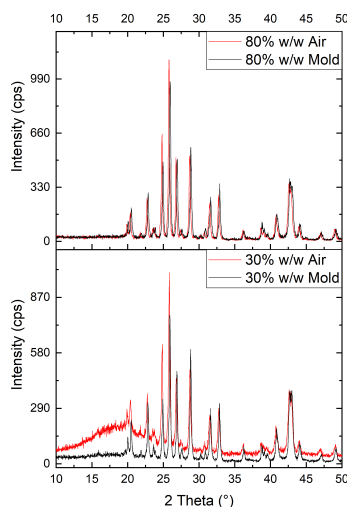
Figure 3. XRPD patterns collected on both sides of sample 2 (30% w/w in BaSO₄) and sample 7 (80% in BaSO₄).
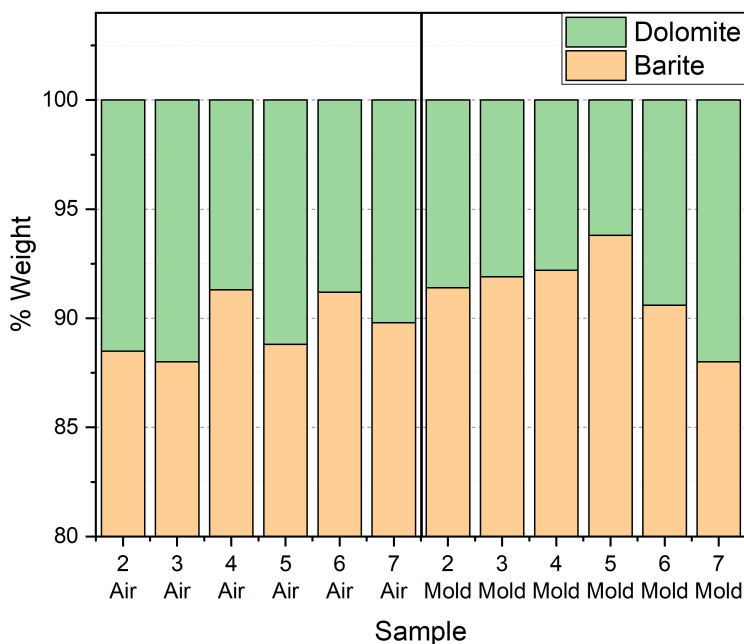
Figure 4. Quantitative analysis of crystalline phases of barite (BaSO$_4$) and dolomite (CaMg(CO$_3$)$_2$) was done on air and mold sides of samples of epoxy/barite.

2.3. Experimental Design

Sample compositions were selected applying the Simplex-Lattice design algorithm described in Appendix A. The extension of the simplex, therefore the minimum amount of each component of the mixture, was decided considering the miscibility limit for the binary mixture BaSO$_4$-epoxy, which was observed as 85% w/w, as discussed in Section 2.2. To avoid using the exact limits of the experimental domain the upper limit on the quantity of additive in the epoxy precursor was set to 80%. Simplex-Lattice design described in Appendix A explores all the experimental domain, which in this case would not be useful due to the fact that the lone resin is completely transparent to X-rays and the other two vertexes of the simplex would lead to two slabs of pure compacted powder with no mechanical properties. Being the minimal content of epoxy resin equal to the 20% w/w of the total weight, the consequent simplex obtained is the one that can be seen in Figure 5. Then, applying Equation (A2) for three components and second grade interactions, the result obtained was:

$$\frac{(q+m-1)!}{m! \cdot (q-1)!} = \frac{(3+2-1)!}{2! \cdot (3-2)!} = 6 \tag{1}$$

The result pinpoints the number of mixtures that had to be explored. Each sample of the simplex-lattice design was simulated with Geant4, but only the three black-dotted samples (a–c, in Table 2) had been prepared in laboratory. The three remaining samples: (d–f) provide low shielding from hard X-rays, but are still interesting for applications involving low energies (0–60 keV) and requiring good mechanical resistance to strain.

Experimental domain for the ternary mixture.
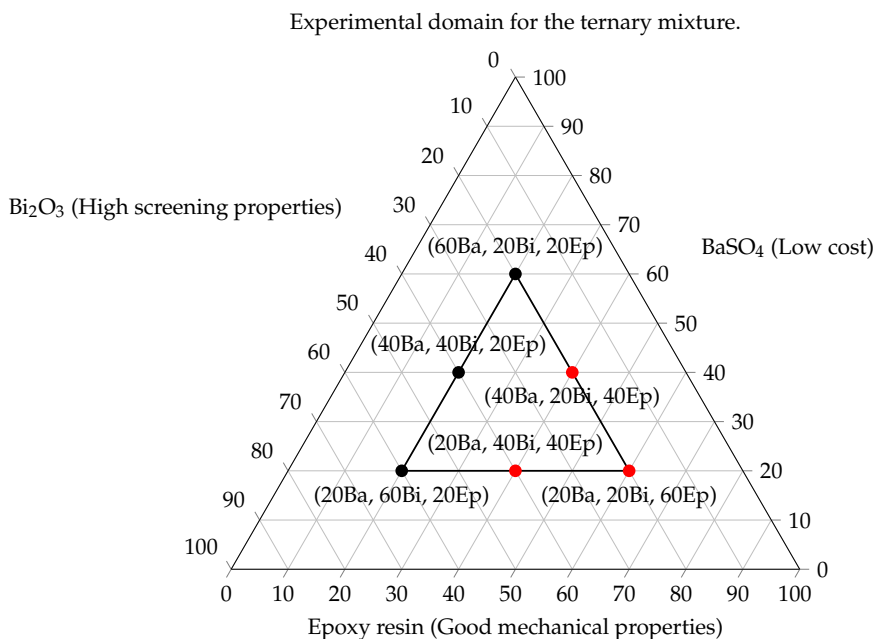
Figure 5. Simplex-lattice design algorithm applied to a mixture for a 3-dimensional experimental domain. To each of the three component of the mixture domain a property was associated: low cost for barite, highest radiopacity for bismuth oxide and high mechanical performances for the epoxy resin. Black dotted samples were developed in laboratory, while red dotted samples were not due to an excessive radiotransparency to hard X-rays.

Table 2. Mixtures provided by Simplex-lattice design.

BaSO₄–Bi₂O₃ Samples			
Sample Name	$BaSO_4$ Weight %	Bi_2O_3 Weight %	Epoxy Weight %
a	20	60	20
b	40	40	20
c	60	20	20
d	40	20	40
e	20	20	60
f	20	40	40

2.4. Direct Radiography

Figure 6 shows the radiographies collected over the nine first-generation samples, plus a reference made of steel, positioned on the bottom-right corner of the images. A graph of the performances of each sample compared to steel can be observed in Figure 6f. The curves were obtained by considering the gray scale values of the samples in the picture. The data were obtained by calculating the average gray scale value (from 0 to 255) over the whole sample area and then calculating the relative absorption. Curve 9, referred to the sample 85% in weight of barite, overperforms steel in terms of radiation absorption, a property that can be appreciated also by eye in Figure 6e. This result apparently clashes with the results in Figure 1, which instead shows that at 220 keV steel should be a better screen than this mixture. The reason of these discrepancies resides once again in the structure of the first simulation, which involved a monochromatic source of X-rays, which is not the real-world case, in the radiographic system. Also, a generator on which is applied an electric potential of 220 kV, provides just

few photons with energy of 220 keV; it has instead a maximum of the emission band at one third of the supplied tension (which gives about 70–75 keV, a range where the Epoxy-BaSO$_4$ composite effectively performs better than steel). Another information that comes from these images resides in the high defectivity ratio that characterize the most additivated samples. These defects are mainly air bubbles that remain trapped in the highly viscous matrix. Voids represents points in the samples in which the optical path for the photons is shorter compared to the rest of the bulk. Also, this kind of defect lowers the resistance of the samples in terms of tensile strength. The second set of simulations with Geant4 suggested that the second generation of samples would be more radiopaque than the previous ones due to the presence of bismuth oxide, therefore the setup and the experimental conditions were changed increasing the flux and detector sensitivity. Therefore, a direct comparison between the two results could not be made. In Figure 2 it can be observed that all samples strongly overperform steel, which is fully transparent at 180 kV. In the same image, sample *c* shows a large amount of bubbles in the bulk. As foretold by the hard simulations, an increase of bismuth oxide corresponds to a higher screening performance of the shields (Figure 7).

(**a**)　　　　　　　　　　　　(**b**)

(**c**)　　　　　　　　　　　　(**d**)

(**e**)　　　　　　　　　　　　(**f**)
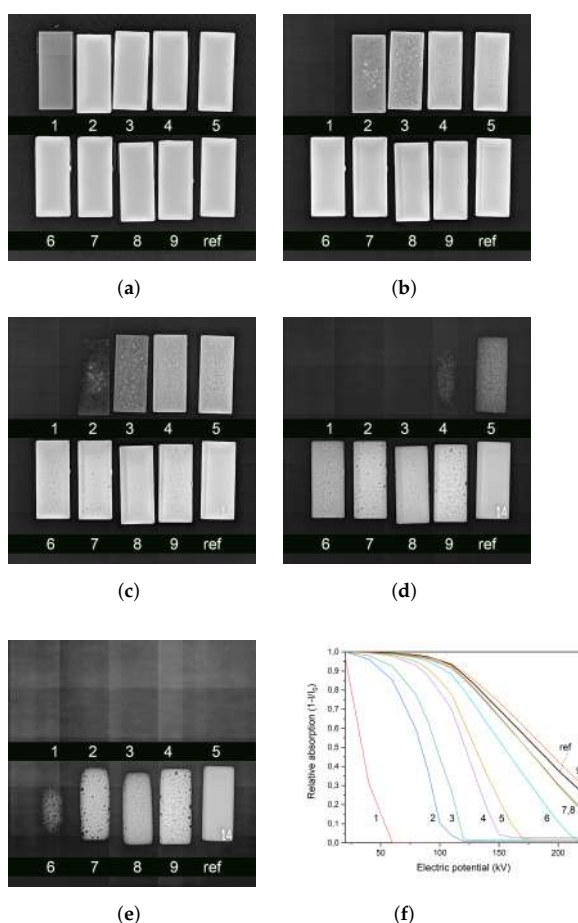
Figure 6. Radiographies of epoxy-barite samples at increasing percentage *w/w* in BaSO$_4$. Samples are labeled as in Table 2. Ref sample is the reference of steel. In (**f**), increasing X-ray absorbance profiles can be osberved, from left (0% *w/w* barite) to right (85% *w/w* barite). Greyscale data associated to (**f**) and relative statistics are available as supplementary material. (**a**) 20 kV; (**b**) 60 kV; (**c**) 100 kV; (**d**) 150 kV; (**e**) 220 kV; (**f**) Profile comparison.
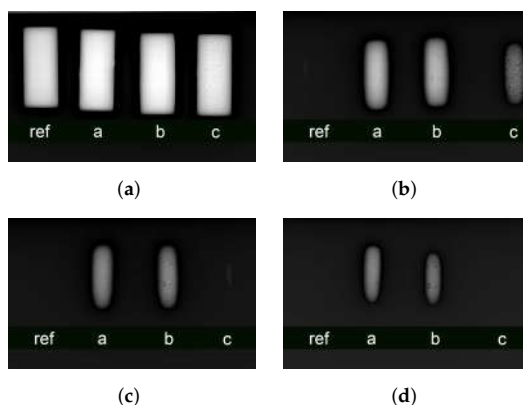
Figure 7. Radiographies on the three ternary mixtures (samples a, b, c in Table 2) developed in laboratory compared with the same steel sample for reference. In this case the photon flux was raised by increasing the current intensity to explore the behavior of the screens in a more severe experimental condition. (**a**) 120 kV; (**b**) 180 kV; (**c**) 200 kV; (**d**) 220 kV.

2.5. Mechanical Characterization

To evaluate the mechanical performances of the composite samples, a study of stress/strain properties was done. Five dog bone shaped samples suitable for the tensile tests were obtained for each mixture of the second generation series of samples. Another five samples of pure epoxy resin were prepared and used as a reference. These samples were subject to traction until break point. Data reported in Table 3 refer to each mixture performances under stress. The pure epoxy resin, showed a plastic behavior, with plastic deformation before the break point. This was not observed for mixture samples, which showed fragile behavior and lower resistance if compared to the pure epoxy resin. The sections of the fracture point were observed with SEM (Figure 8), which showed, in additivated samples, micrometric domains of inorganic powder which are responsible for the fracture. The SEM images evidenced an increase of the size of bismuth oxide domains in the matrix proportional to the increase of its amount in the sample. This agglomeration (particle segregation) phenomenon is related to the large uncertainty on the strain resistance of the sample *a*. On the contrary, barium sulfate is finely dispersed in the sample, but having a lower density than bismuth oxide, the overall inorganic percentage by volume in sample *c* is higher than the percentage in the *a* sample. This explains well also the high uncertainty and the low strain resistance of this sample. Sample *b* has the best mechanical performances because of the low amount of bismuth oxide, whose big grains are the main initiators of the fractures, and an acceptable volume ratio of powders over the resin. In the same images bubbles, which developed during the polymerization and were not expelled from the matrix due to the high viscosity of the samples, can be observed.

Table 3. Each mixture was subject to tensile testing with five replicas for each sample. Pure epoxy resin samples were tested as a reference. The data show that epoxy resin would break in the range 26–305 MPa after plastic deformation. Samples *a* and *c* show a low tensile resistance, accompanied with a huge variation coefficient. Sample *b* has instead a good resistance and a low variation coefficient, suggesting a very good reproducibility.

Sample	Average Stress at Break Point	Standard Deviation	Variation Coefficient %
Epoxy resin	28.68 MPa	±1.98 MPa	6.91%
a	9.654 MPa	±5.34 MPa	55.30%
b	14.12 MPa	±1.19 MPa	8.46%
c	5.06 MPa	±1.62 MPa	31.99%

(**a**)　　　　　　　　　　　　　　　　　　　　　　(**b**)

(**c**)　　　　　　　　　　　　　　　　　　　　　　(**d**)
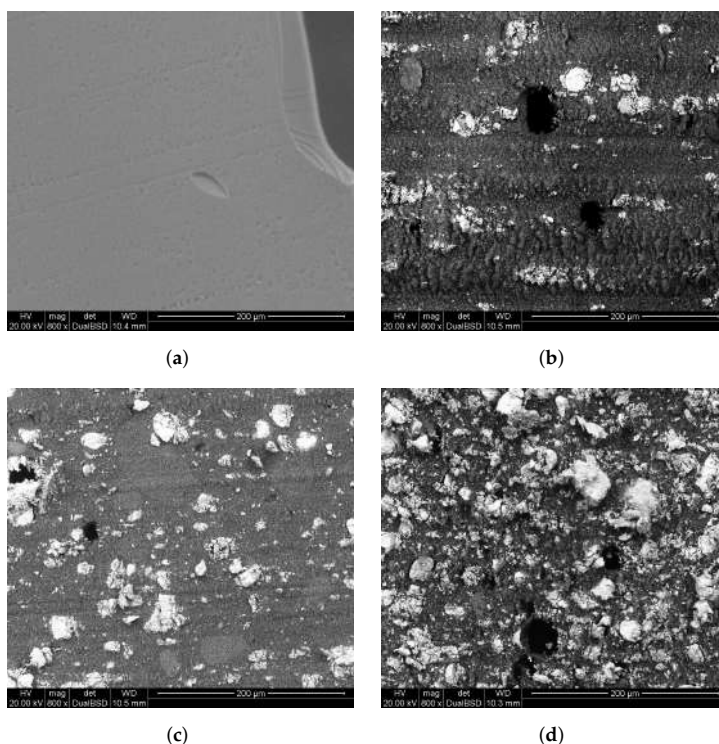
Figure 8. The four pictures show the sample section surface after the tensile test. The large Bi_2O_3 domains, visible in Figure 8d, are the main cause of fracture of the samples, while in Figure 8b, it can be seen that barium sulfate has a finer grain size. Figure 8c shows sample *b*, which has few large inorganic domains and a higher volumetric ratio of epoxy resin. (**a**) Epoxy resin; (**b**) Sample *a*; (**c**) Sample *b*; (**d**) Sample *c*.

2.6. LCA Study

A "from cradle to gate" LCA calculation was performed to assess the environmental performances of the produced epoxy-additive composites. Then, the results were compared with traditional screens made of lead and stainless steel. The LCA model was built using the openLCA software tool as described in Appendix D. The release 3.5 of the ecoinvent database was used as a reference for all the background data included in the LCA model. Foreground inventory data about raw materials, energy and processes, used for the making of the epoxy-additive samples, were taken directly from formulations while inventory data about the "from cradle to gate" life cycle of both screens of lead and stainless steel were taken from the literature. In this calculations a wide set of factors were considered and Life Cycle Impact Assessment results can be seen in Table 4. For reference, just sample *b* was compared to the traditional screens. This sample was selected among the three mixtures developed because of its intermediate screening properties, costs, environmental and human impact. Choosing just one of the three simplex samples does not heavily affects the following calculations, as the three epoxy samples were previously compared between them, and they showed little differences in the impacts. The variation of 20% in weight of Bi_2O_3 between the simplex samples does not affect the results heavily since the main reason due to the change in the impact relies in the relative scarcity of bismuth minerals and the consequent ore extraction. This process, compared to barium minerals, which instead are very common, is the main reason for the higher impact of bismuth on the calculation. Except for fossil resource scarcity, composite shielding materials are more sustainable than lead, and in terms of carcinogenicity they take a huge advantage over steel, as shown in Figure 9. In Table 4,

impacts referring to the composite samples are generally lower than the ones referred to lead, except the parameters that depend on the quantity of the source ores (fossil resource scarcity, mineral resource scarcity...). Stainless steel impacts, compared to the composite ones are generally lower. However, human carcinogenic toxicity of steel is strongly higher (two orders of magnitude) than that of the samples described in this work.

Table 4. LCA study results using the ReCipe 2016 method. The comparison was made among lead, steel and the average composite sample (*b*), since a comparison between the three developed mixtures would show very similar impacts.

Impact Category	Composite	Lead	Steel	Unit
Fine particulate matter formation	3.0083×10^{-3}	1.7537×10^{-2}	2.5890×10^{-3}	kg PM2.5 eq
Fossil resource scarcity	7.6487×10^{-1}	6.4664×10^{-1}	4.1914×10^{-1}	kg oil eq
Freshwater ecotoxicity	8.4606×10^{-2}	9.1613×10^{-1}	9.3025×10^{-2}	kg 1,4-DCB
Freshwater eutrophication	6.1143×10^{-4}	5.4034×10^{-3}	6.4810×10^{-4}	kg P eq
Global warming	2.0190	2.9701	1.4331	kg CO_2 eq
Human carcinogenic toxicity	7.7873×10^{-2}	3.8059×10^{-1}	2.3177	kg 1,4-DCB
Human non-carcinogenic toxicity	2.3725	4.4880×10^{1}	1.6433	kg 1,4-DCB
Ionizing radiation	1.5145×10^{-1}	1.0113×10^{-1}	2.8174×10^{-1}	kBq ^{60}Co eq
Land use	1.9765×10^{-2}	2.8625×10^{-2}	7.5114×10^{-3}	m^2a crop eq
Marine ecotoxicity	1.0682×10^{-1}	1.2924	1.3559×10^{-1}	kg 1,4-DCB
Marine eutrophication	2.8346×10^{-4}	1.2057×10^{-4}	4.5165×10^{-5}	kg N eq
Mineral resource scarcity	1.7336	5.0973×10^{-1}	2.1350×10^{-3}	kg Cu eq
Ozone formation, Human health	6.0554×10^{-3}	1.6108×10^{-2}	3.4478×10^{-3}	kg NOx eq
Ozone formation, Terrestrial ecosystems	6.3136×10^{-3}	1.6403×10^{-2}	3.5129×10^{-3}	kg NOx eq
Stratospheric ozone depletion	1.1278×10^{-6}	2.8819×10^{-6}	9.7955×10^{-7}	kg CFC11 eq
Terrestrial acidification	7.1376×10^{-3}	5.4225×10^{-2}	8.7846×10^{-3}	kg SO_2 eq
Terrestrial ecotoxicity	7.2130	4.9729×10^{1}	1.0801×10^{1}	kg 1,4-DCB
Water consumption	3.5767×10^{-2}	2.7976×10^{-2}	2.6284×10^{-2}	m^3
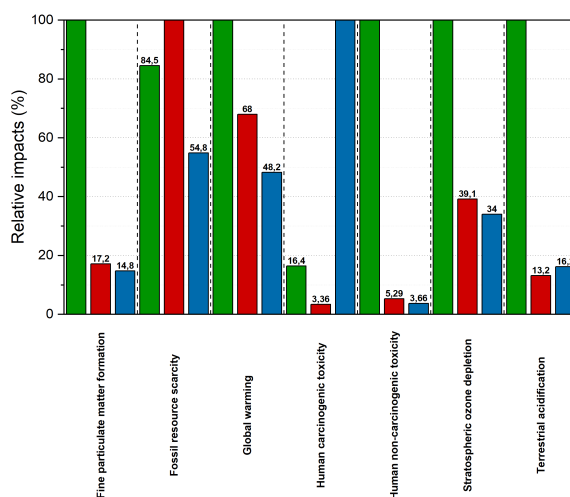
Figure 9. The histogram is an extract from the previous table which shows the relative impacts for the main and most reliable factors showed in Table 4. Data were normalized to the maximum value for a rapid evaluation of the advantages and disadvantages of each material. Green bars refer to the impacts calculated for lead, red bars for the composite samples and blue bars are referred to steel impacts.

3. Discussion

This study identified mixtures of composite materials for X-ray shielding that have low toxicity for human health, low environmental impact as assessed by LCA analysis, low costs of production and processing and good mechanic resistance. Simulations through Geant4 of pure materials from scientific literature, showed in Figure 1b, allowed to identify the best performing materials in X-ray shielding. The chosen additives were bismuth oxide and barium sulfate. $BaSO_4$ was chosen because it has similar performances in shielding to zinc oxide, but its cost is about 100 times lower. Nine $BaSO_4$ - Epoxy composites in increasing weight percentage of additive were prepared and the simulations made with Geant4 were confirmed. Moreover, the upper limit of mixability between the resin and the inorganic additive was tested resulting in 85% w/w of additives. Bismuth, which showed excellent shielding properties in simulations, was selected to be mixed with barium sulphate to obtain high performances mixtures. The simplex-lattice experimental design for mixtures of Figure 5 was then developed, identifying each of the three components with a predominant factor (high screening properties, high stress resistance and low costs). Of the six resulting mixtures, only three were produced in laboratory, as the main requested property was the high x-ray absorption. The three others mixtures were not prepared because the observed transmission factors resulting from the simulations were too high for being integrated as industrial shielding materials. These samples can still be applied where the energies of produced X-rays are lower than 50 keV (such as the medical applications) and the strain resistance required has to be upper than 13–15 MPa.The three simplex mixtures were then analyzed through direct radiography and showed a screening effect trend in agreement with Geant4 prediction. Produced samples overperformed steel in terms of radiopacity with a much easier formability and workability and weight reduced up to the one third of a steel screen. It was thus possible to develop composite formulations depending in shielding performance, weight and costs requirements: mixture *c* is suitable as steel replacement. For systems that involve higher energies, mixtures *a* and *b* are the best choice. For other applications, like the medical ones, where energies involved are lower than 50 keV, the three remaining mixtures (d, e, f) are well suited. Looking to the molecular level, it was not possible obtaining direct indications about the interaction and the adhesion between the filler and the matrix. On one hand, the composites showed sufficient mechanical properties also at high loadings and this suggests that some polymer/additive interaction occurred. On the other hand, the aggregation of the additive suggest that it should be modified to improve its interaction with the epoxy matrix to improve the adhesion and thus optimizing both dispersion and mechanical properties. This can be done by improving the hydrophobicity of the additive surface by binding an organic molecule such as stearic acid or sodium dodecylsulfate. This approach will be studied and developed in a future work.

4. Conclusions

In this study, different formulation for easily formable composites lightweight shielding materials were proposed. The work explored the best performing mixtures between bismuth oxide, barium sulfate and epoxy resin, using a simplex-lattice experimental design for mixtures. The resulting mixtures (see Section 2.3 for details) can be used in different fields based on the requirements of shielding ratio, mechanical properties and lightness. For low photon-energy applications, such as the medical field, 20:20:60, 20:40:40 and 40:20:40 $BaSO_4/Bi_3O_3$/epoxy resin w/w mixtures are the best ones, due to their lightweight and good performances in shielding and mechanical resistance. For hard X-ray industrial applications, such as radiography and computed tomography with energies in the 20-220keV range, the best performing mixtures are: 60:20:20, 40:40:20 and 20:60:20 $BaSO_4/Bi_3O_3$/epoxy resin w/w. In details, three mixtures (labeled *a–c*) have performances higher than steel (mixture *a* has 4.5% more shielding capability, mixture *b* has 23.4% and mixture *c* has 33.1% with a weight reduction ranging from 55% to 62% depending on which mixture is chosen), becoming good candidates for traditional screen replacement. Besides physical, chemical, morphological and mechanical characterization to demonstrate their suitability for real world usage, an LCA study was conducted to compare screens

made of lead and steel with the produced mixtures. Results show that the produced samples have an overall environmental impact lower than those based on lead (Global warming 32% less, fine particular matter formation 82.8% less, human non-carcirogenic toxicity 94.71% less,...) and a lower human carcinogenic impact (96.64% less) than those based on steel.

5. Materials and Methods

5.1. Materials and Preparation

All samples were prepared starting from technical grade reagents. A two-components epoxy resin was purchased by S.E. Special Engine S.r.l. (Torino, Italy). Component A (Sepox 225) of the epoxy was made up by 80% w/w of bisphenol-A-(epichlorhydrin) and epoxy resins with average molecular mass lower than 700 *Dalton*. Component B (DK 505) was 35% w/w of 3-aminomethyl-3 5 5-trimethylcyclohexylamine and between 18% w/w of polyoxypropylenediamine.

Barite (85% w/w $BaSO_4$, 0.8% w/w calcite, 13.6% w/w dolomite) was given by Itaprochim (Garlasco, Italy) and other two samples of Barite (Blanc Fixe JM3B and Blanc Fixe G) were given by Universal Services S.r.l. (Milano, Italy) and produced by Solvay (Massa, Italy), Bi_2O_3 (>99% w/w) and SnO_2 (>99% w/w) was given by Todini (Monza, Italy) and Thermo Fischer (Kandel, Germany). Samples were prepared as described in Appendix C.

5.2. Analysis Methods

Powder materials were analyzed through XRPD and the diffraction patterns were compared with the ones simulated with the corresponding .cif files downloaded from the Crystallographic Open Database (COD) [15]. PXRD pattern were collected with a Thermo ARL XTRA48 X-ray diffractometer. Patterns were collected in the 2θ angle range from 15 to 65 degrees. X-ray tube's electric potential was set to 45 kV and current intensity to 40 mA. Slits were set as a standard measurement 2 mm, 4 mm, 0.5 mm, 0.2 mm. Resolution was set to 0.02° and scan speed to 2.00°/min. Radiographic tests for sample of binary mixture $BaSO_4$/Epoxy were performed by the direct digital radiography technique; an Yxlon Y.XMB X-ray module was used as X-ray source and a Carestream DRX-1 as detector (filament current: 10 mA; voltage: 20 kV–220 kV). In the case of simplex samples, the computed digital radiography technique was used with the same previous X-ray source and a GE CRxFlex IPS imaging plate as detector (current: 5 mA; voltage 20 mA–220 kV). Radiographies collected were processed with ImageJ to extract grey-scale values for confrontations. Sections 10 μm in thickness were cut on a Leica RM 2125 RT rotary microtome; SEM images at different magnification were recorded on a Quanta 200 FEI Scanning Electron Microscope equipped with EDAX EDS attachment, using a tungsten filament as the electron source at 20 kV. All samples were coated with an Au layer of 20 nm to prevent surface charging.

5.3. Modeling

5.3.1. Geant4 Simulations

Simulations of radiopacity were performed (on a Sony Vaio laptop 4 GB RAM, 1.4 GHz i7 processor with Ubuntu 18.10) by Geant4. The simulations were performed in two steps: a first approach with monochromatic X radiation and a second one considering the generation of a Bremsstrahlung spectrum of tungsten as source for the sample irradiation, as described in Appendix B. (By using Geant4, a first screening of materials was conducted over the different solution found in the scientific literature. The simulation setup was designed by creating a 1 cm sided cube of material irradiated along the X-axis with a monochromatic beam of X-rays counting 10^4 photons. The experiment was repeated at steps of 25 keV in the range of 0–350 keV so that the best performing materials could be selected).

5.3.2. openLCA Simulations

For this project the open source professional solution named openLCA 1.9 and the ecoinvent 3.5 database were used. openLCA by implementing powerful and flexible ways to model life cycle systems, with the ability to calculate environmental, social and economic indicators, with plugins which are providing different more specific elements, and with its open architecture which eases import and export of data and integration in other IT landscapes, is the free and open source software for modeling the life cycle of things [16]. The ecoinvent database is the world's leading LCI database which delivers both in terms of transparency and consistency [17].

Appendix A. Design of Experiments (DOE)

Experimental design consists in planning experiments in order to obtain the maximum information contained in a system with the least experiments possible. Even if the construction of a regression model is not the aim of a series of experiments, using experimental designs is common practice to explore an experimental domain in the most complete way. Mixtures, however, require more attention than other studied systems, mainly because the properties of the product depends on the relative quantity of the components introduced in the mixture, not on their absolute quantity. This leads to a consequence: none of the components can vary independently, because the sum of the relative quantities of each mixture has to be equal to 1.

$$\sum_{i=1}^{q} x_i = 1 \tag{A1}$$

Equation (A1) represents the said constraints to the mixture, that prevents the use of common experimental designs such as Factor Designs. The three components of the studied mixture: epoxy resin, $BaSO_4$ and Bi_2O_3 can be associated with properties of the final samples, respectively: mechanical resistance, low costs and best radiopacity. Mixing these three components would lead to a compromise between these three properties, directly connected to the chemicals. To explore this experimental domain, a *Simplex-lattice design* for three components and two as maximal degree of the theoretical model was studied. These kinds of DOE are component-independent and are generated only from the algorithm:

$$\binom{q+m-1}{m} = \frac{(q+m-1)!}{m! \cdot (q-1)!} \tag{A2}$$

which leads to six experiments. Mixtures are then defined, for each component, by the series:

$$x_i = 0, \frac{1}{m}, \frac{2}{m}, \frac{3}{m}, \ldots 1 \tag{A3}$$

which respectively represent the vertexes of an equilateral triangle and the midpoint of each side, as represented in Figure 5. These experiments make up a *simplex* which will be the explored part of the domain.

Appendix B. Geant4 Simulations

To avoid wasting materials and optimize the experiments, different sets of simulations were performed by using Geant4: a toolkit for the simulation of the passage of particles through matter with Monte Carlo methods [18,19].
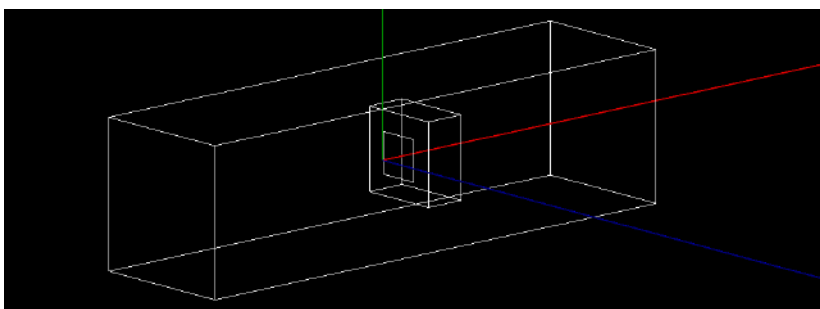

Figure A1. Simulation of shielding properties of the materials. Electrons are generated from one side of the envelope and travel through the space filled with vacuum via "*G4_Galactic*" material. Electrons hit the tungsten target, which generates characteristic X-ray emission. This spectrum (the Bremsstrahlung spectrum of W) is focused on the sample, in order to evaluate its radiopacity by measuring the number of the transmitted X-rays.

Once defined the experimental domain by consisting in $BaSO_4$, Bi_2O_3 and epoxy resin, a simplex mixture design was chosen to explore it and the six samples of the experimental design (see Figure 5) had to be more accurately simulated by reproducing the phenomenon that occurs in the radiographic cabin. For these samples, the geometry of the simulation changed. A target of tungsten of 300 μm of thickness was positioned between the radiopaque screen and the source of the beam, which also had been changed into an electron beam of 10^6 units. Electrons travel for 10 cm in vacuum until they hit the target. The impact generates an emission of the characteristic X-ray spectrum of W (Bremmstrahlung spectrum and characteristic X-rays emissions), which is then focused on the shield sample. Steel was also simulated for reference. Collected data were then plotted and only best-performing samples in radiopacity were then produced.

Appendix C. Sample Preparation

To have reproducible samples in shape and sizes, silicon rubber mold was prepared. The mold was made of a Room-Temperature-Cured (RTC) two component silicon rubber, which was supplied by S.E. Special Engine S.r.l. The components, DD Rubber A and DD Rubber B were mixed together in 1:1 ratio and outgassed for 10 min to eliminate bubbles from the rubber bulk. Steel bars of the same size of the desired samples were glued to a baking tray in order to obtain the negative of the mold. Silicon rubber mixture was poured into the tray and was outgassed for another 10 min. And after three hours of curing at room temperature (RT), the mold was ready to be used Figure A2a. Since the epoxy resin does not adhere to silicon the mold could be used many times.

(**a**)

(**b**)
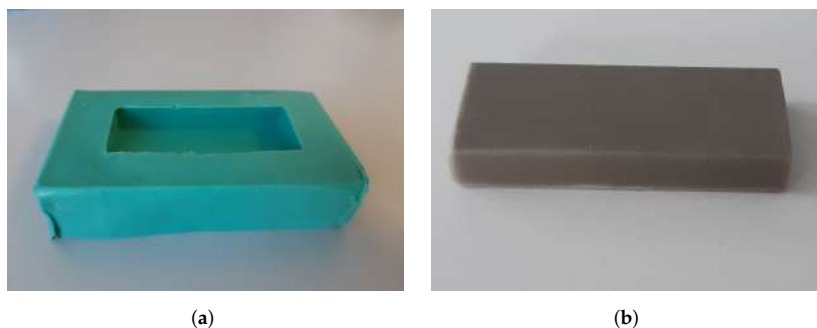
Figure A2. In the image on the left, a photo of a silicon rubber mold that was used for the production of the radiopaque samples. In the image on the right, a photo of one of the produced samples. (**a**) Silicon rubber mold.; (**b**) 30% w/w $BaSO_4$ sample.

Epoxy/inorganic additive composites were prepared dispersing the inorganic additive in Sepox 225 and then adding DK_{505}. The ratio between Sepox 225 and DK_{505} has to be 2:1. The mixture with the two components and the additive was then stirred for 10 min and then outgassed. Then it was cured at RT for 24 h, plus two hours at 60 °C. In highly loaded samples, the stirring could be not performed automatically and they were stirred by hand. As an example, the sample 30% w/w in $BaSO_4$ is shown in Figure A2b.

Appendix D. Life Cycle Assessment

Life Cycle Thinking (LCT) and Life Cycle Assessment (LCA) are the scientific approaches behind modern environmental policies and business decision support related to Sustainable Consumption and Production (SCP). Life Cycle Assessment (LCA) is a structured, comprehensive and internationally standardised method. It quantifies all relevant emissions and resources consumed and the related environmental and health impacts and resource depletion issues that are associated with any goods or services ("products"). Usually, Life Cycle Assessment takes into account a product's full life cycle: from the extraction of resources, through production, use, and recycling, up to the disposal of remaining waste. Critically, LCA studies thereby help to avoid resolving one environmental problem while creating others: This unwanted "shifting of burdens" is where you reduce the environmental impact at one point in the life cycle, only to increase it at another point. Therefore, LCA helps to avoid, for example, causing waste-related issues while improving production technologies, increasing land use or acid rain while reducing greenhouse gases, or increasing emissions in one country while reducing them in another. Life Cycle Assessment is therefore a vital and powerful decision support tool, complementing other methods, which are equally necessary to help effectively and efficiently make consumption and production more sustainable.The ISO 14040 [20] and 14044 [21] standards provide the indispensable framework for Life Cycle Assessment (LCA) (see Figure A3).
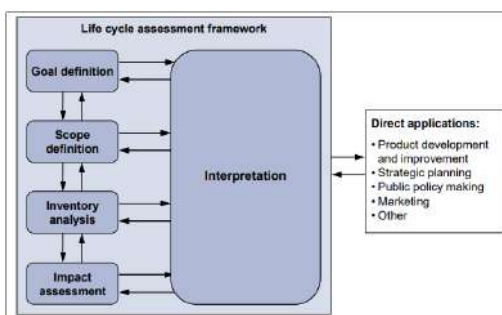
Figure A3. Framework for life cycle assessment (from ISO 14040:2006; modified) [22].

To carry out an LCI or LCA study is almost always an iterative process: once the goal of the work is defined, the initial scope settings are derived that define the requirements on the subsequent work. However, as during the life cycle inventory phase of data collection and during the subsequent impact assessment and interpretation more information becomes available, the initial scope settings will typically need to be refined and sometimes also revised. Figure A4 gives a more detailed overview of the iterations [22].
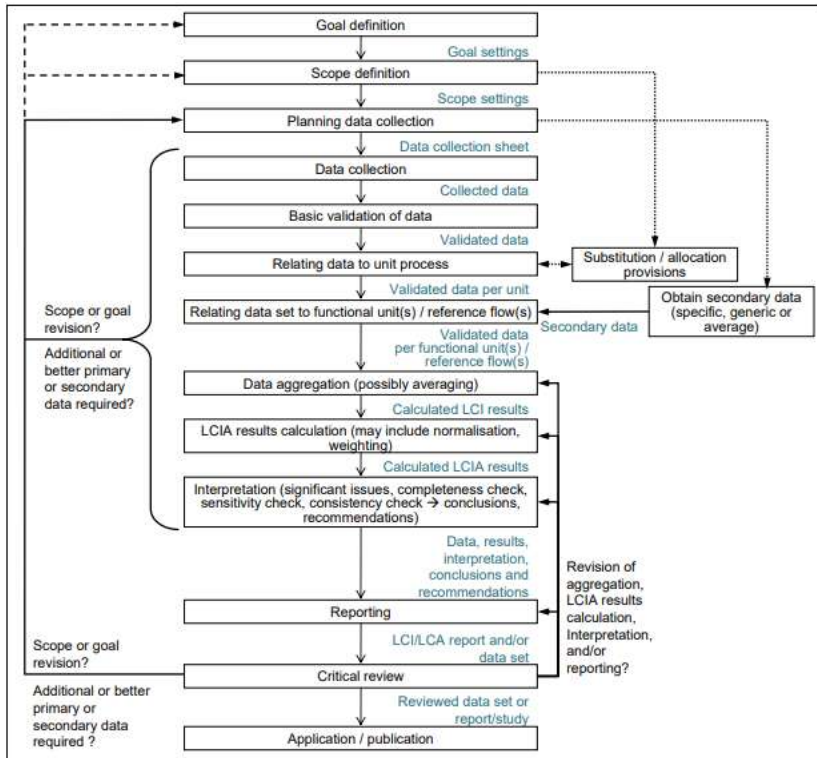

Figure A4. Details of the iterative approach to LCA, with focus on inventory data collection and modelling (from ISO 14044:2006, modified) [22].

Depending on the stages of the life cycle that the study analyzes, three different types of LCA studies can be identified: cradle to grave, cradle to gate, gate to gate (see Figure A5).
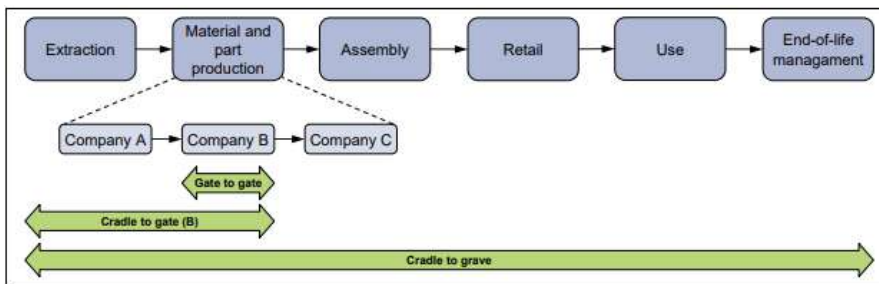
Figure A5. Types of LCA studies classified by system boundaries taken into account [22].

Since the building of an LCA model is a quite often complex operation which requires to define and connect the existing network of relationships between processes that belongs to different stages of their life cycle, a software tool and a reference database to which refer environmental data that are not directly collectable, are commonly used. A software tool helps and allow the LCA modeler to speed up the calculation and to have some features available to better interpret the results of the assessment while a comprehensive database provides well documented process data for different families of products and helps the LCA modeler to make truly informed choices about their environmental impact.

References

1. McCaffrey, J.P.; Shen, H.; Downton, B.; Mainegra-Hing, E. Radiation attenuation by lead and nonlead materials used in radiation shielding garments. *Med. Phys.* **2007**, *34*, 530–537, doi:10.1118/1.2426404. [CrossRef] [PubMed]

2. Suman, S.K.; Mondal, R.K.; Kumar, J.; Dubey, K.A.; Kadam, R.M.; Melo, J.S.; Bhardwaj, Y.K.; Varshney, L. Development of highly radiopaque flexible polymer composites for X-ray imaging applications and copolymer architecture-morphology-property correlations. *Eur. Polym. J.* **2017**, *95*, 41–55, doi:10.1016/j.eurpolymj.2017.07.021. [CrossRef]

3. Petrantonaki, M.; Kappas, C.; Efstathopoulos, E.P.; Theodorakos, Y.; Panayiotakis, G. Calculating shielding requirements in diagnostic X-ray departments. *Br. J. Radiol.* **1999**, *72*, 179–185. [CrossRef] [PubMed]

4. Nisha, V.S.; Joseph, R. Preparation and Properties of Iodine-Doped Radiopaque Natural Rubber. *J. Appl. Polym. Sci.* **2007**, doi:10.1002/app26040. [CrossRef]

5. Wang, W.; Wei, Z.; Sang, L.; Wang, Y.; Zhang, J.; Bian, Y. Development of X-ray opaque poly (lactic acid) end-capped by triiodobenzoic acid towards non-invasive micro-CT imaging biodegradable embolic microspheres. *Eur. Polym. J.* **2018**, *108*, 337–347. doi:10.1016/j.eurpolymj.2018.09.018. [CrossRef]

6. Houston, K.R.; Brosnan, S.M.; Burk, L.M.; Lee, Y.Z.; Luft, J.C.; Ashby, V.S. Iodinated Polyesters as a Versatile Platform for Radiopaque Biomaterials. *J. Polym. Sci. Part A Polym. Chem.* **2017**, 2171–2177, doi:10.1002/pola.28596. [CrossRef]

7. Kazempour, M.; Saeedimoghadam, F.; Shekoohi Shooli, N.S. Assessment of the Radiation Attenuation Properties of Several Lead Free Composites by Monte Carlo Simulation. *J. Biomed. Phys. Eng.* **2015**, *5*, 67–76. [PubMed]

8. Nambiar, S.; Osei, E.K.; Yeow, J.T. Polymer nanocomposite-based shielding against diagnostic X-rays. *J. Appl. Polym. Sci.* **2013**, *127*, 4939–4946, doi:10.1002/app.37980. [CrossRef]

9. Ambika, M.R.; Nagaiah, N.; Suman, S.K. Role of bismuth oxide as a reinforcer on gamma shielding ability of unsaturated polyester based polymer composites. *J. Appl. Polym. Sci.* **2017**, *134*, 1–7, doi:10.1002/app.44657. [CrossRef]

10. Mirji, R.; Lobo, B. Radiation shielding materials: A brief review on methods, scope and significance. In Proceedings of the National Conference on Advances in VLS and Microelectronics, Hubali, India, 27 January 2017.

11. Omar, K.; Al-khazaleh, K.A.; Saadi, S.A. Barium Sulfate Epoxy Mixture Effects on Attenuation of Short Wavelength Barium Sulfate Epoxy Mixture Effects on Attenuation of Short Wavelength Radiation. *Nuclear Radiat. Phys.* **2015**, *80*, 31333–31338.

12. Prolongo, S.G.; Moriche, R.; Sánchez, M.; Ureña, A. Self-stratifying and orientation of exfoliated few-layer graphene nanoplatelets in epoxy composites. *Compos. Sci. Technol.* **2013**, *85*, 136–141, doi:10.1016/j.compscitech.2013.06.015. [CrossRef]

13. Altomare, A.; Corriero, N.; Cuocci, C.; Falcicchio, A.; Moliterni, A.; Rizzi, R. *QUALX2.0*: A qualitative phase analysis software using the freely available database *POW$_C$OD*. *J. Appl. Crystallogr.* **2015**, *48*, 598–603, doi:10.1107/S1600576715002319. [CrossRef]

14. Coelho, A.A. *TOPAS* and *TOPAS-Academic*: An optimization program integrating computer algebra and crystallographic objects written in C++. *J. Appl. Crystallogr.* **2018**, *51*, 210–218, doi:10.1107/S1600576718000183. [CrossRef]

15. Gražulis, S.; Chateigner, D.; Downs, R.T.; Yokochi, A.F.T.; Quirós, M.; Lutterotti, L.; Manakova, E.; Butkus, J.; Moeck, P.; Le Bail, A. Crystallography Open Database—An open-access collection of crystal structures. *J. Appl. Crystallogr.* **2009**, *42*, 726–729, doi:10.1107/S0021889809016690. [CrossRef] [PubMed]

16. Available online: http://www.openlca.org (accessed on 23 January 2020).

17. Available online: https://www.ecoinvent.org (accessed on 23 January 2020).

18. Agostinelli, S.; Allison, J.; Amako, K.; Apostolakis, J.; Araujo, H.; Arce, P.; Asai, M.; Axen, D.; Banerjee, S.; Barrand, G.; et al. GEANT4—A simulation toolkit. *Nuclear Instruments and Methods in Physics Research, Section A: Accelerators, Spectrometers, Detectors and Associated Equipment*; Elsevier: Amsterdam, The Netherlands, 2003; Volume 506, pp. 250–303, doi:10.1016/S0168-9002(03)01368-8. [CrossRef]

19. Allison, J.; Amako, K.; Apostolakis, J.; Arce, P.; Asai, M.; Aso, T.; Bagli, E.; Bagulya, A.; Banerjee, S.; Barrand, G.; et al. Recent developments in GEANT4. *Nuclear Instruments and Methods in Physics Research, Section A: Accelerators, Spectrometers, Detectors and Associated Equipment*; Elsevier: Amsterdam, The Netherlands, 2016; Volume 835, pp. 186–225, doi:10.1016/j.nima.2016.06.125. [CrossRef]

20. ISO. *14040:2006, Environmental Management—Life Cycle Assessment—Principles and Framework*; European Union: Brussels, Belgium, 2006.

21. ISO. *14044:2006, Environmental Management—Life Cycle Assessment—Requirements and Guidelines*; European Union: Brussels, Belgium, 2006.

22. JRC. *International Reference Life Cycle Data System (ILCD) Handbook, General Guide for Life Cycle Assessment, Detailed Guidance*; European Commission: Brussels, Belgium, 2010, doi:10.2788/38479. [CrossRef]

A N N E X

VI

Epoxy resins composites for X-ray shielding materials additivated by coated barium sulfate with improved dispersibility

Homer? Who is Homer?

Incognito, G.

Epoxy resins composites for X-ray shielding materials additivated by coated barium sulfate with improved dispersibility

Mattia Lopresti [a], Luca Palin [a,b], Gabriele Alberto [c], Simone Cantamessa [a], Marco Milanesio [a,*]

[a] *Università del Piemonte Orientale, Dipartimento di Scienze e Innovazione Tecnologica, Via Michel 11, 28100 Alessandria, Italy*
[b] *Nova Res s.r.l., Via D. Bello 3, 28100 Novara, Italy*
[c] *Bytest s.r.l.-TÜV SÜD Group, Research Center, via Pisa 12, 10088 Volpiano, Italy*

A R T I C L E I N F O

Keywords:
X-ray shielding
Barite-epoxy resin composites
Surface modifications
Liquid assisted grinding

A B S T R A C T

Epoxy resins additivated by barium sulfate proved to be promising low cost, easy workable and environmentally friendly alternative to lead and steel as X-ray shielding materials, but the composites tends to be stratified, with the additive accumulating in the bottom side of the sample. This sedimentation process has been, at first, studied by *in situ* X-ray powder diffraction, thermogravimetric techniques and X-ray tomography and then inhibited by exploiting finer barite sources, implementing a grinding procedure, combined to a surface modification of the inorganic additives. Stearic acid and sodium dodecyl sulfate were used to coat barite surface, using a liquid assisted grinding (LAG) approach. The functionalized additives resulted more compatible with the resin and their dispersion within the polymer resulted much improved. The produced composite samples were then studied by optical and electron microscopy, X-ray radiography, X-ray diffraction, thermogravimetric analysis and tensile strength test. The use of a finer additive and the grinding procedure allowed to limit the sedimentation and induced a marked hardening of the samples, with the drawback of a reduction of their plasticity. Stearic acid coating was able to eliminate sedimentation maintaining good mechanical properties.

1. Introduction

Environmentally friendly X-ray shielding materials exploit minerals with high Z number elements such as Ba [1], Bi [2], Gd [3]. To obtain objects and artifacts with good mechanical performances such compounds are used as additive for polymers to obtain high performing composites. However, composite materials development must face the issues due to an unsuitable interaction between the different components used in their preparation. The low compatibility among the components might induce a reduced uniformity of the composite materials, with a general decrease of their performances and increase of defects. These effects are particularly common when dealing with polymers additivated with inorganic materials. Common behaviors are segregation, sedimentation and formation of voids and, in general, of interfaces between non or weakly bound components. These phenomena have been observed for instance in rubbers [4], biopolymers [5], bio-resorbable materials [6] and thermoplastic polymers [7]. The problem is well documented for epoxy composites, especially for fiber-reinforced materials [8–10]. These problems were faced by some of us [1] when dealing with epoxy resins additivated with commercial

barium sulfate, to obtain X-ray shielding materials with low cost, easy workability and environmental impact smaller than lead and steel. In fact, the produced samples showed segregation and sedimentation of barite with a dramatic reduction of mechanical properties. This issue can be solved by disaggregating the particles, reducing their size and functionalizing their surface to improve the compatibility with the organic matrix [11,12]. In the case of inorganic/epoxy resin composites, the main issue is the striking contrast between the polarity of the inorganic surface (additives are typically oxides, carbonates and sulfates) and the hydrophobicity of the polymer [13]. The typical approach is using low cost surfactants or fatty acids, able to bond the inorganic surface with their carboxylate or sulfonate heads and compatible with the polymers exploiting their apolar tails. The more common compounds used to obtain hydrophobic coated (nano) particles are stearic acid (SA) [14,15, 16] and sodium dodecyl sulfate (SDS) [17]. Nihal Tüzün et al. demonstrated that finely dispersed barite gave good results in adhesion test compared to coated calcite [18]. Sun et al. proposed the modification of barite with sodium stearate in a water slurry to improve hydrophobicity [19]. The addition of bismite fillers modified by multiwalled carbon nanotubes allowed to improve dispersion and thus increase the X-ray

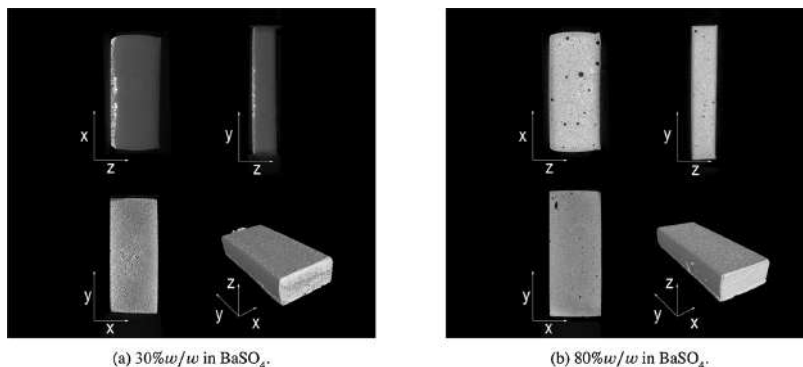(a) 30%*w/w* in BaSO₄.

(b) 80%*w/w* in BaSO₄.

Fig. 1. Tomography of two standard samples produced as in Ref. [1].

attenuation coefficient of the composite [20]. The addition of silica nanoparticles to bismite allowed to improve thermal stability [21]. Nanometric Gd_2O_3 appeared to be the unique filler giving good dispersion and attenuation coefficients without surface modification [3]. The aim of the present work is obtaining X-ray shielding materials using the methodology by Lopresti et al. [1], but by extensively studying and optimizing the interactions at the organic-inorganic interface to improve additive dispersion and increase attenuation coefficients, when using a low cost additive as barite. At first, the sedimentation process during composite gelation was studied by *in situ* X-ray powder diffraction (XRPD), X-ray tomography and thermogravimetric (TGA) analysis to understand the features and critical issues of additive sedimentation. Then, the inorganic additive surface are functionalized, to obtain a better dispersion, limited or absent sedimentation and good mechanical performances. Low cost inorganic fillers (barium sulfate) and functionalizing agents (SA and SDS) were used. To have a facile and easily scalable functionalizing strategy, liquid assisted grinding [22,23] and quasi solid-state reactions is used [24], for the first time in polymer additive field. On the sample preparation view point, the goal is understanding the better preparation conditions to obtain well dispersed samples and to reduce sedimentation. TGA, SEM and XRPD were used to investigate additive dispersion and sedimentation. The effect of the functionalization on mechanical properties was investigated by a tensile strength test to infer possible applications in the real world. On a more general viewpoint, we intend to demonstrate the potentialities of LAG approach in the field of polymer additive coating.

2. Experimental

2.1. Materials

A two-components epoxy resin was purchased by S.E. Special Engine S.r.l. (Torino, Italy); the first component (Sepox 225) consists in 80% (w/w) of bisphenol-A-(epichlorohydrin) and epoxy resins with an average molecular mass lower than 700 Da. The second component (DK505) consists in 35% (w/w) of 3-aminomethyl-3,5,5-trimethylcyclo-hexylamine and about 18% (w/w) of polyoxypropylenediamine. Two different kinds of barium sulfate (>99% (w/w)), Blanc Fixe G and Blanc Fixe JM3B were given by Universal Services S.r.l. (Milano, Italy) and produced by Solvay (Massa, Italy). Samples from Ref. [1] were produced with technical grade barite (85% (w/w) BaSO₄, 0.8% (w/w) calcite, 13.6% (w/w) dolomite) which was given by Itaprochim (Garlasco,

Italy). Sodium dodecyl sulfate and stearic acid were purchased by Sigma Aldrich (a Merck KGaA company, Darmstadt, Germany).

2.2. Measurements and analysis

Tomographic analyses were made by a GE v|tomex|m 300 with a tube voltage of 265 kV and current of 125*mA*. *In situ* XRPD experiments were performed with a Thermo ARL XTRA48 X-ray diffractometer equipped with a sample holder with a particular geometry designed and developed by Panero Elevatori (Cherasco, Italy). Patterns were collected in the 2θ range from 15° to 65° (standard full collection) and from 23° to 26.5° (*in situ* fast collection). X-ray tube' operative electric potential was set to 45 kV and the current intensity was set to 40 mA. Slits were set as standard measurement: 2, 4, 0.5, 0.2 mm. The resolution was set to 0.02 and scan to 1.00°/min. Thermogravimetric analyses was performed with a Mettler TGA/SDTA 851e in a range from room temperature to 1000 °C at 10°/min in N_2 atmosphere. A STEMI 508 microscope with 2× frontal optics, Zeiss fiber optics halogen bulb and 20 MPx SONY sensor camera was used to collect optical images with high resolution. Radiopacity measurements (in both horizontal and vertical directions) for all prepared BaSO₄/epoxy composite samples were performed by the direct digital radiography technique. The instrument is equipped by a Yxlon Y. XMB X-ray source and a Carestream DRX-1 detector (operating conditions: filament current 10 mA and voltage 20–220 kV). Radiography data were processed by ImageJ [25] to extract the grey-scale values used for the analyses. 10 μm-thickness sections were cut by a Leica RM 2125 RT rotary microtome; SEM images at different magnification were recorded using two microscopes. A Quanta 200 FEI Scanning Electron Microscope equipped with EDAX – EDS attachment, using a tungsten filament as the electron source at 20 kV and an Hitachi FLEXSEM 1000 I equipped with AZtecOne Oxford EDS, using a tungsten filament as the electron source at 15 kV were used for electron microscopy analysis. The samples were coated with an Au layer of 20 nm to prevent surface charging. Barite powders were measured without coatings. Tensile strength measurements were performed by a Zwick/Roell dynamometer on *ad hoc* prepared 15 cm long dog bones.

2.3. Preparation of composite samples

The samples were prepared as detailed in a previous work [1]. The inorganic additives were modified by a liquid assisted grinding (LAG) methodology [22]: the powders were initially ground for 20 min by
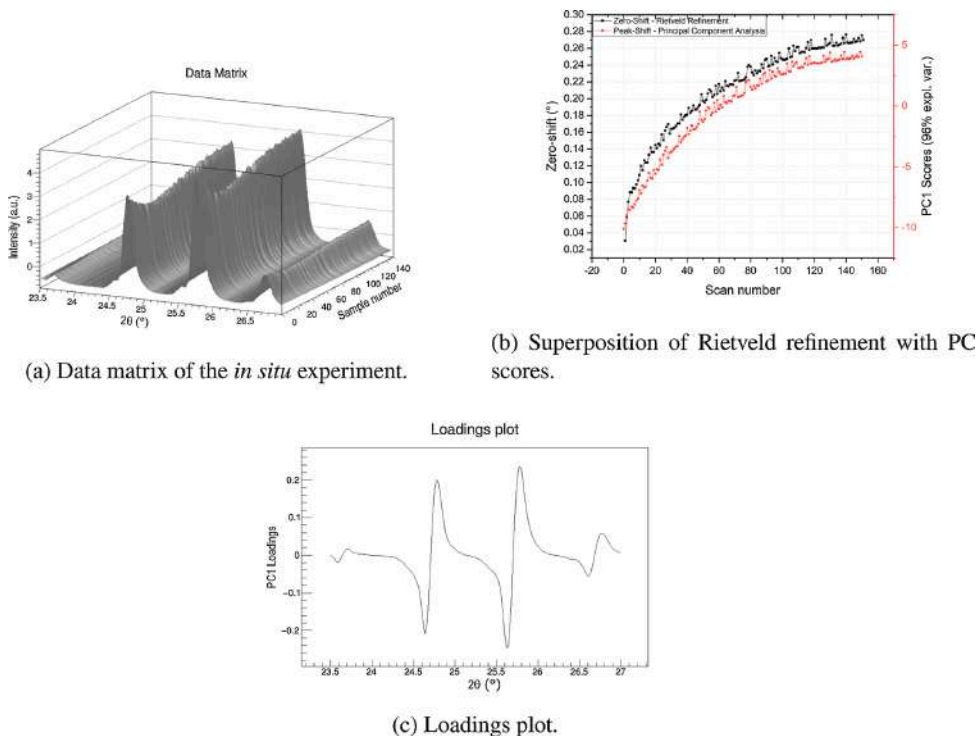
(a) Data matrix of the *in situ* experiment.

(b) Superposition of Rietveld refinement with PC scores.

(c) Loadings plot.

Fig. 2. PCA analysis of *in situ* X-ray diffraction data during composite gelation process of samples produced as in Ref. [1]. (For interpretation of the references to color in this figure citation, the reader is referred to the web version of this article.)

hand; successively, 1 ml of solution 0.1 M of NaOH in 50% EtOH by volume – 50% water was added and the mixture was ground for another 10 minutes; finally, depending on which sample was to be prepared, sodium dodecyl sulfate and stearic acid were added in different amounts (0.250, 0.500 and 0.750 g) to explore the functionalizing agent

concentrations. After the grinding process, the powder mixture was put in the laboratory stove at 50 °C for 2 h to eliminate residual water and ethanol.
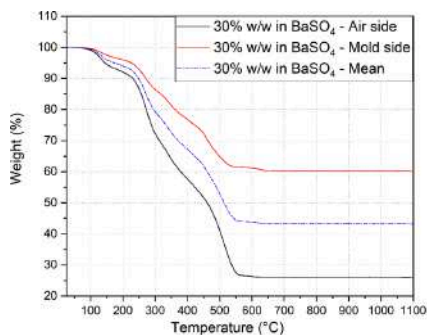
(a) TGA of 30% w/w in $BaSO_4$ sample.
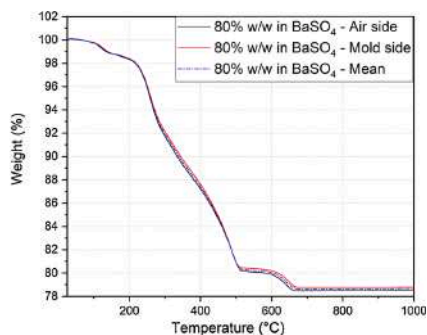
(b) TGA of 80% w/w in $BaSO_4$ sample.

Fig. 3. TGA data collected using specimen cutter on top and bottom sides of 30% (A) and 80% (B) samples, produced as in Ref. [1].

(a) Particle of BaSO₄ without surface coating.

(b) Estimation of 9Å² occupied area by molecule.

(c) Estimation of 16Å² occupied area by single molecule.
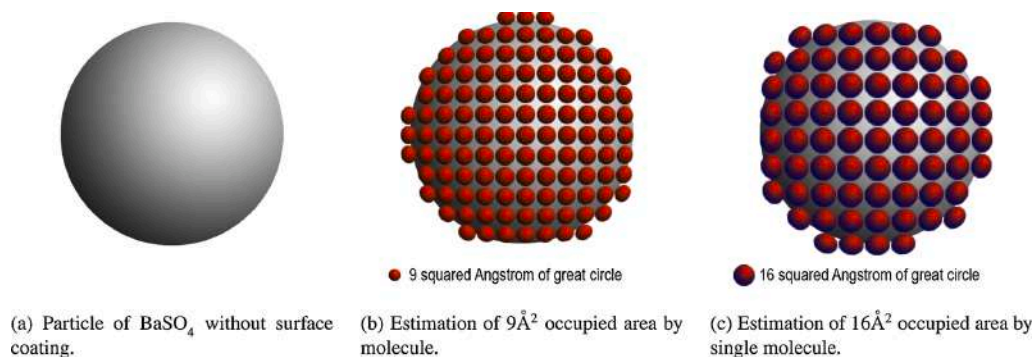
Fig. 4. Surface coating by an estimated occupied are of 9 and 16 $Å^2$ per surfactant molecule. (For interpretation of the references to color in this figure citation, the reader is referred to the web version of this article.)

3. Results and discussion

Lowly additivated samples from a previous work [1] presented a strong sedimentation behavior, which was observed by X-ray computed tomography. The dynamic of the sedimentation was then analyzed with an *in situ* X-ray diffraction experiment and by thermogravimetric analysis (Section 3.1). Grinding and surface coating strategies for powder additives were then designed and two biosurfactants (stearic acid and sodium dodecyl sulfate) were chosen as functionalizing agents (Section 3.2). Samples were finally characterized by a multi-technique approach with increasingly invasive techniques to investigate additive dispersion and sedimentation, to test radiopacity of samples and to evaluate tensile strength (Section 3.3).

3.1. Study of the additive dispersion and segregation during epoxy resin-barite composite curing

The sedimentation and segregation in the samples prepared as described in Lopresti et al. [1] was, at first, studied by X-ray tomography. Two samples were investigated (80% and 30% in weight of barite by Itaprochim) and the results are reported in Fig. 1. The samples are markedly different. 80% one, although with pores and a not homogeneous additive dispersion, did not show large aggregates and no or very limited sedimentation along the *c* direction. Conversely, large aggregated particles on the bottom side can be seen in the 30% barite sample. At lower additive %, the as made epoxy resin/barite mixture maintains the low viscosity of pure epoxy resin and since the gel time about 1–4 h depending on hardener concentration and temperature, sedimentation is likely to occur. The viscosity increases at larger barite % and, in particular in the 80% sample, and the starting mixture appears, in these cases, as a cement-like "paste", able to hinder or at least limit sedimentation and aggregation. The features of the two samples can be better appreciated by the movies (given as supplementary information files), produced scanning the tomographic data along the direction of the sedimentation. The bullet proof of sedimentation was obtained by an *in situ* XRPD experiment carried out during gelation process of the 30% (w/w) sample starting mixture. The *ad hoc* designed XRPD sample holder was used as mold, as detailed in the experimental section. The data were collected in a small *2θ* range containing barite main peaks to have a short data collection, able to properly follow the changes in the XRPD pattern during gelation with a good time resolution (Fig. 2a). The data

were analyzed online during data collection by the fast approach offered by PCA [26,27,24] and a clear trend in the pattern is found (red curve in Fig. 2b). The PCA loadings (Fig. 2c) shows that the variations in the patterns are mostly due to the drift and intensity change of the barite peaks, confirming a movement of the inorganic additive within the sample during the experiment duration, when gelation occurs and the sample becomes solid. It must be noted the efficiency of PCA for the *in situ* data analysis, being carried out already during experiment execution, as an optimal "online" tool to check the quality of the collected data and to control if experiment conditions were properly set. Standard post-experimental data analyses by Rietveld refinement indicated that the XRPD pattern changes are due to a zero error (black curve in Fig. 2b) changes with a reduction of intensity, confirming that barite is moving toward the bottom side of the mold within the gelation process of the mixture. Finally, to quantify the sedimentation effect, the epoxy/barite ratio on the top and bottom of the 30% and 80% samples was estimated by TGA. Without sedimentation, the air and mold TGA profiles must be identical. In Fig. 3, the TGA profiles of both layers show very similar residuals of about 80% as expected, being the polymer totally eliminated above 700 °C. Conversely, the 30% sample show residuals of 62% and 28% on bottom and top sides respectively, indicating that about half the additive moved toward the bottom mold side during gelation. As a further indication, TGA data indicated that the samples are perfectly stable up to 100 °C and a very small weigh loss is observed up to 220 °C suggesting a very good stability in standard environmental conditions. It can be noticed a marked difference in the two profiles in Fig. 3 above 550 °C. The weight loss between 600 and 700 °C in 80% barite composite is not present in epoxy and barite alone, nor in 30% sample. This loss can thus be ascribed formation of carbonaceous species, induced by barite epoxy interactions. The formation of barium carbonates from barium sulfate is usually unlikely because of the high stability of the sulfate, but it must be noted that $BaCO_3$ is stable up to 650 °C and then decomposed at the temperature where a loss is observed in Fig. 3b for 80% sample [28].

3.2. Optimization of additive dispersion to reduce segregation and sedimentation

The aggregation and sedimentation effects demonstrated in the previous section are often ascribed to the large particle size of the inorganic additive (barium sulfate in our case) and to its low

Table 1

Summary of the produced sample's composition, description upon observation with the optical microscope and the further analysis were performed on each sample.

Sample	Barite	Grinding	EtOH	SA/SDS	Optical analysis[a]	F.A.[b]
1	G	Yes	No	No	Stratification in a very thin sub-millimetric layer. Homogeneous hue suggests a better dispersion of the finest particles.	Yes
2	G	No	No	No	Stratification in 1 mm thick layer, showing large particles. Resin homogeneous with no presence of large bubbles.	No
3	G	Yes	1 mL	SA 0.25 g	Homogeneous with no sedimentation nor segregation. Presence of bubbles in the upper half of the sample.	No
4	G	Yes	1 mL	SA 0.50 g	Homogeneous with no sedimentation nor segregation.	No
5	G	Yes	1 mL	SA 0.75 g	Homogeneous with no sedimentation nor segregation.	Yes
6	G	Yes	1 mL	No	Sample seems homogeneous but presents bubbles in the upper half of the sample.	Yes
7	G	Yes	1 mL	SDS 0.50 g	No sign of sedimentation, but slight segregation with some large not well dispersparticles. Bubbles in the upper half of the sample.	No
8	JM3B	Yes	No	No	Sedimentation in a thin layer (*circa* half millimeter) some bigger particles are still visible due to segregation effects. More homogeneous hue suggests better dispersion of the thinner portion of the additive. Bubbles in the upper half of the sample.	Yes
9	JM3B	No	No	No	Stratification in large particles thick circa 2:3 mm. Partial segregation of particles. Bubbles in the upper third of the sample.	No
10	JM3B	Yes	1 mL	SA 0.25 g	Homogeneous with no sedimentation nor segregation. Presence of micro bubbles.	No
11	JM3B	Yes	1 mL	SA 0.50 g	Homogeneous with no sedimentation nor segregation. Presence of micro-bubbles along all its height.	No
12	JM3B	Yes	1 mL	SA 0.75 g	Homogeneous with no sedimentation nor segregation. Slight presence of micro-bubbles along all its height, hardly detectable by optical microscopy.	Yes
13	JM3B	Yes	1 mL	No	Heavy sedimentation, worsened with respect to the only grinded one. Bubbles in the upper half of the sample.	Yes
14	JM3B	Yes	1 mL	SDS 0.50 g	No sign of sedimentation, but presence of segregation with large particles dispersed in the lower half of the sample. The sample shows bubbles along all its height	No

[a] Evaluation performed with the optical microscope.
[b] Further analyses: SEM, XRPD, TGA tensile strength.

compatibility with the much more hydrophobic epoxy resin matrix. To limit or eliminate additive sedimentation and aggregation, three actions were undertaken, with respect to Ref. [1] procedure. At first, Itaprochim barite, used for the experiments described in the previous section, was substituted by barites with a reduced and controlled particle size (about 1 μm), currently used as polymer additives to whiten and improve the density of the final plastic products. The two used barite additives from now on are Blank Fixe G and Blank Fixe JM3B. Then, a standardized grinding procedure was adopted to further reduce particle size and limit the aggregation of the particles. Finally, to improve the compatibility between the additive and the epoxy resin, two common surfactants – stearic acid (SA) and sodium dodecyl sulfate (SDS) – were used to functionalize the surface of barium sulfate particle. The functionalized particles were produced by LAG as described in the experimental section by standardizing the grinding time and varying the amount of surfactant and of the liquid (ethanol) used during liquid assisted grinding. Different amounts of coating agents were used and their range of variation was obtained using the scheme depicted in Fig. 4, where the free area (*A*) of the bare particles (Fig. 4a) is that calculated by BET data. Then this area is occupied by homogeneously dispersed SA/SDS molecules, assuming that each molecule (red dots in Fig. 4b and c) occupies an area ranging from 9 (full coverage) to 16 (less crowded coverage) Å^2 as in Fig. 4b and c. In this way, the number of molecules of SA and SDS needed to coat the barite surface is estimated dividing the surface area *A* of BaSO$_4$ (A_{BFG} = 1 m^2/g for Blanc Fixe G and A_{BFJM3B} = 3 m^2/g for Blanc Fixe JM3B, as reported in the technical data sheet) by the estimated area (σ_{SA} = 9–16 Å^2 = 9 to 16 × 10^{-20} m^2) occupied by a single coating molecule. Then the amount of SA and SDS is obtained using the Avogadro number (N_A) and the molecular weight (MM_S) of SA or SDS as in the following equation:

$$\chi = \frac{A \cdot MM_S}{\sigma_{SA} \cdot N_A} \tag{1}$$

Eq. (1) gives, using *A* = 1 : 3 m^2/g a range from 3 × 10^{-3} g of surfactant per gram of barite to 1.6 × 10^{-2} g of surfactant per gram of barite

as showed in Fig. 4. Functionalized barites were prepared in LAG conditions [22,23] using SA or SDS. The functionalized barites (together with bare barites as references) were used to prepare additive/epoxy resin composites at the lower inorganic amount (30%). In fact, with this barite amount, a sufficient X-ray shielding can be observed and the sedimentation problem occurs at its maximum, because of the low viscosity of the starting mixture, as indicated by X-ray tomography and TGA data. As a result, 14 samples were produced as summarized in Table 1. For both series of barite samples (Blank Fixe G and JM3B), three references epoxy/barite composites were prepared using the additives "as purchased" (2 and 9), after grinding in dry condition (1 and 8) and after grinding with ethanol 0.5M to see the effect of LAG conditions but without the surfactant (6 and 13). The SDS- and SA-functionalized barites with 0.50 g of surfactant were then used to prepare samples 4, 7, 11, 14. Optical microscopy and radiography were used for a preliminary evaluation and selection of most promising samples. Optical microscopy indicated that SA-coated barites give much less sedimentation and bubbles than SDS, the effect of SA amount was further explored by preparing functionalized barites at 0.25 and 0.75 SA % weight. All the samples were at first examined by optical microscopy with a 64× magnification and X-ray radiography to assess the effects (single or synergic) of barite grinding and functionalization on aggregation and sedimentation during the gelation process and the obtained indications are summarized in Table 1. These data were used to exclude samples with evident sedimentation problems. Selected samples with functionalized barites, together with reference samples, are reported in Fig. 5. Comparing samples 1 vs. 2 and 8 vs. 9, it can be noted that for both barites, the grinding itself without SA/SDS and ethanol is already able to induce a limited reduction of the aggregation and sedimentation. In fact, the "as purchased" barites (sample 2 and 9) showed marked sedimentation as in Ref. [1]. This is probably due to the unbundling effect of the grinding procedure itself, able to moderately improve the dispersion. As purchased G (2) seems better than JM3B (9). The addition of ethanol while grinding in LAG conditions (samples 6, 13) does not give significant changes with respect to dry grinding in the case of G barite (samples
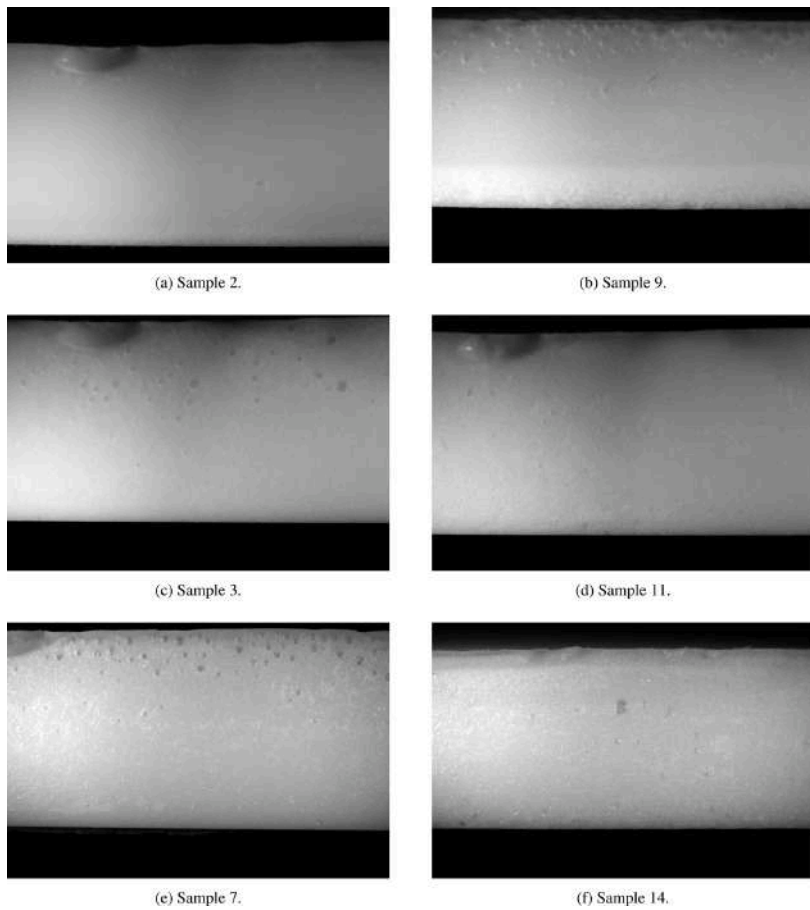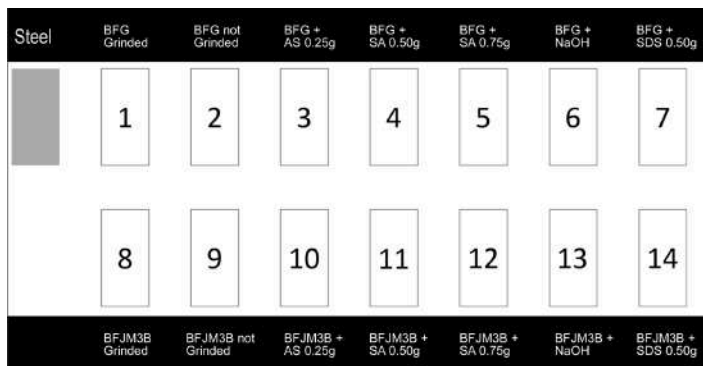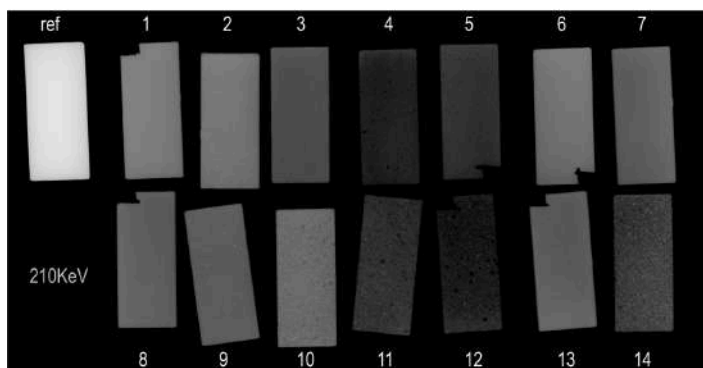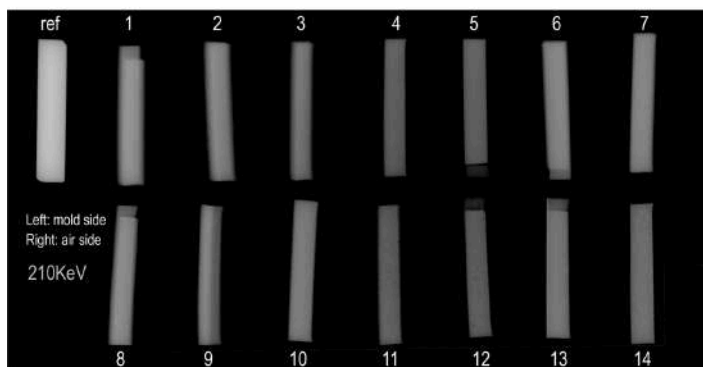
(a) Sample 2.

(b) Sample 9.

(c) Sample 3.

(d) Sample 11.

(e) Sample 7.

(f) Sample 14.

Fig. 5. Optical microscope images of selected samples of Blanc Fixe G (left) and Blanc Fixe JM3B (right) barite with different additives as detailed in Table 1.

(a) Sample disposition on the analysis plate.

(b) Radiographies on lying samples.

(c) Radiographies on section samples.

Fig. 6. Radiographies on all the produced samples. (b) shows samples radiographed on their widest side, to evaluate their radiopacity. (c) shows samples on their lateral side to evaluate barite's vertical distribution.
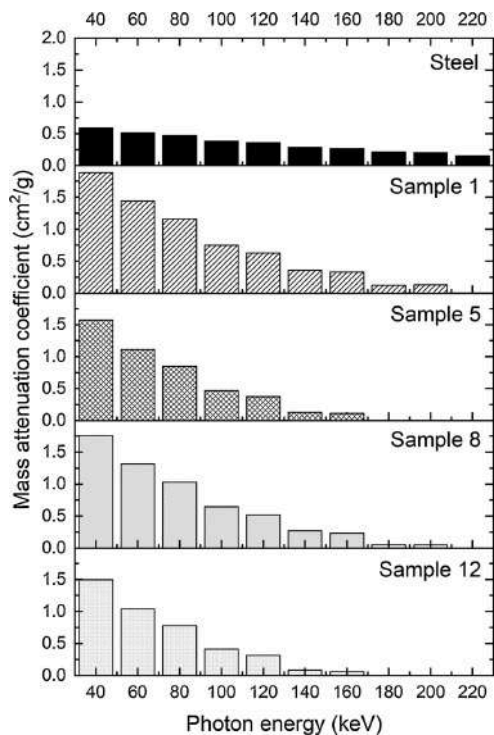
Fig. 7. Mass attenuation coefficients of selected samples. Full data can be found in Table S2 of the ESI file.

1 vs. 8) but large sedimentation effects are observed on sample 13 (grinding in ethanol for JM3B). Conversely, reduced or undetectable sedimentation was observed in several samples, when using SA or SDS to functionalize the barite particles, as reported in Table 1. As a drawback, a moderate increase in bubble formation was observed when using the coating agents. From this viewpoint comparing 4 vs. 7 and 11 vs. 14, SA coating resulted better than SDS one with 0.5% in weight of surfactant. For this reason, barites with functionalization in presence of 0.25% and 0.75% SA were selected (samples 3, 5, 10 and 12). Moreover, further characterization (XRPD/SEM/TGA/Tensile strength) were carried out on SA samples and references only. Optical microscopy indicated that the percent of SA coating on both barites (samples 3-5 and 11-3) does not change markedly the sedimentation effects. X-ray radiography analysis was then carried out by setting the samples horizontally to assess X-ray shielding power and its homogeneity and then vertically to further investigate sedimentation and confirm the indications previously obtained by optical microscopy. From this viewpoints all samples appear much more homogeneous and with less bubbles than samples in ref. [1]. Despite the barite weight % is identical in all samples, a moderate difference in X-ray shielding performances is observed with sample 10 being the more radiopaque. A detectable porosity is observed for sample 4, 11, 12, not evident in optical microscopy images (Fig. 6), with a markedly reduced radiopacity in both horizontal and vertical views. This effects can be explained by the different dispersion of the additive and by bubble formation during preparation, giving rise to locally less

dense zones in these samples. The more opaque samples are those subjected to grinding only without surface functionalization. Looking to side radiography data (Fig. 6c), the increased formation of bubbles in sample 4, 5, 11 and 12 is confirmed. Grey-scale values were read from radiography data and averaged with ImageJ software and then normalized between 0 and 1 using the reference of steel at 20 keV as lowest value of transparency and the underlying background value at 220 keV as the highest value of transparency. The raw data measured by ImageJ (reported in ESI file, Fig. S68) were used to estimate mass attenuation coefficients of each sample at the various acceleration voltages, using the method described in Ref. [14] and the results are plotted in Fig. 7. Without using a monochromatic parallel beam, the calculated coefficients are not exact on the absolute scale but they are very useful to compare samples each other and with the reference (steel). The composites outperform steel up to 80–120 kV acceleration voltage, with sample 1 competing with steel up to 160 kV. In the 140–200 keV range, the shielding performances rapidly decrease (as expected with a medium-low barite percentage) and the sample defectivity plays a major role. In fact, despite the additive amount is always the same, large differences between sample 1 and sample 12 are observed, because of the porosity evidenced in Fig. 6b. These informations allowed selecting the samples for more detailed analysis, as summarized in (Table 1).

### 3.3. Characterization of the samples showing better additive dispersion

The more promising samples, together with the references, were analyxed by XRPD, SEM and TGA after cutting slices from top and bottom sides to analyze in more detail additive dispersion and its effect on sedimentation. At the same time, dog bones were prepared for the same samples and mechanical properties assessed by a tensile test. SEM images showed in general a much better dispersion than samples in ref. [1]. The unique case where larger particles can be observed is on the "as purchased" barite (sample 2 and 9), indicating that dry (1 and 8) or LAG grinding (6 and 13) only, in absence of the coating agent, helped improving additive dispersion, but only SA-functionalized barite (sample 12) allowed eliminating sedimentation. However, bubble formation (already suspected by optical microscopy) is the drawback of coating agent usage. Comparing SEM images of as purchased powders and massive samples (Figs. S15–S38 in ESI file), the morphology and size of barite does not change after grinding during LAG functionalization: sizes between 0.7 and 4 μm for JM3B and G barite powders respectively are observed before and after the treatment. The better dispersion, observed by SEM at the micron scale, of the functionalized samples can be thus ascribed only to the chemistry of the particles' surfaces after LAG coating. XRPD data showed only small differences between up and bottom sides of the samples, indicating that the adopted strategies allowed a reduced sedimentation in all the cases, confirming that the proposed approach limited the sedimentation, because of the improved dispersion induced by barite coating. A larger amorphous signal in the upper side with respect to bottom one is observed only in sample 1, indicating that the as purchased barite is not suitable for an optimal dispersion. The Rietveld analysis of XRPD data collected from mold and air sides of more relevant and reference samples allowed evaluating both sedimentation and dispersion by refining the zero error and estimating the ordered crystalline domains respectively (Table 2). Sample 5 and 12 showed limited zero error, indicating that the top and bottom sides are similar with no or limited sedimentation. The absence of preferred orientations in sample 12 suggested a well dispersed and finely ground barite. Similarly, sample 8 shows good features, indicating that grinding
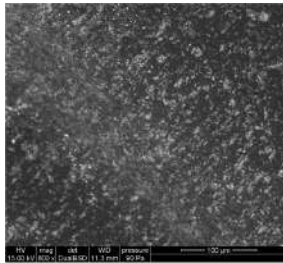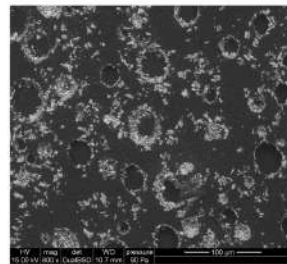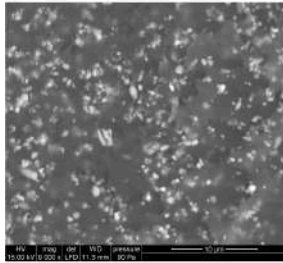
(a) Sample 1, bottom side.
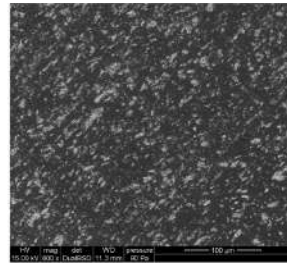
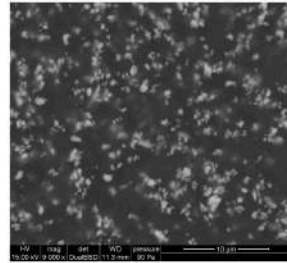
(b) Sample 1, top side.
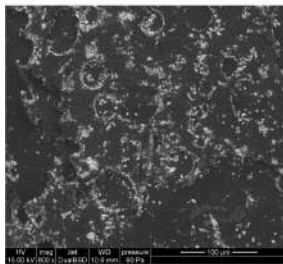
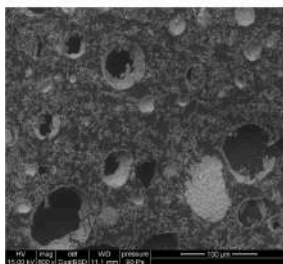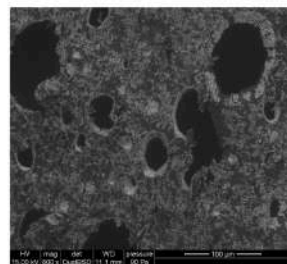(c) Sample 5, bottom side.

(d) Sample 5, top side.

(e) Sample 8, bottom side.

(f) Sample 8, top side.

(g) Sample 12, bottom side.

(h) Sample 12, top side.

Fig. 8. Electron microscope images of samples made using Blanc Fixe G with (5) and without (1) SA and JM3B with (12) and without (8) SA as additives.

Table 2
Rietveld refinement performed on selected samples.

| Sample	Zero	err	CS_L (nm)	Presence of preferred orientations
Sample 1 – air side	0.30934	0.00166	45	PO
Sample 1 – mold side	−0.46827	0.00128	98	PO
Sample 5 – air side	0.08638	0.00144	77	PO
Sample 5 – mold side	−0.01011	0.00051	868	PO
Sample 6 – air side	0.36719	0.00112	45	PO
Sample 6 – mold side	0.00624	0.00059	1145	Narrow peaks
Sample 8 – air side	−0.02832	0.00076	91	PO
Sample 8 – mold side	0.00346	0.0003	327	Good fit, no PO
Sample 12 – air side	0.02415	0.00059	81	Good fit, no PO
Sample 12 – mold side	−0.0294	0.00032	297	Good fit, no PO
Sample 13 – air side	−0.59186	0.00099	131	PO
Sample 13 – mold side	−1.14537	0.00173	45	PO

only already gives good results. Samples 6 and 13 show the larger preferred orientation effects, confirming a statistically relevant amount of large crystallites, sedimented in the bottom side. Sample 1 has a relevant zero error but small crystal size, confirming that grinding allows a good dispersion (as suggested by similar crystal sizes between air and mold sides) but still with a relevant degree of sedimentation as suggested by the important zero error differences between top and bottom sides. To quantify the sedimentation effects highlighted by electron and optical microscopy and XRPD, equivalent amounts of massive samples were cut from the top air and bottom mold sides and analyzed by TGA. Fig. 9 reports the measured weight losses together with the average between air and mold profiles for selected samples, while the weight loss data are reported in ESI file, Table S2. The mold and air TGA profiles should be identical in well dispersed samples at the mm level and absence of sedimentation. As a general comment, all the profiles show a first limited loss before 330 °C due to the degradation of the epoxy component, followed by the main loss due to epoxy decomposition between 330 and 450 °C and a third loss between 750 and 850 °C consistent with the elimination of carbonaceous residuals and losses by barite [29] as detailed in Table S1 in the ESI file. The main indication is that samples 5 and 12 show no sedimentation being the air and mold profiles identical up to 700 °C. Samples 8 and 2 showed limited sedimentation, while large differences are observed between 400 and 700 °C for samples 6 and 13, confirming for these sample a marked sedimentation. Finer differences between the profiles (a larger loss at 330 °C for sample 5, differences in the ratio of weight losses at 550 and 900 °C and different slopes of the plateau above 800 °C) indicates that LAG and coating conditions improve dispersion by promoting interactions at the interface between the epoxy matrix and the inorganic additive. The increased slope of air profile in samples 2 and 6 can be ascribed to the larger presence of finer fraction in the air side, losing more weight than barite in large crystallites (more frequent in the mold side) above 450° temperature as highlighted by Patel et al. [29]. The composite samples analyzed by TGA, SEM and XRPD were finally subjected to tensile test with eight dog bone replicas for each sample. Epoxy resin alone was tested as Ref. (3). To make data more robust and to reduce the presence of the outliers, data were trimmered, eliminating the first and the fourth quartile [30]. Mean, standard deviation and variation coefficient were then calculated on the remnant data, in order to evaluate the significance of the measure. The tensile test indicated that the ground additives acted as reinforcer, with four samples (1, 6, 8, 13) showing bulk modulus larger than epoxy resin alone. The drawback in these samples is a reduced plasticity. The SA functionalization (sample 5) allowed to obtain a larger elongation but with bulk modulus reduction. The improved performances with respect to epoxy resin alone are promising for their technological applications.

4. Conclusions

The sedimentation and aggregation of a commercial technical grade barite during composite gelation and curing was investigated by X-ray tomography, TGA and *in situ* XRPD. The observed bad additive dispersion is the main cause of defect formation and reduction of the mechanical properties, due to a not optimal additive/polymer interaction and of sedimentation, causing anisotropic X-ray shielding properties in composite samples and real world artifacts. To improve the compatibility of barite with the epoxy resin, grinding and functionalization with SA and SDS was exploited. The easily scalable LAG approach was successfully exploited for the first time in the polymer additive world as coating strategy. The functionalization conditions were optimized producing 14 samples, analyzed by optical microscopy and X-ray radiography to assess which strategy reduced the sedimentation, while improving barite dispersion. The best ones were further investigated by XRPD, TGA, SEM and tensile test, to further analyze the dispersion and assess mechanical properties. XRPD data and TGA of samples cut from top and bottom sides of the samples give information on additive dispersion at the mm scale. The collected data indicated that grinding only (in dry and LAG conditions) allowed a good dispersion, with reduced sedimentation and hardening of the materials, in agreement with the good performances in adhesion of epoxy resins additivated by un-coated finely dispersed barite [18]. SA-functionalized samples allowed a perfect dispersion with no sedimentation, but bubble formation reduced the bulk modulus. Combining TGA, radiography and mechanical data, the best composite preparation strategies can be chosen depending of the requested properties. If perfect isotropic X-ray shielding is needed, recipe 5 and 12 (SA-coated barites prepared in LAG conditions) can be used, with a bit smaller radiopacity and reduced mechanical properties. Sample 5 is the only sample retaining some of the original plasticity of the pure epoxy resin (8.3% elongation). The hydrophobicity increase of coated barite is consistent with those reported by Sun et al. [25], but the surface modification method proposed in the present paper is almost solvent free with much less solvent consumption and no production of waste solutions. Concerning specific technological applications where mechanical properties are the main requests, recipes 1 and 8 (dry ground barites) can be chosen, with increased hardness, good radiopacity, with the drawback of a limited sedimentation causing little anisotropy in the X-ray shielding across the sample.
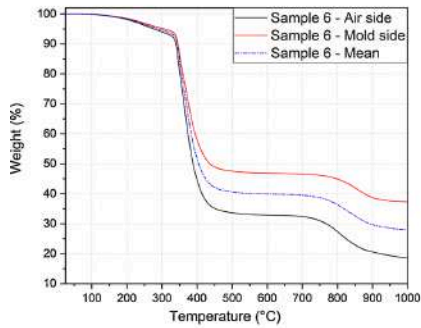
Declaration of Competing Interest
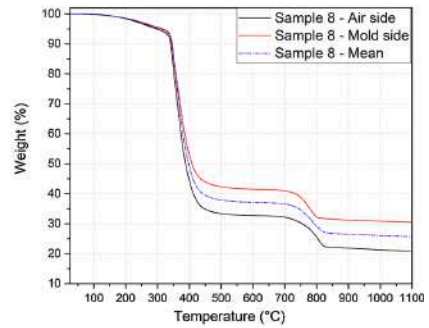
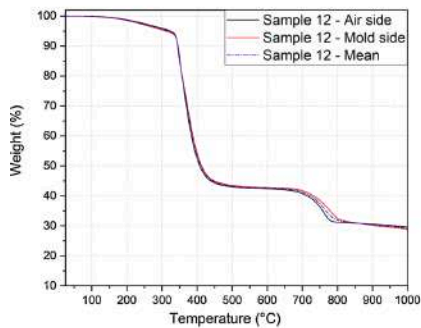The authors report no declarations of interest.
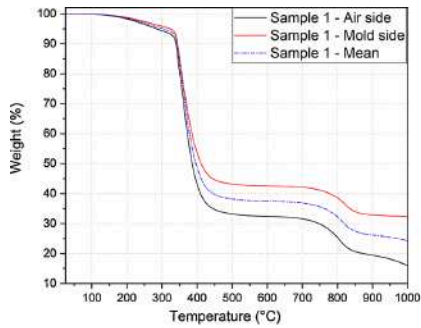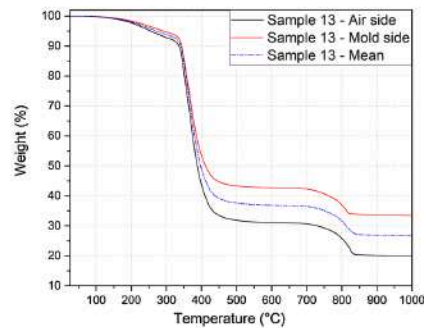
(a) Sample 1.
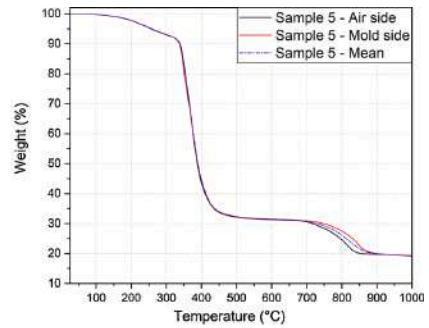
(b) Sample 5.

(c) Sample 6.

(d) Sample 8.

(e) Sample 12.

(f) Sample 13.

Fig. 9. TGA data collected using specimens cutr from top (air) and bottom (mold) sides of samples 1, 5, 6, 8, 12, 13 as labeled in Table 1.

Table 3

Tensile strength data.

Sample	σ_B [a]	Std. Dev.	Variation coef.	ε_B [b]	Std. Dev.	Variation coef.
Epoxy resin	26.68 MPa	±0.56 MPa	2.08%	27.00%	±4.24%	15.71%
Sample 1	42.08 MPa	±1.39 MPa	3.32%	4.75%	±0.29%	6.08%
Sample 8	43.72 MPa	±2.29 MPa	5.24%	5.98%	±0.29%	4.81%
Sample 6	33.90 MPa	±1.37 MPa	4.04%	4.70%	±0.08%	1.74%
Sample 13	33.28 MPa	±1.26 MPa	3.79%	5.40%	±0.29%	5.45%
Sample 5	14.44 MPa	±0.32 MPa	2.22%	8.28%	±0.63%	7.60%
Sample 12	22.36 MPa	±0.79 MPa	3.53%	5.80%	±0.29%	5.08%

[a] Average stress at breakpoint.

[b] Average elongation at breakpoint.

Appendix A. Supplementary data

Supplementary data associated with this article can be found, in the online version, at https://doi.org/10.1016/j.mtcomm.2020.101888.

References

[1] M. Lopresti, G. Alberto, S. Cantamessa, G. Cantino, L. Palin, M. Milanesio, Light weight easy formable and non-toxic polymer-based composites for hard X-ray shielding: a theoretical and experimental study, Int. J. Mol. Sci. 21 (2020) 833, https://doi.org/10.3390/ijms21030833.

[2] S. Nambiar, E.K. Osei, J.T. Yeow, Polymer nanocomposite-based shielding against diagnostic X-rays, J. Appl. Polym. Sci. 127 (2013) 4939–4946, https://doi.org/10.1002/app.37980.

[3] S. Jayakumar, T. Saravanan, J. Philip, Preparation, characterization and X-ray attenuation property of gd2 o3-based nanocomposites, Appl. Nanosci. (Switzerland) 7 (2017) 919–931, https://doi.org/10.1007/s13204-017-0631-6.

[4] K. Roy, S.C. Debnath, P. Potiyaraj, A critical review on the utilization of various reinforcement modifiers in filled composites, J. Elastomers Plast. 52 (2019) 167–193, https://doi.org/10.1177/0095244319835869.

[5] F.G. Torres, S. Rodriguez, A.C. Saavedra, Green composite materials from biopolymers reinforced with agroforestry waste, J. Polym. Environ. 27 (2019) 2651–2673, https://doi.org/10.1007/s10924-019-01561-5.

[6] J. Aragón, R. González, G. Fuentes, L. Palin, G. Croce, D. Viterbo, Development and characterization of a novel bioresorbable and bioactive biomaterial based on polyvinyl acetate calcium carbonate and coralline hydroxyapatite, Mater. Res. 14 (2011) 25–30, https://doi.org/10.1590/s1516-14392011005000012.

[7] X. Zhang, X. Fan, C. Yan, H. Li, Y. Zhu, X. Li, L. Yu, Interfacial microstructure and properties of carbon fiber composites modified with graphene oxide, ACS Appl. Mater. Interfaces 4 (2012) 1543–1552, https://doi.org/10.1021/am201757v.

[8] J. Leite, M. Rasteiro, G. Salmoria, C. Ahrens, A. Pouzada, Epoxy/steel fiber composites – a simple model to predict the fiber sedimentation, Polym. Compos. 31 (2010) 1378–1386, https://doi.org/10.1002/pc.20923.

[9] Q. Zhang, J. Wu, L. Gao, T. Liu, W. Zhong, G. Sui, G. Zheng, W. Fang, X. Yang, Dispersion stability of functionalized mwcnt in the epoxy-amine system and its effects on mechanical and interfacial properties of carbon fiber composites, Mater. Des. 94 (2016) 392–402, https://doi.org/10.1016/j.matdes.2016.01.062.

[10] N. Hiremath, S. Young, H. Ghossein, D. Penumadu, U. Vaidya, M. Theodore, Low cost textile-grade carbon-fiber epoxy composites for automotive and wind energy applications, Compos. Part B: Eng. 198 (2020) 108156, https://doi.org/10.1016/j.compositesb.2020.108156.

[11] V. Sabatini, T. Taroni, R. Rampazzo, M. Bompieri, D. Maggioni, D. Meroni, M. A. Ortenzi, S. Ardizzone, PA6 and halloysite nanotubes composites with improved hydrothermal ageing resistance: role of filler physicochemical properties functionalization and dispersion technique, Polymers 12 (2020) 211, https://doi.org/10.3390/polym12010211.

[12] G. Huang, S. Huo, X. Xu, W. Chen, Y. Jin, R. Li, P. Song, H. Wang, Realizing simultaneous improvements in mechanical strength flame retardancy and smoke suppression of ABS nanocomposites from multifunctional graphene, Compos. Part B: Eng. 177 (2019) 107377, https://doi.org/10.1016/j.compositesb.2019.107377.

[13] N. Hameed, S. Thomas, R. Abraham, S. Thomas, Morphology and contact angle studies of poly(styrene-co-acrylonitrile) modified epoxy resin blends and their glass fibre reinforced composites, eXPRESS Polym. Lett. 1 (2007) 345–355, https://doi.org/10.3144/expresspolymlett.2007.49.

[14] Z. Cao, M. Daly, L. Clémence, L.M. Geever, I. Major, C.L. Higginbotham, D. M. Devine, Chemical surface modification of calcium carbonate particles with stearic acid using different treating methods, Appl. Surf. Sci. 378 (2016) 320–329, https://doi.org/10.1016/j.apsusc.2016.03.205.

[15] A. Wołowicz, K. Staszak, Study of surface properties of aqueous solutions of sodium dodecyl sulfate in the presence of hydrochloric acid and heavy metal ions, J. Mol. Liq. 299 (2020) 112170, https://doi.org/10.1016/j.molliq.2019.112170.

[16] J. Hu, S. He, Z. Wang, J. Zhu, L. Wei, Z. Chen, Stearic acid-coated superhydrophobic Fe2O3/Fe3O4 composite film on N80 steel for corrosion protection, Surf. Coat. Technol. 359 (2019) 47–54, https://doi.org/10.1016/j.surfcoat.2018.12.040.

[17] Y.J. Yang, A.V. Kelkar, X. Zhu, G. Bai, H.T. Ng, D.S. Corti, E.I. Franses, Effect of sodium dodecylsulfate monomers and micelles on the stability of aqueous dispersions of titanium dioxide pigment nanoparticles against agglomeration and sedimentation, J. Colloid Interface Sci. 450 (2015) 434–445, https://doi.org/10.1016/j.jcis.2015.02.051.

[18] F. Nihal Tüzün, M. Safak Tunalioğlu, The effect of finely-divided fillers on the adhesion strengths of epoxy-based adhesives, Compos. Struct. 121 (2015) 296–303, https://doi.org/10.1016/j.compstruct.2014.11.007.

[19] S. Sun, H. Ding, H. Zhou, Preparation of TiO2-coated barite composite pigments by the hydrophobic aggregation method and their structure and properties, Sci. Rep. 7 (2017) 1–12, https://doi.org/10.1038/s41598-017-10620-7.

[20] S. Jayakumar, T. Saravanan, M. Vadivel, J. Philip, Synergistic effect of β-Bi2O3 and graphene/MWCNT in silicone-based polymeric matrices on diagnostic X-ray attenuation, Appl. Nanosci. (Switzerland) 9 (2019) 1891–1913, https://doi.org/10.1007/s13204-019-00972-z.

[21] S. Jayakumar, T. Saravanan, J. Philip, Polymer nanocomposites containing β-Bi$_2$O$_3$ and silica nanoparticles: thermal stability, surface topography and X-ray attenuation properties, J. Appl. Polym. Sci. 137 (2020) 49048, https://doi.org/10.1002/app.49048.

[22] V. Toson, E. Conterosito, L. Palin, E. Boccaleri, M. Milanesio, V. Gianotti, Facile intercalation of organic molecules into hydrotalcites by liquid-assisted grinding: yield optimization by a chemometric approach, Cryst. Growth Des. 15 (2015) 5368–5374, https://doi.org/10.1021/acs.cgd.5b00968.

[23] E. Conterosito, I. Benesperi, V. Toson, D. Saccone, N. Barbero, L. Palin, C. Barolo, V. Gianotti, M. Milanesio, High-throughput preparation of new photoactive nanocomposites, ChemSusChem 9 (2016) 1279–1289, https://doi.org/10.1002/cssc.201600325.

[24] L. Palin, M. Milanesio, W. van Beek, E. Conterosito, Understanding the ion exchange process in LDH NANOMATERIALS by fast in situ XRPD and PCA-assisted kinetic analysis, J. Nanomater. 2019 (2019) 1–9, https://doi.org/10.1155/2019/4612493.

[25] W. Rasband, ImageJ, 1997–2020. https://imagej.nih.gov/ij.

[26] P. Guccione, L. Palin, M. Milanesio, B.D. Belviso, R. Caliandro, Improved multivariate analysis for fast and selective monitoring of structural dynamics by in situ X-ray powder diffraction, Phys. Chem. Chem. Phys. 20 (2018) 2175–2187, https://doi.org/10.1039/c7cp06326a.

[27] R. Caliandro, V. Toson, L. Palin, E. Conterosito, M. Aceto, V. Gianotti, E. Boccaleri, E. Dooryhee, M. Milanesio, New hints on the Maya blue formation process by PCA-assisted in situ XRPD/PDF and optical spectroscopy, Chemistry - Eur. J. 25 (2019) 11503–11511, https://doi.org/10.1002/chem.201901932.

[28] V. Ischenko, J. Woltersdorf, E. Pippel, R. Köferstein, H.P. Abicht, Formation of metastable calcite-type barium carbonate during low-temperature decomposition of (Ba,Ti)-precursor complexes, Solid State Sci. 9 (2007) 303–309, https://doi.org/10.1016/j.solidstatesciences.2007.02.003.

[29] C.M. Patel, M. Chakraborty, Z.V. Murthy, Study on the stability and microstructural properties of barium sulfate nanoparticles produced by nanomilling, Adv. Powder Technol. 25 (2014) 226–235, https://doi.org/10.1016/j.apt.2013.04.003.

[30] L. Soliani, E. Siri, F. Sartore, Manuale di statistica per la ricerca e la professione: statistica univariata e bivariata, parametrica e non parametrica per le discipline ambientali. Uninova. https://books.google.it/books?id=myj5oAEACAAJ.

VII

Low-Cost Biobased Coatings for AM60 Magnesium Alloys for Food Contact and Harsh Environment Applications

Duffman is thrusting in the direction of the problem!

Duff Man

Article

Low-Cost Biobased Coatings for AM60 Magnesium Alloys for Food Contact and Harsh Environment Applications

Beatrice Mangolini [1] , Mattia Lopresti [1] , Eleonora Conterosito [1,*] , Giuseppe Rombolà [1], Luca Palin [1,2] , Valentina Gianotti [1] and Marco Milanesio [1]

[1] Dipartimento di Scienze e Innovazione Tecnologica, Università del Piemonte Orientale, Via Michel 11, 28100 Alessandria, Italy; beatrice.mangolini@uniupo.it (B.M.); mattia.lopresti@uniupo.it (M.L.); giuseppe.rombola@uniupo.it (G.R.); luca.palin@uniupo.it (L.P.); Valentina.gianotti@uniupo.it (V.G.); marco.milanesio@uniupo.it (M.M.)
[2] Nova Res s.r.l., Via D. Bello 3, 28100 Novara, Italy
* Correspondence: eleonora.conterosito@uniupo.it

Abstract: Low-cost, environmentally friendly and easily applicable coating for Mg alloys, able to resist in real world conditions, are studied. Coatings already used for other metals (aluminum, steel) and never tested on Mg alloy for its different surface and reactivity were deposited on AM60 magnesium alloys to facilitate their technological applications, also in presence of chemically aggressive conditions . A biobased PA11 powder coating was compared to synthetic silicon-based and polyester coatings, producing lab scale samples, probed by drop deposition tests and dipping in increasingly aggressive, salty, basic and acid solutions, at RT and at higher temperatures. Coatings were analyzed by SEM/EDX to assess their morphology and compositions, by optical and IR-ATR microscopy analyses, before and after the drop tests. Migration analyses from the samples were performed by immersion tests using food simulants followed by ICP-OES analysis of the recovered simulant to explore applications also in the food contact field. A 30 μm thick white lacquer and a 120 μm PA11 coating resulted the best solutions. The thinner siliconic and lacquer coatings, appearing brittle and thin in the SEM analysis, failed some drop and/or dipping test, with damages especially at the edges. The larger thickness is thus the unique solution for edgy or pointy samples. Finally, coffee cups in AM60 alloy were produced, as real word prototypes, with the best performing coatings and tested for both migration by dipping, simulating also real world aging (2 h in acetic acid at 70° and 24 h in hot coffee at 60 °C): PA11 resulted stable in all the tests and no migration of toxic metals was observed, resulting a promising candidate for many real world application in chemically aggressive environments and also food and beverage related applications.

Keywords: magnesium alloy; AM60; biobased coating; PA11; silicon-based coating; polyester lacquer; food contact; chemically aggressive environment; specific migration

1. Introduction

Magnesium alloys have huge potential uses in food contact and general industry applications, because of their low density and high strength-to-weight ratio. In fact, magnesium is the lightest metal used in structural applications, with a density of $1.74\,g/cm^3$ which makes it 35% lighter than aluminum and close to polymeric materials, which have a density ranging from the $\sim 0.90\,g/cm^3$ of PP to the $\sim 2.00\,g/cm^3$ of PTFE. Magnesium alloys show shock absorption and damping properties and the melting temperature of 650 °C makes them suitable for casting and die-casting [1]. Production by machining is also possible with a wide variety of possible applications. Its mechanical properties, paired with lightness, make magnesium an interesting subject of research and development in the automotive and aerospace industries where CO_2 emissions can be contained by vehicles unloading and subsequent fuel savings [1,2]. Wide applications of magnesium alloys are forecast as an answer to the request of reducing emissions for the transport of people and products.

One of the major drawbacks of magnesium, being an alkaline earth metal, is its reactivity with water and acids, which can produce hydrogen gas because of Mg oxidation [1]. This reactivity is increased significantly when magnesium is in powder form, and shavings produced during mechanical processing need to be handled with precautions [1]. Today, Mg alloys machining problems were faced successfully and tools and procedures are available. Conversely, corrosion is still a limiting factor to the possible applications despite the attempts in its prevention. Differently from Al alloys, the quasi-passive hydroxide film on the exposed surface is not stable and galvanic corrosion often occurs due to other elements in the alloy as alligands or impurities. To obtain more durable magnesium alloy objects, there are at least three aspects that can be improved [3] (i) the alloy composition, (ii) the exposed surface, (iii) the design of the piece itself. Regarding the alloy composition, the presence of particular elements can be harmful because they can promote the beginning of corrosion. Iron, nickel and copper are the most dangerous impurities for magnesium as they cause galvanic corrosion. Conversely, some other metals (Al, Zn, Mn…) provide protection because of the formation of stable surface phases. The most commonly used magnesium alloys are the AM and AZ types, both have aluminum as main solute, then the first has manganese and the second has zinc and manganese as the other main solutes [3,4]. The use of rare earths or also lithium in the alloys leads to peculiar materials whose use is limited to the aerospace industry due to the higher cost.

It is common use to identify the most suitable alloy for each specific purpose (application and cost), hence proceeding considering the two other aspects (surface exposition and design) which are closely linked. Macroscopic grooves and pores due to design (examples are screws or low-angle bent particulars) are the preferred places where corrosive attacks could occur. Such sites can store the corrosion products which have an auto-catalytic effect on corrosion progress [3,5] and are preferably avoided by means of the piece's shape forming. The shape is thus optimized by design to avoid such issues, but they cannot be completely eliminated in real world applications. When Mg alloys must be coupled with other metals such as copper, corrosion phenomena are inevitable. After optimizing the alloy composition and shape, the surface exposed to the aggressive environment can be smoothed to hinder the corrosion start by limiting possible corrosion sites [6]. Although these precautions are generally effective for corrosion prevention for most alloys in variable applications, magnesium alloys require further protection with coatings. This is particularly true in outdoor environments and/or in contact with many products, food included. Coatings have the scope of preventing the contact between the alloy and the oxidants, and must be effective on planar but especially on edgy or pointy parts of the artifact.

The optimal coating must be, on one hand, cost effective, with easy applicability and low environmental impact and, on the other hand, able to protect artifacts in a chemically aggressive environment regardless of the sharp edges and the corrosion susceptibility of the alloy. A coating fulfilling these conditions would allow a wider diffusion of magnesium alloys both in general industry and in the food contact field [7]. There are many types of treatments, substances and materials which are promising for protecting the alloy depending on the environment of application. Cost, easiness of applicability, performance and environmental impact depend of course on the chosen strategy and the best solution can be a balance of these four aspects. To be exploited in general industry and/or food industry, they must meet cost, scalability and low toxicity requirements other than providing corrosion protection. For instance, electrophoretic deposition of graphene oxide [8] allows an optimal protection but it is very expensive, and it also requires polluting reactants like concentrated sulfuric acid and NaOH 5M in the preparation. Laser surface melting [6], despite very efficient, is an energy and time-consuming process. Two strategies, based on vacuum or ambient surface treatment, can be envisaged for high level applications: the formation of stable oxide layers on the surface with further application of paints and enamels or plasma enhanced processes, such as deposition of hard and dense materials, or strong oxidation of the surface. High Velocity Oxygen Fuel (HVOF) is one of the thermal spray techniques that have shown an enormous potential for surface modification of different metals. The high

particle velocities and moderate temperatures achieved by HVOF drew a good academic interest towards Mg alloys treatment, as they lead to very dense coatings with outstanding wear behavior and superior bond strengths [9,10]. The Plasma Electrolytic Oxidation (PEO) [11] method is environmentally friendly, and the treatment is normally performed in aqueous solutions without the addition of toxic compounds. The formation of PEO coatings is possible on almost all cast and wrought magnesium alloys [12,13], with the result of dense coating structures and good corrosion resistance. These methods, despite very performing, are costly and hardly applicable on the wide scale required at industry and commercial levels, where powder or spray coating are widely employed.

With the aim or pursuing low-cost, environmentally friendly, biocompatible and easily up-scalable solutions for the protection of the lightweight alloy, AM60 magnesium planar edgy test samples and then artifacts were coated exploiting three different approaches. A powder coating (polyamide 11, from now on PA11), commercially known as Rilsan® [14] was chosen, as its use is well established on iron-based alloys especially concerning pipelines [15]. PA11 has the advantage of being biobased, it is obtained from renewable resources. e.g., from castor oil, thus exploiting poor and semi-arid soils not suitable for food cultivars. It is very versatile, due to the possibilities for its functionalization with silanes [16] or for blending with poly(butadiene succinate) (PBS) to obtain a partially biodegradable matrix [17]. In addition, PA11 exhibit antibacterial properties as recently demonstrated [18]. These examples support good features which allow the tailoring of the coating according to specific requests.

Two synthetic coating families, one silicon-based and the other consisting of polyester lacquers, typically used for Al alloys, were tested as a comparison. These three kinds of coatings are commonly used in the protection of iron [14] and aluminum alloys [19,20] which are among the most widespread alloys but, to the best of our knowledge, they were never tested on magnesium ones, probably for the different reactivity of its surface, and for the very limited applications in general industry.

Therefore, the scope of this work is evaluating if these coatings can be repurposed for the application of different materials such as Mg alloys (with different surface reactivity with respect to traditional substrates of these coatings), and which is the best solution in terms of both protection and facility of scaling-up toward industrial applications Planar edgy samples and, finally, prototype artifacts were tested in increasingly aggressive environments (i.e., solutions with increasingly acidic or basic nature and salinity, to simulate their use in harsh conditions such as automotive field during de-icing or marine environment, and contact with aggressive chemicals or foods) and particular attention was dedicated to resistance in contact with food and cleaning solutions, at room and higher temperatures to simulate real world usage. Migration studies have been carried out by immersion of the sample as indicated by UNI EN 1186-3:2002 [21] for plastics and the simulants were analyzed by ICP-OES. Optical and ATR-IR microscopies were used to assess the effects of chemicals and simulants on the coatings. These two methods allowed a non-destructive analysis of the samples before and after chemical tests, contrary to Electron microscopy (SEM/EDS) analysis of corrosion products, which required the samples to be cut to fit inside the vacuum chamber. SEM/EDS was thus used for textural observation of the coatings (cut from samples) and for element analysis assessment to investigate coating and additional features.

2. Results

The performance of the biobased PA11 coating on AM60 alloy were compared to organic lacquers and silicon-based coatings. Several samples were produced, and a variety of test were carried out to cover both chemically aggressive environments and food contact applications, as detailed in the experimental section. The experimental strategy is summarized in Figure 1 and it is divided in three levels:

1. all the samples initially faced soft chemical and food drop test to carry out a first selection (first level of Figure 1), and the results are summarized in Table 1;

2. the samples passing the first tests were subjected to hard chemical aggression and contact with real world household products (second level of Figure 1) and the results are given in Table 2, Section 2.1.1. Drop tests using aggressive solutions of strong acids, bases and salts were carried out at increasing concentrations and temperatures to assess possible usages in harsh environments and to simulate aging during long term usage. These tests allowed to understand the intrinsic shape-independent resistance of each coating;

3. the suitability for food contact applications of the best performing samples was then tested using the food simulant solutions described in the UNI EN 1186-3:2002 norm (third level of Figure 1 and Table 3); finally, immersion tests were carried out (also using real world prototypes, e.g., coffee cups) to measure, by ICP-OES, the amount of metals released and to calculate the specific migration. Dipping tests allowed to introduce the shape effect, since edgy parts are very critical in favoring corrosion.
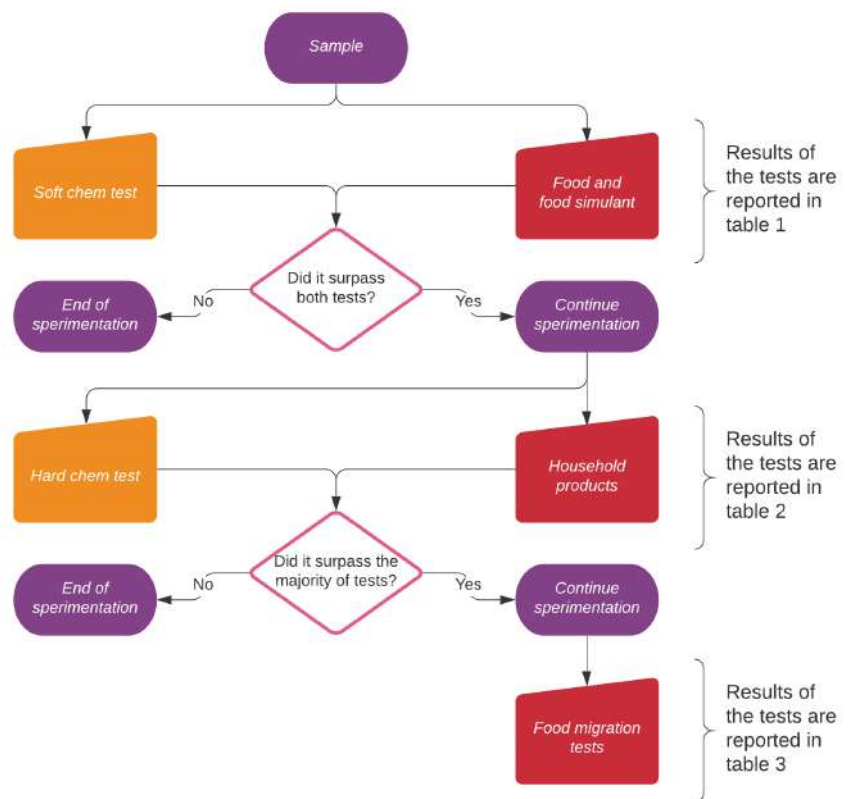
Figure 1. The samples were tested in three levels of increasing aggressivity. The first level is composed of two mild drop tests (one chemical and one with food and food simulants). The second level includes more aggressive agents, including harsh cleaning products. The last level concerns immersion migration tests on samples and on prototypes of coffee cups.

Real world prototypes in the form of coffee cups were produced using the AM60 alloy to assess the effects of size and shape in the migration tests carried out just by filling the cup in real use conditions. Prototypes were tested in parallel with standard flat laboratory samples.

Table 1. Results of the food and soft chemicals tests for all tested samples.

Sample Name [1]	Soft Chemical Aggression			Food Simulant Drop Test				Food Drop Test		
	HCl 1M	Salt Mixture	MilliQ H_2O	Acetic Ac. 3%	EtOH 10%	Oil	Acetic Ac. 10%	Coffee	Cola®	White Wine
● Nanoc. Easysol	Fail	Fail	Pass	Fail	Pass	Pass	Fail	Fail	Fail	Fail
● Ceramic techsol	Fail	Pass	Pass	Fail	Pass	Pass	Fail	Pass	Fail	Fail
● Siliconic white	Pass	Pass	Pass	Pass	Pass	Pass	Pass	Pass	Pass	Pass
● Siliconic brown	Pass	Pass	Pass	Pass	Pass	Pass	Pass	Pass	Pass	Pass
● Lacquer GSF 12 µm	Fail	Fail	Pass	Pass	Pass	Pass	Pass	Pass	Pass	Pass
● Lacquer GSF 30 µm	Pass	Pass	Pass	Pass	Pass	Pass	Pass	Pass	Pass	Pass
● Lacquer GSF white 13 µm	-	-	Pass	Pass	Pass	Pass	Fail	Pass	Pass	Pass
● Lacquer GSF white 40 µm	Pass	Pass	Pass	Pass	Pass	Pass	Pass	Pass	Pass	Pass
● PA11 transparent	Pass	Pass	Pass	Pass	Pass	Pass	Pass	Pass	Pass	Pass
● PA11 white	Pass	Pass	Pass	Pass	Pass	Pass	Pass	Pass	Pass	Pass

[1] For a faster recognition of the class of each sample, a colored dot was added to the names of the samples in all the tables. A pale brown dot (●) indicates that the sample has a silicon-based coating. A black dot (●) indicates that the sample has an organic-based coating. A green dot (●) indicates that the sample has a biobased coating. The same color code apply to Tables 2 and 3.

Table 2. Results of harsh chemicals tests for samples passing the first level of tests.

Sample Name	Hard Chemical Aggression			Household Drop Test	
	HCl 4M	NaOH 4M	Conc. Salt Mixture	Chanteclair®	Chillit Bang®
● Siliconic white	Pass	Fail	Pass	Pass	Pass
● Siliconic brown	Pass	Fail	Pass	Pass	Pass
● Lacquer GSF 30 µm	Fail	Fail	Fail	Fail	Fail
● Lacquer GSF white 40 µm	Pass	Pass	Pass	Pass	Pass
● PA11 transparent	Pass	Pass	Pass	Pass	Pass
● PA11 white	Pass	Pass	Pass	Pass	Pass

Table 3. Results of the migration tests for the more promising coatings.

Sample Name	Migration Test and Coffee Test	Migration Test on Prototypes	
	Acetic Ac. 3% on Flat Samples	Simulants A B C in Cups	Coffee
● Siliconic white	Fail	Fail	Fail
● Siliconic brown	Fail	-	-
● Lacquer GSF white 40 µm	Pass	Pass	Pass
● PA11 transparent	Pass	Pass	Pass
● PA11 white	Pass	Pass	Pass

2.1. Drop Tests

Drop test were carried out by deposing a drop of solution on a flat sample. This approach allows the efficient investigation of the intrinsic shape-independent resistance of the coating and the effect of repeated contact within time as detailed in Section 5.2) . Moreover, it allowed the inspection of the damages by optical and ATR-IR analysis.

2.1.1. Chemical Aggression Tests

The samples listed in Table 1 underwent drop tests to obtain a first screening with respect to their chemical resistance. The GSF organic lacquers, after the failure of some of the first tests, were prepared again increasing the thickness of the coating. For this reason, the thinner (12 µm to 13 µm) GSF coatings were not subjected to soft chemical aggression tests since they failed the acetic acid 10% test. To undergo food simulant tests, thicker (30 µm to 40 µm) versions of the same coatings (both transparent and white) were prepared, and passed the same tests. The drop tests with saline, acidic and basic solutions (described in the materials and methods Section 5.2) were performed by increasing the concentration of the solutions and then introducing the temperature effect.

Soft Chemicals

A HCl 1M solution and a salt mixture with both NaCl 5% *m/v* and CaCl$_2$ 5% *m/v* were used. The test was performed adding a drop every hour as detailed in Section 5.3.1. After five hours, the samples were pat dried and examined under the optical microscope. Surface alterations were visible on the bare magnesium (Figure 2b) while signs of reaction (bubbles)

could be seen on the transparent nanoceramic coated sample (Figure 2d). The transparent polyester lacquer sample (Figure 2e) was uneven on the edges, suggesting bad adherence to the substrate. Thus, these three samples were not subjected to more aggressive tests. The other samples, like the transparent PA11 (Figure 2c), passed the test, as summarized in Table 1 and underwent harsh solution and higher temperature tests. Samples failing the chemical aggression tests were still tested for food applications, since the conditions are usually milder. These data are detailed in Section 2.2, where all food contact tests are grouped.
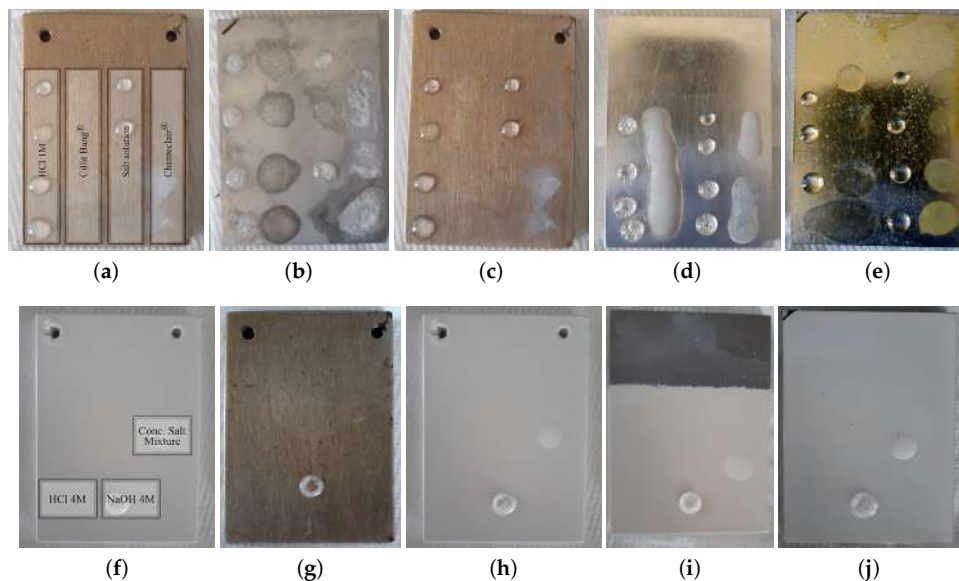
Figure 2. Selected planar samples at different stages of RT (top) and high temperature (bottom) drop tests: (**a**,**f**) show the scheme of the solutions used for the drop tests; (**b**) bare magnesium shown as a reference; (**c**–**e**) are transparent PA11, transparent nanoceramic and polyester coated samples respectively; (**g**,**h**) are transparent and white PA11 coated samples; (**i**) is the white siliconic coated sample; (**j**) is the white GSF lacquer 40 μm coated sample. Bottom pictures are taken after the high temperature test in the oven, and the NaOH pellet formed during drop evaporation is evident.

Harsh Solutions and Household Products

In the perspective of household and office use, as real world aggressive test, two commercial cleaning products (a degreaser and a descaler) were then tested. The products were chosen to be opposite in the pH scale, in fact the descaler Cillit Bang® is acid (pH = 0.8) and the degreaser Chanteclair® is basic (pH = 11.5). Due to the surfactants inside these commercial products, some drops joined together as it is clearly visible in Figure 2d. PA11 samples are much less wettable by polar solutions as can be seen by the drop shape in Figure 2c with respect to Figure 2d,e. Only GSF transparent lacquer failed these tests.

Three solutions were used on the samples which passed the tests in Table 1: HCl 4M, NaOH 4M and a concentrated salt mixture with both NaCl 10% m/v and CaCl$_2$ 10% m/v. One drop of each solution with a volume of 30 μL, was deposited every hour, and after the third hour, the samples were rinsed and dried. The samples were not visibly damaged in this case. Then, the same test was repeated using a single drop of 40 μL (to limit evaporation) for each solution but the samples were in a muffle oven at 50 °C for 1 h. The results are summarized in Table 2. The PA11 and the GSF lacquers coated samples resisted to this last testing step as it is shown for the transparent and white versions in Figure 2g,h. The white siliconic and the white GSF lacquer 40 μm coatings were slightly damaged by the hot NaOH solution that left a stain where the drops were

deposed. The samples are shown in Figure 2i,j but the staining is not easily appreciable from the pictures.

2.1.2. Optical Microscopy Analysis

After the drop tests, the samples were examined under the optical microscope to find possible signs of corrosion or damages in the coatings. In Figure 3 some pictures of damaged spots are reported. The commercial cleaning products left some residues which appeared like tiny crystals or stains. When the coating underneath was not damaged, the residues were eliminated by scratching or washing with deionized water. These residues were found on the transparent PA11 coated samples and on the GSF white lacquer coated sample as shown in Figure 3a–c. This and all other PA11 samples resulted inert to the test and all residues were easily removed by simply rinsing with water. On both the GSF transparent lacquer coated samples, a reaction occurred as the texture changed in the spots attacked by the liquids. There, the coating became sticky, and the paper used to dry it remained stuck on the spot as it can be seen in Figure 3f. The white GSF sample passed the test without damages, thanks to its increased thickness (evident by the cross-section SEM image reported in Figure S1 of the supplementary information file) and/or the protective effect of the inorganic additive inserted to obtain the white color. The Nanoceramic Easysol coated sample was damaged by all four solutions employed in the test as shown in Figure 3d,e. The white and brown siliconic coated samples were not damaged and no residue was left on their surfaces, hence they are not shown. As expected, the bare magnesium was corroded by all the solutions and the affected spots are clearly visible in Figure 3g,h.
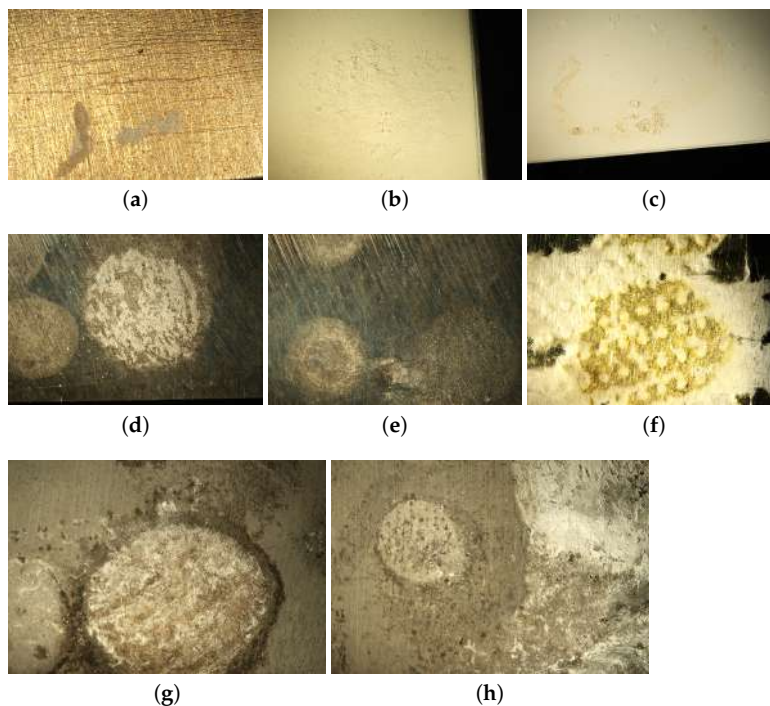
Figure 3. Optical Microscope images of selected samples at 6.5× magnification. Salt residues deposed on transparent PA11 transparent coating (**a**) and on white GSF lacquer (**b**,**c**); damaged spots on transparent nanoceramic Easysol (**d**,**e**); damaged spots on transparent GSF lacquer (**f**); corrosion signs on the bare magnesium sample (**g**,**h**).

2.1.3. Infrared Microscopy Analysis

Infrared spectroscopy was performed in ATR mode. Each sample was tested in each spot that was altered after initial the drop test and, as a reference, on a uniform and regular area where the coating was untouched (top part of the sample or its rear side). The spectra of the three classes of coatings before and after the attacks are reported in Figure 4 and the position of the main bands in each sample summarized in Table S4 in the supplementary information file. The transparent nanoceramic sample is silicon-based and its spectrum in Figure 4a is similar to those of the two siliconic samples in Figure 4b. In particular the bands around $1092\,cm^{-1}$ is due to the Si−O−Si asymmetric stretching while the band at $1423\,cm^{-1}$ is related to Si−CH$_3$ groups deformation. The nanoceramic coating is very thin and the spectra acquisition suffered from this, leading to non-sharp peaks, hard to be identified. However, the difference between the reference and the spot where the drop of saline solution was deposed is clear: the saline solution, after four hours of contact, chemically modified the coating deeply and permanently, already at room temperature. White and brown siliconic samples have characteristic signals similar to the nanoceramic due to the presence of silicon atoms. The FTIR-ATR spectra of the brown sample before (black line) and after the aggression by NaOH at room temperature (blue line) and at $50\,°C$ (red line) are shown in Figure 4b. The spectra of the white siliconic coating are not shown since they are very similar to those of the brown one, except for the band at $1659\,cm^{-1}$ which is not present in white one. The characteristic bands are the Si−OH stretching around $844\,cm^{-1}$ and the large multiple band of Si−O−Si asymmetric stretching vibration in the range $1050\,cm^{-1}$ to $1200\,cm^{-1}$. The length of the polymer chain influences the width of the band, which appears divided into three peaks in the region $1100\,cm^{-1}$ to $1000\,cm^{-1}$: the longer the chain, the broader is the peak. The deformation vibration band of Si−CH$_2$R groups is located at $1228\,cm^{-1}$ and it is sensible to the chain length, decreasing in intensity as the length of the aliphatic chain increases. The spectra collected in the spot in contact with hot sodium hydroxide solution reveal different intensities with respect to the reference spectra. By looking at the spectra, it can be seen that the most intense band at $1069\,cm^{-1}$ decreases in intensity while other peaks change in shape (at about $1533\,cm^{-1}$ and $1659\,cm^{-1}$) meaning that both brown and white coatings were damaged. Moreover, in the spot after contact with hot NaOH the color of the brown siliconic sample was visibly faded while in the white siliconic sample there were no visible changes. The GSF lacquers coatings are resins of polyester *tere-* and *iso-* phthalic acids. The main features in their FTIR spectra (shown in Figure 4c,d) are the strong band at $1720\,cm^{-1}$, typical of C=O stretchings of ester groups while the band at $1234\,cm^{-1}$ is due to the C−O−C asymmetric stretching of saturated aliphatic esters. The band at $2935\,cm^{-1}$ and $2854\,cm^{-1}$ is due to aliphatic CH stretching vibrations. The wide band centered at $3350\,cm^{-1}$ in the white GSF coating (Figure 4d) is attributable to OH stretchings due to the white TiO$_2$ pigment as well as the bands under $800\,cm^{-1}$. The transparent GSF coating was heavily damaged by the contact with the basic degreaser. The spectra reported in Figure 4c show in particular the appearance of new signals in the coating damaged by the degreaser in the region around $3350\,cm^{-1}$ that can be related to NH and OH stretchings of an ethanolammine residue from the product as well as the new bands in the region between $1080\,cm^{-1}$ to $1000\,cm^{-1}$. The spectra of the white GSF lacquer, after the test with hot HCl, shown in Figure 2j, are reported in Figure 4d and do not show any sign of degradation from the test. Since their compositions are identical except the inorganic additive used to obtain the white color (demonstrated by SEM/EDX analysis), the protective effect in the white GSF lacquer version can be ascribed to its increased thickness and/or to the presence the titanium oxide in its formulation. The spectra of the PA11 coatings are shown in Figure 4e,f and have few characteristic bands. At $3305\,cm^{-1}$ falls the NH group stretching while the bending for the same group is found at $1543\,cm^{-1}$. Asymmetrical and symmetrical stretching bands involving CH$_2$ groups are visible at $2920\,cm^{-1}$ and $2850\,cm^{-1}$ respectively. The CO stretching band is located at $1635\,cm^{-1}$ while the CH$_2$ bending falls at $1469\,cm^{-1}$. The out-of-plane bending for the same group is at lower wave numbers ($717\,cm^{-1}$). The

typical PA11 coating bands and signals were detected unchanged after all the drop tests confirming that the coating was not damaged, also at the chemical level. In Figure 4e,f, the reference spectra of transparent and white PA11 coatings are shown together with those measured in the hot HCl spot, i.e., the more aggressive situation for a magnesium alloy. Visual inspection suggested a faint change in the surface appearance, looking opaquer than before contact, but the spectra do not show any variation suggesting only minor modifications and thus very good resistance also to hot acid attack.

2.2. Food Contact Tests

To the present date, the principles of safety and inertness for all Food Contact Materials are regulated in the EU by the Commission Regulation (EC) No 1935/2004 for specific types of materials such as plastics, while the regulation for other materials are adopted locally by each EU Member State in accordance with Article 6 of Regulation 1935/2004. In Italy the characteristics of stainless steel for food contact are dictated by D.M. 21 marzo 1973 and subsequent amendments; and D.P.R. 777/1982. The coatings used in this study are commercial and compliant to the EU regulations about plastic materials, but our interest is to determine if there is migration from the underlying magnesium alloy, therefore we devised a procedure to evaluate the specific migration based on the existent legislation.

Food contact tests are milder than the test in the previous section. For this reason, also the samples failing some harsh chemical tests were considered in the experimentation, in view of possible applications in less aggressive food contact environments (neutral foods and drinks, greasy and oily substances). Also in this case, the first selection is done by the drop tests, while the more promising samples underwent migration tests also on real world prototypes. The contact with food did not usually leave visible marks on the surface of the coating but the reaction with acidic solutions was demonstrated by bubbles indicating the aggression of the alloy with the reaction:

$$Mg_{(s)} + 2\,H_3O^+_{(l)} \longrightarrow Mg(OH)_{2(s)} \downarrow + 2\,H_{2(g)} \uparrow \qquad \{1\}$$
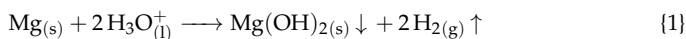
2.2.1. Food Contact Drop Tests

Four samples were used for this test: the first one was not coated bare AM60 as reference, one was covered with the transparent lacquer coating, one treated with a primer and then coated with white PA11, one treated with a primer and then covered with transparent PA11. The first test was done placing a drop each of coffee, Coca Cola® and white sparkling wine every hour and refilling the previous drops every hour to obtain different contact times with the solutions. On another spot of the sample, drops of the simulants A, B, C, D and 10% acetic acid were deposed on the surface and left there for 4 h proceeding as in the previous test. Although the surface of the unprotected AM60 alloy was noticeably damaged by the contact with all solutions, as also demonstrated by the bubbles, due to hydrogen gas formation, during the test, the coated samples did not show any trace of damage after removing the drops, as shown in Figure 5. The different wettability of the surface is evident by looking at the shapes of the drops of these polar water-based foods: on white and transparent PA11 the drops are well formed and raise from the surface with a higher contact angle, indicating a hydrophobic less wettable surface. On bare magnesium (Figure 5b) the drops are flat and widened because of its polar surface and higher wettability by polar solutions. GSF lacquer (Figure 5d) has intermediate wettability between the bare alloy and PA11 samples (Figure 5e,f).

(**a**)

(**b**)

(**c**)

(**d**)

(**e**)

(**f**)
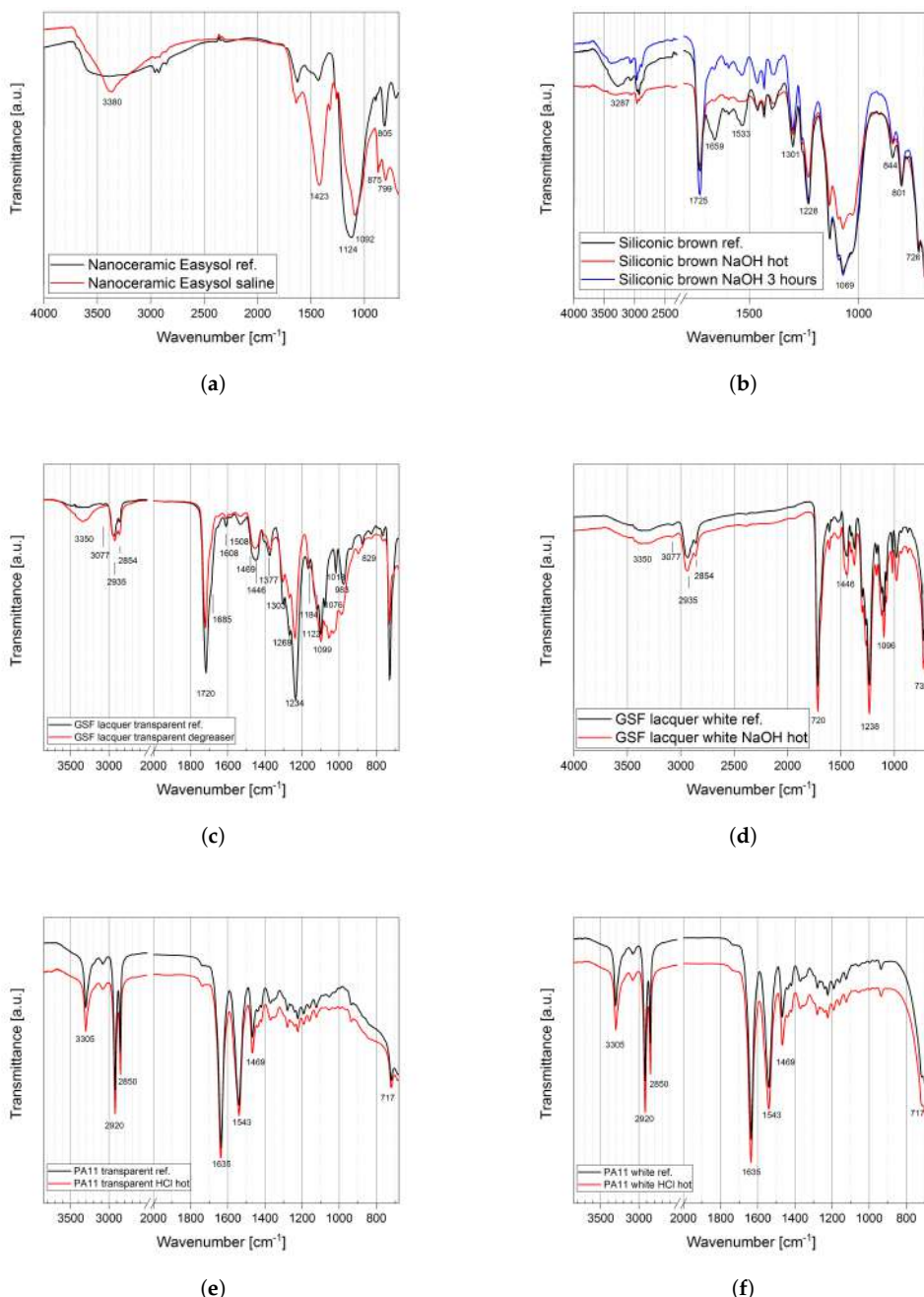
Figure 4. ATR spectra of sample before and after contact with chemicals at different levels of aggressivity to highlight corrosion or inertness of the coatings: (**a**) damages on the transparent nanoceramic coating by the saline solution; (**b**) brown siliconic coating showing slightly different spectra; (**c**,**d**) transparent and white thick GSF lacquers showing that the basic degreaser corroded the transparent coating but not the white one; (**e**,**f**) transparent and white PA11 samples showing no difference between the spectra of the reference and of the spots in contact with hot 4M HCl solution.
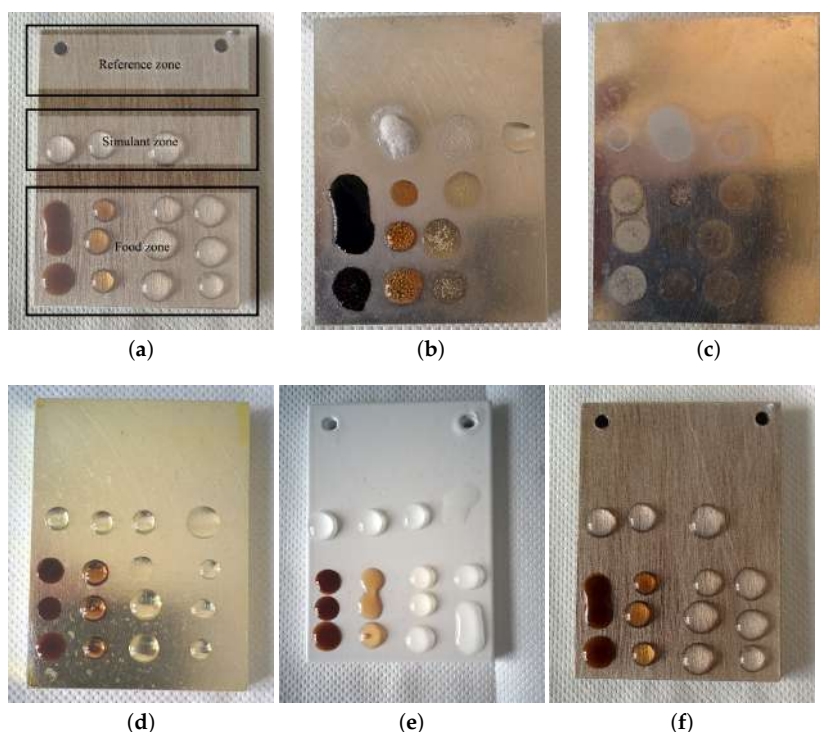
Figure 5. Drop test on uncoated AM60 alloy (top) and (**d**) GSF lacquer, (**e**) white and (**f**) transparent PA11 coatings (bottom); (**a**) shows how samples were divided for the different analyses: In simulant zone the four drops are A, B, C, D solutions; In food zone, from left to right coffee, Coca Cola®, white sparkling wine and 10% acetic acid. (**b**,**c**) show the bare magnesium sample during the test and after rinsing. (**d**–**f**) show GSF transparent lacquer 12 µm, white PA11 and transparent PA11 transparent respectively.

2.2.2. Migration Tests by Dipping and Elemental ICP-OES Analysis

The samples were tested by immersion into the simulant solutions to determine the specific migration from the samples. To perform this test, simulant B, i.e., the most aggressive solution for the alloy among the four suggested by the norm, was chosen. Each beaker was filled with 100 mL of solution B and the samples were dipped in the solution for 24 h at RT. A similar beaker containing only 100 mL of solution B was left in the same conditions to be used as a reference. The simulants were then analyzed by ICP-OES to assess both the presence of the metals that are known to be part of the alloy and of other metals that pose health risks, the aim being on one hand to assess the corrosion protection given by the coating and on the other hand the safety of use. The lacquer GSF 30 µm coating showed the formation of evident bubbles (see Figure 6a) on the edges of the sample. The test was stopped after about 2 h after observing the formation of a dark precipitate in the solution and noticeable corrosion of the edges (see Figure 6b). Despite performing better than the with GSF 40 µm sample, the white siliconic coating proved to not be suited to protect the sharp edges of the standard planar edgy sample and signs of corrosion were observed during the dipping test. Therefore, a new sample with rounded edges was produced and coated with the siliconic brown coating and used for all subsequent tests. Also in this case, despite the stability increased, small bubbles were noticed on the edges, indicating the aggression of the alloy. The specific migration of Mg across the siliconic brown coating resulted in being 1.2(4) mg/dm^2. The complete set of data are reported in table S1. The use of this siliconic coating is therefore limited by the geometry of the sample

when a uniform and thick coating is difficult to achieve such as in the case of sharp parts and/or irregular surfaces.


(**a**)   (**b**)
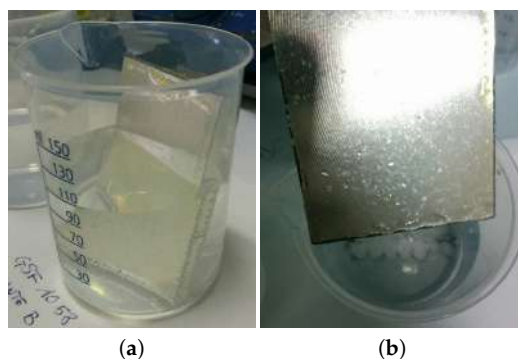
Figure 6. Dipping test on AM60 alloy with lacquer GSF coating during (**a**) and after (**b**) the test.

When testing the PA11 samples, the formation of bubbles was not detected and there were no visible signs of corrosion neither in the white nor in the transparent sample. The ICP-OES measurements did not reveal migration of Mg or other metals from the sample in the simulant B used in the contact. The specific migration for each element calculated from these tests is available in Table S2 in the Supplementary Materials.

The thickness of the coating proved to be a critical factor to prevent corrosion especially when the object has sharp edges, on which the coatings tend to be thinner, and imperfections are more frequent.

The set of tests on prototypes (Figure 7) was carried out on the best performing coatings from the first and second levels drop tests as in Figure 1. Transparent and white PA, the white siliconic coating and the thicker GSF white lacquer 40 µm were tested using simulant A and B at 20 °C for 24 h and at 70 °C for 2 h. Simulant C (10% ethanol) was only tested at 20 °C for 24 h. The cups were filled with 40 mL (small coffee cups,) and 120 mL (large coffee cups,) of simulant. The surface to volume ratios were 1.23 and 0.95, respectively. ICP-OES analysis on the recovered simulants revealed traces of metals in the simulant B that was in contact with the white siliconic and the white GSF lacquer coating for 2 h at 70 °C (Table 3 and Table S2). The specific migration of Mg resulted in being $0.09(5)$ mg/dm^2 for the GSF lacquer and $0.70(2)$ mg/dm^2 for the siliconic coating. The migration of Mg is not limited by the regulations since it does not cause concerns on health, therefore we evaluated it as an indicator of the amount of corrosion. When the corrosion is significant, traces of Al (a known bio-active and possibly harmful element) are also found in the solution, being the main alloying element. Also in this test, the PA coatings proved to be effective in protecting the underlying alloy since no significant amount of magnesium is released from any of the samples coated with PA11. Most releases of toxic metals were below the LOD or, if significant, very small and below the norm values (Table S3). All the results and the calculated specific migration from these samples are reported in the supplementary information file in Table S2. At last, a real world usage was simulated by an "aging coffee test", carried out on the prototypes with PA11 transparent and white coatings, siliconic white coating and with GSF white lacquer using hot coffee. The cups were filled with coffee produced by an Italian Moka and kept continuously in an oven at 60 °C for 24 h to simulate aging. At the end of the test the cups were emptied and washed with water and soap. The result was similar for the PA11 coatings and white GSF lacquer that were stained at the end of the test but kept a perfect adhesion. The mild staining in such conditions of continuous contact with hot coffee should not be a problem in real world conditions where usage is alternated to cleaning. However, to fully pass the "aging coffee test" without any staining of PA11, the only solution is the deposition of an

additional inorganic coating (a preliminary successful test was made by silica deposition by CVD), but it is beyond the scopes of the present work, i.e., exploring low-cost and easily scalable process. The siliconic coating did not pass the "aging coffee test" because even if it was not stained a severe detachment was observed.

(**a**) Lacquer GSF white 40 µm   (**b**) PA11 transparent   (**c**) PA11 white
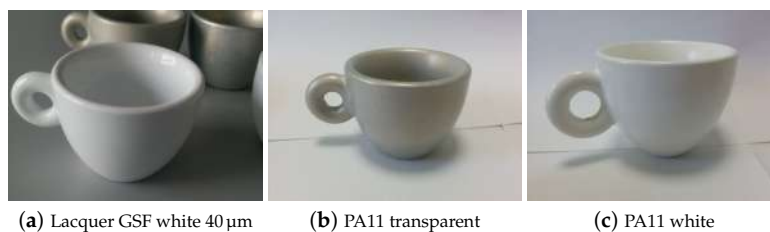
Figure 7. Prototypes of coffee cups made in AM60 magnesium alloy with different coatings.

3. Discussion

The results of the tests and characterizations are discussed in light of the compositional/morphological features of the samples, obtained by SEM/EDX, using literature data as reference. The bare alloy showed moderate reactivity with real drinks and food simulant (Figure 5b,c) suggesting its intrinsic resistance, without any coating [5]. Moreover, also in the presence of corrosion and coating failure during migration tests, a reduced metal migration with the absence of toxic metals was observed, thanks to the AM60 alloy composition and purity: this aspect allows envisaging larger applications of AM60 in food contact and all those fields where low releases of toxic metals are mandatory, as, for instance, medical and dentistry fields. The three investigated classes of coatings showed good to optimal responses when drop tests are carried out, with none or very limited corrosion (Figure 5d–f). The drop test approach resulted very time-saving and gave preliminary indications about the specific resistance of the coating to chemicals and simulants, and, at the same time, allowed an efficient study of the damages by optical and ATR-IR microscopies. Drop tests allowed (i) to exclude the coatings with very poor performance, (ii) to check if preliminary treatments such as tumbling and sandblasting influence the performance of the coating, (iii) to assess that the effects of the primer under the PA11 coating are negligible.

The main limitation of drop test resides in neglecting the shape effects, since edgy and pointy part of the sample are not tested. Migration tests by total immersion of planar samples are complementary to the drop test and they highlighted the limitation of the thinner GSF and silicon-based coatings (10 µm to 20 µm), failing these tests due to the insufficient thickness on the edges and presence of defects. Since the siliconic coating is already rather thick, smoothed edges samples were tested showing limited yet present corrosion, thus suggesting restricted applications of silicon-based coatings and GSF lacquers only on rounded artifacts. The combination of drop and dipping tests allowed selecting the best coating for real world prototypes, e.g., small and large coffee cups (Figure 7). Interestingly, the white version of the organic lacquer (GSF white 40 µm, obtained by adding a titania-based pigment in about 15% weight, to transparent GSF recipe) performed much better in real world tests with hot food. This result can be ascribed to the protective effect of the inorganic additives ($CaCO_3$ and TiO_2 as indicated by SEM/EDX), added for aesthetic purposes. As envisaged by Rong-Gang Hu et al. [7] powder coating allows the preparation of uniform coatings of high thickness that proved to be the most effective in protecting the underlying AM60 alloy and are also environmentally friendly since they do not require the use of polluting solvents. The application of PA11 on AM60 alloy proved to be feasible and the performance of this coating were similar to those obtained when deposed on steel [15]. Biobased PA11, in both transparent and white versions, resulted inert to concentrated acid and basic solutions at room and higher temperature. They resisted also to concentrated salt solutions common in food and marine environments (NaCl) and in the presence of de-icing agents ($CaCl_2$), very important for automotive industry applications. These performances,

despite known on steel [22], were demonstrated for the first time on Mg alloys, showing completely different surface features and reactivity. Moreover, the white PA11 also allows the use of primers to further improve adhesion, without modification of the color, occurring when using a transparent PA11 with a colored primer.

Overall migration tests, performed on the selected PA, organic and silicon-based coatings, allowed to assess their suitability for food industry, where it is important to prevent any migration of metals in the food. ICP-OES measurements reported in the Supplementary materials showed that the best performing coatings are the PA11 ones. Conversely, the analyses on other coatings highlighted signs of permeability, allowing the substrate to be attacked by the simulant solution and therefore releasing Mg and Al.

The SEM micrographs of Figure 8, superimposed to EDX elemental analysis maps allowed explaining the results here above discussed. The PA11 coating (Figure 8a) can be cut from the surface as a "bulky fragment" with homogeneous aspect and without pores and defects, also in a large area of about half a mm. In the bottom right corner a slice of AM60 alloy is visible and was cut attached to the PA11 coating. These features explain the very good adhesion of the coating and its optimal barrier to chemicals to provide the best protection. Conversely, the organic polyester lacquer (Figure 8b) is cut in a tiny and still homogeneous slice, but with evidence of some degree of porosity. This morphology assures a good continuity of the coating explaining the good performance when used in the thicker versions. The pores explain the releases observed in the migration tests. The silicon-based coatings (Figure 8c,d) are vitreous and, when cut, they resulted broken in much smaller fragments, requiring a higher magnification to visualize a single piece. Many fractures are present, explaining the permeability to chemicals and the failures in the aggressive and real world test.

(**a**) PA11 white

(**b**) lacquer GSF white 40 µm

(**c**) Siliconic white

(**d**) Siliconic brown
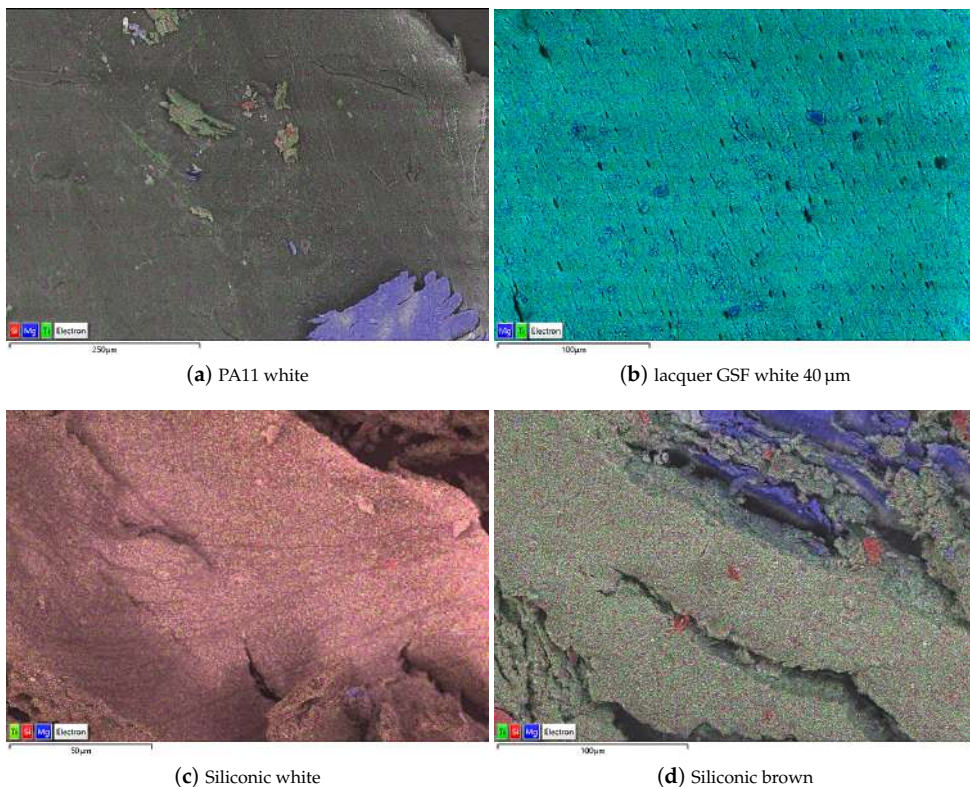
Figure 8. EDS maps of the four samples of the third step of analysis.

4. Conclusions

Considering all the tests (drops, dipping, real world prototypes), the biobased PA11 coating is the unique with no failures. PA11, especially in its white version, resulted thus a good candidate for technological applications of various kinds, from harsh environment (salty, acid and basic chemicals up to 70 °C) to food contact applications. Colored versions of the PA11 coating to fulfill aesthetic purposes, can be easily obtained with commercial grades, already exploited in steel coating industry. The combination of an alloy with low impurity levels to a biobased very stable coating allowed obtaining migration levels of toxic metals beyond detection limits, very interesting for many fields (food but also medical/dentistry). Thanks to its thickness, PA11 showed good performance also with edgy shapes. Its low cost and already known wide applications as steel coating suggests an easy industrialization of the proposed coatings also on magnesium alloys. In fact, the PA11 powder coating can also be deposited by dipping the sample in polymer powder fluidized bed. The powders adhere electrostatically and are then fused and polymerized in an oven. The biobased origin of PA11 suggests a lower environmental impact with respect to other coating and the low or absent toxic metal release an optimal level of biocompatibility. Finally, the chance of easily modifying the PA11 properties as in ref. [18], suggests the possibility of tailoring and improving coating properties to specific purposes, such as improved oxygen barrier effects and/or specific bioactivity such as biocide activity and controlled drug release.

5. Materials and Methods

5.1. Samples

The samples are rectangular pieces 50 mm × 70 mm × 5 mm, with 90° cut edges, if not differently specified, of AM60 magnesium alloy (composition 93.5% magnesium, 6% aluminum, 0.35% manganese and 0.1% zinc), with edgy borders to simulate real world critical shapes. AM60 samples (with this shape or customized) can be purchased by Dongguan Dechuang Hardware Co. (Vanke Center, No. 1, Changqing South Road, Chang 'an Town, Dongguan City, Guangdong Province, China) by Alibaba website [23]. The samples were treated with three classes of coatings. Biobased commercial Polyamide (PA11) coatings called Rilsan® [16], produced by Arkema (Rho, Milano, Italy) was deposited as powder coating, after heating the metallic samples at 200 °C. Four samples were prepared: 2 in a transparent version and 2 in the white one. Coatings were used as purchased and white version contains a standard commercial inorganic pigment as confirmed by SEM/EDS analysis. The samples differ also for the superficial treatments applied to favor the adhesion: one of each color was subjected to tumbling and the other to sandblasting. In a preliminary test, each kind was coated by an epoxy acrylate-based resin solution as primer (commercial name PRIMGREEN LAT 12035) and then powder coated with PA11. However, the primer is slightly yellowish, and it is visible under the transparent PA, with a bad aesthetic effect. Because corrosion performance, in these preliminary tests, was almost independent using the primer, the transparent coatings were applied without the underlying primer. Since the performance of tumbled and sandblasted samples was identical, only sandblasted samples are presented. Then three routes were explored in the family of silicon-based coatings. Nanoceramic Easysol is a transparent coating [24], formulated by polymeric glasses comprising sodium and/or potassium silicate solutions, lithium polysilicate solutions, silanes and water-soluble polysiloxane-based surfactants. Ceramic Techsol is a white coating based on Sol-Gel technology [19], in which hybrid organic/inorganic substances as alkoxides are reacted by heating in water in the presence of a mineral acid and a non-ionic surfactant to obtain a hard and rigid matrix with specific surface properties. The use of an organyl oxysilane species up to 37% in the mixture can increase the hydrophobic behavior of the surface. Siliconic white and brown are polysiloxane-polyester coatings, similar to the Sol-Gel ceramic component but with a more organic character. All silicon-based coatings were produced by SIVE (Cirié, Torino, Italy). The nanoceramic transparent coating was applied by dipping; the sample was then cured at 250 °C. The ceramic coating was obtained

by spraying two different layers, where the overlying layer had a hydrophobic behavior. The siliconic coatings in white and light brown color were applied by spraying the samples and then curing them at 280 °C. Standard polyester lacquers (white and transparent with different thicknesses) typically used for aluminum coating for food application were deposited by spray coating and then cured by UV lamp by Geolac S.r.l. (Tortona, Alessandria, Italy) [20]. The thickness of the siliconing coatings and GSF lacquers were defined by (spraying or dipping) machine parameters. Thickness is increasing from nanoceramic and ceramic coatings (5 µm to 10 µm) to siliconic and GSF lacquers (10 µm to 40 µm) to PA11, where the thickness depend on the size of the starting powders (120 µm to 150 µm). To confirm the coatings' thicknesses, first a profilometer and then the SEM analysis were led, on those samples where a coating slice could be cut in a suitable size for the SEM sample holder. The cross-section of the GSF 40 µm lacquer is reported in Figure S1 of the supplementary information file.

5.2. Solutions

Different liquid solutions were used in the tests with different purposes. To test the possibility of using the alloys in increasingly aggressive real world or laboratory environments, a salt mixture with both 5% w/v of NaCl and 5% w/v of CaCl$_2$ (pH 5.5) and a solution of HCl 1M (pH 0) were used at first. Then NaOH 4M (pH 14), HCl 4M (pH 0) and a concentrated salt mixture with both 10% w/v of NaCl and 10% w/v of CaCl$_2$ (pH 5) were tested on the best performing samples of Table 1. Moving to a household/office environment, aggressive cleaning products such as a commercial basic degreaser (Chanteclair®) and a commercial acid detergent (Cillit Bang®) were tested. At last, food contact tests were performed using deionized water (MilliQ), acetic acid 3% w/v, ethanol 10% v/v and olive oil as food simulants named A, B, C and D respectively, according to UNI EN 1186-3:2002 and acetic acid 10 % w/v as a more aggressive test. Drop tests were also performed using real foods: Coca Cola®, sparkling white wine and hot coffee as produced by an Italian moka (approx. temperature 90° [25]).

5.3. Tests and Analysis Methods

5.3.1. Drop Test

A direct, fast and very simple way of testing the resistance towards corrosion is the drop test. A drop of 30 µL of solution is deposed on the sample at time t_0, then after one hour (t_1), another drop of the same solution and volume is added on the previous drop and another drop is deposed on a new spot. At the end of the second hour t_2 two drops are added on those deposed at t_0 and t_1 and an extra third is deposed. When the test stops, usually after five hours (i.e., four drops) the drops are dried with paper towels and the samples are washed with deionized water and dried. In this way, the time effect can be demonstrated very easily, as can be seen in Figure 5. In the high temperature test, samples were put in a muffle at 50 °C for an hour. For this test, a 40 µL drop was used to compensate for evaporation. Since these analyses are qualitative, no replicates were carried out.

5.3.2. Specific Migration Test

The migration in food simulants is determined using a procedure adapted from UNI EN 1186-1:2003 [26] and UNI EN 1186-3:2003 and the Guidelines on testing conditions for articles in contact with foodstuff [27] that are originally intended for testing plastics, as no specific regulation is available for magnesium alloys and all the used coatings are polymeric. The scope of the test in this case is to assess if the coating can prevent the migration of metals from the alloy. Each coated planar sample was immersed in deionized water (simulant A), or 3% acetic acid (simulant B) or 10% ethanol (simulant C), as showed in Figure 6. Polypropylene beakers with a diameter of 56 mm, height of 80 mm and capacity of 150 mL were used. The samples were immersed in 100 mL of simulant obtaining a surface/volume ratio of about 0.52. The tests were performed in different conditions ranging from 24 h at room temperature to 2 h at 70 °C.

5.3.3. ICP-OES Analysis for Specific Migration Test

The analyses to determine the number of metals in the simulant solutions were carried out by emission spectroscopy by inductively coupled plasma (ICP-OES) using a Spectro Genesis ICP-OES spectrometer (Spectro Analytical Instruments, Kleve, Germany), equipped with a crossflow nebulizer and a Scott spray chamber. After the test, the recovered simulants were prepared for ICP-OES analysis adding 0.1 mL of HNO_3 69% to 1 mL of the solution and then MilliQ water to a volume of 10 mL. The elements were determined considering the spectral line providing the best signal/intensity ratio and on each solution three scans were performed and averaged. After the analysis of each solution the instrument performs a rinse cycle with 1% HNO_3 solution to avoid contamination and memory effect between samples. The specific migration was calculated for each ICP-OES measure with three replicates. The data were multiplied by 10 to account for the dilution and scaled on the initial amount of simulant when evaporation was significant. The avg. of the measures on the reference was subtracted and the result (mg/L) divided by the exposed surface (dm^2) to calculate the specific migration for each element. The three values for each measure were then averaged and the standard deviation calculated. The results are reported in the Supplementary Materials in Tables S1 and S2.

5.3.4. ATR Analysis

The ATR analysis was performed on a Nicolet iN10 by Thermo Fischer Scientific (Waltham, MA, USA) with a Slide-On MicroTip Ge ATR crystal (throughput > 50%, 27° average angle). The detector was cooled with liquid nitrogen. The samples were tested after the drop test with the commercial products and after the aggressive drop test in the oven. A reference on the backside of the sample was first measured, followed by a measurement on the zone of the sample affected by the drop. Each time the background of air was taken before measuring the samples with an acquisition time of 51 s and a total number of acquisitions equal to 256.

5.3.5. Electron and Optical Microscopy

A Hitachi FLEXSEM 1000 equipped with AZtecOne Oxford EDS was used for electron microscopy observation and EDS analysis. A tungsten filament was used as the electron source at 15 kV. The different coating materials were collected from the samples with a cutter and analyzed as such without coating (using low vacuum conditions to prevent samples from charging). Thickness was measured for those samples where a slice could be cut without fragmentation (PA11 and GSF). EDS analysis was performed on an average area of $0.010\ mm^2$ to $0.025\ mm^2$ on SE images. A STEMI 508 microscope with 2× frontal optics, Zeiss fiber optics halogen bulb and 20 MPx SONY sensor camera was used to collect optical images with high resolution.

References

1. Esmaily, M.; Svensson, J.E.; Fajardo, S.; Birbilis, N.; Frankel, G.S.; Virtanen, S.; Johansson, L.G. Fundamentals and advances in magnesium alloy corrosion. *Prog. Mater. Sci.* **2017**, *89*, 92–193. [CrossRef]
2. Aghion, E.; Bronfin, B.; Eliezer, D. The role of magnesium industry in protecting the environment. *J. Mater. Process. Technol.* **2001**, *117*, 381–385. [CrossRef]
3. Song, G.L.; Atrens, A. Corrosion Mechanisms of Magnesium Alloys. *Adv. Eng. Mater.* **1999**, *1*, 11–33. [CrossRef]
4. Moosbrugger, C. Introduction to Magnesium Alloys. In *Engineering Properties of Magnesium Alloys*; ASM International: Novelty, OH, USA, 2017; pp. 1–10.
5. Song, G. Recent progress in corrosion protection of magnesium alloys. *Adv. Eng. Mater.* **2005**, *7*, 563. [CrossRef]
6. Majumdar, J.D.; Galun, R.; Mordike, B.L.; Manna, I. Effect of laser surface melting on corrosion and wear resistance of a commercial magnesium alloy. *Mater. Sci. Eng.* **2003**, *A361*, 119–129. [CrossRef]
7. Hu, R.G.; Zhang, S.; Bu, J.F.; Lin, C.J.; Song, G.L. Recent progress in corrosion protection of magnesium alloys by organic coatings. *Prog. Org. Coat.* **2011**, *73*, 129. [CrossRef]
8. Zhang, K.; Zhang, H.; Liu, P.; Zhang, C.; Li, W.; Chen, X.; Ma, F. Electrophoretic deposition of graphene oxide on NiTi alloy for corrosion prevention. *Vacuum* **2019**, *161*, 276–282. [CrossRef]
9. Parco, M. Investigation of HVOF spraying on magnesium alloys. *Surf. Coat. Technol.* **2006**, *201*, 3269–3274. [CrossRef]
10. Raj, R.V. The characteristics study of HVOF coated AZ91D magnesium alloy with silicon carbide and stainless steel. *AIP Conf. Proc.* **2019**, *2015*, 020024.
11. Rakoch, A.G.; Monakhova, E.P.; Khabibullina, Z.V.; Serdechnova, M.; Blawert, C.; Zheludkevich, M.L.; Gladkova, A.A. Plasma electrolytic oxidation of AZ31 and AZ91 magnesium alloys: Comparison of coatings formation mechanism. *J. Magnes. Alloy.* **2020**, *8*, 587–600. [CrossRef]
12. Sinebryukhov, S.L.; Sidorova, M.V.; Egorkin, V.S.; Nedozorov, P.M.; Ustinov, A.Y.; Volkova, E.F.; Gnedenkov, S.V. Protective oxide coatings on Mg-Mn-Ce, Mg-Zn-Zr, Mg-Al-Zn-Mn, Mg-Zn-Zr-Y, and Mg-Zr-Nd magnesium-based alloys. *Prot. Met. Phys. Chem. Surf. Vol.* **2012**, *48*, 678–687. [CrossRef]
13. Martin, J. The influence of metallurgical state of substrate on the efficiency of plasma electrolytic oxidation (PEO) process on magnesium alloy. *Mater. Des.* **2019**, *178*, 107859. [CrossRef]
14. Borg, P.; Lê, G.; Lebrun, S.; Pées, B. Example of industrial valorisation of derivative products of Castor oil. *Lipides Trop.* **2009**, *16*, 211–214. [CrossRef]
15. Pey, J.L. Corrosion protection of pipes, fittings and component pieces of water treatment and pumping stations. *Anti-Corros. Methods Mater.* **1997**, *44*, 94–99. [CrossRef]
16. Fernández-Álvarez, M.; Velasco, F.; Bautista, A.; Lobo, F.C.M.; Fernes, E.M.; Reis, R.L. Manufacturing and Characterization of Coatings from Polyamide Powders Functionalized with Nanosilica. *Polymers* **2020**, *12*, 2298. [CrossRef] [PubMed]
17. Di Lorenzo, M.L.; Longo, A.; Androsch, R. Polyamide 11/Poly(butylene succinate) Bio-Based Polymer Blends. *Materials* **2019**, *12*, 2833. [CrossRef] [PubMed]
18. Moshynets, O.; Bardeau, J.F.; Tarasyuk, O.; Makhno, S.; Cherniavska, T.; Dzhuzha, O.; Rogalsky, S. Antibiofilm Activity of Polyamide 11 Modified with Thermally Stable Polymeric Biocide Polyhexamethylene Guanidine 2-Naphtalenesulfonate. *Int. J. Mol. Sci.* **2019**, *20*, 348. [CrossRef]
19. Baldi, G.; Cioni, A.; Dami, V.; Barzanti, A.; Lorenzi, G.; Marchese, E.M.; Bitossi, M. Ceramers, Their Application and Use. International Application Number PCT/IB2012/050997, 7 September 2012.
20. Mirone, G.; Pesce, R. Photo-Crosslinkable Multi-Coating System Having Improved Gas Barrier Properties. U.S. Patent US7341791B2, 11 March 2008.
21. UNI EN 1186-3:2003. Materials and Articles in Contact with Foodstuffs-Plastics-Guide to the Selection of Conditions and Test Methods for Overall Migration. 2003. Available online: http://store.uni.com/catalogo/uni-en-1186-3-2003 (accessed on 26 April 2021).
22. Polyamide 11 Coatings Polyamide 11 Coatingsabrasion Resistance Study. Available online: https://www.rilsanfinepowders.com/export/sites/rilsanfinepowders/.content/medias/rfp-downloads/rfp-literature/rfp-cs-polyamide-11-coatings-abrasion-resistance-study.pdf (accessed on 26 April 2021).
23. Dongguan Dechuang Hardware Co. Available online: https://dgdechuang.en.alibaba.com/ (accessed on 26 April 2021).
24. Baldi, G.; Cioni, A.; Valentina, D.A.M.I. Polymeric Glass Based Compositions for Vitreous Coating. U.S. Patent 9,637,642, 2 May 2017.
25. King, W.D. The physics of a stove-top espresso machine. *Am. J. Phys.* **2008**, *76*, 558. [CrossRef]

26.   UNI EN 1186-1:2003. Materials and Articles in Contact with Foodstuffs-Plastics-Test Methods for Overall Migration into Aqueous Food Simulants by Total Immersion. 2003. Available online: http://store.uni.com/catalogo/uni-en-1186-1-2003 (accessed on 26 April 2021).
27.   Simoneau, C. Guidelines on Testing Conditions for Articles. In *Contact with Foodstuffs (with a Focus on Kitchenware)*, 1st ed.; A CRL-NRL-FCM Publication: Luxembourg, 2009.